

High-capacity Optical Wireless Communication by Directed Narrow Beams

Citation for published version (APA):

Koonen, A. M. J. (2023). *High-capacity Optical Wireless Communication by Directed Narrow Beams*. [Phd Thesis 1 (Research TU/e / Graduation TU/e), Electrical Engineering]. Eindhoven University of Technology.

Document status and date:

Published: 12/12/2023

Document Version:

Publisher's PDF, also known as Version of Record (includes final page, issue and volume numbers)

Please check the document version of this publication:

- A submitted manuscript is the version of the article upon submission and before peer-review. There can be important differences between the submitted version and the official published version of record. People interested in the research are advised to contact the author for the final version of the publication, or visit the DOI to the publisher's website.
- The final author version and the galley proof are versions of the publication after peer review.
- The final published version features the final layout of the paper including the volume, issue and page numbers.

[Link to publication](#)

General rights

Copyright and moral rights for the publications made accessible in the public portal are retained by the authors and/or other copyright owners and it is a condition of accessing publications that users recognise and abide by the legal requirements associated with these rights.

- Users may download and print one copy of any publication from the public portal for the purpose of private study or research.
- You may not further distribute the material or use it for any profit-making activity or commercial gain
- You may freely distribute the URL identifying the publication in the public portal.

If the publication is distributed under the terms of Article 25fa of the Dutch Copyright Act, indicated by the "Taverne" license above, please follow below link for the End User Agreement:

www.tue.nl/taverne

Take down policy

If you believe that this document breaches copyright please contact us at:

openaccess@tue.nl

providing details and we will investigate your claim.

High-capacity Optical Wireless Communication by Directed Narrow Beams

PROEFSCHRIFT

ter verkrijging van de graad van doctor aan de Technische Universiteit
Eindhoven, op gezag van de rector magnificus prof.dr. S.K. Lenaerts,
voor een commissie aangewezen door het College voor Promoties,
in het openbaar te verdedigen op 12 december 2023 om 16:00 uur

door

Antonius Marcellus Jozef Koonen

geboren te Oss

Dit proefschrift is goedgekeurd door de promotoren en de samenstelling van de promotiecommissie is als volgt:

voorzitter:	prof.dr.ir. J.P.M. Voeten
1e promotor:	prof.dr.ir. S.M. Heemstra de Groot
2e promotor:	dr.ir. E. Tangdionga
leden:	prof.dr. D.C. O'Brien (University of Oxford)
	prof.dr.dr.(h.c.) J. Capmany Francoy (Universitat Politècnica de València)
	prof.dr. V. Jungnickel (TU Berlin)
	prof.dr.ir. A.B. Smolders
	prof.dr. M. Matters-Kammerer
	prof.dr.ir. I.G.M.M. Niemegeers

Het onderzoek of ontwerp dat in dit proefschrift wordt beschreven is uitgevoerd in overeenstemming met de TU/e Gedragscode Wetenschapsbeoefening.

A catalogue record is available from the Eindhoven University of Technology Library.

ISBN: 978-90-386-5902-2

NUR: 959

Title: *High-capacity Optical Wireless Communication by Directed Narrow Beams*

Author: Antonius Marcellus Jozef Koonen

Eindhoven: Technische Universiteit Eindhoven, 2023. Proefschrift.

Keywords: Optical wireless communication, optical beam steering, bidirectional communication, optical retro-reflector, lens aberrations, device localization, photodiode matrix

Copyright © 2023 by A.M.J. Koonen. All Rights Reserved. No part of this publication may be reproduced, stored in a retrieval system, or transmitted in any form or by any means without the prior written consent of the author.

This research has been supported by the European Research Council in the Advanced Investigator project no. 291632 ‘BROWSE - Beam-steered Reconfigurable Optical-Wireless System for Energy-efficient communication’, and in the Proof-of-Concept project no. 790395 ‘BROWSE+’, as well as by the Netherlands Organization for Scientific Research (NWO) in the Gravitation 2013 project 024.002.033 ‘Research Centre for Integrated Nanophotonics’.

'Numquam minus otiosus sum, quam cum otiosus.'

(I am never as busy as during my leisure hours.)

after *Marcus Tullius Cicero*, 106 - 43 B.C., in *De Officiis III, 1,1*

*Dedicated to Annemie,
Martijn, Robin, Laurens,
and my parents*

Summary

Optical wireless communication (OWC) brings a number of distinct advantages beyond radio-based wireless communication (such as 4G and 5G mobile, WiFi): the visible and near-IR optical spectrum offer orders of magnitude more bandwidth than the RF spectrum (even in the THz frequency bands), crosstalk between users is eliminated by narrow beams and/or opaque walls, the connection is not hampered by electro-magnetic interference nor does it generate EMI, and with narrow beams the energy can be brought only to those places where and when needed, thus yielding high energy efficiency. The small footprints of the beams also support a high user density. By deploying near-IR light such as widely used in fiber-optic communication, relatively high beam powers (up to 10 mW at wavelengths beyond 1.4 μm) can be used without eye safety issues, and OWC systems can build on the vast set of mature optical modules already widely used in fiber-optic networks. In contrast to systems using widely diverging beams (such as LiFi systems), systems using narrow (nearly-) collimated beams ensure a good link power budget which enables high-capacity connections with a longer reach at high user densities, and enhanced privacy.

This thesis surveys our research efforts in high-capacity beam-steered optical wireless communication systems using narrow 2D-steered beams for indoor (/short-to-medium range) service delivery. After discussing the indoor OWC network architecture and its design aspects, it summarizes the key functionalities required and the novel solutions we propose for their realization:

- 2D steering of multiple narrow beams by means of a passive diffractive unit (containing a pair of crossed gratings, or alternatively a high-port-count arrayed waveguide grating router) and remotely tuning the wavelength of each beam's signal,
- accurate and autonomous localization of the OWC receivers in order to aid the beam steering for downstream and upstream communication, by means of passive optical retro-reflector techniques and single-sided beam scanning

algorithms without the need for a pre-existing return channel to confirm adequate beam alignment, and

- broadband wide aperture and wide Field-of View (FoV) energy-efficient optical receivers, which are based on scalable matrices of photodiodes followed by a single preamplifier.

The solutions have been designed, analyzed both analytically and numerically, implemented, and first implementations have been experimentally validated in laboratory demonstrator systems, culminating in bi-directional optical wireless links with a FoV up to ± 10 deg. (full angle) which can bring data at Gigabit Ethernet speeds to up to 128 densely spaced users individually, e.g., for real-time streaming of high-definition video content.

List of acronyms and symbols

Acronyms

2D	two-dimensional
ADR	Angular Diversity Receiver
AoA	Angle of Arrival
ASE	Amplified Stimulated Emission
AWGR	Arrayed Waveguide Grating Router
BER	Bit Error Ratio
BFL	back focal length
BROWSE	Beam-steered Reconfigurable Optical-Wireless System for Energy-efficient communication (ERC Advanced Grant project)
BS-ILC	beam-steered infrared light communication
BW	bandwidth
CapEx	Capital Expenditures
CC	corner cube (retro-reflector)
CCC	Central Communication Controller
CMOS	Complementary Metal Oxide Semiconductor
CoG	Center of Gravity
CPC	Compound Parabolic Concentrator
CWDM	Coarse Wavelength Division Multiplexing
CW	continuous wave
DBR	Distributed Bragg Reflector
DMT	Discrete Multi-Tone (modulation)
DS	downstream
DSB	Double Side-Band
DWDM	Dense Wavelength Division Multiplexing
EDFA	Erbium-Doped Fiber Amplifier
EFL	Effective Focal Length
EMI	Electro-Magnetic Interference
ERC	European Research Council
FoV	Field of View
FP	Fabry Perot (cavity)
FSR	Free Spectral Range
FttH	Fiber-to-the-Home
FWHM	Full Width at Half Maximum

GPON	Gigabit Passive Optical Network
GEAPON	Gigabit Ethernet Passive Optical Network
HD	high definition (video)
IEEE	Institute of Electrical and Electronics Engineers
IM	intensity modulation
IoT	Internet of Things
IR	infrared
ISM	Industrial, Scientific and Medical (frequency bands)
ITU	International Telecommunication Union
LD	laser diode
LED	Light Emitting Diode
LiFi	Light Fidelity
LO	local oscillator
LoS	Line of Sight
MD	mobile device
MDU	Multi-Dwelling Unit
MEMS	Micro Electro-Mechanical System
MGDM	Mode Group Division Multiplexing
MIMO	Multiple Input Multiple Output
MMF	Multi-Mode Fiber
MZI	Mach Zehnder Interferometer
MZM	Mach Zehnder Modulator
NA	Numerical Aperture
NLoS	Non-Line-of-Sight
NPV	Net Present Value
NRZ	Non-Return-to-Zero (modulation)
NWO	Nederlandse Organisatie voor Wetenschappelijk Onderzoek (Netherlands Organization for Scientific Research)
O/E	Optical-to-Electrical (conversion)
OOK	On-Off Keying (modulation)
OPA	Optical Phased Array
OpEx	Operating Expenses
OWC	Optical Wireless Communication
OXC	Optical Crossconnect
PAA	Phased Array Antenna
PAM	Pulse Amplitude Modulation
PD	photodiode
PDL	Polarization-Dependent Loss
PIC	Photonic Integrated Circuit
PMMA	Polymethylmethacrylaat
POF	Plastic Optical Fiber
PON	Passive Optical Network

PRA	Pencil Radiating Antenna
PRBS	Pseudo-Random Bit Sequence
P2P	point-to-point
P2MP	point-to-multipoint
QAM	Quadrature Amplitude Modulation
RAP	Radio Access Point
REAM	Reflective Electro-Absorption Modulator
RF	radio frequency
RG	Residential Gateway
RoF	Radio over Fiber
RR	retro-reflector
RSS	Received Signal Strength
Rx	receiver
SDM	Spatial Division Multiplexing
SGC	Surface Grating Coupler
SLM	Spatial Light Modulator
SMF	Single-Mode Fiber
SOA	Semiconductor Optical Amplifier
SSB	Single Sideband
TDM	Time Division Multiplexing
TDMA	Time Division Multiple Access
TIA	Transimpedance amplifier
TRL	Technology Readiness Level
TRx	transceiver
TTD	True Time Delay
Tx	transmitter
US	upstream
USP	Unique Selling Point
UTC	uni-traveling-carrier (photodiode)
UWB	ultra-wideband (radio)
VCSEL	Vertical Cavity Surface Emitting Laser diode
VIPA	Virtually Imaged Phased Array
VLC	Visible Light Communication
WDM	Wavelength Division Multiplexing
XG-PON	10-Gigabit-capable passive optical network

Symbols

α	incidence angle (of optical beam)
$\Delta\lambda_{\text{tun}}$	wavelength tuning range
$\Delta\lambda_{\text{FSR}}$	wavelength Free Spectral Range
η	fill factor (of photodiode matrix)

η_A	radiation efficiency (of an antenna)
λ	wavelength (of light, or radio wave)
φ, ψ	beam steering angles (in two dimensions)
ω	radial frequency
c_0	speed of light (in vacuum)
C_d	capacitance of photodiode
D_A	directivity (of an antenna)
D_{beam}	beam diameter
D_{lens}	lens diameter
f	focal length (of a lens)
G_A	antenna gain
H	room height
K	numbers of rays in a beam (in ray tracing)
K, M	dimensions of matrix (of photodiodes)
L	length and width (of square area covered by optical beam steerer)
M, N	dimensions of matrix (of fibers in AWGR optical beam steerer)
m	order of interference
p	defocusing parameter
P_{beam}	power of a beam
\mathcal{R}	responsivity (of a photodiode)
R_d	resistance (parallel resistance in photodiode)
R_s	resistance (serial resistance in photodiode)
w_0	mode field radius (of Gaussian beam at its minimum width)

Table of Contents

Summary	vii
List of acronyms and symbols	ix
Acronyms	ix
Symbols	xi
Table of Contents	xiii
1 Introduction.....	1
1.1 Motivation.....	1
1.2 Scope of the thesis	5
1.3 Structure of the thesis.....	6
1.4 References.....	11
2 Photonic home area networks	13
2.1 Introduction.....	13
2.2 Economics of home networks	17
2.3 Optical fibers for in-home networks	23
2.4 Residential Gateway	26
2.5 High-capacity transmission for wirebound delivery of services.....	26
2.6 High-capacity transmission for wireless delivery of services.....	31
2.7 Converged indoor networks	36
2.8 2D radio beam steering in a radio-over-fiber system.....	38
2.8.1 Radio beam steering	38
2.8.2 Wavelength-controlled 2D TTD radio beam steering	40
2.8.3 Integrated 2D TTD beam steering circuit.....	43
2.8.4 Conclusions	44

2.9	Dynamic capacity allocation	45
2.10	Mode Group Division Multiplexing.....	46
2.11	Optical wireless communication	47
2.11.1	Eye safety	48
2.11.2	Optical wireless communication using visible light	49
2.11.3	Optical wireless communication using infrared light	50
2.12	Evolution trends	52
2.13	Concluding remarks	54
2.14	References.....	55
3	Optical wireless communication technologies.....	61
3.1	Introduction.....	61
3.2	OWC's application domains	63
3.3	Indoor OWC techniques.....	64
3.4	Visible Light Communication techniques.....	67
3.5	Light Fidelity (LiFi) techniques	69
3.6	Beam-steered IR optical communication techniques	69
3.6.1	Active beam-steering devices	70
3.6.2	Passive beam-steering devices.....	71
3.7	OWC receiver.....	76
3.8	Localization.....	78
3.9	Hybrid Optical/Radio wireless Networks	80
3.10	Beam-steered OWC vs. wide-beam OWC	82
3.10.1	Electromagnetic interference	82
3.10.2	Data capacity per device.....	83
3.10.3	Latency	84
3.10.4	Energy efficiency.....	85
3.11	Photonic integrated circuits for optical wireless communication	88
3.11.1	Photonic integrated OWC transmitters.....	89
3.11.2	Photonic integrated OWC receivers	91

3.12	Concluding remarks	94
3.13	References.....	95
4	Beam-steered indoor OWC system.....	103
4.1	The BROWSE system concept	105
4.2	2D beam steering using diffractive means	108
4.3	The indoor fiber backbone network	113
4.3.1	Hybrid OWC downstream/RF upstream system	114
4.4	Concluding remarks	116
4.5	References.....	117
5	Beam steering techniques for indoor OWC	121
5.1	Introduction.....	121
5.2	2D diffractive beam steerer using crossed gratings	122
5.2.1	Beam steerer design.....	122
5.2.2	System experiments.....	130
5.2.3	Concluding remarks	133
5.3	2D diffractive beam steerer using an AWGR and 2D fiber array	133
5.3.1	Beam steerer design.....	134
5.3.2	System experiments.....	141
5.3.3	Concluding remarks	146
5.4	2D beam steering by mechanical translators.....	147
5.4.1	Concluding remarks	148
5.5	Summarizing conclusions	149
5.6	References.....	150
6	User localization	155
6.1	Introduction	155
6.2	Localization in an indoor beam-steered system	156
6.3	Localization when using discrete diffractive beam steering	158
6.3.1	Matrix of miniature corner cubes	159
6.3.2	System experiments.....	163

6.3.3	Concluding remarks.....	167
6.4	Localization when using analog mechanical beam steering	168
6.4.1	Center-of-gravity algorithm.....	168
6.4.2	Impact of lens aberrations on beam alignment accuracy.....	170
6.4.3	System experiments.....	175
6.4.4	Concluding remarks.....	178
6.5	Summarizing conclusions	178
6.6	References	178
7	Broadband OWC receiver with wide Field-of-View	181
7.1	Receiver based on a matrix of photodiodes	182
7.1.1	Frequency characteristics	185
7.1.2	Bias conditions in the photodiode matrix	186
7.1.3	SNR performance	192
7.1.4	Comparison with angular diversity receiver.....	194
7.2	Capturing the optical beam by the photodiode matrix	195
7.2.1	Theoretical analysis of the beam-to-photodiode matrix coupling.....	196
7.2.2	Numerical analysis of the beam-to-photodiode matrix coupling.....	199
7.2.3	Impact of the fill factor of the photodiode matrix	204
7.2.4	Shifting the receiver's aperture over the beam's footprint	206
7.2.4.1	Impact of crosstalk from neighbouring cells.....	206
7.2.4.2	Impact of cropping the beam's spot by the lens' aperture....	213
7.3	Implementing the receiver.....	216
7.4	Experimental validation	220
7.5	Scaling the PD matrix	222
7.6	Concluding remarks	223
7.7	References	224
8	Bidirectional all-optical OWC indoor system.....	226
8.1	Introduction.....	226
8.2	Bidirectional OWC system architecture.....	227

8.3	Upstream optical path design.....	229
8.4	System demonstrator.....	231
8.5	Conclusions.....	236
8.6	References.....	237
9	Conclusions and outlook on further research.....	239
9.1	Conclusions.....	239
9.2	Outlook and suggestions for further research	242
9.2.1	Applying the OWC key functions in other OWC domains	243
9.2.2	Photonic integration	243
9.2.3	Next 2D beam steering concepts	244
9.2.4	Next localization schemes	245
9.2.5	Next OWC receiver concepts	245
9.2.6	New OWC networking aspects	246
9.3	References.....	247
Appendix A: 3D ray tracing.....		249
A.1	Elementary 3D ray tracing algorithms	249
A.1.1.	3D ray propagation modelling.....	249
A.1.2.	Reflection	251
A.1.3.	Ideal thin lens	251
A.1.4.	Refraction at a plane surface boundary	252
A.1.5.	Refraction at a spherical surface boundary	252
A.2	Homogeneous ray launching.....	254
A.3	Aspheric Fresnel lens modelling.....	260
A.3.1.	Some Fresnel lens design results	262
A.4	References.....	266
List of publications		267
Curriculum vitae		273
Acknowledgments.....		275

1 Introduction

1.1 Motivation

Since its first introduction in field trial networks in the early seventies, optical fiber has rapidly become the medium-of-choice for data transport in communication networks, starting in long-distance links, next in regional and metropolitan networks, and since a few years also conquering the last kilometers to the home. Fiber widely outperforms copper-based cables by its very low losses and low dispersion, and has pushed the transport capacity of communication networks to great heights. Moreover, its wavelength dimension provides a multiplier for transport capacity, as well as extra traffic routing functionalities. Recently, exploiting the spatial dimension in few-moded fiber has raised the capacity and flexibility even further.

The powerful Internet as we know it today would not have been possible without fiber. Fiber has already arrived at the doorstep of many households. Extending its potential into the home, however, has not truly happened. The outdoor fiber highway is handed-over to a variety of copper- and radio-based indoor networks, and only part of the high bandwidth potential of fiber is experienced by the indoor users.

On the other hand, there is a fast rise of capacity demand by the users and their devices. The variety of services offered by the Internet is booming, encompassing tele-shopping, tele-education, tele-conferencing, entertainment, ultra-high definition video streaming, large file transfer, and many more; the traffic volume they generate is enormous (Fig. 1-1). The number of users of the Internet is increasing fast (Fig. 1-2), and most of them access the internet by wireless devices (laptops, smartphones). In particular, video-based services require a large share of the capacity of the home access network. Moreover, there are also intra-home data transport needs, such as posed by the transport of the broadband data streams and large files between the in-home laptops, tablet computers, smart phones, video and audio sets, networked attached storage (NAS) units, scanners, printers, etc., as well as by transport of bursty low-volume data between various home devices being part of the Internet-of-Things (IoT; see Fig. 1-3). The intra-home traffic volume may exceed the traffic volume going into/out of the home, making the load on the in-home network even heavier.



Fig. 1-1 What happens on the Internet worldwide in 2023 in every minute (source: eDiscovery Today & LTMG)

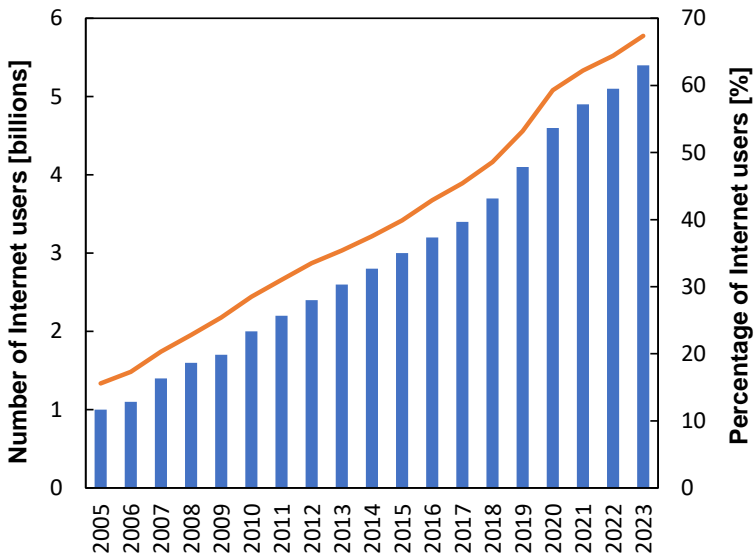


Fig. 1-2 Growth of the number of individuals using the Internet (source: ITU, Dec. 2022)

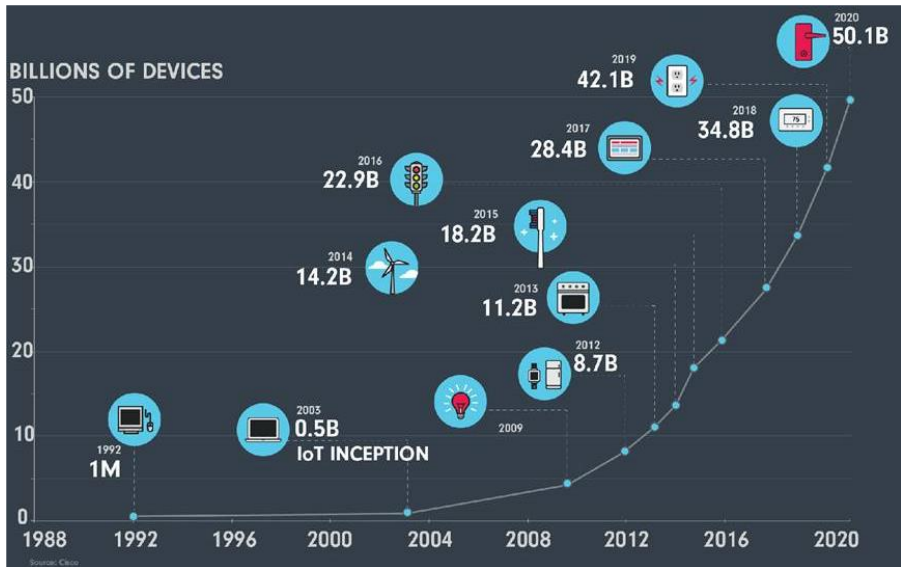


Fig. 1-3 Growth of the Internet-of-Things (source: NCTA)

Hence, following their successes in the public network, photonic solutions also should be considered for the indoor network. Moreover, the use of multi-wavelength technology can enable the convergence of different service families within a single fiber infrastructure, which saves indoor network installation costs.

The users increasingly prefer wireless service delivery instead of wire-bound delivery, thus getting more freedom in their mobility and reducing installation efforts of the indoor physical cabling infrastructure. Radio-based wireless indoor networks are widely deployed, in particular WiFi ones operating in the 2.5 and 5GHz bands. The use of mm-wave and microwave technologies (e.g., 60GHz and sub-THz) is being considered for extra bandwidth, and for creating pico-cell network architectures in order to increase the network's aggregate capacity by spatial multiplexing. Radio-over-fiber for such high frequencies can combine the best of two worlds, and by photonic integrated circuitry powerful microwave signal processing can be done [1][2]. The load on the radio-based networks is booming, fueled by the growth of the number of IoT devices as well as of the bandwidth needs of broadband services. This growth is leading to radio spectrum congestion and incidentally even is resulting in service denials. Optical wireless communication (OWC) by means of dedicated free-space optical technologies can open a huge amount of additional spectrum and enhance the wireless service delivery capabilities in many domains [3]-[5].

Indoors, OWC can counteract the congestion of the radio spectrum, and can offload much traffic from the radio-based network [6]. It also offers enhanced

privacy and reduces crosstalk from/into neighbouring rooms as it does not penetrate walls. The additional spectrum needs no licenses. Moreover, OWC is immune to electro-magnetic interference (EMI), and also does not generate EMI itself. OWC, however, needs line-of-sight (LoS), which WiFi technology does not. In OWC even with non-directive receivers LoS is needed, as the reception of LoS signals is much stronger than of diffuse non-LoS signals. When using mm-waves (with frequencies in the range 30-300GHz) LoS is needed as well, as they need directional antennas with high gain for establishing the transmission link power budget according to Friis' transmission equation [7]

$$\frac{P_R}{P_T} = G_T G_R \left(\frac{\lambda}{4 \pi d} \right)^2 \quad (1-1)$$

where P_T is the power fed into the transmitter antenna terminal, P_R the power out of the receiver antenna terminal, G_T and G_R are the gain of the transmitter and receiver antenna, respectively, d is the length of the mm-wave propagation path, and λ is the (short) wavelength of the mm-wave. WiFi typically uses frequency bands in the 2.5 and 5GHz region, and thus has lower radio path losses than mm-waves; these frequencies can even penetrate through walls (which compromises privacy). By offloading the broadband traffic, the optical wireless communication network creates adequate room for the radio wireless network to handle the large amount of lower volume (bursty) traffic flows, in particular the traffic for IoT devices which may need to operate in non-line of sight (NLoS) conditions [8].

Outdoors, OWC can bring a range of benefits as well and can offer relief for overloading of the radio spectrum and other issues. Unlike in indoor networks, atmospheric effects (fog, rain, snow, air turbulence) can hamper the optical path, causing loss and phase fluctuations in it (scintillation [9]). For the particular case of underwater communication, radio transmission is not feasible and compared to sonar OWC can provide transmission at higher data rates which e.g., is useful for video inspection by and control of unmanned underwater maintenance/repair robots [10]. While the short reach of OWC links for indoor applications typically is a few meters only and is limited to some tens of meters, for outdoor it can be considerably longer. Medium reach free-space optics (FSO) applications encompass, e.g., fixed optical wireless access to remote buildings, backhaul links for mobile telephony base stations, mobile communication on the road between vehicles and vehicle-to-roadside, street level communication, inter-drones communication, communication in big outdoor areas such as sport stadiums and outdoor festivals. Examples of long to ultra-long FSO applications are ground-to-airplane, ground-to-satellite, and inter-satellite communication [11]. Medium to

(ultra-) long optical wireless links can be established with OWC technologies deploying narrow (nearly) collimated optical beams which are carefully steered to their receiver destinations; the reach of wide diverging beams is strongly power-limited and thus reach-limited. The steering of such narrow beams needs to be highly accurate and their divergence very small, in particular for establishing long-reach links, hence requiring sophisticated beam-steering and -shaping techniques. On the other hand, the Field-of-View of the receiver typically does not need to be as large as for short-reach indoor communication, as typically in long-reach links only a single beam is used (or very few beams) of which the incident angle at the receiver varies only over a tiny angle.

1.2 Scope of the thesis

The research described in this thesis has focused on OWC system architectures and techniques to be applied in the domain of short-reach indoor communication, with the goal to enable the delivery of broadband services wirelessly to indoor users and devices at high user densities, while complementing radio-based wireless techniques such as the IEEE 802.11 WiFi suite. It should enable the wireless extension of the data highway capabilities of (fiber) access networks to users and devices individually, as well as support intra-building high-capacity data communication.

The research described has in particular been focused on the architecture and enabling techniques for indoor short-reach OWC by means of narrow 2D-steered beams which can bring the powerful functionalities of optical fiber wirelessly. Next to the general advantages of OWC (such as no need for spectrum licensing, and the adding of the ample bandwidth available in the optical spectrum), beam-steered infrared light communication (BS-ILC) can bring a number of particularly powerful advantages with respect to radio-based wireless communication and wide-beam OWC:

- it can offer very high (fiber-like) capacity to users individually. The transport performance of a narrow infrared beam may theoretically even exceed that of an optical fiber, as unlike a fiber an optical beam is not affected by waveguide dispersion. As the beams are highly directive and each follow a single path, no multi-path effects and their associated fading occur. The larger bandwidth of the beam link may reduce the signal processing efforts needed for compressing the signal's bandwidth, and thus reduce the latency time incurred during that processing. Moreover, the latency of the beam link is about 33% smaller than of an equally-long silica fiber link due to the refractive index of the fiber core

glass. The latency reduction increases the link capacity in bi-directional operation, such as in machine-to-machine communication.

- high user densities. Due to the small footprint of a beam, very small picocells can be created, which enables dense spatial division multiplexing.
- a high privacy and security level. Light does not penetrate walls, and the small footprint ensures negligible crosstalk with nearby users.
- high energy efficiency. The beams are directed on demand, so only there where and when needed.
- immunity for externally originated EMI, and it also does not generate EMI itself.
- it can build on the mature optical device technologies already readily available and widely used in optical fiber networks.

BS-ILC also has a few disadvantages:

- Line-of-Sight (LoS) is needed for a beam to reach a user (work-arounds can be devised, such as applying multiple spatially separated beam steerers which can create alternative paths and may be arranged in a multiple-input multiple-output (MIMO) setting, or adaptively relaying by reflective surfaces, at the cost of comprehensive control measures and signal processing).
- accurate beam steering and user tracking is needed, which takes time and compromises mobility of the user (hence, the BS-ILC is mainly intended to serve nomadic and static users/devices who/which do not require connectivity when moving; this operation mode may often hold in delivery of broadband services such as high-definition video streaming and exchanging large data files).
- the beam steering and tracking also makes the higher layer protocols more complex; extra room (in-band in the time domain, or out-of-band in the frequency domain) is needed to coordinate the network control plane with the data plane.
- when using multiple beam steerers, the beam steering needs to be coordinated among them in order to avoid interference; this requires additional protocols.

1.3 Structure of the thesis

The research described in this thesis is about the studies done to bring the benefits of optical communication into the indoor domain of the individual users, both in their professional work environment and their residential environment. It has

largely been published in a range of journal and conference papers, and also has been laid down in a number of patents. The adjective ‘indoor’ in combination with communication networks is used to distinguish it from ‘outdoor’ networks, i.e., in an environment not governed by strict regulations of standards and largely set up by the user(s) according to his/their personal wishes, not hampered by atmospheric effects, and typically involving short reach links (up to a few tens of meters).

Chapter 2 introduces the potential of optical technologies to enhance the performance of indoor communication networks, and among these technologies positions the research in optical wireless communication described in this thesis. It discusses how photonic technologies can be introduced in indoor networks in order to bridge the gap between the capacity offered by the optical fiber-to-the-home (FttH) access network and the capacity accessible for the users, and also in order to improve the intra-home network performance. Indoor networks have to carry a large variety of services, with widely differing needs regarding e.g., bandwidth, quality of service, and reliability. They have to support both wirebound and wireless connectivity, at low costs and low energy consumption levels. The chapter reviews the architectures, economics (both from an installation and an operational viewpoint), and techniques for converged optical fiber indoor networks which are cost- and energy-efficient, and compares them with current copper-based solutions. Particular attention is given to high-capacity multimode (plastic) optical fiber techniques, radio-over-fiber techniques including adaptive radio beam steering, techniques for providing capacity on demand, and optical wireless communication techniques. An evolution perspective is outlined how the growing indoor communication demands can be met by gradually introducing these powerful techniques and network architectures.

Chapter 3 zooms in on optical wireless communication as the main topic of this thesis. OWC offers powerful solutions for resolving the imminent capacity crunch of radio-based wireless networks. OWC is not intended to fully replace radio wireless techniques such as WiFi, but to rather complement these and off-load their high traffic loads. After discussing OWC’s strengths in various application domains, a non-exhaustive tutorial overview is given of two major directions in OWC: wide-coverage visible light communication (VLC) and LiFi which build on LED illumination techniques and shares capacity among multiple devices, and communication with narrow 2-dimensionally steered infrared beams which offers unshared high capacity to devices individually. The latter constitutes

the main area of research addressed in this thesis. A non-exhaustive review is given of the research on key techniques supporting beam-steered OWC: active and passive beam steering techniques, device localization, wide Field-of-View receivers. Their application in bi-directional hybrid optical/radio networks and bi-directional all-optical wireless networks is discussed. The performance characteristics of beam-steered OWC are compared with those of wide-beam OWC (encompassing VLC and LiFi), and of the radio-based IEEE 802.11 systems (the WiFi suite), regarding sensitivity for electro-magnetic interference (EMI), data capacity available per device, latency, and energy efficiency aspects. Photonic integration will become a key enabler for the introduction of indoor OWC; a non-exhaustive review is given of photonic integrated circuit (PIC) solutions for OWC beam-steered transmitters and receivers.

Chapter 4 outlines the architecture we propose for indoor broadband beam-steered OWC systems, termed the ‘BROWSE - Beam-steered Reconfigurable Optical-Wireless System for Energy-efficient communication’ architecture. The architecture comprises a broadband fiber backbone network feeding the optical data streams to the rooms, in which they are conveyed by optical free-space beams to the individual users/devices. The BROWSE network design guidelines are derived, which serve as the basis for the design of the OWC key functionalities (beam steering, localization, wide Field-of-View reception). The architecture is intended to provide broadband services wirelessly on demand where and when needed to individual users, tailored to their wishes. By e.g. using passive modules for the beam steering at the ceiling sites (the network access points), it intends to centralize the active service delivery functions and control functions as much as possible in order to ease upgrading and maintenance, and reduce energy consumption.

Chapter 5 focuses on techniques for the adaptive indoor 2D beam steering to multiple users individually who are not stationary. For downstream, beams to the users are to be emitted from a common ceiling unit in a point-to-multipoint scheme. Diffractive techniques are investigated where the wavelength of each data signal fed to the beam steerer determines in which 2D direction the associated beam is steered. Two options are analyzed in depth: using a pair of crossed diffraction gratings which enables semi-continuous steering, and using an arrayed waveguide grating wavelength demultiplexer of which the output ports are arranged in front of a lens shaping the beams which enables discrete steering. Both options include only passive elements which minimize maintenance efforts and failure risks, and are readily scalable to serve more users individually by just

feeding more wavelengths. Moreover, the signals can be generated remotely by tunable laser diode transmitters, which facilitates greatly upgrading of the system. For upstream beam steering, continuous beam steering deploying a 2D electro-mechanical translator stage is investigated. Laser diodes with an arbitrary wavelength can be used, which is attractive for the cost-sensitive user terminal; there, diffractive steering is less attractive as wavelength tunable sources and their control entail higher costs.

Chapter 6 deals with techniques to localize the user, which is a key requirement for automatic operation of indoor OWC networks. Accurate device localization for steering the beams is required. Self-calibrated localization has been investigated by beam scanning and deploying optical retro-reflector technologies at the target device, in particular foils containing matrices of miniature corner cube reflectors, which enable monitoring of the reflected power of the incident scanning beam. This approach avoids the need for a pre-existing return path, which eases the set-up of an OWC link per user. Also, parallax errors are avoided which can occur when the localization and the signal reception aperture are physically separated; the compensation of such errors would need a pre-established calibration process. For downstream, localizing each user individually is done by scanning with a relatively wide downstream beam in order to reduce the time needed for scanning the full user area in conjunction with monitoring the reflected power from the retro-reflecting foil at the user's device. For upstream, in order to save battery power and enhance eye safety at the user side, each user device launches a narrow beam fitting within the aperture of the ceiling's receiver. By means of beam scanning and a center-of-gravity algorithm accurate upstream beam alignment is achieved. The design considerations, performance analysis, implementation and experimental validation of both localization methods are discussed.

Chapter 7 discusses the research efforts to create a broadband OWC receiver with large aperture as well as large Field-of-View. Such characteristics are attractive for avoiding tedious alignment efforts of the receiver with respect to the beam steerer. The approach proposed involves a novel concept of arranging identical high-speed photodiodes in a 2D matrix and interconnecting them in such a way that the bandwidth of the photodiode matrix receiver equals the bandwidth of an individual photodiode. When applying the matrix and carefully designing the receiver's lens collecting the beam's power, the attainable receiver's performance enhancement in terms of Field-of-View and captured optical power has been assessed both analytically and numerically by extensive ray tracing. The studies include the tolerance against moving the receiver across the footprint of a

beam, the signal-to-noise performance in comparison with other OWC receiver concepts, and the impact of upscaling the photodiode matrix. Implementation of the receiver's concept and its validation in a laboratory testbed is discussed.

Chapter 8 discusses the design and implementation of a bi-directional all-optical wireless communication system. Hybrid bi-directional systems have been reported which deploy downstream optical links and RF upstream links, in which part of OWC's key advantages such as EMI-immunity may be lost. Alternatively, all-optical bi-directional systems have been reported which duplicate the downstream technology and re-use it for the upstream link. This approach does not align well with the more cost- and space-effective point-to-multipoint (P2MP) physical architecture according to BROWSE having a single ceiling unit serving multiple users. We propose a P2MP architecture for a bi-directional all-optical wireless communication system which builds on the key functions we designed, analyzed and realized in chapters 5 – 7. We validated its performance in our laboratory OWC system testbed, and demonstrated real-time streaming of high-definition video streams at Gigabit Ethernet (GbE) speed to closely spaced users individually with their laptop computers.

Chapter 9 summarizes the main findings of this thesis, and provides an outlook on how further steps can be made towards elevating the bi-directional broadband beam-steered OWC system to higher technology-readiness levels (TRLs).

Appendix A describes the methods for 3-dimensional ray tracing which the author has developed for modelling the propagation of rays in homogeneous media, the refraction of a ray at a plane and at a spherical surface boundary between two media with different refractive index, and the reflection of a ray at a surface boundary. Thus, ray propagation through (multi-element) spherical lenses can be analyzed, including the occurrence of various lens aberrations. Also, a ray tracing model has been developed for a Fresnel lens with large numerical aperture which fully corrects for spherical aberration. These methods have been implemented for numerical processing in MATLAB programs, and have been extensively used for analyzing the imaging of the received beams onto the photodetector and thus analyzing the performance of the OWC receiver concepts presented in chapter 7. The ray tracing programs actually enable to do 'virtual lab experiments' in which the parameters of the optical modules can be changed easily, and thus provide valuable support for optimizing the design of an OWC system.

1.4 References

- [1] J. Capmany, D. Novak, "Microwave photonics combines two worlds," *Nature Photonics* | Vol. 1, June 2007, www.nature.com/naturephotonics
- [2] José Capmany, Beatriz Ortega, Daniel Pastor, "A tutorial on microwave photonic filters," *J. of Lightw. Technol.*, Vol. 24, No. 1, Jan. 2006, pp. 201-229. <https://doi.org/10.1109/JLT.2005.860478>.
- [3] H. Haas, J. Elmighani, I. White, "Optical wireless communication," *Philosophical Trans. Royal Soc. A*, Mar. 2020, 11 pp., <https://doi.org/10.1098/rsta.2020.0051>
- [4] D.C. O'Brien, S. Rajbhandari, H. Chun, "Transmitter and receiver technologies for optical wireless," *Philosophical Trans. Royal Soc. A*, Mar. 2020, 21 pp., <https://doi.org/10.1098/rsta.2019.0182>
- [5] A.M.J. Koonen, "Optical wireless systems: technology, trends and applications," *webinar IEEE Phot. Soc.*, Feb. 21, 2018, <https://www.photonicssociety.org/education-careers/webinars/optical-wireless-communication-webinar>
- [6] A. M. J. Koonen, K. A. Mekonnen, Z. Cao, F. M. Huijskens, N.-Q. Pham, E. Tangdiongga, "Ultra-high capacity wireless communication by means of steered narrow optical beams," *Philosophical Trans. Royal Soc. A*, Mar. 2020, 19 pp., <https://doi.org/10.1098/rsta.2019.0192>
- [7] Friis' transmission equation for wireless links [on-line]. Available: https://en.wikipedia.org/wiki/Friis_transmission_equation
- [8] J.P. Linnartz, C.R.B Corrêa, T.E.B. Cunha, E. Tangdiongga, T. Koonen, X. Deng, M. Wendt, A. Abbo, P.J. Stobbelaar, M. Müller, D. Behnke, M. Vazquez, S.V. Colouques, M. Bech, T. Metin, M. Emmelmann, S.M. Kouhini, K.L. Bober, C. Kottke, V. Jungnickel, "ELIoT: New features in LiFi for next-generation IoT," *Proc. ECOC2021*, Bordeaux, Sep. 2021, paper WO5.
- [9] Ahmed; S. Gupta; Y. Luthra; K. Gupta; S. Kaur, "Analysing the effect of scintillation on free space optics using different scintillation models," *Proc. 6th Internat. conf. on Signal Processing and Integrated Networks (SPIN)*, Mar. 7-8, pp. 799-804, <https://doi.org/10.1109/SPIN.2019.8711574>
- [10] Ke Wang, T. Song, Y. Wang, C. Fang, J. He, A. Nirmalathas, C. Lim, E. Wong, S. Kandeepan, "Evolution of short-range optical wireless communications," *J. of Lightw. Technol.*, Vol. 41, No. 4, Feb. 2023, pp. 1019-1040, <https://doi.org/10.1109/JLT.2022.3215590>
- [11] Laser satellite communication, cf. [online] <https://www.tno.nl/en/sustainable/space-scientific-instrumentation/satellite-communication/laser-satellite-communication/>

2 Photonic home area networks¹

2.1 Introduction

Home area networks, unlike many other communication networks, are a domain where optical fiber has not made significant inroads yet. Fiber has arrived at the doorsteps of our homes in fiber-to-the-home (FtTH) access networks, but its huge capabilities are yet to be extended up to the users' devices inside the home [1]. Current home networks are predominantly a mixture of different network technologies, each originally optimized to carry a particular kind of communication services. Coaxial cable networks were installed to connect television and radio receiver sets and video recorders, twisted-pair copper lines to connect telephone sets and facsimile machines, and Cat-5 unshielded twisted pair cables to connect desktop PCs, printers, scanners, data storage units, and so on. Power line communication (PLC) technologies have also emerged to offer data connectivity without requiring new cabling. In the last decades wireless connectivity by means of wireless LAN IEEE 802.11 technology (WiFi) has become more and more popular, replacing partly wired networks in serving laptop computers, tablet computers, smartphones, and many more wireless gadgets appearing in the Internet-of-Things environment. The booming number of wireless devices is causing congestion in the Industrial, Scientific and Medical (ISM) radio spectrum, and their mutual interference is hampering reliable communication. Trends are emerging to transition to pico-cells, which cover smaller areas in the home (such as a single room, or even parts of a room) and thus reduce the interference and congestion issues within a radio cell. The pico-cells approach implies the requirement for more radio antenna stations, which need to be simplified for cost reasons and need connectivity to a wired indoor backbone network.

¹ This chapter is largely based on A.M.J. Koonen, E. Tangdiongga, "Photonic home area networks," *IEEE/OSA J. of Lightwave Technology*, vol. 32, no. 4, Feb. 2014, pp. 591-604.

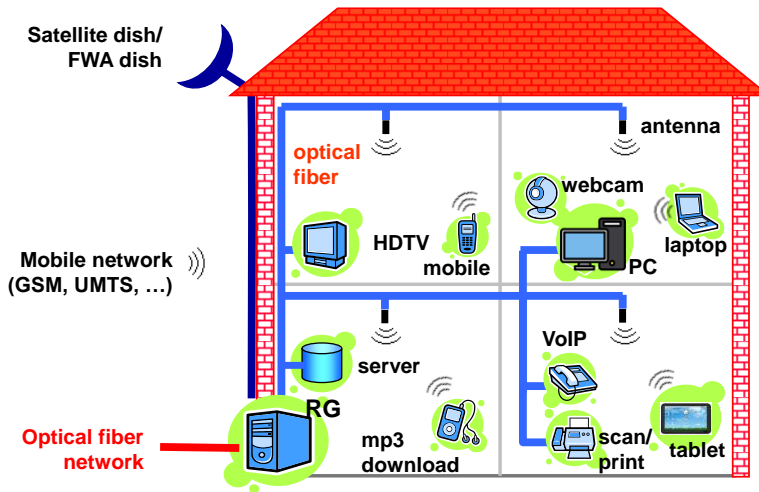


Fig. 2-1 Converged indoor network

The co-existence of so many different indoor networks entails considerable installation and maintenance costs. It also complicates the upgrade to new service types, and the inter-operation of services running on multiple platforms (e.g., between video sets and computers). Moreover, these networks show bandwidth limitations that prohibit the extension of the broadband capabilities of the (FtH) access network to the users. It is noteworthy that the bandwidth demand from in-home networks may even exceed the demand on the FttH access line, due to for instance the home-internal fast data streaming needs to and from servers. E.g., transferring a DVD movie of 4.7GB within 10 seconds requires a rate of 3.8Gbit/s; a BluRay movie of 50GB even 40Gbit/s. All these issues could be alleviated significantly by a converged indoor network architecture with truly broadband capabilities, i.e., a single broadband network architecture which is capable of carrying many types of services simultaneously without mutual interference nor design compromises. Research has started to look into optical fiber for such converged novel indoor network solutions, as illustrated in Fig. 2-1. By its virtues of high bandwidth, low losses, small dimensions and insensitivity for electromagnetic interference (EMI), optical fiber is an eminent candidate to integrate a wealth of services within a single network.

In designing in-home communication networks, one may note a range of differences with access networks. The latter are owned by a network operator, are installed by professionals with high-tech tools, need to conform to standards and run standardized protocols (e.g., in Fiber-to-the-Home (FtH) there are GEPON, GPON, XGPON,...), are installed with a return-on-investment perspective, and their costs are to be shared by many households. An in-home network, however, is (predominantly) privately owned, it should be easy to use ('plug-and-play') not requiring professionals, the user decides himself which equipment to install, and

that single household has to bear all the costs. Obviously, the design of home networks and their technologies needs a quite different approach from that of operator-owned outdoor networks.

The interface rates with which consumer electronic devices want to communicate are rising fast. As illustrated in Fig. 2-2 and Fig. 2-3, the most demanding ones already require more than 10Gbit/s and in the near future the bandwidth demands keep growing [4][7][8]. The dominant connected consumer device in the home is the smartphone, with on average 6 of them per home. Video traffic is driving the bandwidth needs, and virtual reality applications need even larger bandwidths. With respect to the consumer demands, copper and WLAN network technologies (WiFi), however, are seriously lagging. Clearly new network technologies are needed to bridge this gap. As already proven in outdoor network domains, optical fiber is the best suited technology for wired connectivity, and optical wireless communication will become an important complement to radio-based wireless communication.

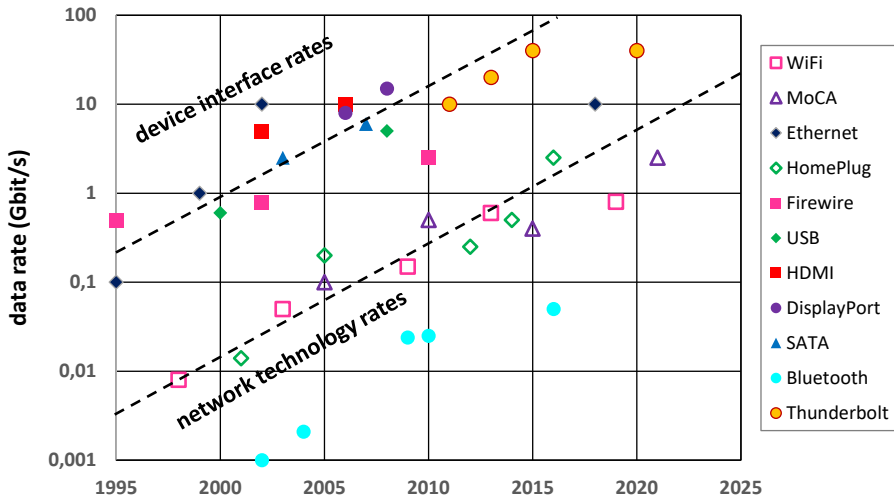


Fig. 2-2 Evolution of interface rates of consumer devices and of data capacity of wireless and copper-based indoor network technologies (from [4], updated)

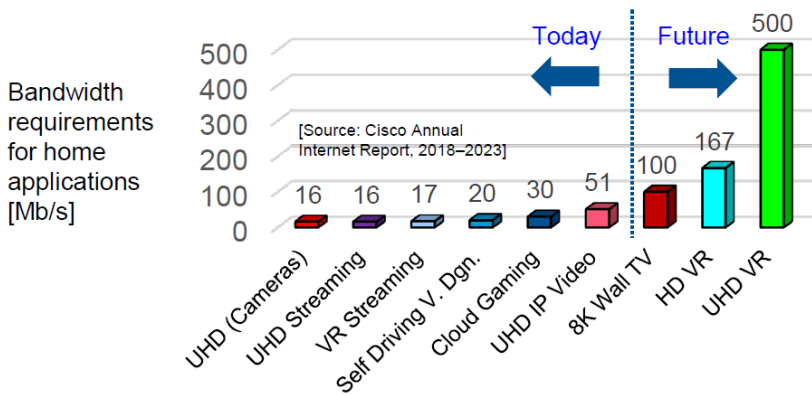


Fig. 2-3 Consumer devices are requiring ever more bandwidth [7][8]

In the remainder of this chapter, in section 2.2 first the economic viability of photonic network solutions is assessed in comparison with established copper-based network solutions (Cat-5e), in order to identify which network topology is to be preferred for which application area. The chapter proceeds in section 2.3 with discussing the pros and cons of different optical fiber types, identifying which type suits which application field, and paying special attention to multimode large-core polymer optical fiber (POF) as a fiber type particularly suited for cost-efficient (do-it-yourself) installation in in-home networks. However, such POF has technical performance limitations, notably a severely restricted bandwidth. After briefly describing in section 2.4 the functionalities of the residential gateway (the bridge between the access and the in-home network), in sections 2.5 and 2.6 techniques are discussed which enable to overcome the bandwidth restrictions and enable the wirebound delivery of high-capacity data streams in particular via POF and with advanced modulation methods, and the wireless delivery by radio signals (in particular by radio-over-fiber techniques) of high-capacity services. It subsequently discusses in section 2.7 how services for wirebound and wireless devices can together be delivered by means of a converged network approach. Techniques for advanced network functions are described: 2D radio beam steering by optical techniques in radio-over-fiber systems in section 2.8, dynamic routing of signals in the photonic in-home network in order to better meet fluctuating capacity demands and avoid congestion in section 2.9, and mode group division multiplexing as an interesting option to open an additional dimension for increasing the capacity and routing flexibility of multimode fiber in-home networks in section 2.10. To solve radio spectrum congestion issues, in section 2.11 optical wireless communication (OWC) techniques and their strong potential to solve this congestion are discussed as an advanced alternative for radio wireless communication (indoor OWC will be the main topic in the remainder of this thesis). To conclude, in

section 2.12 an evolution path is outlined along which the overviewed communication techniques and network solutions may be introduced in order to meet the evolving in-home network capacity needs. Concluding remarks about the potential of optical techniques for indoor communication are made in section 2.13.

2.2 Economics of home networks²

The residential home is a very cost-sensitive environment. The lifetime costs of a home network infrastructure may be split in its installation costs (CapEx – capital expenditure) and operational costs (OpEx – operational expenditure) which include powering and maintenance [2].

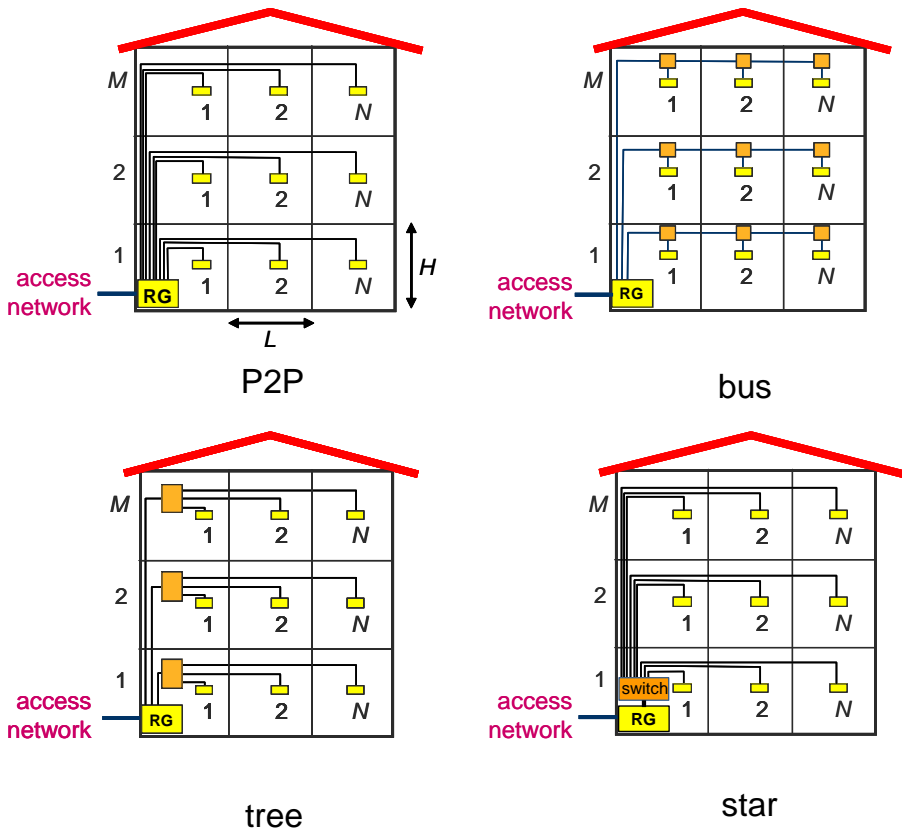


Fig. 2-4 In-building network architectures

² This section is largely based on A.M.J. Koonen, H.P.A. van den Boom, E. Ortego Martinez, A. Pizzinat, Ph. Guignard, B. Lannoo, C.M. Okonkwo, and E. Tangdiangga, "Cost optimization of optical in-building networks", *Opt. Exp.*, vol. 19, no. 26, pp. B399-B405, Nov. 2011.

The CapEx is largely dominated by the choices made for the network topology and for the network medium. In order to gain a basic insight in the impact of these choices, one may consider four fundamental network topologies, as illustrated in Fig. 2-4: point-to-point (P2P), bus, tree, and star. In practice, hybrid versions of these topologies may be used, depending on the design of the building. A residential gateway (RG) is interfacing the in-home network with the access network. In the P2P topology, individual cables run from the RG to every room in the building. The bus and tree are point-to-multipoint (P2MP) topologies, in which a riser cable connects the RG to a floor. In the bus topology, the rooms on that floor are served by add/drop nodes positioned along a horizontal cable, whereas in the tree topology the rooms are served by individual horizontal cables connected to a star splitter node. Up to now, LAN structured cabling solutions typically use a star topology with an Ethernet switch at the star splitting point (close to the RG); its physical topology corresponds largely to the P2P topology.

The P2P topology obviously requires the highest amount of cabling, which may lead to high installation costs and duct congestion issues, in particular in larger buildings. On the other hand, it eases the maintenance and upgrading per room. For smaller buildings, such as single-family homes, the amount of cabling may still be acceptable. In the P2MP bus and tree topologies, there is cable sharing and multiple access techniques are needed to give each room an appropriate share of the cable's capacity. When using fiber as the network medium, the network splitting nodes internally may use active opto-electronic-optical (OEO) signal conversion for signal routing (such as in Ethernet hubs and switches), or passive optical signal splitting functions such as optical power splitting or wavelength routing. The bus topology is the most cable-lean and needs the least duct space, but also requires many add/drop nodes (and thus consumes more power in case of active nodes). The tree topology needs only a single splitter node, but requires more cabling and duct space. In general, P2P topologies may be preferred for smaller buildings (such as single-family homes), whereas tree or bus topologies are preferred for larger buildings (apartment buildings, office buildings, etc.). When in the P2P physical topology an optical star coupler is deployed at the RG, a passive multipoint-to-multipoint (MP2MP) architecture can be established in which the rooms can communicate transparently with each other through this coupler.

For the network medium, optical fiber is the most powerful choice, as outlined in the introduction of this section. Moreover, as it is EMI-insensitive and not electrically conducting, it can be co-installed with electrical power cabling in the same ducts. For safety reasons, this is not allowed for coaxial cables nor for Cat-x cables; they require separate (new) ducts. Cat-5e is presently the most popular cabling for connecting Ethernet-based devices, and therefore a good benchmark for assessing the economics of fiber-based home networks. Several optical fiber types may be considered for in-home deployment (see section 2.3): silica single-

mode fiber (SMF), silica multimode fiber (MMF), and plastic optical fiber (POF). Large-core POF is in particular interesting due to its ease of connectorizing and splicing [3]; 1mm core diameter POF requires only low-precision connectors or even does not need a connector as the bare ends may be simply cut and inserted into a module or butt-faced together. Silica SMF and MMF require dedicated tools, delicate handling and skilled personnel for installation, and thus incur higher installation costs. On the other hand, for silica SMF (and to a lesser extent for MMF) a wide range of modules is readily available for upgrading the network by power splitting and wavelength multiplexing for hosting more users and services. Large-core POF is more lossy and has more dispersion than silica SMF and MMF. The main benefit of large-core POF is therefore its suitability for cost-effective ‘do-it-yourself’ installation in indoor links with limited length and limited bandwidth needs.

The OpEx is considered over the lifetime of the home’s network and is largely attributable to the power consumption costs. When SMF is used, the add/drop nodes and the splitter nodes in the P2MP topologies can be implemented by passive optical power splitting or wavelength routing modules, which minimizes the power consumption to only the power consumption of the O/E modules at the edges of the network. These passive optical modules are fully transparent: they can operate with any type of signal format. An SMF-based in-home network with passive optical nodes is therefore not only the most power consumption-lean solution, it also is the most future-proof solution as it is robust to handle upgrading to any new signal format and to multiple service bundles carried on separate wavelengths. For SMF networks, optical power splitters and wavelength routers are commercially widely available and enable the implementation of physically point-to-multipoint network topologies which can offer advantages in installation (in contrast to today’s the point-to-point topologies for Ethernet-based home networks). Optical power splitters and wavelength routers are not readily available (yet) for MMF networks. Hence the add/drop nodes and splitter nodes for MMF and POF networks need O/E conversion at their I/O ports plus internal electrical signal splitting/routing functions. These nodes may therefore not be able to transport any type of signal format (they are ‘opaque’), and they perform active functions which are power-consuming. For Ethernet signals, such nodes are commonly known as Ethernet hubs and switches.

We have made CapEx and OpEx analyses for the various basic topologies P2P, bus and tree, for the cases of SMF, MMF and POF cabling, with Cat-5e cabling as a benchmark [2]. The analyses were made for three building scenarios: single-family residential home (3 floors, 4 rooms/floor; floor spacing 3.3 meters, duct length between rooms 8 meters), multi-dwelling units building (MDU, a.k.a. apartment building; 10 floors, 16 living units per floor; floor spacing 4.0 meters, duct length between rooms 14 meters), and office building (10 floors, 50 office units/floor; floor spacing 3.8 meters, duct length between rooms 10 meters). The

analysis results are critically dependent on the assumptions regarding the costs and the power consumption of the network elements. These assumptions have been based on Fast Ethernet (100Mbit/s) equipment and on market surveys done in 2010; the survey outcomes are represented by the typical values listed in Table 2-1.

Table 2-1 Costs and power consumption of the network items

	Cat-5E	POF*	SMF	MMF
Installed cable costs	1.8 €/m	1.7 €/m	1.74 €/m	1.95 €/m
Max. link length	100 m	70 m	1000 m	550 m
Mounted connector costs	13 €	3 €	15 € **	14 € **
Media converter costs; power consumption	(negligible); 0.65 W	30 €; 0.85 W	70 €; 1.15 W	40 €; 1.15 W
Hub/tap costs; power consumption	20 €; 0.2 W	20 €; 0.2 W	20€; 0.2 W	20€; 0.2 W
Switch costs, power consumption	10 €/port; 0.3 W/port	10€/port; 0.3 W/port	10 €/port; 0.3 W/port	10 €/port; 0.3 W/port

Prices are based on market surveys done in 2010

* for \varnothing 1mm large-core PMMA POF

** these prices vary considerably for the various connector types and their mounting methods; we assumed SC connectors, and about 10 minutes in-field mounting time per connector (labour costs about 10€)

The fiber solutions allow sharing of the ducts with the electrical power cabling, whereas the Cat-5e solutions need new ducts. Duct costs are dependent on the duct mounting methods (e.g., buried inside a wall, or mounted on a wall) and the duct diameter, so on the number of cables in the duct and the cable diameter. Building on the topology and network element assumptions, CapEx and OpEx for the various scenarios have been assessed [2].

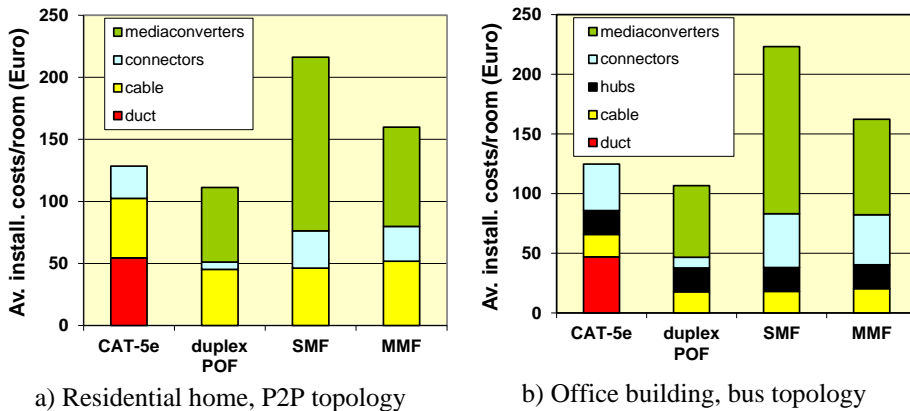


Fig. 2-5 Network installation costs per room for various cabling media

From a CapEx perspective, it has been found that the installation costs for the residential home scenario are lowest when adopting a P2P topology. The optical fiber cables may be installed in the same (existing) ducts as the electrical power cables, but this duct sharing is not allowed for Cat-5e cables due to electrical

shock hazards. Exploiting this duct-sharing advantage of the fiber solutions which Cat-5e do not have, Fig. 2-5.a shows the average installation costs per room for the various cabling choices (note that these are calculated with the 2010 price levels from Table 2-1, which have changed since then; the relative price comparison between the cabling choices should still hold in reasonably good approximation). It illustrates that duplex POF cabling (i.e., two POFs jointly being a bidirectional link) is already cost-competitive with the mature Cat-5e solutions, notwithstanding the fact that POF technologies are just at the beginning of a learning curve. POF technologies have not reached large market volumes yet, and hence have not experienced yet the price reductions accompanying economy-of-scale. For the office building scenario, it is found that a bus topology is the most cost-effective. Again, as Fig. 2-5.b shows, duplex POF cabling is already cost-competitive with Cat-5e cabling. In both scenarios, the ease of connecting and the lower costs of the O/E media converters are the main CapEx-saving factors offered by the POF solutions, and put them in a better position than the silica SMF and MMF solutions.

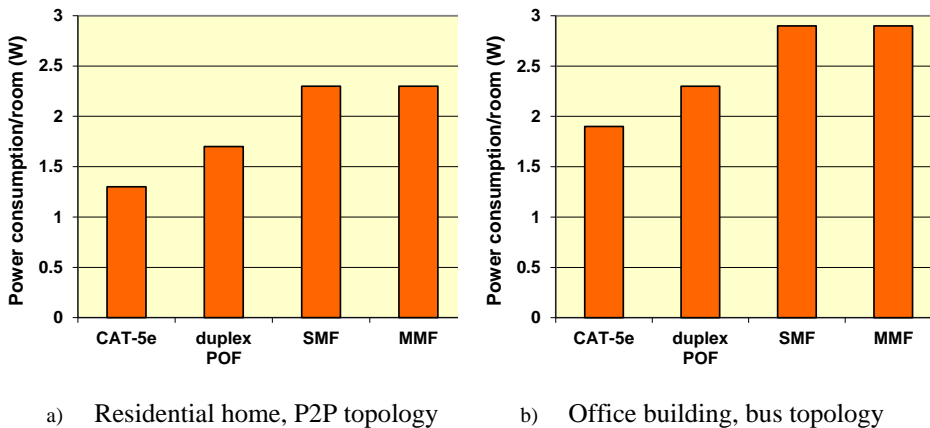


Fig. 2-6 Power consumption per room for various cabling media

From an OpEx perspective, the power consumption in the active network elements has been assessed using the data from Table 2-1, which includes the O/E media converters at the terminals of these elements and the active hubs and switches in the P2MP bus and tree topologies. For the residential home scenario, obviously the P2P topology is the most power-lean. As shown in Fig. 2-6.a, the POF solution consumes a bit more power than the Cat-5e one, but less than the SMF and MMF solutions. For large buildings, a tree topology needs fewer active elements than a bus topology. The advantage of reduced power consumption of the tree topology may, however, be offset by the larger amount of horizontal cabling needed causing duct congestion. Hence, we consider the bus topology as

the preferred one for large buildings. Due to the active network nodes, the power consumption per room is slightly higher than for the residential home scenario. Fig. 2-6.b confirms that also for the office scenario the POF solution performs slightly worse than the Cat-5e solutions, but better than the SMF and MMF ones.

To assess the total costs incurred during the lifetime of the in-home network, both the CapEx (the installation costs, occurring once at the beginning of the life cycle) and the OpEx (the operational costs, accumulating during the life cycle) have to be taken into account [2]. These costs may be partitioned in labor costs, material costs, and energy costs. Assumptions have been made on the expected evolution of these costs in the future, on the breakdown in labor costs and material costs per installed network item, and on a typical lifetime of 25 years of the in-home network infrastructure. E.g., it is assumed that labor costs will rise with a money inflation rate of 2% per year, energy costs will rise 5% per year, POF product prices will drop with 10% per year due to a growing market volume, SMF and MMF prices rise by 2% per year due to inflation, and Cat-5e cable prices will rise with 5% per year due to copper becoming more scarce. For the residential home scenario with P2P topology, the impact of these trends on the Net Present Value (i.e., eliminating the impact of money inflation) of the total network costs per room has been assessed.

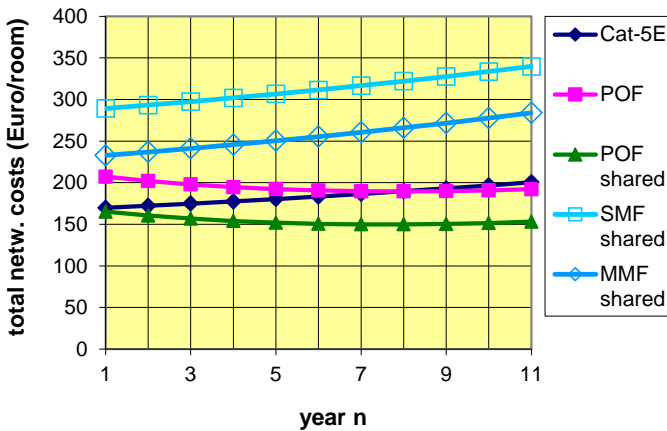


Fig. 2-7 Comparison of total lifetime costs of the network

Fig. 2-7 shows how the NPV evolves when installing the network in year n (where $n=1$ means today). The graphs basically underline that POF can be more cost-effective than SMF and MMF installations. And they show that if one has to install an in-home network today and duct sharing is possible (and the reach and bandwidth limits are not prohibitive for the POF solution), POF is already a better choice than Cat-5e from the perspective of minimization of total costs. If duct sharing is not possible, then Cat-5e is the better choice, but in the near future POF

may already offer an economically more attractive solution.

In summary, it may be concluded that optical fiber solutions are attractive for in-home networks not only in a technical performance sense, but also in an economic sense. In particular when ease-of-installation is a first priority, solutions based on POF are attractive. Depending on adoption in the mass market and associated decline of component prices, POF may gain wide deployment, notably in (do-it-yourself) home networks. When in the (near) future upgrading to higher demands on bandwidth and reach is expected, silica SMF or MMF may be the better option. As a disclaimer, it should be noted that the cost analysis presented is based on 2010 market survey studies, and the results should be interpreted as an approximate comparison of costs to provide guidance among the media and network topology options.

2.3 Optical fibers for in-home networks

The demands put on optical fiber for in-home applications differ in several respects from those for outdoor applications. As in-home link lengths are relatively short, the performances regarding bandwidth \times length product and regarding attenuation per unit length are less important. On the other hand, ease of handling (splicing, connectorization), bend-insensitivity, small cable diameter, flexibility and small form-factor connectors are more relevant factors [3]. A larger core diameter and a higher numerical aperture make alignment errors in fiber connectors and splices less serious. Hence, the installation of multimode silica and plastic optical fiber is easier than that of single-mode fiber and thus entails lower labor costs. A larger core also implies that small dust particles and scratches on the fiber endface are less harmful in connectors.

Fig. 2-8 shows a comparison of the core sizes of some well-known fiber types (all drawn with the same scaling factor). In silica fibers, a trench of glass with a lower refractive index around the core can enforce the modes to stay inside the core, and thus makes the fiber less sensitive to bends. Bend-insensitive silica graded-index multimode fiber (GI-MMF) has become available commercially, e.g. with an 80 μ m core diameter and large numerical aperture $NA=0.29$; for a 3mm bend diameter, it can have >7 dB less loss than OM1 and OM2 GI-MMF [4]. OM4 silica MMF with 50 μ m core diameter and ≥ 4.7 GHz \times km with 7.5mm minimum bending radius is commercially available and particularly attractive for data center networks and LANs [5]. Also bend-insensitive SMF conform standard ITU G.652.A2 with a minimum bending radius of 7.5mm is on the market [6].

Plastic (/polymer) optical fiber (POF) is commercially available and particularly easy to handle due to its ductility and large core diameters of up to 1mm [9]. The POF cables are easy to install together with electrical power wires by pulling them through the same ducts. The large core diameters allow manual butt-joint splicing by unskilled people while precision tools are not needed nor a

microscope. Connector ferrules may not even be needed; the POF can be cut by for instance a razor blade and the POF's bare end may be directly inserted in a module to make a fiber connection.

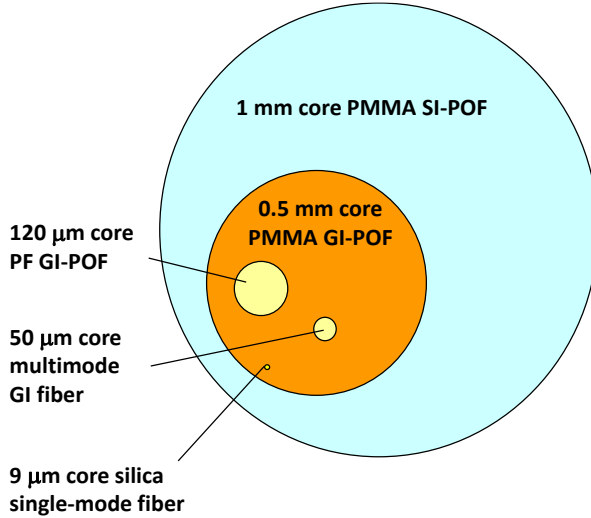
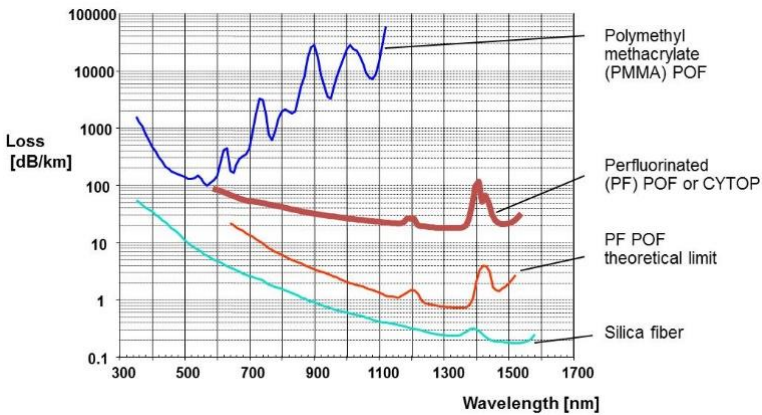
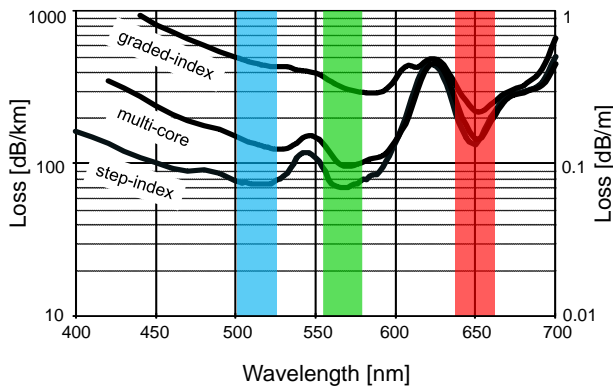


Fig. 2-8 Core diameters of various fiber types

The optical properties of POF are, however, clearly less good than those of silica fiber. The production processes of silica fiber have since the '70-s evolved to very sophisticated levels, and silica fiber losses have attained extremely low levels. Polymethylmethacrylate (PMMA) is the most popular material for making POF; it is widely known as Perspex or plexiglass. The attenuation performance of PMMA-POF versus wavelength is shown in Fig. 2-9.



a) Loss versus wavelength of silica fiber and of various types of POF



b) Loss in the visible wavelength range of various types of PMMA-POF

Fig. 2-9 Losses of POF

The losses are lowest around $\lambda=550\text{nm}$ (green light), but still around 70-100dB/km; the C-H bonds cause a quickly rising loss at longer wavelengths. PMMA-POF is therefore only applicable in the visible wavelength range, from say 450 to 700nm. Replacing these C-H bonds partly by C-F bonds gives an extended low-loss characteristic up to more than 1350nm; this so-called perfluorinated POF (PF-POF) thus allows the use of similar laser diodes and photodiodes as used for silica fiber systems [10]. Although the losses can reach around 20dB/km and thus are considerably lower than for PMMA-POF, they are still much higher than for silica fiber (ca. 0.3dB/km at $\lambda=1.3\mu\text{m}$). The fluoride-content of POF may bring some issues in installation with respect to low smoke zero halogen (LSZH) constraints. PF-POF is commercially available up to limited core diameters, up to 250 μm , typically 50-62 μm . As outlined before, because a large core diameter is desired and in view of the relatively short links in in-home networks the fiber loss per unit length is less important, PMMA has become the most popular POF material. The limited wavelength operation range of PMMA-POF, $\lambda=450$ to 700nm, implies that visible light must be used for communication. As operational optical power levels are typically low this can be perceived safely by the naked human eye, which allows visual inspection for network diagnostics and thus eases installation, in particular for do-it-yourself purposes.

Several options for the refractive index profile of the core are available for large 1mm-core diameter PMMA-POF. The most simple and easy-to-produce profile is the step-index profile (SI-POF). This 1mm core diameter SI-POF with an $NA=0.5$ has become the most popular, mass-produced POF, and has been standardized according to IEC 60793-2-40 class A4a.2. Such a profile suffers from heavy multimodal dispersion, and hence has a poor bandwidth \times length product, in particular for such a large NA . Up to link lengths of around 50 meters, simple on-off keyed modulated data streams of up to 1Gbit/s can be carried.

Fiber bends down to a radius of about 5mm are allowable. The large core can also be composed of many small cores, which each guide a part of the total optical signal. Such PMMA multi-core POF (MC-POF) offers a slightly better bandwidth, and most importantly a much better bending performance; down to 3mm bending radius is allowable [11]. For data rates beyond 1Gbit/s, a graded-index refractive index profile is needed, which offers much less modal dispersion. Large 1mm-core PMMA graded-index POF (GI-POF) is, however, more sensitive for bending than SI-POF. Modified GI-POF designs have been proposed using a more complex core index profile [12] or a non-PMMA core material to yield a higher numerical aperture [13]; these designs have shown a bending sensitivity comparable with SI-POF. With smaller core diameters, so at the expense of more difficult handling, perfluorinated GI-POF can enable much higher data rates in the order of tens of Gbit/s [24]. Micro-structured POF designs have been explored in research laboratories, which can combine low bending losses with large bandwidths, but again at the expense of a smaller core size [14].

Sections 2.5 and 2.6 will expand on the suitability of various PMMA-POF types in wirebound and wireless system applications, respectively.

2.4 Residential Gateway

As illustrated in Fig. 2-1, the residential gateway (RG) provides the interfacing between the (FttH) access network and the in-home network. It should translate IP addresses and modulation formats to match those of the in-home devices. It may provide the opportunity to external third parties to do maintenance and upgrading of services in the in-home network, and to do remote diagnostics and performance measurements. On the other hand, it should also ensure the security and privacy of the residential users. In addition, the RG may host several home-internal functions, such as the local storage of data (file server) and the intermediation to allow interoperation of devices in the home. In view of the evolving user demands, the data rates of these home-internal data streams may surpass the data rate of the access network line (and are already doing that today; cf. 1Gbit Ethernet home networks vs. 100Mbit/s VDSL or FttH access lines), which underlines once more the importance of a truly broadband services-converged home network.

2.5 High-capacity transmission for wirebound delivery of services

Large-core POF is attractive due to its ease of installation, but on the other hand it hampers high data rate transmission by its poor bandwidth \times length performance due to modal dispersion. Three roads may be pursued to surmount the bandwidth barrier. Baseband amplitude modulation formats may be used in combination

with strong equalization techniques at the receiver, e.g., binary on-off signaling, or multi-level pulse amplitude modulation schemes which reduce the symbol rate (e.g., 4-level PAM, 8-PAM). Secondly, a single-carrier technique may be used with a quadrature amplitude modulation scheme, which combines more bits into a symbol (e.g., 16-QAM carrying 4 bits/symbol, or quadrature phase shift keying, QPSK, carrying 2 bits/symbol). Thirdly, multiple carriers may be used in parallel which each carry a fraction of the total data rate. Such OFDM (orthogonal frequency division multiplex) or DMT (discrete multitone transmission, the baseband variant of OFDM) techniques effectively smear out the time of a symbol period, and thus make the transmission less vulnerable for dispersion in the transmission path. As shown in Fig. 2-10, these techniques involve considerable signal processing at the transmit and the receive site. OFDM and DMT techniques are already widely used in e.g., wireless LAN, xDSL modems, DVB-C and DOCSIS cable modems, and thus can benefit from economy-of-scale. Moreover, the spectrum spreading of the multiple carriers in OFDM and DMT allows to adaptively tune the modulation format and the power per carrier, in order to match optimally the characteristics of the transmission path. By deploying this so-called bit- and power-loading, OFDM and DMT have proven to be very robust against changing dispersion conditions.

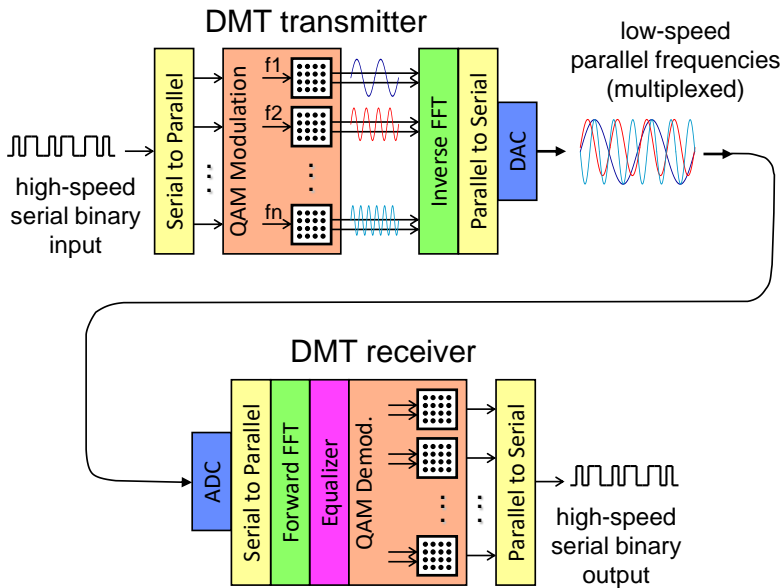


Fig. 2-10 Discrete Multitone Modulation

When the number of levels in multi-level PAM and QAM signaling increases, the symbol rate decreases and hence the transmission performance degradation due to bandwidth limitations becomes less. On the other hand, the noise margins

between the signal constellation points become less too, which increases the transmission performance degradation due to noise. With OFDM and DMT, at particular time instants the many subcarriers may add up leading to a high instantaneous peak level causing clipping in the transmitter and/or in the receiver. The performance of OFDM or DMT schemes thus is mainly limited by clipping noise, and this limitation becomes more severe with more subcarriers. Comprehensive studies which compare the suitability of the various modulation schemes for bandwidth-limited channels have been made. Fig. 2-11 [15] shows the optical power margin of a Gigabit Ethernet link (1.25Gbit/s) versus the available bandwidth of the link normalized on the bitrate. The margin was defined at a BER= 10^{-3} , which is below the forward error correction (FEC) level. Using zero-forcing decision feedback equalization (DFE), 2PAM (equivalent to on-off signaling) performs the best at bandwidths exceeding 20% of the bitrate. For bandwidths which are lower, but above 5% of the bitrate, 4PAM+DFE performs better, whereas for low bandwidths less than 5%, DMT is preferable. For DMT, symmetrical clipping was assumed. The margin was calculated for a Gaussian low-pass channel; SI-POF typically has a slower response decay which may make 2PAM the best choice for bandwidths even lower than 20% of the bitrate.

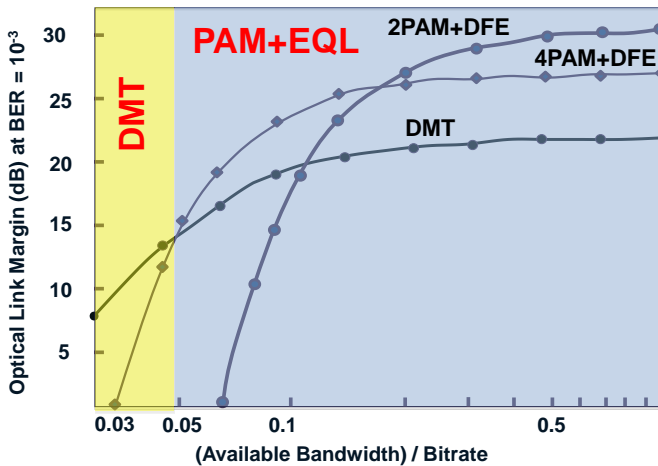


Fig. 2-11 Optical link margin versus bandwidth of Gaussian low-pass channel (from [15])

Research on high-capacity POF links was the topic of the European project POF-PLUS [16]. Real-time 2PAM experiments have been reported at 1.25Gbit/s over 75 meters, with 1mm core SI-POF using DFE and a new Gigabit Ethernet compliant physical layer for POF [17], and at 10.7Gbit/s over shorter POF lengths (15 meters 1mm core SI-POF using FFE (feed forward equalization) and DFE, and 35 meters 1mm core GI-POF using MLSE (maximum likelihood sequence

estimation)) [18]. 10.7Gbit/s in PAM-4 format was carried over 25 meters SI-POF and 60 meters GI-POF using DFE [18]. Using DMT with adaptive bit- and power-loading over 256 subcarriers, 5.6Gbit/s was transported over 50 meters 1mm core GI-POF using an eye-safe laser [19], and 10.7Gbit/s over the same length using a high-power laser diode [18]. An overview of multi-Gbit/s system experiments using 1mm core POF is given in Table 2-2 [20]. Even 51.8Gbit/s gross (47.4Gbit/s net) has been transported at $\lambda=1302\text{nm}$ over a link of 100 meters PF GI-POF with a core diameter of only $50\mu\text{m}$, using DMT with power-loading and bit-loading up to 64-QAM [24].

Standardization for POF transmission systems is progressing. A 1 Gbit/s standard for POF based on OOK PAM was published in 2017 [21]. The G.hn standard contains medium-specific support for the PHY layer for POF using OFDM with adaptive bit loading [22]; there were no implementations so far, however. From 2022, studies are ongoing towards a 25Gbit/s point-to-point over 15 m GI-POF in the IEEE 802.3dh project for automotive applications [23].

Table 2-2 Multi-Gbit/s system experiments (using 1mm core PMMA-POF, unless indicated otherwise)

Data rate	POF type	Core \varnothing	Tx	Wavelength	Rx	Format	Length	Year
1.25 Gb/s (real time)	SI-POF	1 mm	Eye-safe RCLED	650 nm	Large area receiver	OOK	50 m	2010
2.2Gb/s (wired) +480Mb/s (wireless)	GIPOF-PON (1×4)	1 mm	High power laser	650 nm	APD	DMT/OFDM	50 m	2012
3Gb/s (wired) +480Mb/s (wireless)	GI-POF	1 mm	VCSEL	665 nm	APD	DMT/OFDM	50 m	2011
4.7Gb/s	MC-POF	1 mm	Eye-safe VCSEL	665 nm	APD	DMT	50 m	2010
5.3Gb/s	GI-POF	1 mm	Eye-safe VCSEL	665 nm	PIN+TIA	DMT	50 m	2010
5.8 Gb/s	GI-POF	1 mm	High power laser	650 nm	PIN+TIA	PAM2+DFE	75 m	2011
7.3 Gb/s	mPOF	140 μ m	High power laser	650 nm	APD	DMT	50 m	2012
4×2.5Gb/s	Ribbon		VCSEL array	665 nm	PIN Diode array	OOK	25 m	2011
10 Gb/s	MC-POF	1 mm	High power laser	650 nm	PIN+TIA	DMT	25m	2011
10 Gb/s	GI-POF	1 mm	High power laser	650 nm	PIN+TIA	DMT	35 m	2011
10.7Gb/s	SI-POF	1 mm	WDM high power lasers	405, 515, and 650 nm	PIN+TIA	DMT	50m	2012
10.7 Gb/s	GI-POF	1 mm	VCSEL	665 nm	MSM PD+TIA	NRZ+MLSE+PLL	35m	2012
47.4 Gb/s	PF GI-POF	50 μ m	DFB	1302 nm	\varnothing 25 μ m PD	DMT	100 m	2010

2.6 High-capacity transmission for wireless delivery of services

Within the home, there is a booming need for wireless connectivity. Users often carry multiple wireless communication devices (smart phone, tablet computer, laptop, ...). We are entering the era of ‘the Internet of Things’ where not only human-human and human-machine communication but also machine-machine communication is becoming ever more intense. In order to counteract ISM radio spectrum congestion and mutual interference which limit the network’s throughput, indoor radio networks consisting of many pico-cells are being created. To make this economically feasible, the antenna sites should be simple and the radio signal generation and processing functions be centralized. A fixed wired backbone network is needed to feed all the antenna sites from a central location which hosts the radio functions. Due to its virtues of high bandwidth and low losses, optical fiber is the preferred medium to build such a backbone.

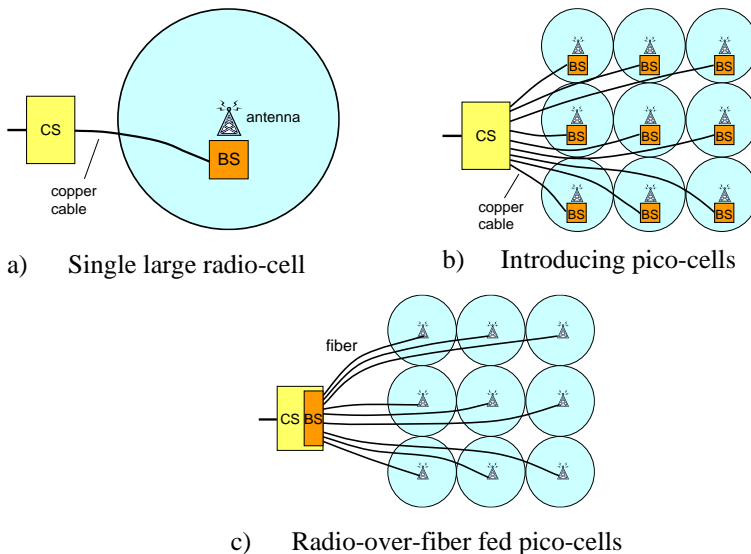


Fig. 2-12 Increasing the capacity of wireless networks by introducing pico-cells and radio-over-fiber techniques

In the radio-over-fiber approach illustrated in Fig. 2-12, when transporting the RF signals modulated in their native analog format onto an optical carrier (i.e., AroF, analog radio over fiber), the antenna sites only need to convert the radio signals from an optical to an electrical format, thus yielding the most simple antenna stations. However, the optical bandwidth available in a fiber link may be more effectively used when the RF signals are transposed to a lower intermediate frequency and put back onto their original position at the antenna site (i.e.,

intermediate frequency over fiber, IFoF). Or alternatively, the radio signal may be digitized and transported on an optical carrier by digital modulation techniques (i.e., digital radio-over-fiber, DRoF), which brings the advantages of digital transport well-known for extended reach such as regeneration without SNR degradation and more network routing capabilities (such as add-drop and crossconnect). Both IFoF and DRoF require more active equipment at the antenna site than ARoF, thus need more local supply power and maintenance.

The centralized provisioning of the radio functions eases maintenance and upgrading of the wireless network. The many non-overlapping pico-cells enable radio frequency reuse, and thus provide a higher total network capacity. The radio-over-fiber approach also brings energy savings in various ways. Less radio power needs to be emitted by the antenna because in a pico-cell the distance from the wireless device to the antenna is reduced. Reversely, the wireless device needs to emit less radio power to communicate upstream, thus prolonging its battery life. The pico-cells may be individually activated depending on the wireless traffic load in that cell, which allows several of them to be operated in ‘sleep mode’. The central processing of the radio signals facilitates many advanced wireless network functions, such as smart antenna functions (multiple-input multiple-output, MIMO), adaptive radio beam-shaping and –steering, spectrum sensing for cognitive radio techniques, which also can contribute to improved delivery of wireless services and energy savings.

For indoor wireless communication, a wide range of wireless standards has been developed (and is still expanding). As listed in Table 2-3, a wide range of frequency bands is used, with widely ranging modulation formats and data rates. For higher data rates, WiFi and 5G indoor are the dominant indoor standards. The higher frequency bands are mostly intended for short reach, i.e., in-room; 60GHz even requires line-of-sight. Optical fiber can carry multiple signals independently on different wavelengths, and indoor fiber links are typically so short that they do not add delays large enough to have a noticeable impact on the radio medium access control protocols [25], hence radio-over-fiber is well suited for indoor operation with multiple radio standards.

Table 2-3 Indoor wireless technology standards

Technology	Standards	Coverage	Frequency bands	Modulation	Data rates (peak downlink)	Bandwidth
WiFi	802.11g	Up to 38 m (indoor)	2.4 GHz	OFDM, DSSS	54 Mbit/s	20 MHz
	802.11n (WiFi 4)	Up to 70 m (indoor)	2.4, 5 GHz	OFDM	150 Mbit/s (4x4 MIMO, in 40MHz channel)	20, 40 MHz
	802.11ac (WiFi 5)	Up to 70 m (indoor)	5 GHz	OFDM	867 Mbit/s (8x8 MIMO, in 160 MHz channel)	20, 40, 80, 160 MHz
	802.11ax (WiFi 6)	Up to 70 m (indoor)	2.4, 5, 6 GHz	OFDMA, 1024 QAM	1200 Mbit/s (8 MU-MIMO)	20, 40, 80, 160 MHz
	802.11ad (WiFi 7)	Up to 70 m (indoor)	2.4, 5, 6 GHz	OFDMA, 4096 QAM	2400 Mbit/s (16 MU-MIMO)	20 ~320 MHz
5G indoor	5G NR	-	<1, 1-6, 6-60 GHz	OFDMA, 16-256 QAM	10 ~20 Gbit/s (8x8 MIMO and higher)	Up to 100 MHz
Bluetooth	802.15.1	10 m (class 1) 30 m (class 2, 3) 60 m (class 4) 240 m (class 5)	2.4 GHz	GFSK, T1/4-DQPSK and 8DPSK with FHSS	1 Mbit/s class 1 ~ 50Mbit/s EDR class 5)	1 MHz (79 bands in total)
Zigbee	802.15.4	70 m	868, 915 MHz and 2.4 GHz	OQPSK with DSSS	250 kbit/s	5 MHz (16 bands in total)
UWB	802.15.3/ ECMA368	10 m	3.1-10.6 GHz	QPSK/OFDM (MB-OFDM)	480 Mbit/s (MB-OFDM)	528MHz for each sub-band (MB-OFDM)
				BPAM(DS-UWB)	1 Gbit/s(DS-UWB)	<7.5 GHz(DS-UWB)
WiGig	802.11ad	In-room, >10 m (with beamforming)	2.4, 5, 60GHz	Single carrier / OFDM	7 Gbit/s	4x2.16GHz

SMF has plenty of bandwidth to carry any standard. When intensity modulation is used, however, double sidebands around the carrier occur, which due to fiber dispersion may suffer from fading; i.e., for certain radio frequencies and at periodic length positions along the fiber the two sidebands may show a π radians phase difference and extinguish each other. The length period is inversely proportional to the square of the carrier frequency; the fading effect is therefore in particular a problem at high radio carrier frequencies. Single-sideband (SSB) modulation can effectively avoid this fading, but requires more complicated modulation circuitry. Alternatively, one may use a modulation scheme which suppresses the carrier, thus mitigating the fading and making the system insensitive for fiber dispersion. By driving a Mach Zehnder Modulator (MZM) symmetrically around a bias point at V_π (the MZM's inflexion point), the carrier is suppressed and the resulting microwave frequency is twice the frequency of the drive signal [26]. An other dispersion-robust technique is Optical Frequency Multiplying (OFM) [27], in which the optical frequency of the light source is periodically swept at a relatively low frequency, and the resulting FM signal is converted by an interferometric filter (e.g., a Mach Zehnder Interferometer, MZI) into an IM signal containing many harmonics of the sweep frequency. The data signal is intensity-modulated on the envelope of this signal. After photodetection, a simple electrical bandpass filter can select the desired higher harmonic to be the microwave radio signal to be emitted. It can be shown that this OFM technique is very robust against fiber dispersion, and suppresses laser phase noise; e.g., transmission of 120Mbit/s 64-QAM at 17.2GHz over 4.4km of silica MMF has been demonstrated [27].

The very limited bandwidth of large-core POF links seriously limits the feasibility to transport radio signals in their original spectral position. A relatively simple solution can be offered by spectrum translation, where the radio signal at the headend site is down-converted by mixing it with the help of an electrical local oscillator (LO) to a frequency band within the POF's bandwidth. At the antenna site, after photodetection a similar LO is used to upconvert the signal to its original spectral position, and subsequently radiated as a radio wave. As illustrated in Fig. 2-13, with this approach it has been demonstrated that a HD video signal up to 480Mbit/s can be carried in an ultra-wideband (UWB) OFDM channel (TFC6, 3.696-4.224GHz) over 50 meters 1mm core PMMA GI-POF and 3 meters wireless, by down-converting it to the 0.836-1.364GHz band for transport in the POF link [28].

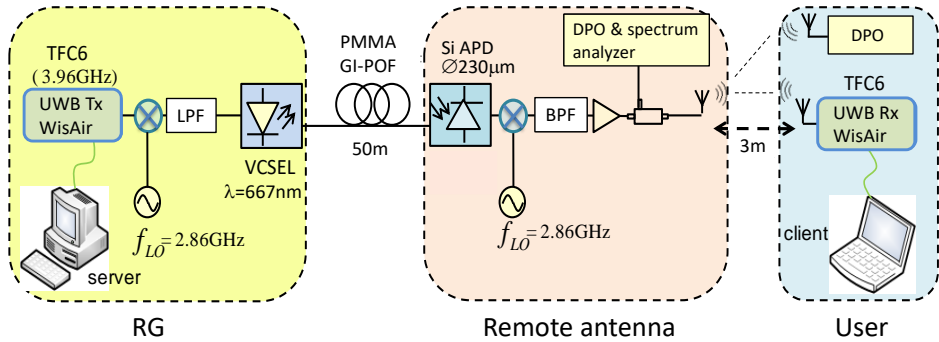


Fig. 2-13 UWB radio over 1mm core PMMA GI-POF using spectrum translation

Also, impulse-radio UWB techniques may be deployed in radio-over-fiber links. Such techniques may aid indoor localization of wireless devices [29]. They use specifically shaped narrow optical pulses covering the UWB spectrum up to 10GHz. Typically, they require a small fiber dispersion, and are not compatible with large-core POF; data rates of 2Gbit/s have been shown over 100 meters of 50 μ m core diameter PF GI-POF [30].

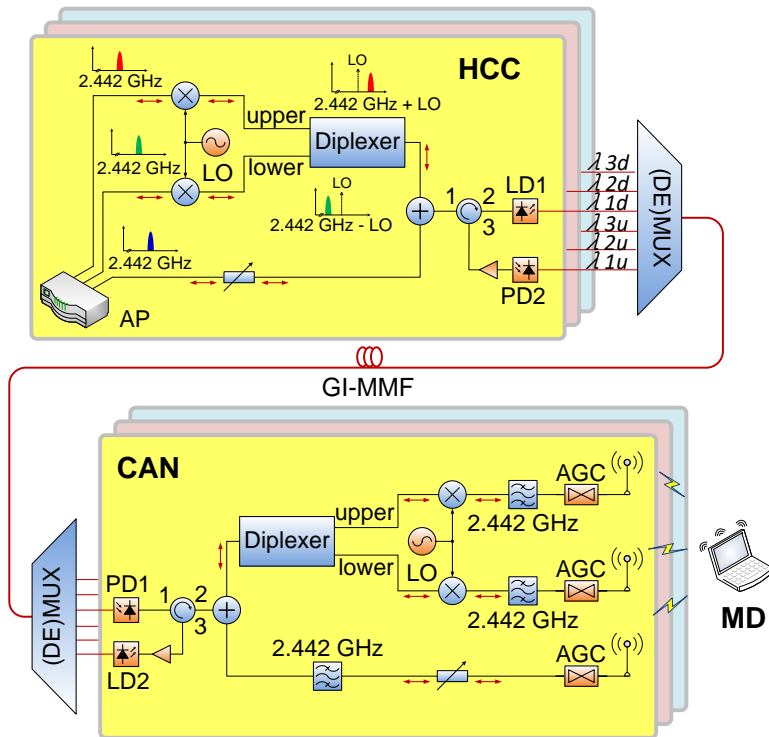


Fig. 2-14 3x3 MIMO over fiber using subcarrier multiplexing

The central radio signal processing enabled by radio-over-fiber techniques offers nice opportunities for advanced radio signal processing. E.g., while performing the MIMO signal processing in the headend station, the separate MIMO channels may be carried over a single fiber by subcarrier multiplexing. Using an electrical LO in the headend station, a 3x3 MIMO system can be created by shifting two channels at the LO frequency distance below and above the original carrier frequency of 2.4GHz respectively, and leaving the third channel at its original 2.4GHz location (see Fig. 2-14) [31]; the composite subcarrier-multiplexed signal is launched by a laser diode in the MMF link. At the antenna site, after photodetection and subcarrier-demultiplexing using another LO, the three channels are put back to their original 2.4GHz locations for driving the three MIMO antennas. The same architecture can be used in reverse for MIMO upstream traffic.

2.7 Converged indoor networks

Optical fiber is well suited to carry multiple services with different characteristics within a single converged network. When using SMF, coarse wavelength division multiplexing (CWDM) may be deployed to carry each type of services on a separate wavelength. By means of a centrally located $N \times N$ power splitter, a multipoint-to-multipoint multi-wavelength network can be created, by which every device broadcasts its output signals to all other devices, and each device uses a wavelength filter to select the service it wants. A 16x16 splitter-based indoor SMF network carrying 9 service types at 9 coarsely spaced wavelengths in the 1305-1610nm range has been reported [32].

Due to the limited wavelength operation range of PMMA-POF and the restricted availability of sources operating at different visible wavelengths, wavelength multiplexing offers only limited possibilities for the convergence of services. Alternatively, services may be converged on a large-core POF link by means of electrical spectrum division. Fig. 2-15 shows how wirebound services (e.g. Gigabit Ethernet) and wireless services (e.g. on UWB) can be combined by locating the wirebound ones carried by DMT modulation in the lower part of the POF's passband and the wireless ones carried by multiband OFDM UWB in the upper part deploying spectrum translation [33].

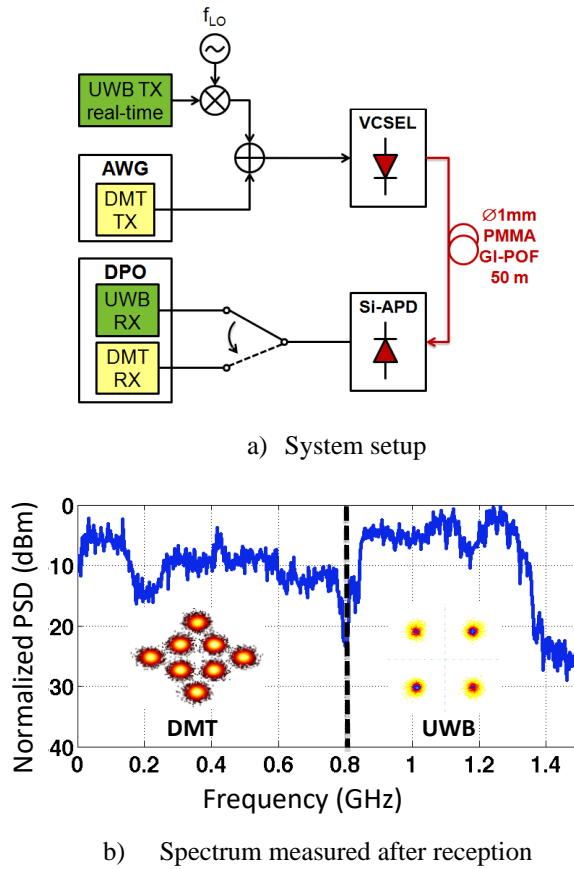


Fig. 2-15 Converged transport of wirebound and wireless services over a 1mm core PMMA GI-POF link

The lack of multiport optical power splitters and wavelength routers with large-core POF ports limits the point-to-multipoint POF networking possibilities. Commercially available 1×2 power splitters with 1mm core GI-POF ports show excess losses of 2.5-3dB. First POF network experiments used a cascade of 1×2 power splitters to show a 1×4 split network carrying bidirectional UWB signals over 30-50 meters of 1mm core GI-POF [34] [35]. Using bulk-optic ball lenses and an interference filter, a 2-wavelength red/green demultiplexer with PMMA-POF has been created [36]. Considerable advances in POF power splitter and WDM multiplexer/demultiplexer techniques are needed to enable more comprehensive POF networking.

2.8 2D radio beam steering in a radio-over-fiber system³

The need for wireless broadband connectivity is growing rapidly, not only because the numbers of devices to be connected are increasing but also because each device is requiring more capacity. The radio spectrum is getting exhausted, and devices start to interfere with each other. This is seriously affecting the data throughput per device. The data collisions due to interference make retransmissions of these data necessary, and thus reduce the data throughput rate. The increased data rates also require higher received radio powers. To overcome the arising bottleneck in wireless connectivity, solutions to reduce the interference and to improve the power efficiency of high-capacity radio systems are needed.

This section introduces an optical system concept for shaping and steering of radio beams in two angular dimensions, by which interference between the wireless devices is substantially reduced, radio power is directed to the devices more efficiently, and thus considerably less power is needed.

2.8.1 Radio beam steering

Phased array antennas (PAA-s) are well known for radio beam-shaping and -steering. The phase differences between the antenna elements determine the direction in which the radio waves emerging from these elements interfere constructively, and thus the direction in which the resulting radio beam is pointing. The shape of the beam is determined by the number of active antenna elements. Typically, a PAA with N antenna elements gives a power gain of a factor N . When the PAA is composed of a 2-dimensional grid of antenna elements, the beam can be steered in two angular dimensions; this is illustrated in Fig. 2-16 and Fig. 2-17, respectively. Steering the beam direction is done by tuning the phase differences between the antenna elements, and typically involves comprehensive electronic signal processing to create the required phase differences between the radio-frequency (RF) signals fed to each antenna element. Moreover, the RF signal generation and modulation preceding this comprehensive processing also need to take place close to the antenna elements, which makes the whole antenna site complex to build and to maintain.

³ This section is largely based on A.M.J. Koonen, Z. Cao, "Optically controlled 2D radio beam steering system," and in A.M.J. Koonen, "Optical techniques for Gbit/s wireless indoor access" (keynote paper), in *Proc. Microwave Photonics conference (MWP 2014)*, Sapporo, Oct. 20-23, 2014.

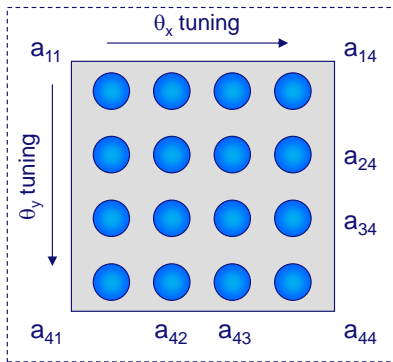


Fig. 2-16 4×4 phased array antenna for 2D radio beam steering

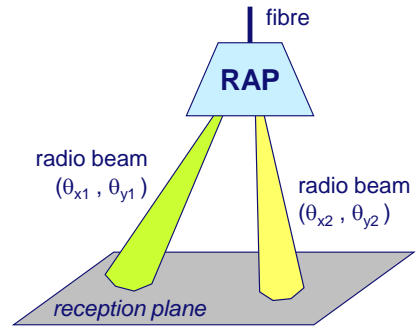


Fig. 2-17 2D steering of multiple radio beams from a Radio Access Point (RAP) containing the antenna array

Radio-over-fiber (RoF) techniques have been developed which enable to simplify considerably the antenna sites (see e.g., [37]). They allow to generate and modulate the RF signals remotely in a central site, and to feed them from there via fiber to simplified antenna stations, where for the downstream RF transmission only optical-to-electrical signal conversion by means of a photodiode is needed followed by a simple RF power amplifier and the antenna. For the uplink, the possibly large power variations of the upstream RF signals from the users need to be accommodated into the optical upstream channel which brings additional transport challenges.

Next to the remote generation and modulation of the RF signals, the system setup proposed in this section provides an additional advantage of RoF techniques, namely that the tuning of the phase differences between the antenna elements in a PAA can also be done by relatively simple optical means (e.g., true time delay lines by means of optical waveguides of different lengths, cf. Fig. 2-19), instead of by comprehensive electronic processing. In literature, the use of optical ring resonators with thermal heater elements to tune the phase shift per ring has been reported [38]. However, due to the strong frequency dependence of a ring this phase shift is highly dependent on the frequency of the radio signal. When the radio signal is modulated and hence its bandwidth is extended, the phase shift is no longer the same across the spectrum of the signal, and thus the beam direction is blurred; this beam distortion is known as ‘beam squint’. Typically, the ring resonator’s bandwidth is below 2GHz, which limits its suitability for broadband communication (e.g., for deploying a 7GHz band at 60GHz). The beam squint can be avoided by using true-time-delay (TTD) techniques to create a frequency-independent time delay between the antenna elements, thus allowing steering of a radio beam with a broad spectrum. An

optical 1D TTD steering solution using bulky discrete components was reported in [39]. TTD techniques can be approximated by comprehensive electronic signal processing. Using optical micro-ring resonators, it can also be approximated by a complex structure with multiple rings [40]. Moreover, optical TTD solutions using comprehensive micro-electro-mechanical system (MEMS) switches have been proposed, which require complex electronic control circuitry [41]. However, the complexity of these one-dimensional (1D) TTD solutions makes a 2D TTD beam steering solution prohibitively complex.

2.8.2 Wavelength-controlled 2D TTD radio beam steering

We introduced a simple yet powerful solution to provide remotely controlled broadband squint-free 2-dimensional radio beam steering by means of radio-over-fiber techniques and wavelength-tunable optical signal processing which is accomplished by an integrated 2-dimensional optical TTD circuit [46] and based on earlier 1-dimensional work in [44] [45]. The circuit enables discrete steering of the radio beam in 2 angular directions by the step-wise tuning of only a single parameter, namely the wavelength λ of the input light carrying the radio signal. This light signal can be fed from a remote location via optical fiber to the antenna site. By feeding multiple light signals each at a different tunable wavelength and each carrying a radio signal at a different radio frequency, multiple radio beams can be steered individually in two dimensions by tuning their wavelengths separately.

As an application example, Fig. 2-18 shows an indoor network where in each room of a building a Radio Access Point is located. This RAP contains a phased array antenna which directs radio beams towards the mobile devices in the room.

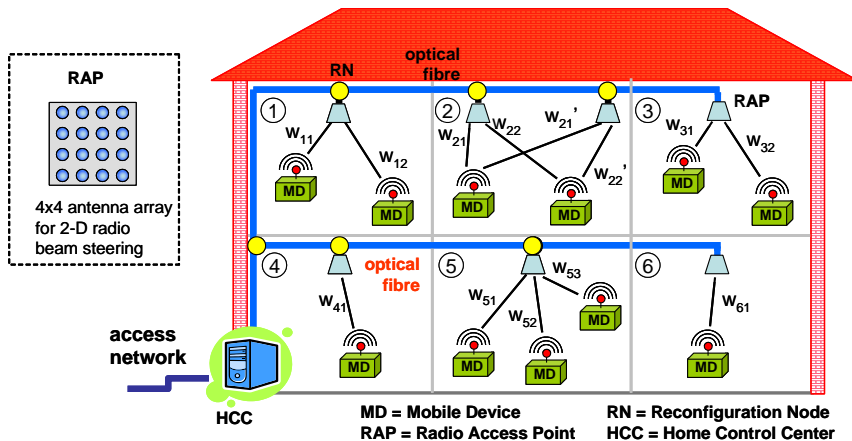


Fig. 2-18 Fiber-wireless in-home network with smart radio beam steering

The key optical element in the beam steering system is a step-wise tunable optical delay line, composed of an Arrayed Waveguide Grating (AWG) with feedback loops. This concept has been reported before in various forms [43][44][45]. As illustrated in Fig. 2-19, depending on the value of its wavelength λ the light entering the AWG at input port 0 exits the AWG at a specific output port n ($n=0, 1, 2, \dots$). From this output port, the light with wavelength λ_n enters a feedback loop with a length such that it is delayed over a time $\tau_n = \tau_0 + n \cdot \Delta\tau$, and then is re-entering the AWG. Due to the internal symmetry of the AWG, this light is then exiting at output port 0. The light exiting this TTD element has thus experienced a delay τ with respect to its entry time, where τ is a step-wise function of the wavelength λ of the light (see Fig. 2-20). The cyclic behavior of the AWG causes not only the light with wavelength λ_n to exit from output port n and thus to experience a time delay τ_n , but also light with a wavelength which is larger by a multiple of the Free Spectral Range (FSR) of the AWG. Hence the step-wise delay characteristic is periodic with a wavelength period equal to the FSR.

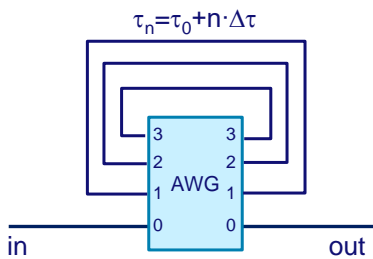


Fig. 2-19 Step-wise λ -tunable TTD element, with delay step size $\Delta\tau$

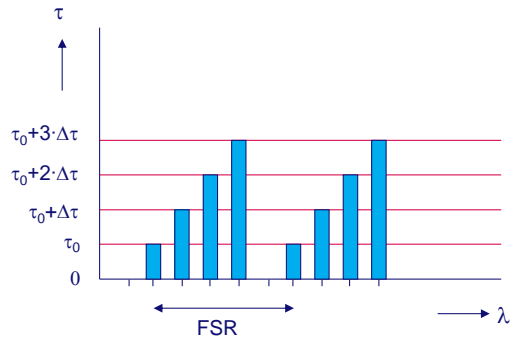


Fig. 2-20 Step-wise tunable time delay τ

The AWG can be designed such that it has a finite bandpass characteristic per port: not only for a particular wavelength, but for a small range of wavelengths around that wavelength the light is directed from an AWG input to an AWG output. Thus, when an RF signal with a wide bandwidth is modulated on an optical carrier with wavelength λ_n , where the modulation process implies a spectral broadening of that carrier, this modulated carrier still experiences a constant delay time value τ_n (and not a delay time which is gradually changing across the signal's bandwidth). Hence the setup in Fig. 2-21 acts as a real TTD element (under the assumption that the delay in the feedback loops themselves is not wavelength-dependent, which is a very good approximation of the reality), and thus the RF beam steering is squint-free.

As depicted in Fig. 2-18, two-dimensional radio beam steering is needed to cover a certain area. This beam steering can be achieved by using a 2-dimensional array of antenna elements; Fig. 2-16 gives an example of a 4×4 array which steers both in the θ_x angular dimension and in the θ_y angular dimension, by tuning the corresponding time delays between the columns and rows of the 4×4 matrix of antenna elements, respectively. Multiple beams may be directed simultaneously by a single 2D phased antenna array, as illustrated in Fig. 2-17, by deploying a different radio frequency for each of them.

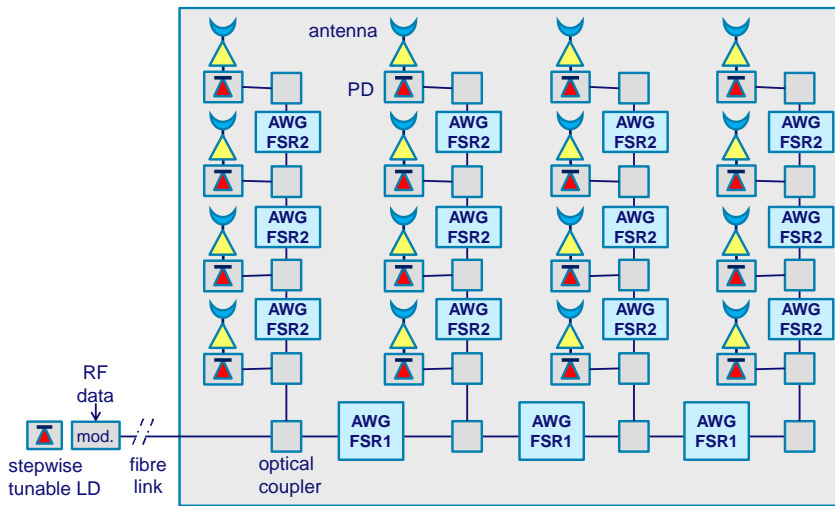


Fig. 2-21 Wavelength-tunable 2D beam steering PIC including a combination of TTD stages with a large FSR and TTD stages with a small FSR , co-integrated with O/E RF drivers for the antenna units

We propose a concept with which the 2D beam steering can be realized by tuning just one parameter, namely the wavelength λ of the input light. Fig. 2-21 illustrates how this single-parameter tuning can be implemented by means of a photonic integrated circuit (PIC) which is using jointly TTD elements with a large FSR and TTD elements with a small FSR , co-integrated with O/E RF conversion and driver stages for the antenna elements. An AWG with a smaller channel spacing and a smaller FSR requires a larger structure than an AWG with a larger channel spacing and a larger FSR ; for a smaller channel spacing, the length difference between its internal waveguiding structures needs to be larger. Hence, to minimize the total required area of the integrated optical chip, it is advantageous to design the TTD elements in the lower row in Fig. 2-21 such that they have a small FSR , and the TTD elements in the columns to have a large FSR as they are more numerous.

As shown in Fig. 2-22, the respective FSR-s must be designed such that a full wavelength passband of the AWG with a large FSR_2 comprises the full width of the small FSR_1 . Thus, while tuning λ through that full wavelength band the angular direction θ_y remains fixed, while the angular direction θ_x is step-wise tuned over its full range. While extending the λ -tuning over the full FSR_2 range, due to the periodicity of the TTD-s with the small FSR_1 the angular direction θ_x is periodically tuned over its full range, while also the angular direction θ_y is slowly and step-wise tuned over its full range. With this tuning scheme, both θ_x and θ_y are consecutively tuned over their full ranges, and a 2-dimensional area is covered by the beam steering while tuning only the parameter λ of the input light signal.

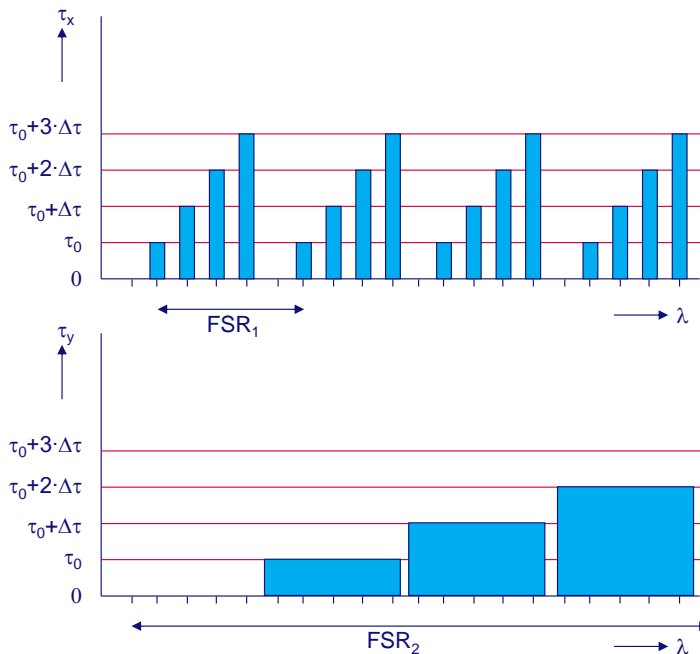


Fig. 2-22 2D beam steering by tuning only the wavelength λ of the input light

2.8.3 Integrated 2D TTD beam steering circuit

A first integrated optical circuit has been made for a 2×2 PAA, in silicon-on-insulator optical integration technology [47]. Fig. 2-23 shows a photograph and the performance characteristics measured on a 1D TTD circuit with 7 feedback loops. One of the loops was defective, hence the graphs show the performance of the phase delays versus frequency of the RF signal for 6 different wavelengths of the optical input signal, which each activate one of the loops. As Fig. 2-23 shows, the phase delays increase linearly when the frequency is increased, with a step-

wise increasing slope when the wavelength is increased. This behavior confirms the step-wise TTD tuning, as a constant time delay corresponds with a linear phase delay slope for increasing frequency.

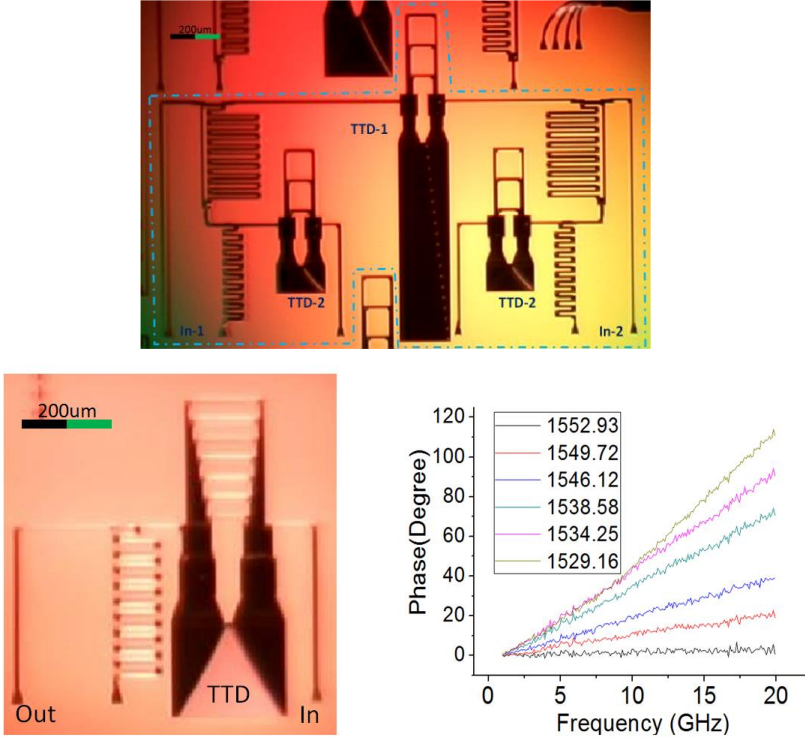


Fig. 2-23 First realization of a 2D TTD optical integrated circuit for a 2×2 phased antenna array, and measured performance of a basic 1-D TTD optical integrated circuit with 6 working feedback loops [47]

2.8.4 Conclusions

We propose an optically-controlled 2-dimensional radio beam steering system, based on a novel integrated optical circuit with true-time-delay elements arranged in two groups which each take care of the beam steering in one dimension and which have interlaced periodic characteristics in order to jointly provide beam steering in two dimensions. The feasibility of a basic integrated 1D TTD stage has been shown.

The integrated optical circuit is located at the antenna site, and can be remotely driven via a fiber by a step-wise wavelength-tunable laser diode. The antenna site thus can be compact and robust, requiring minimum installation effort. Moreover, the beam steering can be done by varying only the wavelength of the input light signal, which can be fed from the remote location containing a tunable laser diode

transmitter by means of a fiber link; this solution therefore eases the control algorithms for fast beam steering, and avoids the burden of comprehensive electronic signal processing at the antenna site, with the associated maintenance issues.

Because a fiber link can carry multiple wavelength signals simultaneously, each coming from a separate tunable laser diode at the central site, the proposed system also allows that a multitude of radio beams, each individually tunable in two angular dimensions, can be generated. The beam steering requires constructive interference between the radio waves emitted from the antenna elements, and therefore the steering of multiple beams individually requires that each beam carries a different radio frequency.

2.9 Dynamic capacity allocation

In order to improve the operational efficiency of the installed network resources, dynamic routing of capacity inside the indoor network may be introduced such that local traffic needs are met on demand. E.g., users carrying wireless broadband devices may roam throughout the building, and wireless capacity may be intensely needed in rooms where many of them meet whereas other rooms are not or sparsely populated and therefore need less capacity; this situation may alter frequently due to the roaming. To accommodate these locally changing traffic demands, dynamic wavelength routing in SMF-based indoor networks may be used to allocate wavelength channels to rooms or to clusters of rooms, as illustrated in Fig. 2-24.a and .b. Studies have shown that by using time-division-multiplexing inside wavelength channels, and moving time slots to other wavelength channels when the original wavelength channel gets congested (this idea is also being taken up as Multi-Link Operation, MLO, in IEEE 802.be, a.k.a. WiFi 7, to be adopted in 2024), the network congestion probability can be reduced significantly without installing extra network resources [48]. This reduction will be larger when the clusters are smaller, as the capacity can then more efficiently be rearranged with a finer granularity. Thus, dynamic capacity allocation on demand enables the network to carry more traffic while maintaining the same network resources installed; as Fig. 2-24.c shows, by refining the allocation granularity the traffic load may be more than tripled while not affecting the network congestion probability.

The flexible assignment of wavelength channels to rooms can be done by tunable wavelength conversion of the radio-over-fiber signals followed by a static wavelength router in the network splitting node. This approach has been demonstrated in an SMF network by means of cross-gain based wavelength conversion in a semiconductor optical amplifier (SOA) applied to an OFM radio signal; tunable routing has been shown of 150Mbit/s 64-QAM WLAN signals in the 1.5 μ m band [49].

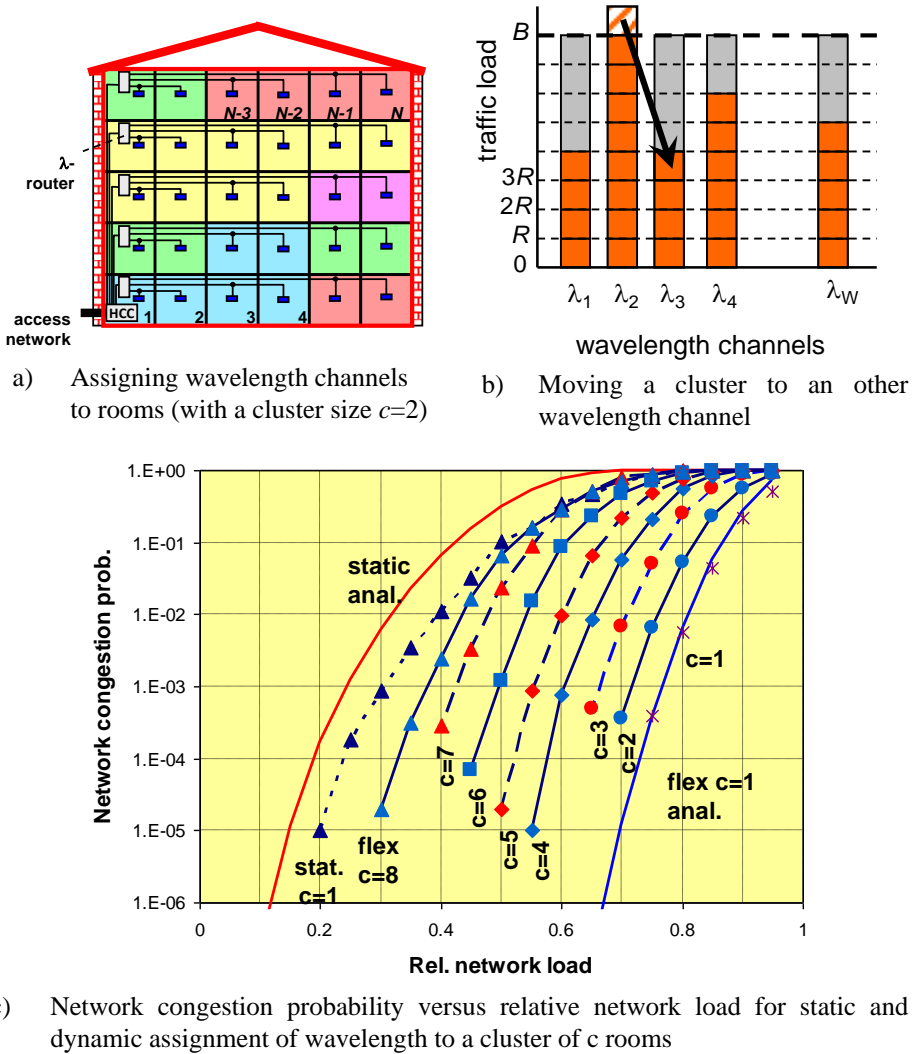


Fig. 2-24 Dynamically or statically assigning capacity to clusters of rooms in a building (with c rooms per cluster) [48]

2.10 Mode Group Division Multiplexing

An alternative option to create multiple independent transmission channels within a single multimode fiber (MMF) is given by mode group division multiplexing (MGDM) [50][51]: the many guided modes inside an MMF may be partitioned in sets of modes, and each set (mode group) can constitute a transmission channel. As illustrated in Fig. 2-25, N lasers may be employed each launching a specific mode group in the fiber, and at the receiving end each element of a set of M

photodiodes receives a mixture of the transmitted signals. Due to mode mixing inside the fiber, the mapping of the transmitted signals to the received signals can be described by a transfer matrix (which changes when the mode mixing conditions change). Provided that these conditions change slowly, signal processing at the receive side (possibly aided by precoding at the transmit side) can unravel the mingling of the channels and yield the originally transmitted channels again. With this MGDM approach, transmission of 3×10 Gbit/s has been demonstrated by means of 3 mode groups over a link of 20 meters silica GI-MMF with $185 \mu\text{m}$ core [52]. The MGDM concept is also feasible for GI-POF [51]; transmission of 2×10.7 Gbit/s data rate has been shown over a link of 10 meters GI-POF with $62.5 \mu\text{m}$ core diameter [53].

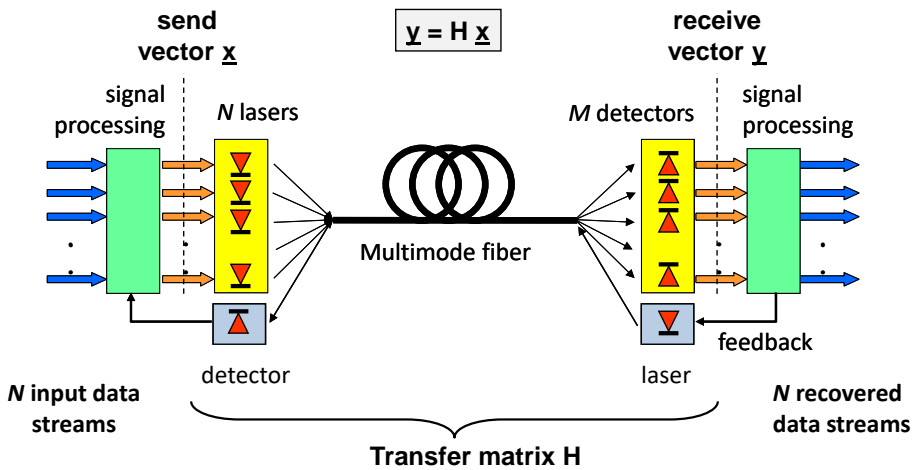


Fig. 2-25 Mode group division multiplexing

A similar mode-multiplexing approach for few-moded fiber has been introduced for increasing the capacity of long-haul fiber links. In this so-called spatial division multiplexing (SDM) approach individual modes are deployed, not sets of modes (in order to avoid modal dispersion which would be detrimental in long-haul links) [54]. Within each mode group, additional multiplexing dimensions may be employed, such as WDM, which can further expand the network's capacity and routing flexibility. Using SDM in combination with DWDM and comprehensive signal modulation (such as QAM-64), data transport capacities in few-moded fibers beyond 10 Pbit/s have been achieved.

2.11 Optical wireless communication

The abundant proliferation of wireless devices is causing radio spectrum congestion and mutual interference, thus hampering wireless connectivity. The free-space optical spectrum can offer an alternative with plenty of unlicensed

bandwidth. Optical wireless communication (OWC) may use the infrared, visible or ultraviolet part of the spectrum. OWC does not cause EMI nor is it affected by it, and it can easily be contained in order to enhance privacy (e.g., within a room as it does not penetrate walls).

2.11.1 Eye safety

Eye safety regulations as formulated in the ANZI Z-136 and IEC 60825-1 standard series state the maximum light intensity levels which may enter the human eye without causing damage [55]. Ultraviolet light with a wavelength up to 300nm will be blocked by the eye's cornea, and up to 400 nm by the lens (see Fig. 2-26).

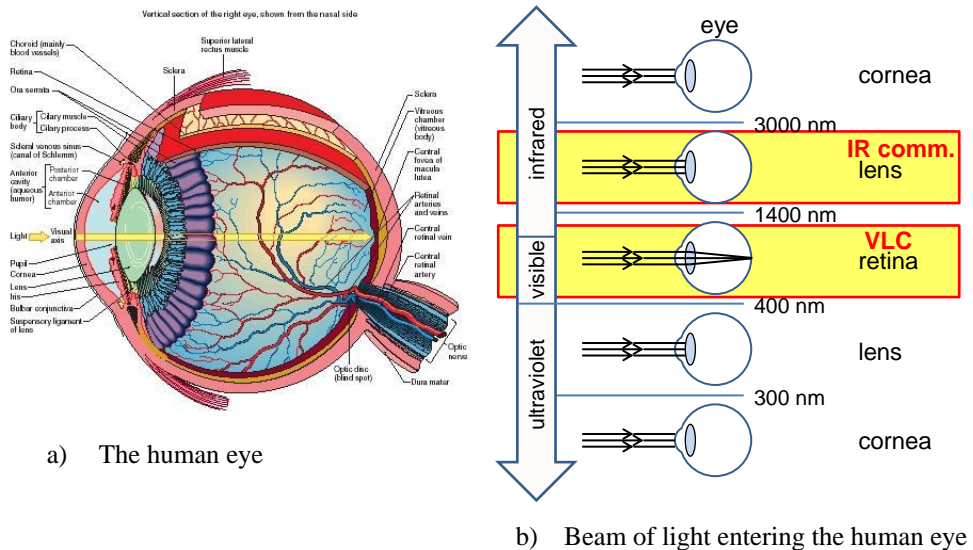


Fig. 2-26 Penetration of light in the human eye

Between 400 and 1400nm, most of the light will reach the retina. From 1400 to 3000nm, it will be absorbed in the vitreous body, the inner transparent part of the eye. Beyond 3000nm, it is blocked by the cornea. The retina runs the highest risk of being damaged. With a fully open pupil (7mm diameter), the maximum optical power which may enter the eye (the Accessible Emission Limit, AEL, for eye-safe Class 1 laser products) varies from 39 to 390 μ W in the visible range (400-700nm). From 1400 to 4000nm, up to 10mW may be allowed. Fig. 2-27 shows the maximum allowed CW power from a laser versus its wavelength for various laser Classes [56]. The graphs only hold for static, point-like laser sources such as collimated or weakly diverging laser beams. A Class 1 laser is safe for normal use, i.e., when a laser is viewed with the naked eye or with support of typical

magnifying optics such as telescope or microscope (except when they have a large aperture). A Class 3B laser brings hazards if the eye is exposed directly, but not when the light is diffusely reflected from paper or other matte surfaces. Lasers of Class 2 and higher have to carry a warning label. For distributed Lambertian sources with a wider source diameter, the eye safety limits are significantly relaxed, also below $\lambda=1\mu\text{m}$ (e.g., $>50\text{mW}$ is allowed for a Lambertian class 1 laser at $\lambda=900\text{nm}$ with diameter 3mm [57]).

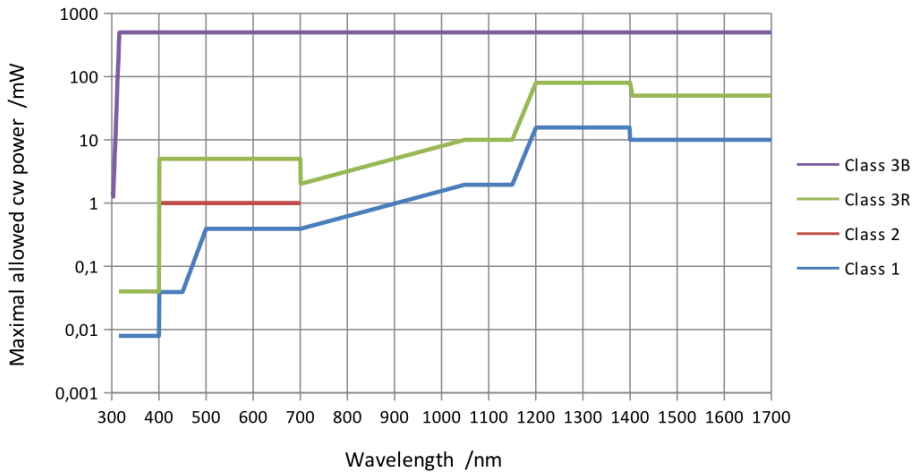


Fig. 2-27 Laser safety according to norm EN 60825-1:2007

2.11.2 Optical wireless communication using visible light

LEDs are increasingly being used for lighting purposes. As they can be modulated at moderate data speeds, visible light communication (VLC) can be ‘piggy-backed’ on illumination, e.g., for applications in offices, industrial or medical environments, public transport, etc.; see Fig. 2-28. White-light LEDs typically are based on a blue-light LED plus a phosphorescent material. For office lighting, light intensities of 200-800 lux are desired; the blue part of the spectrum then represents some 400-1700mW/m². The phosphorescent material introduces slow decay effects and limits the VLC bandwidth to about 3MHz. By detecting the blue part of the spectrum only, the bandwidth can be extended to about 20MHz. By means of adaptive DMT techniques, high data rates may be carried within this limited bandwidth [58]. Using DMT with 127 bit- and power-loaded subcarriers plus clipping to limit the aggregate DMT peak signal excursions, a gross bitrate of 513Mbit/s has been achieved with a single LED over a distance of 30cm to a silicon avalanche photodiode with $\varnothing 3\text{mm}$ diameter preceded by a blue filter [59]. By applying wavelength multiplexing techniques, the VLC data rate may be further increased. With a single white LED module composed of a red, a green

and a blue LED, individually driving the LEDs with DMT signals and performing RGB demultiplexing at the photodetector, an aggregate gross transferred data rate of 3.4Gbit/s over 10cm reach has been demonstrated [61]. The distance can be increased by using an array of LEDs. With an array of 40 white-light LEDs and DMT bit-loading up to 128-QAM, a distance of 0.75m was achieved [58]. The optical communication channel may partly consist of line-of-sight (LoS) paths from the LEDs to the photodetector, and partly of a diffuse part resulting from reflections from objects and walls [62]. The diffuse component may yield a cut-off frequency of about 10MHz for a medium-sized room, but is much smaller than the LoS components (typically 20 to 30 dB electrical below the LoS signal). The limited Field-of-View (FoV) of the photodetector restricts the delay between the received LoS paths. For a typical FoV of 120° and a medium-sized room, optical channel bandwidths well above 90MHz are found, indicating that the achievable VLC data rate is mainly limited by the bandwidth of the LEDs.

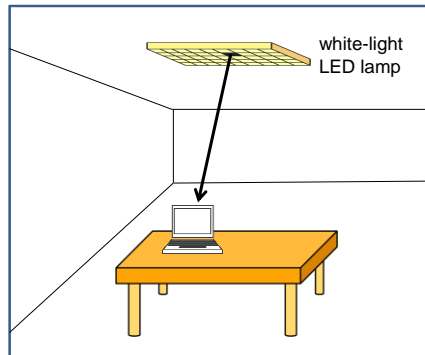


Fig. 2-28 Visible light communication (from [58])

2.11.3 Optical wireless communication using infrared light

As an alternative to VLC, optical wireless communication may use infrared wavelengths, with particular attention for carefully obeying eye safety levels. Design compromises need to be made regarding the FoV: on the one hand the FoV needs to be large enough to provide adequate coverage, on the other hand the FoV of the transmitter must be small enough to deliver enough power density at the receiver. By using multiple transmitter and receiver units, each with a smaller FoV, the total FoV can be increased while preserving enough received power density [63]. Imaging diversity may be deployed, where an array of light sources is mapped to an array of detectors. By means of a 7-channel diversity receiver equipped with a hexagonal MSM InGaAs photodetector array, using MIMO techniques a data throughput of 5Gbit/s can be achieved [64].

Alternatively, angular diversity may be deployed, where the sources emit at different angles and the receiver has multiple detectors looking into different

angles [65]; this angular diversity approach is illustrated in Fig. 2-29 [66]. A three-channel angular diversity system in which each transmitter and receiver had a FoV of about 8° , achieved a data rate of 1.25Gbit/s at $\lambda=830\text{nm}$ over a range of 3 meters. Increasing the FoV to 30° , and using larger APD detectors, an increased area in a range of 5-6 meters could be covered with a data rate of 280Mbit/s. Higher capacities can be envisaged by reducing the FoV and adopting wavelengths beyond 1400nm where the eye safety standards allow higher light flux levels. With narrow light beams, appropriate area coverage at data rates beyond 1Gbit/s may be achieved by adaptive light beam steering techniques, e.g. using spatial light modulators, micro-mechanical mirrors based on MEMS technology, or diffractive modules [67] [68].

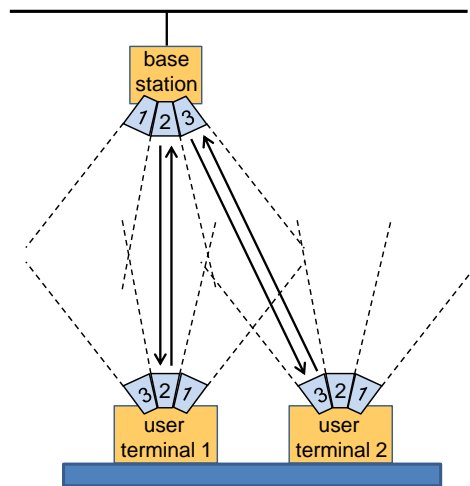


Fig. 2-29 Angle diversity system for optical wireless communication (from [66])

An indoor optical wireless link may also be the extension of an FttH access link. By deploying center launching into the fiber in order to increase the bandwidth of an MMF link and DMT modulation techniques, bidirectional transmission of 30Gbit/s at $\lambda=1.55\mu\text{m}$ over a link of 4.4km MMF in conjunction with a 1.5 meters directional optical wireless link has been demonstrated [69].

Optical wireless communication by means of 2D steered infrared beams can achieve significantly higher aggregate data rates than the wide-beam OWC approaches discussed above, by building on the spatial multiplexing which is enabled by the small footprints of each beam; cf. the beam-steered system proposed as the BROWSE concept in chapter 4 (see Fig. 4-1). Moreover, each beam can be pointed at an individual user, which guarantees high privacy and security, and also can be very energy-efficient as the beams only go where and when needed. A beam actually can provide the capacity of a fiber (and even more, as it does not suffer from waveguide dispersion). A narrow beam may be regarded

as a ‘virtual fiber’ without needing a physical connection. It avoids the mobility problems of a wirebound link, although the beam steering processes require time and thus only support limited mobility, such as nomadic mobility, and static links.

Beam-steered OWC is the main topic of this thesis, including its system architecture and key enabling techniques, and will be discussed in full depth in the chapters 3 to 8.

2.12 Evolution trends

Optical fiber can fulfill a major role in establishing an indoor network which is capable of transporting a wide variety of services and of meeting the ever-growing capacity needs of the users. Taking account of the techniques discussed in the previous sections of this chapter, for the introduction of fiber-based indoor networks the evolution roadmap may be as depicted in Fig. 2-30. The present state of networks is expected to fade out in the near future, and they are to be replaced by fiber-based networks. Each fiber network evolution phase is likely to overlap the next one, as the installation of indoor networks needs sizable capital investments which need to be depreciated over a longer period.

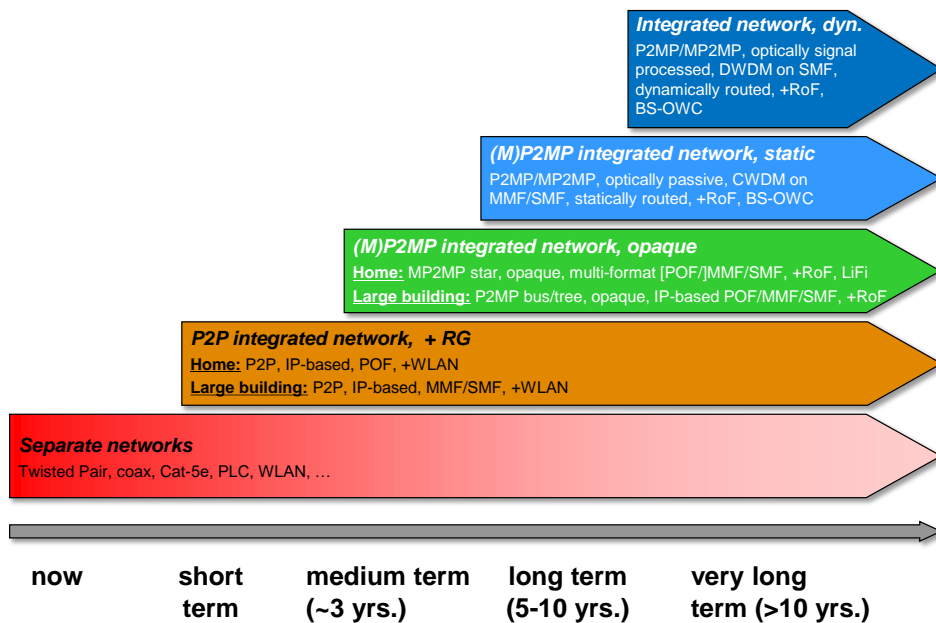


Fig. 2-30 Evolution roadmap for fiber-based indoor networks

From the present status of separate networks each laid out for a particular set of services, fiber may be introduced first in converged P2P topologies, using POF in the home area and bend-insensitive silica MMF or SMF in the larger

(semi-)professional buildings or in the home when POF solutions cannot offer the reach and bandwidth needed. The various types of services may be integrated in this single infrastructure by carrying them on an IP basis. WiFi base stations can be connected on an IP basis too.

In the medium term (around 3 years from now), active P2MP topologies may be introduced, using opaque (O/E/O converting) network nodes; the nodes can do the routing electronically, and do signal restoration which permits the use of (lossy) POF cables as well as silica SMF and MMF cables. In larger buildings, bus or tree topologies may be adopted, which save duct space and cabling costs. Within the home area, as cable lengths are much shorter a multipoint-to-multipoint (MP2MP) star topology with a multi-format electrical switch located in the RG may be adopted, which can handle IP signals but also other signal formats (video and audio streams, control signals for domotica, etc.). To serve the booming needs for wireless connectivity, radio pico-cells may be introduced which can be fed by means of (analog or digital) radio-over-fiber (RoF) techniques, as well as created by first LiFi OWC systems.

In the longer term (some 5 to 10 years from now), passive optical P2MP topologies may be introduced, in which the passive network nodes do just optical power splitting or static wavelength routing. Such functions are readily available with SMF, but not (yet) with MMF or POF; hence the network is likely to be based on bend-insensitive SMF. The optical signals can pass these nodes transparently, without signal conversion, which makes the network compatible for any signal format and readily enables service upgrades. In larger buildings, a bus or tree topology may be preferred; as the dispersed network nodes are fully passive, attractive savings on power consumption and maintenance may be obtained with respect to the active nodes of the medium-term scenario. In the home area, a passive star coupler or multipoint wavelength router (e.g., arrayed waveguide grating router) may be deployed. By means of coarse wavelength multiplexing techniques (CWDM), separate sets of services may be distributed and routed in separate wavelength channels; e.g., to handle the RoF signals. Beam-steered OWC systems may be introduced for providing high-capacity wireless services with low latency and EMI-immunity (such as in intra-data center networks, in industry 4.0 settings for machine-to-machine communication). In residential/office indoor settings they also can releasing spectrum to RF-based wireless networks for serving the plethora of low-bandwidth devices in the Internet-of-Things.

In the more distant future (beyond some 10 years from now), P2MP topologies with dynamically adaptable signal routing in the network nodes may be introduced. To enable such advanced functions, the network will be based on bend-insensitive SMF. By means of optical switching or wavelength conversion, traffic flows (for wirebound and wireless service delivery) in the network may be steered in order to provide capacity on demand and thus improve network

throughput and reduce energy needs, and in order to improve the support of user mobility. These advantages lead to enhanced operational efficiency of the network's resources, as they can be achieved without installing extra equipment. To create adequate granularity for the dynamic routing, a multitude of wavelength channels may be needed, in a dense wavelength division multiplexing (DWDM) scheme. The booming high capacity needs for wireless services may be met by dynamically reconfigurable radio-over-fiber fed pico-cells. In particular dynamically beam-steered optical wireless techniques will be introduced which can deliver on-demand high bandwidth services to densely spaced users in a flexible and energy-efficient way.

Overall, the evolution path of indoor networks is expected to follow a trend of increasing network capacity, reduced power consumption, and increased networking flexibility. This trend can uniquely be supported by fiber-based network solutions and their optically-supported wireless last-meter links.

2.13 Concluding remarks

Indoor networks face an exploding demand for more capacity, versatility and flexibility. Optical fiber is optimally suited to meet this demand; thanks to its large bandwidth, low losses and the extra dimension (namely wavelength) it can offer, it can handle a wide variety of services in a single network infrastructure. For the residential home area, in particular point-to-point network topologies are attractive with large-core PMMA-POF as the fiber medium which provides ease of installation and not only performance-wise but also cost-wise already can outperform mature (Cat-5e) electrical indoor network solutions. Bend-insensitive silica SMF and MMF are less easy to handle, but offer huge bandwidth, very low losses, and readily support optical power splitting and (wavelength) routing functions, which in particular are beneficial in indoor networks in larger (semi-)professional buildings. The severely restricted bandwidth in large-core POF links requires powerful dispersion-robust modulation techniques such as DMT, and for less severely restricted bandwidths multi-level PAM combined with powerful equalization techniques. Gigabit Ethernet POF transceiver modules are entering the market.

In an alliance with wireless links, an indoor fiber network can provide a wide range of services with widely varying bandwidth, while supporting mobility of the users. Radio pico-cell solutions can effectively be supported by radio-over-fiber techniques, and can considerably increase the network's capacity for the delivery of wireless services while reducing the power consumption, in particular when applied in conjunction with optical techniques for dynamic capacity allocation to the pico-cells.

Optical wireless communication techniques are emerging to free up radio spectrum; they can provide the ultimate capacity for wireless connectivity without

EMI disturbances. In particular, beam-steered OWC techniques (as discussed in the remainder of this thesis) can offer huge wireless capacity for broadband services at high user densities and with enhanced energy efficiency. They thus can take away a heavy burden from RF wireless networks giving them more room to handle lower-bandwidth intermittent service delivery as required in the Internet-of-Things with its many diverse devices handling a plethora of services (house keeping, house control, environment and safety control, ...).

2.14 References

- [1] A.M.J. Koonen, E. Tangdiongga, “Photonic home area networks,” *IEEE/OSA J. of Lightwave Technology*, vol. 32, no. 4, Feb. 2014, pp. 591-604.
- [2] A.M.J. Koonen, H.P.A. van den Boom, E. Ortego Martinez, A. Pizzinat, Ph. Guignard, B. Lannoo, C.M. Okonkwo, and E. Tangdiongga, “Cost optimization of optical in-building networks”, *Opt. Exp.*, vol. 19, no. 26, pp. B399-B405, Nov. 2011.
- [3] O. Ziemann, J. Krauser, P. E. Zamzow, and W. Daum, *POF Handbook: Optical Short Range Transmission Systems*, 2nd ed. Berlin: Springer-Verlag, 2008.
- [4] A. Ng’oma, H. Yang, and R. Wagner, “The future of home networking,” in *Proc. ECOC*, Amsterdam, Sep. 2012, Paper Mo.1.G.4.
- [5] Bend-insensitive multimode OM4 fiber [on-line]. Available: <https://www.corning.com/optical-communications/worldwide/en/home/products/fiber/optical-fiber-products/clearcurve-multimode-fiber.html>
- [6] Bend-insensitive single-mode fiber [on-line]. Available: <http://supplier-cables.com/1-4-bend-insensitive-single-mode-optical-fiber.html>
- [7] A. Ng’oma, “Home Networks: Role of Fiber and Wireless Technologies,” *OFC 2023*, in Workshop S2C “Perennial Bandwidth at Home: LiFi or FiWi?,” San Diego, 5 Mar. 2023.
- [8] Cisco Annual Internet Report 2018-2023 [on-line]. Available: <https://www.cisco.com/c/en/us/solutions/collateral/executive-perspectives/annual-internet-report/white-paper-c11-741490.html>
- [9] ESKA plastic optical fiber [on-line]. Available: <https://www.pofeska.com/pofeskae/>
- [10] Y. Koike, T. Ishigure, and E. Nihei, “High-bandwidth graded-index polymer optical fiber,” *J. Lightw. Technol.*, vol. 13, no. 7, July 1995, pp. 1475–1489.
- [11] Multi-core plastic optical fiber [on-line]. Available: <https://i-fiberoptics.com/asahi-multi-core-cable.php>
- [12] T. Ishigure, Y. Aruga, Y. Koike, “High-bandwidth PVDF-clad GI POF with ultra-low bending loss,” *J. Lightw. Technol.*, vol. 25, no. 1, Jan. 2007, pp. 335-345.
- [13] M. Asai, Y. Inuzuka, K. Koike, S. Takahashi, Y. Koike, “High-bandwidth graded-index plastic optical fiber with low-attenuation, high-bending ability, and high-thermal stability for home-networks,” *J. Lightw. Technol.*, vol. 29, no. 11, June 2011, pp. 1620-1626.
- [14] A. Argyros, R. Lwin, S.G. Leon-Saval, J. Poulin, L. Poladian, and M.C.J. Large,

- “Low Loss and Temperature Stable Microstructured Polymer Optical Fibers”, *J. Lightw. Technol.*, vol. 30, no. 1, Jan. 2012, pp. 192-197.
- [15] S. Randel, F. Breyer, S.C.J. Lee, J.W. Walewski, “Advanced modulation schemes for short-range optical communications”, *IEEE J. Sel. Top. Quantum Electr.*, vol. 16, no. 5, pp. 1280-1289, Sep. 2010.
- [16] C. M. Okonkwo, E. Tangdiongga, H. Yang, D. Visani, S. Loquai, R. Kruglov, B. Charbonnier, M. Ouzzif, I. Greiss, O. Ziemann, R. Gaudino, and A. M. J. Koonen, “Recent results from the EU POF-PLUS project: Multi-gigabit transmission over 1 mm core diameter plastic optical fibers,” *J. Lightw. Technol.*, vol. 29, no. 2, pp. 186–193, Feb. 2011.
- [17] A. Nespola, S. Straullu, P. Savio, D. Zeolla, J.C. Ramirez Molina, S. Abrate, R. Gaudino, “A new physical layer capable of record gigabit transmission over 1 mm step index polymer optical fiber,” *J. Lightw. Technol.*, vol. 28, no. 20, pp. 2944-2950, Oct. 2010.
- [18] S. Loquai, R. Kruglov, B. Schmauss, C.-A. Bunge, F. Winkler, O. Ziemann, E. Hartl, T. Kupfer, “Comparison of modulation schemes for 10.7 Gb/s transmission over large-core 1 mm PMMA polymer optical fiber,” *J. Lightw. Technol.*, vol. 31, no. 13, pp. 2170-2176, July 2013.
- [19] D. Visani, C.M. Okonkwo, Y. Shi, H. Yang, H.P.A. van den Boom, G. Tartarini, E. Tangdiongga, and A.M.J. Koonen, “ 3×2^N -QAM constellation formats for DMT over 1-mm core diameter plastic optical fiber,” *IEEE Photon. Technol. Lett.*, vol. 23, no. 12, pp. 768-770, June 2011.
- [20] Y. Shi, E. Tangdiongga, A.M.J. Koonen, A. Bluschke, P. Rietzsch, J. Montalvo, M.M. de Laat, G.N. van den Hoven and B. Huiszoon, “Plastic optical fiber based in-home optical networks,” *IEEE Comm. Mag.*, pp. 186-193, June 2014.
- [21] IEEE Standard for Ethernet Amendment 9: Physical Layer Specifications and Management Parameters for 1000 Mb/s Operation Over Plastic Optical Fiber [on-line]. Available: <https://standards.ieee.org/ieee/802.3bv/6023/>
- [22] Technical paper GSTP-OVHN overview G.hn technology [on-line]. Available: https://www.itu.int/dms_pub/itu-t/opb/tut/T-TUT-HOME-2021-3-PDF-E.pdf
- [23] M. V. Ramana Murty, “Optical link over GI POF” [on-line]. Available: https://www.ieee802.org/3/dh/public/Sep_2022/murty_3dh_01_220912.pdf
- [24] H. Yang, S.C.J. Lee, E. Tangdiongga, C. Okonkwo, H.P.A. van den Boom, F. Breyer, S. Randel, A.M.J. Koonen, “47.4 Gb/s transmission over 100 m graded-index plastic optical fiber based on rate-adaptive discrete multitone modulation”, *J. Lightw. Technol.*, vol. 28, no. 4, pp. 352-359, Feb. 2010.
- [25] B.L. Dang, R.V. Prasad, I. Niemegeers, “On the MAC protocols for radio over fiber indoor networks,” in *Proc. ICCE*, Hanoi, Oct. 10-11, 2006, pp. 112-117.
- [26] R. Griffin, P.M. Lane, and J.J. O’Reilly, “Radio-over-fiber distribution using an optical millimeter-wave/DWDM overlay,” in *Proc. OFC/IOOC 1999*, San Diego, February 1999, Paper WD6-1.
- [27] A.M.J. Koonen, M. Garcia Larrode, “Radio-over-MMF techniques – part II: microwave to millimeter-wave systems”, *J. Lightwave Technol.*, vol. 26, no. 15, pp. 2396-2408, Aug. 2008.

-
- [28] Y. Shi, D. Visani, C. M. Okonkwo, H. Yang, H. P. A. van den Boom, G. Tartarini, E. Tangdiongga, and A. M. J. Koonen, "First demonstration of HD video distribution over large-core POF employing UWB for in-home networks," in *Proc. OFC/NFOEC 2011*, Los Angeles, March 2011, Paper OWB5.
- [29] S.T. Abraha, E. Tangdiongga, A. Crivellaro, R. Gaudino, and A.M.J. Koonen, "Accurate ranging/localization technique using IR-UWB for smart fiber-wireless in-house networks," in *Proc. ECOC 2012*, Amsterdam, Sep. 2012, Paper P6.03.
- [30] S.T. Abraha, H. Yang, C.M. Okonkwo, H.P.A. van den Boom, E. Tangdiongga, and A.M.J. Koonen, "Novel generation and transmission of 2 Gbps impulse radio ultra-wideband over MMF for in-building networks application," in *Proc. OFC/NFOEC*, San Diego, March 2010, Paper OML4.
- [31] S. Zou, H. Chen, F. Huijskens, Z. Cao, E. Tangdiongga, and A.M.J. Koonen, "Demonstration of fully functional MIMO wireless LAN transmission over GI-MMF for in-building networks," in *Proc. OFC/NFOEC*, Anaheim, March 2013, Paper JTh2A.08.
- [32] P. Guignard, J. Guillory, P. Chanclou, A. Pizzinat, O. Bouffant, N. Evanno, J. Etrillard, B. Charbonnier, S. Gosselin, L. Guillo, and F. Richard, "Multi-format home networks using silica fibres," in *Proc. ECOC*, Amsterdam, Sep. 2012, Paper Mo.1.G.5.
- [33] E. Tangdiongga, Y. Shi, C. Okonkwo, H.P.A. van den Boom, and A.M.J. Koonen, "Recent achievements in POF transmission," in *Proc. ECOC*, Amsterdam, Sep. 2012, Paper Mo.2.G.1.
- [34] Y. Shi, C.M. Okonkwo, E. Tangdiongga, and A.M.J. Koonen, "Bi-directional ultra-wideband services over large-core POF-PON based home networks," in *Proc. OFC/NFOEC*, Anaheim, Mar. 2013, Paper NTu3J.4.
- [35] Y. Shi, C. Okonkwo, D. Visani, E. Tangdiongga, T. Koonen, "Distribution of broadband services over 1-mm core diameter plastic optical fiber for point-to-multipoint in-home networks," *J. of Lightw. Technol.*, vol. 31, no. 6, pp. 874-881, Mar. 2013.
- [36] C.R.B. Corrêa, K.A. Mekonnen, F.M. Huijskens, A.M.J. Koonen, E. Tangdiongga, "Multi-Gigabits per Second Spatial Multiplexing Transmission Using Passive OFE and WDM-over-POF", *Proc. ECOC 2022*, paper We3F.4, Basel, Sep. 2022.
- [37] A.M.J. Koonen, M. Garcia Larrode, "Radio-over-MMF techniques - Part II: microwave to millimeter-wave systems", *IEEE J. of Lightwave Technology*, 2008, Vol. 26, No. 15, pp. 2396-2408
- [38] A. Meijerink et al, "Phased array antenna steering using a ring resonator-based optical beam forming network", *Proc. 13th Annual Symposium of the IEEE/CVT Benelux chapter*, 23 Nov. 2006, Liège, Belgium. pp. 7-12.
- [39] Z. Cao, R. Lu, Q. Wang, N. Tessema, Y. Jiao, H. P. A. van den Boom, E. Tangdiongga, and A. M. J. Koonen, "Cyclic additional optical true time delay for microwave beam steering with spectral filtering," *Optics Letters*, vol. 39, pp. 3402-3405, 2014.
- [40] N.M. Tessema, Z. Cao, J.H.C. van Zantvoort, K.A. Mekonnen, A. Dubok, E. Tangdiongga, A.B. Smolders A.M.J. Koonen, "A tunable Si₃N₄ integrated true time delay circuit for optically-controlled K-band radio beamformer in satellite

- communication," *IEEE J. of Lightwave Technology*, Oct. 2016, Vol. 34, No. 20, pp. 4736 - 4743.
- [41] B.-M. Jung, J.-D. Shin, B.-G. Kim, "Optical True Time-Delay for Two-Dimensional X Band Phased Array Antennas", *IEEE Photonics Technology Letters*, Vol. 19, No. 12, June 15, 2007, pp. 877-879
- [42] IEEE 802.11be, a.k.a. WiFi 7 [on-line]. Available: https://en.wikipedia.org/wiki/IEEE_802.11be
- [43] B. Vidal, J. L. Corral, M. A. Piqueras, and J. Marti, "Optical delay line based on arrayed waveguide gratings' spectral periodicity and dispersive media for antenna beamforming applications," *IEEE J. of Selected Topics in Quantum Electronics*, Vol. 8, No. 6, pp. 1202-1210, 2002
- [44] S. Yegnanarayanan, P. D. Trinh, and B. Jalali, "Recirculating photonic filter: a wavelength-selective time delay for phased-array antennas and wavelength code-division multiple access," *Optics Letters*, Vol. 21, No. 10, pp. 740-742, 1996.
- [45] B. Jalali, S.S. Yegnanarayanan, "Method and apparatus for a wavelength selective true-time delay for an optically controlled device", *US Patent 5793907*, Aug. 11, 1998
- [46] A.M.J. Koonen, Z. Cao, E. Tangdionga, "Optically Controlled 2D Radio Beam Steering System," *Proc. MWP 2014*, paper WD-3, Sapporo, Oct. 2014, p. 389-391.
- [47] Z. Cao, Radio beam steering in indoor fibre-wireless networks, PhD thesis, Eindhoven Univ. of Technology, Apr. 15, 2015, Ch. 3.4.
- [48] A.M.J. Koonen, N.C. Tran, and E. Tangdionga, "The merits of reconfigurability in WDM-TDM optical in-building networks," in *Proc. OFC/NFOEC*, Los Angeles, Mar. 2011, Paper JWA63.
- [49] S. Zou, C.M. Okonkwo, Z. Cao, N.C. Tran, E. Tangdionga, and A.M.J. Koonen, "Dynamic optical routing and simultaneous generation of millimeter-wave signals for in-building access network," in *Proc. OFC/NFOEC*, Los Angeles, Mar. 2012, Paper OTh3G6.
- [50] A.M.J. Koonen, H.P.A. van den Boom, G.-D. Khoe, "Broadband access and in-house networks – extending the capabilities of multimode fibre networks", in *Proc. ECOC*, Rimini, Sep. 2003, Paper Mo3.1.5.
- [51] A.M.J. Koonen, H.P.A. van den Boom, I. Tafur Monroy, G.-D. Khoe, "High capacity multi-service in-house networks using mode group diversity multiplexing", in *Proc. OFC/NFOEC*, Anaheim, Feb. 2004, Paper FE-H.
- [52] H.S. Chen, H.P.A. van den Boom, and A.M.J. Koonen, "30-Gb/s 3x3 optical mode-group-division multiplexing system with optimized joint detection," *IEEE Photon. Technol. Lett.*, vol. 23, no. 18, pp. 1283-1285, Sep. 2011.
- [53] S. Schöllmann, W. Rosenkranz, "Experimental Verification of Mode Group Diversity Multiplexing over GI-POF at 21.4 Gb/s without Equalization," in *Proc. Plastic Fiber Conference*, Seoul, Sep. 2006.
- [54] P.J. Winzer, "Spatial multiplexing in fiber optics: the 10x scaling of metro/core capacities," *Nokia Bell Labs Techn. J.*, Vol. 19, 2014, pp. 22-30, <https://doi.org/10.15325/BLTJ.2014.2347431>
- [55] F. Träger (ed.), *Handbook of lasers and Optics*. Berlin: Springer-Verlag, 2012, chapter 25 Laser safety.

-
- [56] Laser safety [on-line]. Available: https://en.wikipedia.org/wiki/Laser_safety
- [57] V. Jungnickel, A. Forck, T. Haustein, U. Krüger, V. Pohl, C. von Helmolt, "Electronic Tracking for Wireless Infrared Communications," *IEEE Tr. on Wireless Comm.*, Vol. 2, No. 5, Sep. 2003, pp. 989-999.
- [58] S. C. J. Lee, J. W. Walewski, S. Randel, F. Breyer, H.P.A. van den Boom, and A. M. J. Koonen, "Discrete multitone for novel application areas of optical communications", in *Proc. IEEE/LEOS Summer Top. Meetings*, Acapulco, July 2008, Paper TuE3.3.
- [59] J. Vucic, C. Kottke, S. Nerreter, K.-D. Langer, J.W. Walewski, "513 Mbit/s visible light communications link based on DMT-modulation of a white LED," *J. Lightw. Technol.*, vol. 28, no. 24, pp. 3512-3518, Dec. 2010.
- [60] Gigabit Home Networking standard [on-line]. Available: <https://en.wikipedia.org/wiki/G.hn>
- [61] G. Cossu, A.M. Khalid, P. Choudhury, R. Corsini, and E. Ciaramella, "3.4 Gbit/s visible optical wireless transmission based on RGB LED," *Opt. Exp.*, vol. 20, no. 26, pp. B501-B506, Dec. 2012.
- [62] J. Grubor, S. Randel, K.-D. Langer, J.W. Walewski, "Broadband Information Broadcasting Using LED-Based Interior Lighting," *J. Lightw. Technol.*, vol. 26, no. 24, pp. 3883-3892, Dec. 2008.
- [63] D. O'Brien, H. Le Minh, G. Faulkner, M. Wolf, L. Grobe, J. Li, O. Bouchet, "High data-rate infra-red optical wireless communications: implementation challenges", in *Digest IEEE Globecom 2010 Workshop on Optical Wireless Communications*, Miami, Dec. 2010, Workshop OWC03.
- [64] J. Zeng, V. Joyner, J. Liao, S. L. Deng, and Z. R. Huang, "A 5 Gb/s 7-channel current-mode imaging receiver front-end for free-space optical MIMO," in *Proc. 52nd IEEE Int. Midwest Symp. Circuits Syst.*, 2009, vol. 1/2, pp. 148-151.
- [65] D. O'Brien, R. Turnbull, H. Le Minh, G. Faulkner, O. Bouchet, P. Porcon, M. El Tabach, E. Gueutier, M. Wolf, L. Grobe, and J. Li, "High-Speed Optical Wireless Demonstrators: Conclusions and Future Directions," *J. Lightw. Technol.*, vol. 30, no. 13, pp. 2181-2187, Jul. 2012.
- [66] H. Le Minh, D. O'Brien, G. Faulkner, O. Bouchet, M. Wolf, L. Grobe, and J. Li, "A 1.25-Gb/s indoor cellular optical wireless communications demonstrator," *IEEE Phot. Technol. Lett.*, vol. 22, no. 21, Nov. 2010, pp. 1598-1600.
- [67] C.J. Henderson, D.G. Leyva, and T.D. Wilkinson, "Free space adaptive optical interconnect at 1.25Gb/s, with beam steering using a ferroelectric liquid-crystal SLM," *J. Lightw. Technol.*, vol. 24, no. 5, May 2006, pp. 1989-1997.
- [68] A.D. Yalcinkaya, H. Urey, D. Brown, T. Montague, and R. Sprague, "Two-axis electromagnetic microscanner for high resolution displays," *IEEE J. Microelectromech. Syst.*, vol. 15, no. 4, Aug. 2006, pp. 786-794.
- [69] H. Chen, H.P.A. van den Boom, E. Tangdiongga, A.M.J. Koonen, "30-Gb/s bidirectional transparent optical transmission with an MMF access and an indoor optical wireless link," *IEEE Phot. Technol. Lett.*, vol. 24, no. 7, Apr. 2012, pp. 572-574.

3 Optical wireless communication technologies⁴

3.1 Introduction

Already for decades, the demand for wireless communication is growing relentlessly. The growth is being fueled by broadband mobile services to smartphones, tablet computers, laptops, etc., and by interaction over the internet among the myriads of devices constituting the Internet of Things. These wireless traffic loads are mainly generated indoors, and are driving today's wireless networks such as those in the IEEE 802.11 suite into serious congestion. New radio spectrum bands are being opened, e.g., sub-THz ones stretching the spectrum up to some 300GHz. Nevertheless, the ongoing exponential traffic growth is quickly exhausting the capabilities offered by radio communication. In the optical domain, however, in the vast frequency regions of the optical domain a wealth of additional spectrum is available, without requiring licensing fees (see Fig. 3-1).

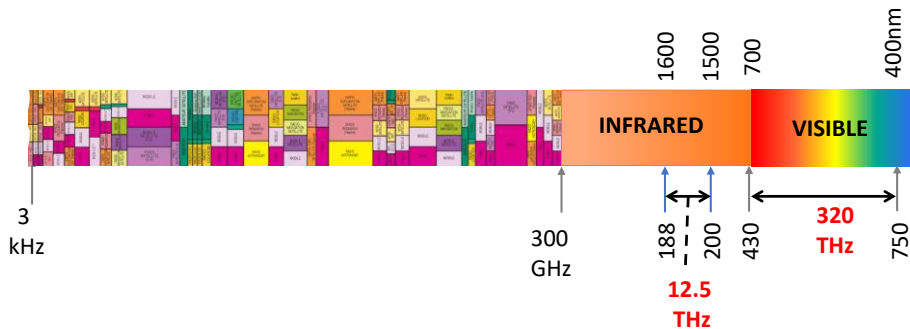
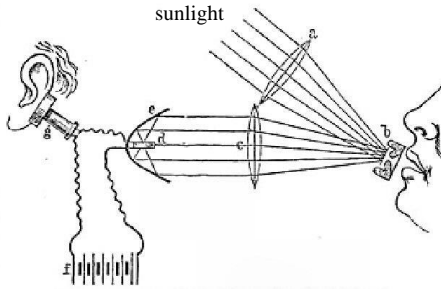


Fig. 3-1 The crowded radio spectrum: the optical domain offers huge extra spectrum This yet unoccupied vast spectrum can be disclosed by Optical Wireless Communication (OWC) techniques. Moreover, OWC enables to create smaller

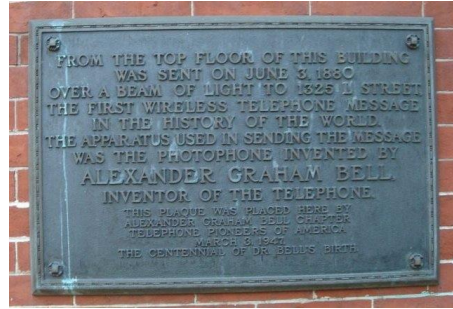
⁴ This chapter is largely based on A.M.J. Koonen, "Indoor optical wireless systems: Technology, trends, and applications," *IEEE/OSA J. of Lightw. Technol.*, vol. 36, no. 8, pp. 1459–1467, Apr. 2018 (doi: 10.1109/JLT.2017.2787614.)

communication cells in the network, which is a vital key to unlock the path to exponential capacity growth. According to Cooper's Law [1], the density of radio communications has increased with a factor of 10^6 in the past 45 years. To this factor, the opening-up of new radio spectrum has contributed with a factor 25, frequency division techniques with factor 5, more comprehensive modulation formats with a factor 5, but the major factor ($1600\times$) was contributed by the introduction of spatial division, in particular by smaller cells and/or more antennas per cell enabling spectrum re-use.

OWC can offload heavy traffic loads from congested radio-based wireless networks, thus making the room available which is desperately needed for intense low-capacity streams such as in the Internet of Things. However, OWC is not intended to fully replace radio wireless communication. E.g., it cannot reach out-of-sight devices (such as smartphones etc. shielded within clothing), while radio techniques (below 60GHz) can do that.



a) Schematic of the photophone



b) Plaque at Franklin School, Washington D.C.

Fig. 3-2 Alexander Graham Bell's photophone

Actually, optical wireless communication by means of beams of light was already proposed by Alexander Graham Bell in 1880 [2]. He invented the 'photophone' together with his assistant Charles Sumner Tainter on Feb. 19, 1880, in his laboratory in Washington D.C. (Fig. 3-2). A voice telephone message was sent by the photophone from the roof of the Franklin School to the window of his laboratory over a distance of about 213 meters. Bell stated that the photophone was 'his greatest, most important invention'. Of his 30 patents, 4 were about the photophone. The master patent was issued in Dec. 1880 (U.S. Patent 235,199 'Apparatus for Signalling and Communicating, called Photophone'). The photophone is regarded as the pre-cursor of fiber-optic communication systems.

This chapter intends to give a tutorial overview of the research domain of OWC. This field is very broad, with a large diversity of activities. The overview

given here therefore cannot be exhaustive, and mainly focuses on OWC techniques for short range (indoor) communication. After discussing the application domains of OWC in section 3.2, techniques for visible light communication (VLC) and its network-based variant Light Fidelity (LiFi), and for beam-steered infrared light communication (BS-ILC), which are the two main methods for OWC, are discussed in sections 3.4, 3.5 and 3.6, respectively. Subsequently, techniques for OWC receivers in order to increase the Field-of-View (FoV) for easing receiver alignment and to enlarge the aperture for capturing more power are addressed in section 3.7. In section 3.8, techniques for the localization of the users' devices (amongst others to support beam steering) are discussed. In section 3.9 the application of these techniques in hybrid bi-directional networks (i.e. combining optical wireless and radio wireless communication) and in all-optical OWC networks is discussed. In section 3.10 the characteristics of beam-steered OWC are compared with those of wide-beam OWC (i.e., VLC/LiFi), regarding EMI immunity, data capacity per device, latency, and energy efficiency. Beam-steered OWC is very strong on these aspects; it is less strong on the support of user/device mobility, and may be hampered by non-line of sight (non-LoS) conditions. Photonic integration technologies may play an important role in enabling robust and compact indoor OWC systems. So far, photonic integrated circuits (PICs) for communication have been mainly explored for optical fiber communication. Their potential for various OWC functions is discussed in section 3.11. The chapter is concluded with some considerations about the prospects of indoor OWC in section 3.12.

3.2 OWC's application domains

OWC is not hampered by electro-magnetic interference (EMI) nor does it generate interference for EM-sensitive devices, it is nearly impossible to jam and offers a high level of privacy (e.g., does not penetrate walls to get to the neighbours), its installation can be relatively easy, and it gives access to a huge amount of spectrum which is license-free. Building on its ability to selectively cover small areas, by means of spatial re-use it can offer a large, aggregated capacity. These characteristics are advantageous in densely populated environments where people generate high traffic loads, such as in open office rooms, conference halls, exhibition halls, airplane cabins, train cabins, (virtual reality) gaming halls, etc. Its relative ease of installation (e.g., VLC may be integrated with lighting) and high privacy level makes it attractive for residential services at home and in office buildings. Its EMI-insensitivity enables robust and highly reliable communication such as needed for industrial manufacturing robots, intra-data center top-of-the-rack interconnects, temporary (disaster-recovery) networks, intensive care hospital rooms and surgery rooms, etc.

Atmospheric conditions may hamper its outdoor use, in particular over longer reaches and in foggy conditions. Mobile backhauling for small radio cells (spaced several hundreds of meters), car-to-car and car-to-roadside communication are examples of attractive outdoor scenarios.

3.3 Indoor OWC techniques

As illustrated in Fig. 3-3, two major categories of indoor OWC techniques may be distinguished: visible light communication (VLC, and its networked variant LiFi) and beam-steered infrared light communication (BS-ILC).

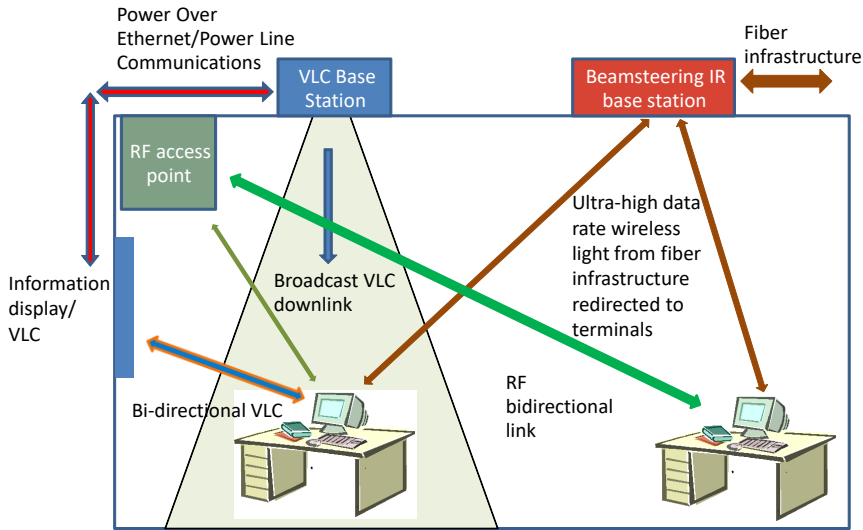


Fig. 3-3 Basic indoor OWC scenarios (from [3])

VLC (and more specifically LiFi [1]) gives access to no less than 320THz in the 400-700nm range. VLC typically is deployed in conjunction with illumination, by modulating the data on the LED luminaries. The re-use of the existing infrastructure can lower the entry threshold for VLC. These LEDs have primarily been designed for generating light in the most efficient way, and have a restricted modulation bandwidth. Moreover, the illumination systems typically serve a large area in which multiple devices have to share this limited VLC capacity by means of a suitable medium access control (MAC) protocol. The received light intensity goes down proportionally with the squared distance to the LED source, thus limiting the SNR and hence the reach. VLC requires that the illumination is switched on, which may not always be desired (e.g., when the room is already filled with bright daylight).

Beam-steered IR light communication (BS-ILC) brings the light only there

where and when it is needed. It operates independently from illumination systems, and needs a separate infrastructure. Benefiting from well-established technologies in the S+C+L wavelength bands for fiber-optic communication, access can be obtained to 20.9THz of frequency spectrum in the 1460-1625nm range. Multiple beams may each serve a user terminal individually within the room, without sharing. Thus, no MAC protocols to arrange shared access are needed. Hence each terminal can get a guaranteed capacity without conflict with other terminals. The directivity of a beam implies that the received power can be substantially higher than with VLC, enabling a higher SNR and thus a higher data rate and longer reach at better power efficiency. Moreover, IR light does not reach the vulnerable retina in the human eye (see Fig. 2-26), which implies that relatively high transmitted power levels are allowed within the eye safety limits (up to 10mW for $\lambda > 1.4\mu\text{m}$, according to IEC 60825, ANSI Z136 standards [5]). Furthermore, the photodiode's responsivity basically is proportional to wavelength⁵, which at high data rates enables receivers to have a higher sensitivity in the IR domain than in the visible domain.

The IEEE 802.11 suite of radio standards is presently widely established and used for indoor wireless communications. Its basic characteristics are compared in a non-exhaustive way with exemplary OWC characteristics in Table 3-1. With BS-ILC, no capacity sharing is incurred, thus a guaranteed very high capacity per device can be provided. With both VLC and BS-ILC, however, line-of-sight (LoS) is needed. With its recently established IEEE 802.11bb standards, LiFi based on its multi-point networking can relax the LoS demands. With the IEEE 802.11 radio techniques (at least below 60GHz) non-LoS devices can be reached also.

Products of the IEEE 802.11 WiFi suite are abundantly available commercially. Empowered by the recent IEEE 802.11bb standard, LiFi products in various embodiments are entering the market. VLC is bringing some first products into the market, and BS-ILC is still largely in the laboratory research phase. Due to the difference in market maturity, cost comparisons are hard to make. Basically, from a capital expenditures (CapEx) perspective the IEEE 802.11 suite, LiFi and VLC tend to incur lower costs, as they need little infrastructure or re-use existing infrastructure (by means of powerline communication, or power-over-ethernet techniques), while BS-ILC needs a new fiber backbone infrastructure. From the perspective of the recurring operating expenditures (OpEx), such as powering, the BS-ILC may be more beneficial as it can be more energy-efficient due to its flexibility to offer capacity-on-demand where and when needed.

⁵ Responsivity $\mathcal{R} = \eta e \lambda / h c_0$ with η the quantum efficiency of the photodiode, e charge of an electron, λ wavelength of the light incident on the photodiode, h Plank's constant, c_0 speed of light in vacuum [6]

Table 3-1 OWC compared with IEEE 802.11 suite
(P2MP: point-to-multipoint links; P2P: point-to-point link)

	VLC	LiFi	BS-ILC	WiFi IEEE802.11
Cap. per user	Shared (P2MP); 9.5Gbit/s over 1m	Shared (P2MP); 220 Mbit/s over few m (845Mbit/s P2P)	Unshared (P2P); very high (up to 112Gbit/s per beam)	Shared; 802.11n (2.4GHz): <150Mbit/s 802.11ac (5GHz): <867Mbit/s 802.11ad (60GHz): <2.4Gbit/s
Reach	Short-to-medium (few m) Needs LoS	Short-to-medium (few m)	Medium (<10m)-long Needs LoS	Medium Does not need LoS (<60GHz)
Energy consumption	High (Watts) if via illumination (needs to be on)	Low/moderate	Low (per beam, <10mW), on-demand only	Base station >100mW
Carrier freq., av. bandwidth	400-700nm; spectrum width 320THz; LED source few tens of MHz	Near-IR, 800-1000nm	1460-1625nm (S+C+L bands); spectrum width 20.9THz, per channel ~35GHz (AWGR steering)	2.4GHz band; width 83.5MHz channels 20 or 40MHz 5GHz band; width 575MHz channels 20 ~160MHz 60GHz band; width 7GHz; channels <320MHz
Safety aspects, power limit	Penetrates eye; if collimated: <<1mW	Reduced eye risk; if collimated, <1mW	Does not penetrate eye; collimated <10mW	EM hypersensitivity issues
Privacy	Good (contained by walls)	Good (contained by walls)	Good (contained by walls)	Open; needs encryption
Infrastructure	Share LED illumination, use electrical infra (w. PLC)	Use of electrical infra (w. PLC)	New indoor (fiber) infra	Electrical cable (Cat5) infra
Standardisation	steps being made in IEEE 802.11 LC study group	IEEE 802.11bb standard ready	Not yet	Extensive, mature, keeps evolving Backwards compatible
Utilisation	Some products on market	Products on the market	Laboratory phase	Very wide spread; more WiFi devices than people on earth; >50% of internet traffic through WiFi

3.4 Visible Light Communication techniques

LEDs which are primarily designed for illumination purposes typically deploy a blue LED chip plus a phosphor coating which generates the white light (see Fig. 3-4.a [7]). The slow decay time of the phosphor severely limits the bandwidth to a few MHz only. Some improvement is obtained when filtering the blue LED light at the receiver, but the bandwidth is still restricted (typically <20MHz). Employing this blue-filtering and basic NRZ-OOK modulation, 40Mbit/s transmission has been achieved at an illumination level of 700 lux (office areas require 200-800 lux) [8]. Spectrum-efficient advanced modulation schemes are to be used in order to realize higher data rates. Applying OFDM with 256 subcarriers and bit-loading, in conjunction with a pre-equalizing filter before the LED driver and a blue filter before a PIN-TIA receiver, a net data rate of 2.0Gbit/s over 1.5m free-space reach was achieved, and 0.79Gbit/s over 3m [12].

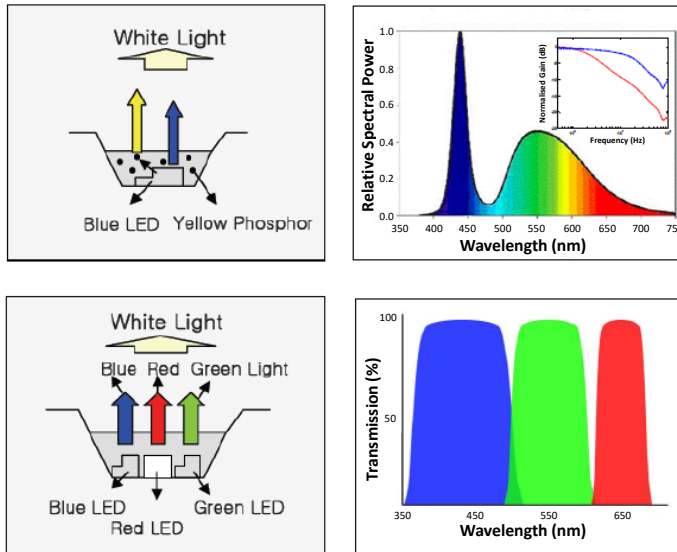


Fig. 3-4 LED types for VLC; a) Blue LED + phosphor, b) RGB multi-element LED [7]

Alternatively, white light may be produced by a multi-element LED, composed of tri-color elements (red + green + blue; see Fig. 3-4.b [7]). Although each of the LED elements may have a limited bandwidth (typically some 15MHz), by modulating them separately the capacity can be tripled. This wavelength division multiplexing (WDM) approach requires a more complex driver at the transmitter end, and three color-filtering stages in parallel at the receiver. Taking this approach and using DMT modulation with 512 subcarriers and color-filtering

APD receivers, 3.4Gbit/s was achieved over 10cm (at 410 lux), and 2.2Gbit/s over 30cm (at 25 lux) [10]. With a quad-color LED (red + green + blue + yellow) and tailored CAP modulation (128-CAP for red, 32-CAP for green, 64-CAP for blue, 128-CAP for yellow), an aggregate capacity of 8Gbit/s over 1m was achieved (see Fig. 3-5) [11].

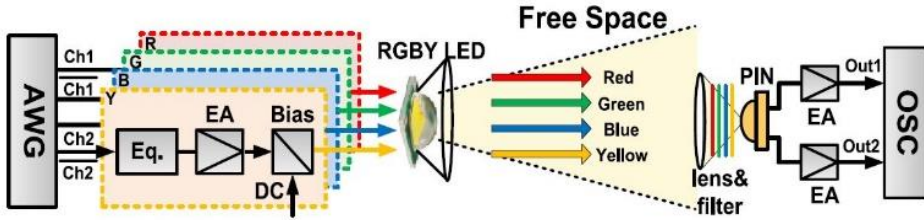


Fig. 3-5 8Gbit/s quad-color VLC system using CAP modulation [11]

The integration of lighting and communication functions brings particular challenges, as the consumer should not perceive any light flickering effects and dimming the light over a wide range should be possible, while communication should continue to be supported. Within IEEE 802.15.7, standards are set for high-speed VLC up to 96Mbit/s. Among their physical layer techniques is the use of multi-color sources using color shift keying (CSK) [12]. Multi-color CSK schemes using three colors (RGB) and four colors (blue, cyan, yellow, red) have been proposed; the four-dimensional coding scheme can have a higher efficiency and better reliability for a given multipath delay spread [13]. CSK uses intensity-modulation of the colored LED elements individually, which implies that the resulting overall color is varying quickly. These instantaneous color variations should not be perceivable by the human eye, so should be faster (i.e., <10ms) than the critical flicker fusion threshold and the critical color fusion threshold. The transmission by the multi-color LED should be set such that when time-averaged a specific constant color is perceived, which requires adequate LED-driving algorithms [14].

Yet another approach is to apply an array of micro-LEDs, which each due to their small active area can have a large bandwidth. Using an array of blue ($\lambda=420\text{nm}$) GaN μLEDs each having an active area diameter of only $42\mu\text{m}$, bandwidth of 400MHz, and 5.7mW output power, with PAM-4 modulation 3.8Gbit/s (3.5Gbit/s excluding 7% FEC) over 0.75m was achieved, and 5.37Gbit/s (5Gbit/s excl. FEC) when using DCO-OFDM with 512 bit-loaded subcarriers[15].

Spatial multiplexing can open another route towards a higher VLC capacity. In a MIMO system setup with a 2-dimensional array of 9 individually addressable $\varnothing 39\mu\text{m}$ blue GaN μLEDs emitting at $\lambda=450\text{nm}$ and with 9 APDs (each

200×200 μm^2 , bandwidth >90MHz) made in a 0.18 μm CMOS process, with PAM-8 modulation about 890Mbit/s per channel was achieved over a free-space link of 50cm, and an aggregate rate of 6.95Gbit/s (excl. 7% FEC) [16].

VLC systems are becoming available commercially. Bi-directional point-to-point systems are offered providing 1Gbit/s connectivity with low latency (<2ms) [17].

3.5 Light Fidelity (LiFi) techniques

Dubbed LiFi (Light Fidelity), VLC techniques which are basically point-to-point are extended into a fully networked system in an atto-cells network architecture, supporting seamless handover between these cells and bi-directional operation [4]. The LiFi-X system of PureLiFi supports 40Mbit/s full-duplex communication, using a USB dongle at the user's device [18]. Trulifi products of Signify offer data rates of 220/160 Mbit/s in down-/up point-to-multipoint link, and up to 845Mbit/s in a down/up point-to-point link [19]. Standardization of LiFi is well underway. The 802.11bb standard ([20], established by the IEEE 802.11 Light Communication Task Group with efforts from PureLiFi and Fraunhofer Heinrich Hertz Institute) builds on the well-established IEEE 802.11 suite of standards, and describes the communication protocols for LiFi devices. Different from VLC, the LiFi technology is not primarily aiming to re-use the existing illumination technology. The 802.11bb standard describes line-of-sight networking using light in the near-infrared spectrum 800-1000nm for data transport between 10 Mbit/s and 9.6 Gbit/s.

3.6 Beam-steered IR optical communication techniques

When working with narrow IR beams, accurate and independent two-dimensional steering of multiple beams is needed in order to establish links to multiple (non-stationary) terminals. First concepts for this were introduced in [22], describing beam steering by a material in which multiple holograms were recorded. By using a specific spatial code on the beam which is impressed by means of a spatial light modulator (SLM), the beam is deflected by the corresponding hologram into a specific direction. An SLM processes a beam by spatially altering the intensity, phase or polarization of the incident light, and as such can perform as a dynamically adaptable diffraction grating. They are typically based on liquid crystal nematic micro-displays, with transmissive (with LCD) or reflective (with LCOS; gives better performance) pixels [21].

Several approaches can be followed to establish beam steering, which may be classified coarsely in those using active steering devices and in those using passive ones.

3.6.1 Active beam-steering devices

In active beam steering devices (e.g., MEMS mirrors, spatial light modulators (SLMs)) the state of the device is changed by means of a separate control channel, and a change in the state implies a change in the beam's direction. Per beam a separate controllable state is needed, which compromises the scaling to many beams. The number of programmable pixels of the SLM and their size determine the beam steering characteristics. As the pixels are typically large with respect to the wavelength, the steering angle is small [23]. Moreover, a comprehensive driver module is needed to program the SLM.

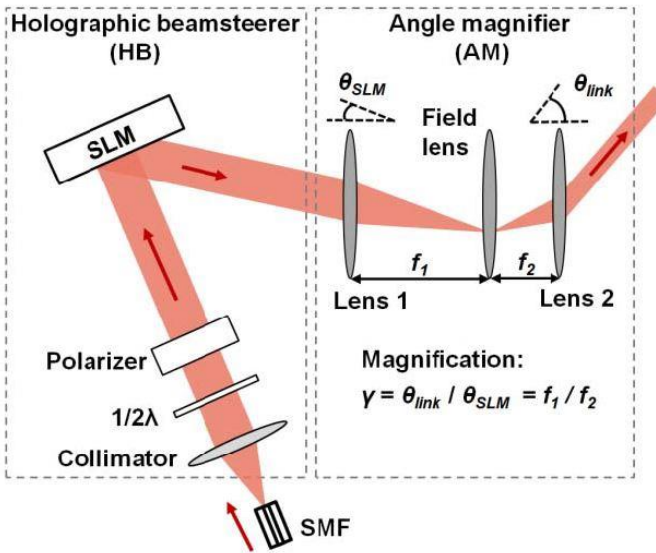


Fig. 3-6 2D beam steering with SLM and angle magnifier [24]

An SLM having 512×512 pixels with 256 phase levels was used for steering a beam at $\lambda = 1.55 \mu\text{m}$ (see Fig. 3-6) [24]. The maximum steering angle θ_{max} attainable by the SLM is determined by the SLM's pitch p ; with a $p = 15 \mu\text{m}$, this was only $\theta_{SLM, \text{max}} = \lambda / 2p \approx 3^\circ$. An angular magnifier composed by an afocal system with 2 lenses having focal lengths f_1 and f_2 was applied, and can yield an angular magnification factor $\gamma = \theta_{\text{link}} / \theta_{SLM} = f_1 / f_2$, which inevitably goes together with a beam narrowing factor f_2 / f_1 . A field lens may be put in between to reduce lens aberrations. Using such angular magnifier with effective $\gamma = 10$, steering was achieved over $\theta_{\text{link}} = 30^\circ$. Operating in WDM mode with 3 channels spaced by 10.1GHz and carrying 16-QAM signals, $3 \times 37.4 \text{ Gbit/s} = 112 \text{ Gbit/s}$ (incl. 7% FEC) over a 3m free-space link was achieved. If its aperture allows, an SLM may also be operated in different zones each steering a beam [25]. Thus, a (limited)

number of beams can be steered by a single SLM, and optionally point-to-multipoint communication can be supported by sharing different zones.

By means of MEMS mirrors, 2D steering over relatively large angles can be achieved. In [26], steering over $>20^\circ$ is reported, providing 10Gbit/s with CAP-16 modulation over 2m downstream communication with 7mW launched power at $\lambda=1551\text{nm}$ (see Fig. 3-7). A compound parabolic reflector (CPC) was used to increase the receiving aperture, followed by a fiber collimator and PIN photodiode receiver. Deploying a similar MEMS steering mirror and a VCSEL emitting 5mW at $\lambda=850\text{nm}$, in the upstream direction 2Gbit/s was transmitted.

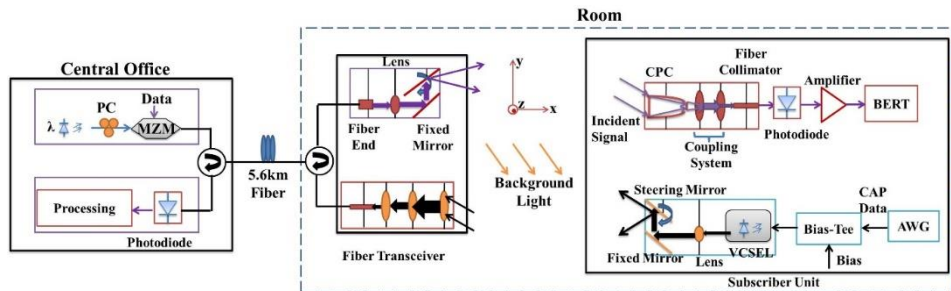


Fig. 3-7 2D beam steering with MEMS mirrors [26]

Beam steering may also be implemented by means of a VCSEL array. Low-divergence IR beams generated by a VCSEL array in conjunction with MIMO techniques have been proposed for meeting the high-density capacity demands in future 6G wireless networks [27], and have been coined as LiFi 2.0 [28].

3.6.2 Passive beam-steering devices

Alternatively, the beam steering can be done by passive devices, which do not change state and have no moving parts. These devices do not need local powering nor a separate control channel. Such passive function may be implemented by a diffractive device, through which the beam steering is controlled by changing the wavelength of the optical data signal fed to the steering device [29]. The control is thus embedded in the data signal and no separate control channel is needed, which simplifies the network's architecture and the system's management, amongst others by avoiding the tedious book-keeping for monitoring which control channel belongs to which data channel. The optical data signals are fed to the steering device by means of an indoor fiber network, and are generated by wavelength-tunable laser transmitters. These transmitters may be jointly located and controlled in a centralized site, which eases maintenance, upgrading and upscaling of the network. Laser tuning times are typically much less than tuning times of a MEMS mirror or SLM, and therefore the beam steering process can be

much faster. If tuning times can be much shorter than the duration of the data packets, a single laser may be able to serve multiple users in a time division multiplexed mode, i.e., in interleaved time slots, thus saving on the amount of tunable laser diodes needed. E.g., wavelength switching of a monolithic widely tunable laser from any channel to any channel in the 100GHz grid of the full C-band within ± 2.5 GHz of the ITU grid frequencies within $1\mu\text{s}$ has been reported in commercially available modules already in 2002 [30].

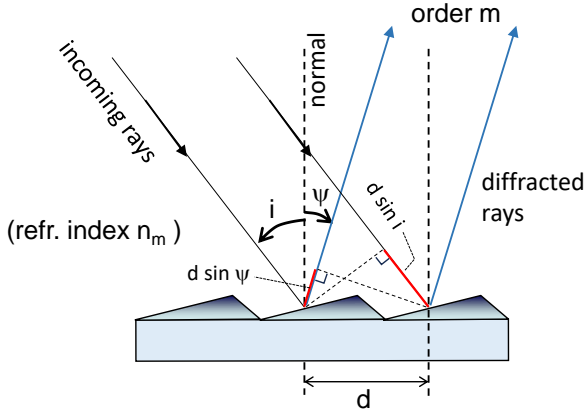


Fig. 3-8 Reflective diffraction grating

Diffraction gratings are well known for deflecting a light beam at an angle ψ as a function of the beam's wavelength λ . For a reflective diffraction grating as illustrated in Fig. 3-8 where constructive interference occurs if neighbouring ray path lengths differ by an integer multiple (the order m) of the wavelength λ , the beam steering is governed by the classical grating equation

$$\sin \psi + \sin i = \frac{m \lambda}{n_m d} \quad (3-1)$$

where i is the beam's incident angle on the grating, ψ the direction in which the diffracted rays constructively interfere in the order of interference m (both i and ψ are measured from the normal, positive if counter-clockwise), d is the grating's period, and n_m the refractive index of the outside medium [31]. The beam is typically deflected in multiple orders m . The free spectral range (FSR) $\Delta\lambda_{FSR,m}$ of order m indicates the width of the wavelength range for which a beam in that order does not enter a neighbouring order. From the grating equation, with $\psi(\lambda_1 + \Delta\lambda_{FSR,m}) = \psi(\lambda)$ it is derived that (see section 5.2)

$$\Delta\lambda_{FSR,m} = \frac{\lambda_1}{m-1} \quad \text{for } m \geq 2 \quad (3-2)$$

where λ_1 is the lowest wavelength of the wavelength range, and that the angular dispersion $d\psi/d\lambda$ is

$$\frac{d\psi}{d\lambda} = \frac{m}{n_m d \cos \psi} \quad (3-3)$$

For the maximum angular tuning range $\Delta\psi_{\max}$ which can be achieved in order m when tuning the wavelength over the full FSR $\Delta\lambda_{FSR,m}$, it is found that [29] (see eq. (5-18))

$$\cos \Delta\psi_{m,\max} = 1 - \frac{\lambda}{d} \frac{m}{m-1} \quad (3-4)$$

Hence, in order to achieve a relatively large angular tuning $\Delta\psi_{\max}$ within a small wavelength tuning range $\Delta\lambda_{FSR,m}$, a large order m and small grating groove spacing d are needed. E.g., when deploying a tuning range from $\lambda=1500$ to 1600nm , it is found that at $m=16$ a $\Delta\psi_{\max}=28.36^\circ$ is achieved for a grating with 75 grooves/mm and a large incidence angle of 66.93° . It may be noted that the efficiency of diffraction gratings depends on the polarization state of the incident beam [32] ; in particular reflection gratings with smaller groove spacings may have noticeably polarization-dependent performance at larger beam incidence angles.

1-Dimensional (1D) beam steering with a plane reflection grating was introduced in [33] for fast optical scanning applications. It was applied for steering of 3.3mm diameter beams transmitting 10Gbit/s with OOK modulation over 2.5m in [34] , employing an echelle grating of 79 grooves/mm, with blaze angle of 75° . An angular steering range of $\Delta\psi=17.2^\circ$ was achieved when tuning over 130nm from $\lambda=1500$ to 1630nm in orders $m=15$ and $m=16$. Upscaling the system to steer multiple beams can be achieved without changing the diffractive device; it just requires that multiple wavelengths are fed to the device, where each wavelength independently determines the direction of its beam.

For 2D optical scanning, it has been proposed to create a number of tilted narrow-band Bragg gratings in a photo-thermo-refractive (PTR) glass volume [35] . Each grating directs the beam with the wavelength which matches that grating into a specific direction. 2D scanning with $M \times N$ beams may be achieved by N PTR plates with each M tilted gratings. Experimentally, a scan over 5° was shown with 4 tilted Bragg gratings at 816 lines/mm when tuning the wavelength over 80nm.

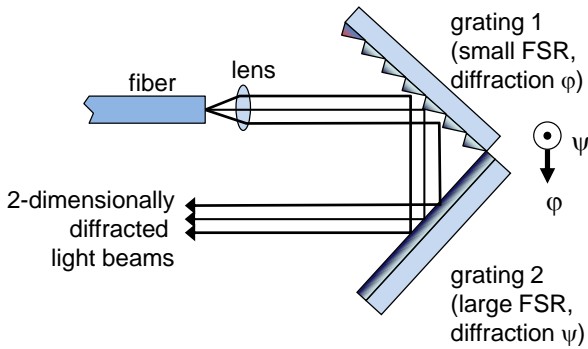
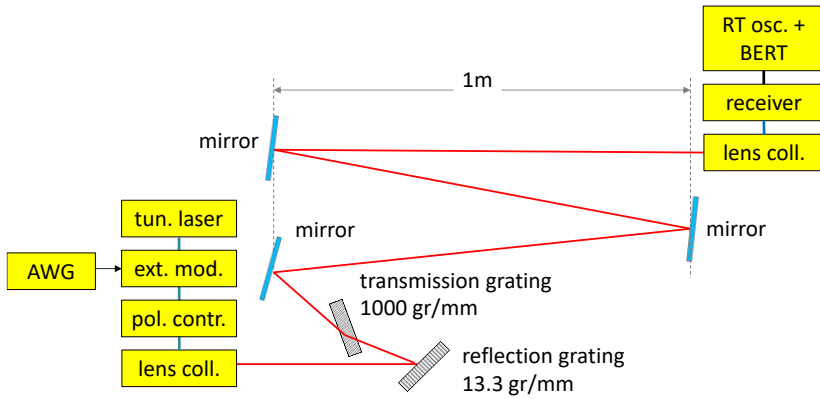
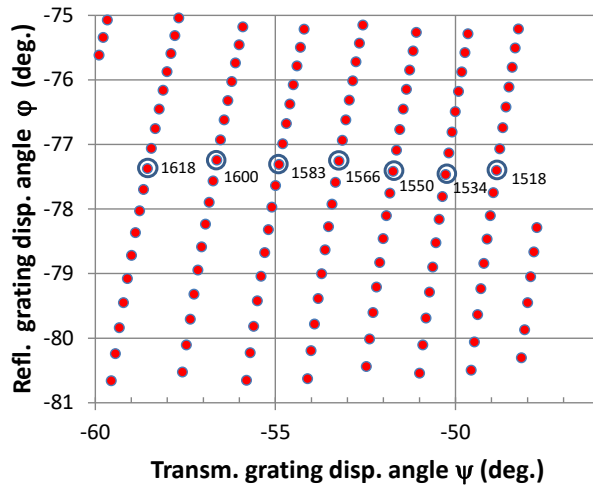


Fig. 3-9 2D beam steering with two crossed gratings [36]

For 2D steering which can be scaled to an arbitrary number of beams, it was proposed to use two crossed diffraction gratings (see Fig. 3-9) [36]. The first grating has a small FSR and many orders of this grating are traversed when tuning the wavelength over the full system range $\Delta\lambda_{\text{tun}}$. The second grating has an FSR which is at least $\Delta\lambda_{\text{tun}}$. As a result, a full line-by-line scanning of a 2D area takes place when tuning the wavelength of the beam over $\Delta\lambda_{\text{tun}}$: the beam is quickly steered along the diffraction direction of the first grating, and slowly along the orthogonal diffraction direction of the second grating. An arbitrary number of beams can independently be steered by feeding an equal number of wavelengths. This crossed-gratings concept is discussed in full detail in section 5.2. 5.3 With 2 crossed reflection gratings with 31.6 and 79 grooves/mm respectively, 2D angular beam steering over $5.6^\circ \times 14^\circ$ has been achieved when tuning the wavelength from 1529 to 1611 nm [37]. Over a free-space link of 2.5 m with a beam diameter of 3.3 mm and path loss up to 14.6 dB (including SMF-coupled lens collimators), 42.8 Gbit/s was transmitted using DMT modulation. With a cross-aligned combination of a transmission grating of 1000 grooves/mm operating in order $m=1$ and a reflection grating of 13.3 grooves/mm operating from order $m=95$, 2D angular beam steering over $5.6^\circ \times 12.7^\circ$ was achieved when tuning from 1505 to 1630 nm for which 8 scanning lines were obtained (see Fig. 3-10) [29]. In combination with the SMF-coupled triplet lens collimators with 18.4 mm focal length, the -3 dB bandwidth of the pencil beam channel was found to be 10.35 GHz. The optical path losses were reduced to less than 6.15 dB, and by means of PAM-4 modulation 32 Gbit/s could be transmitted over a 3 m free-space link.



a) Setup with reflection and transmission grating



b) Wavelength-controlled 2D scanning

Fig. 3-10 2D beam steering with crossed gratings [29]

The crossed-gratings concept can also be realized with a virtually imaged phased array (VIPA) as the element with a small FSR operating in high order m . A VIPA can be implemented by a glass plate with two parallel reflective sides, and its interference order m is about twice the optical thickness of the plate $n_v t$ divided by the wavelength λ [38]. With a VIPA of $t=100\mu\text{m}$ thickness and refractive index of its cavity $n_v=1.5$ (so $m=200$ at $\lambda=1500\text{nm}$), in combination with a transmission grating of 500 lines/mm, 2D line-by-line scanning over $5^\circ \times 9^\circ$ when tuning from 1400 to 1600nm can be achieved [39].

Stepwise wavelength-controlled 2D beam steering may be achieved by means of an arrayed waveguide grating router module which has a large number of

output fiber ports. By arranging the output fibers in a 2D array, and putting this array in front of a lens, each output fiber launches a beam at its specific wavelength into a 2D angular direction given by the lateral position of that fiber with respect to the lens axis [40] [41]; this approach is discussed in full detail in section 5.3. In combination with the lens focal length, the pitch between the fibers in the 2D array is chosen such that the beams create adjacent spots in the 2D user plane to be covered. By putting the 2D fiber array slightly closer to the lens than its focal plane, the beams are slightly diverging, and the module can be made more compact. When using a 1×80 ports AWGR, by applying a defocusing of 12%, the required lens focal length is 10cm, its aperture 5.0cm, and the fiber pitch in the 2D array is 3.7mm. Transmission of 20Gbit/s with NRZ-OOK modulation over 2.5m was shown within the AWGR's -3dB bandwidth of 35GHz, while steering was achieved over $17^\circ \times 17^\circ$ when tuning over C-band (see Fig. 3-11) [42]

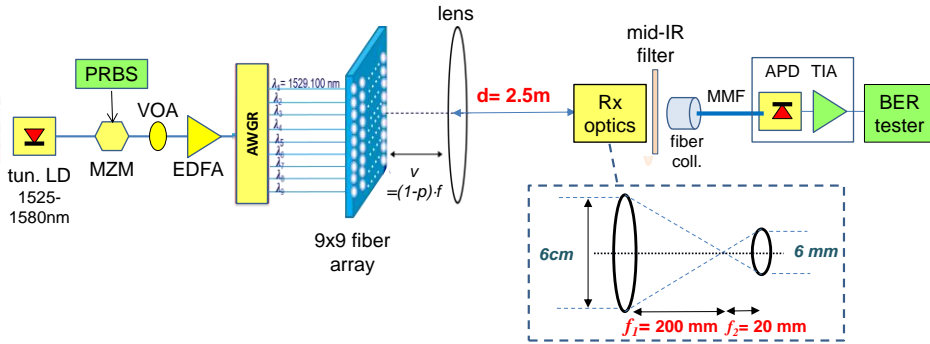


Fig. 3-11 2D beam steering with high port-count AWGR [42]

3.7 OWC receiver

As an OWC receiver is a part of the user's device, it should be compact and low-cost, it should not require tedious alignment with respect to the downstream transmitted optical beams, and it should capture enough optical power to enable a high downstream data capacity. Hence it should have a wide Field-of-View (FoV) and a large aperture. However, increasing the active area of a photodetector is typically accompanied by a reduction of its bandwidth. The "conservation of etendue" law in physics states that etendue (a.k.a. the $A \times \Omega$ product, the product of entrance area A and solid angle Ω subtended by a cone of light) is conserved when light travels through optical systems with perfect, loss-free reflections and refractions. Etendue can then remain constant or increase (e.g., by applying a diffuser), but not decrease [43]. With a compound parabolic reflector (a non-

imaging optical element typically used for solar energy concentration [44] ; cf. Fig. 3-7) put in front of a photodetector, the receiving aperture can be increased, but at the expense of a reduced FoV.

The effective detection area of the OWC receiver may be enlarged while maintaining adequate bandwidth by using a 2D array of fast photodiodes co-integrated with individual electrical preamplifiers followed by a summation amplifier. Fig. 3-12 shows such a so-called angular diversity receiver (ADR) deploying a 2D array of 7 MSM hexagonal photodiodes, each having a side length of $50\mu\text{m}$ and 0.12pF capacitance, followed by a current-summing amplifier, yielding an effective aperture diameter of $260\mu\text{m}$ and overall -3dB bandwidth of 3.7GHz [45] .

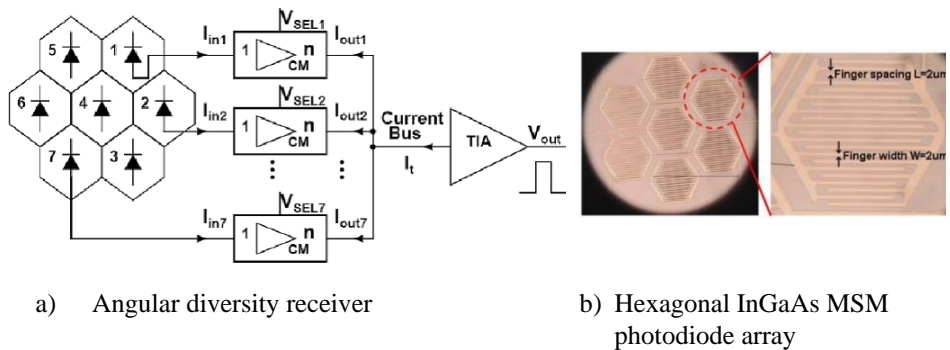


Fig. 3-12 Angular diversity receiver with 7 MSM photodiodes [45]

With a slab concentrator of which the slab waveguide is doped with fluorophore and is terminated with a photodetector, the link between the etendue of the light collection area and that of the detector can be broken [46] . Fig. 3-13 shows how the incoming light is converted to a longer wavelength by the fluorophore and guided to the detector by reflections at the slab surfaces; thus, a wider FoV and higher gain is obtained. Using a quantum dot material as the fluorophore, a gain $50\times$ that of an etendue preserving concentrator with the same FoV can be reached. The long slab may lead to channel dispersion effects, thus reducing the bandwidth and making this solution less suitable for high data rates.

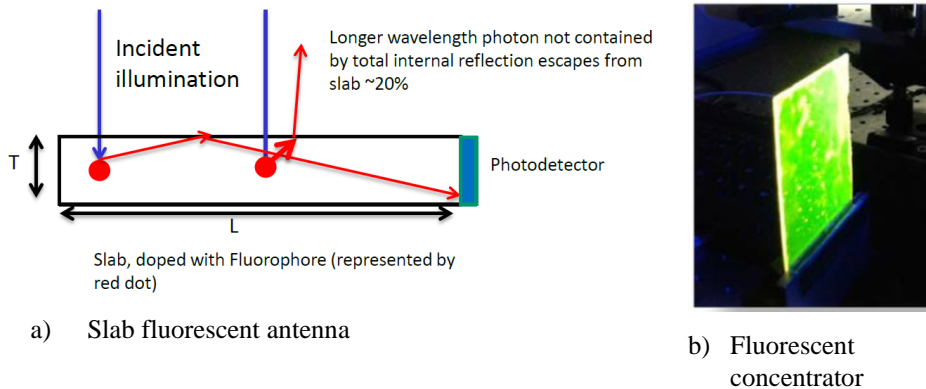


Fig. 3-13 Wide Field-of-View receiver breaking the law of etendue [46]

The light collection function may be separated from the light detection function, which allows optimization of each function separately. This has been proposed by the integrated cascaded aperture optical receiver concept, which is described in section 3.11.2.

3.8 Localization

Localizing the user is needed in a beam-steered OWC system, and may also be applied in wide-beam OWC systems such as LiFi or VLC systems, e.g., for tracking in an industry 4.0 setting and in warehouses.

Next to sending data for communication, a VLC system composed of (multiple) LED luminaries can send signals which contain the identity information of the LEDs and with this can assist in determining the position of a device. As compared to RF, visible light suffers less from multipath effects, and can provide more accurate positioning. The location of the device may be determined by an algorithm using tri-angulation based on time-of-arrival (ToA, like in GPS) data of the light signals from various directions, on time difference of arrival (TDoA) data, on angle of arrival (AoA) data, or on received signal strength (RSS) data [47]. The ToA and TDoA methods require accurate synchronization. AoA can achieve the highest accuracy but is the most complex to realize. RSS is the most popular one in VLC systems as it operates asynchronously and is simple to implement, but it needs well-known path loss models.

Optical Camera Communication (OCC) [48] [49] is being explored for low-to-moderate speed data transfer by LED lighting, and deploys an image sensor or camera at the user's device, e.g. in a smartphone. The data speed is basically limited by the camera's frame rate. MIMO techniques can be exploited using an

LED array and image sensor with pixel-to-bit mapping. By means of computer vision analysis techniques which enable extraction of the LED coordinates, OCC can also enable accurate device positioning.

Alternatively, localization may use an algorithm based on finger printing, or on vision analysis (using a camera at the device). In [50], a 16×16 array of $100 \times 100 \mu\text{m}^2$ GaN μLEDs emitting at $\lambda=450\text{nm}$ is used to generate a time sequence of spatial illumination patterns. These patterns create a specific fingerprint optical signal sequence per site, which when detected by a simple photodetector can provide the device's location. Fast positioning within 10ms was shown, with an accuracy better than 5mm over 40cm distance; accuracy and area coverage can be improved when more emitters are used.

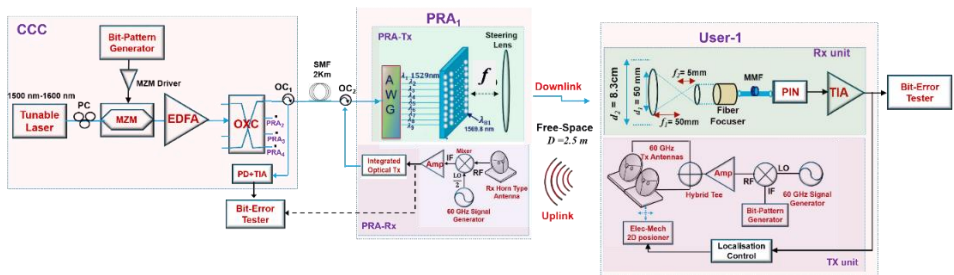


Fig. 3-14 Hybrid system with 2D beam-steered OWC downstream and 60GHz-based radio communication upstream [51]

For beam-steered OWC, the position of the user's device needs to be known with an accuracy depending on the beam's width. For localizing and tracking a device in a hybrid system which uses beam-steered OWC techniques for downstream and radio techniques for upstream, WiFi positioning techniques may be deployed, or more accurately 60GHz antenna pattern nulling. In [51], at the device side two high-gain horn antennas with 30dBi gain are sending upstream data at 60GHz, and RSS pattern nulling techniques at the central ceiling site are used to determine the device's location and direct the downstream optical beam accordingly (see Fig. 3-14).

When using a 2D diffractive beam steerer (e.g., one based on a crossed grating pair, or on a high port-count AWGR, as discussed in chapter 5), the localization may be done by means of the wavelength-to-position mapping function of the steerer. The user's device may send light with a broad spectrum (such as ASE from an SOA) upstream, and the 2D diffractive beam steerer will pass a narrow slice of this upstream light. By assessing the wavelength of this slice with a sensitive spectrum analyzer, the location of the device can be determined [52]. Alternatively, at the ceiling a camera may be installed which when aided by vision analysis enables quick localization and tracking of the devices. A device may be

equipped with a beacon which is traced by the camera. In [53], a circular array of 12 near-IR LEDs emitting at $\lambda=890\text{nm}$ is used, mounted around the aperture of the optical receiver (see Fig. 3-15). The LEDs have a large emission half angle of 50° , which fits within the FoV's half angle of 30° of the system. By means of a CMOS wide-FoV camera, multiple devices can be localized with an accuracy of 0.05° (i.e., 2.5mm at 3m room height). In [54], a similar approach with 4 LED tags around the receiver's aperture has been realized, where the LEDs have a specific blinking sequence which represents the receiver's ID.

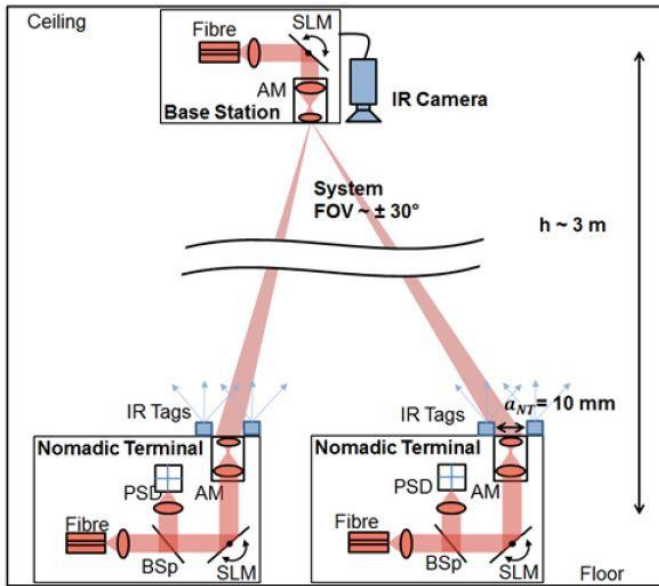


Fig. 3-15 Device localization using IR tags and a camera (AM: angular magnifier, BSp: beam splitter, PSD: position-sensitive detector) [53]

3.9 Hybrid Optical/Radio wireless Networks

Many network concepts which have been reported focus on high-capacity downstream transmission using OWC and provide the upstream path by means of (established) lower-capacity radio techniques. The capacity asymmetry of such a hybrid optical/RF wireless system is acceptable in many service scenarios, such as the downloading of large video files, but may be inadequate for symmetric capacity needs such as fast bi-directional file transfer between data servers or computers.

A symmetric high-capacity full-duplex OWC system is shown in Fig. 3-16 [55]. Based on wavelength-controlled 2D beam steering with crossed gratings, it employs the principle of reversibility of an optical path when operated

at the same wavelength. Fiber-pigtailed triplet lens collimators were used to send/receive beams with 3.3mm diameter, and optical circulators at the central site and at the user’s device site separate the up- and downstream signals. The downstream beam carries 10Gbit/s OOK at a moderate optical extinction ratio of 3.6dB. This enables the receiver at the device side to remove the modulation by means of an SOA operating in the gain-saturated regime, and to regain an almost clean optical carrier. This carrier is subsequently re-modulated by a Mach Zehnder Modulator (MZM) with 10Gbit/s OOK upstream data. As the upstream signal thus has the same wavelength as the downstream signal, it takes the same path backwards through the crossed-gratings module.

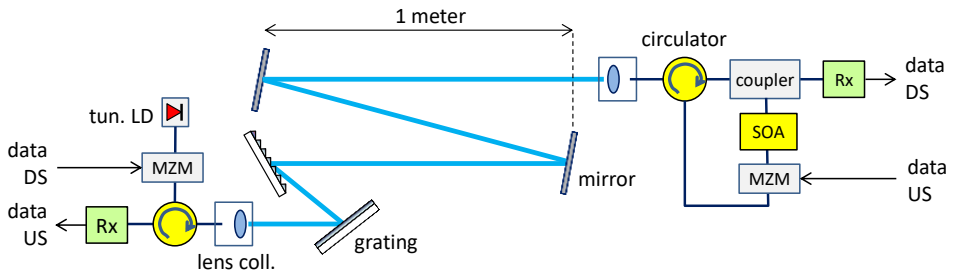


Fig. 3-16 Bi-directional all-optical wireless communication [55]

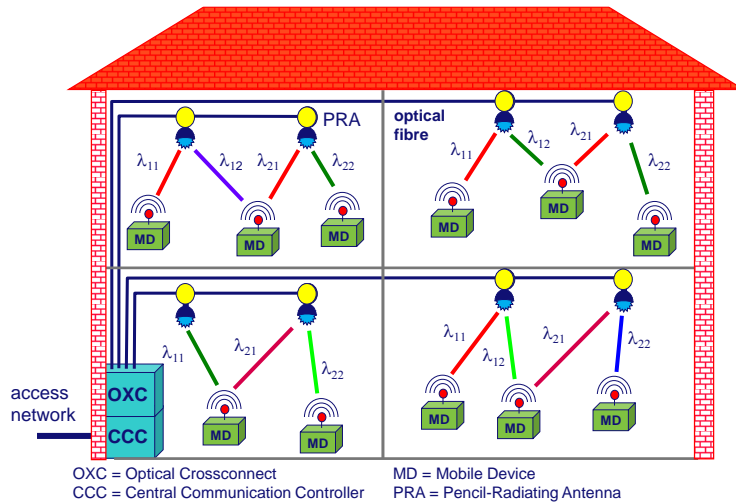


Fig. 3-17 Hybrid OWC/radio network using wavelength-controlled 2D infrared steered beams [29]

Within the European Research Council’s project BROWSE - Beam-steered Reconfigurable Optical-Wireless System for Energy-efficient communication,

we have investigated a hybrid OWC/radio network architecture as shown in Fig. 3-17 [29]. This architecture is discussed in detail in chapter 4. An indoor fiber backbone network routes the optical signals on-demand to the appropriate rooms. For the downstream optical wireless communication, each room has a diffractive pencil-radiating antenna (PRA), which can steer multiple beams two-dimensionally in directions determined by their wavelengths. The upstream path from each mobile device (MD) is established with 60GHz radio beams steered with phased array antennas. An integrated full-duplex hybrid system has been reported in [51] which provides 35Gbit/s with OOK modulation downstream per infrared beam steered by a PRA composed of an 80-ports C-band AWGR with 35GHz channel bandwidth driving a 2D fiber matrix and $f=40\text{cm}$ condenser lens structure (see Fig. 3-14). The beam diameter was 8.3cm, and with a reach of 2.5m, an angular coverage of $17^\circ \times 17^\circ$ was achieved. Upstream, 5Gbit/s ASK was sent by 60GHz radio beams, deploying two 30dBi gain horn antennas at the device side and a 16dBi antenna at the central communication controller (CCC) side. The horn antennas were placed on a 2D electro-mechanical positioning stage, which enabled the device localization function. By applying PAM-4 modulation, the system's downstream throughput has been upgraded to 112Gbit/s per beam [56].

3.10 Beam-steered OWC vs. wide-beam OWC⁶

Offering wireless connectivity in the wide variety of its application domains (e.g., in indoor offices and residential settings, in industry 4.0 applications, in exhibition pavilions, in mobile transport settings such as trains, busses, airplanes) by means of optical wireless communication using narrow (infrared) beams can bring a number of advantages with respect to radio-based wireless communication and VLC/LiFi, as outlined below. In the chapters 4 to 8, we will focus on beam-steered communication using narrow infrared beams.

3.10.1 Electromagnetic interference

Radio technologies using the ISM band or mm-wave frequencies may suffer from the electromagnetic interference (EMI) generated by the automated manufacturing equipment, such as arc-welding robots and heavily powered electromagnetic machines, and by jamming from neighboring sites. Optical wireless links are not affected by EMI nor jamming, hence can enhance link reliability in harsh industry 4.0 environments.

⁶ Extracted from A.M.J. Koonen, K.A. Mekonnen, Z. Cao, F.M. Huijskens, N.-Q. Pham, E. Tangdiongga, "Beam-steered optical wireless communication for Industry 4.0," invited paper, *IEEE J. of Selected Topics in Quantum Electronics*, Vol. 27, No. 6, Nov./Dec. 2021.

3.10.2 Data capacity per device

Radio-based wireless links typically operate with relatively wide beam profiles. When closely spaced items have to be connected, e.g., several arms of a robot, or a swarm of transporters, they may need to share the same beam, and thus have to share the data capacity of it. This complicates the communication with each one individually, necessitating robust MAC protocols. By using higher radio frequencies and high-gain (e.g., horn-shaped) antennas, the radio beam profile may be narrowed, and more power delivered into the restricted aperture of the receiver. By means of simple optical elements such as lenses, however, optical beams can be created with much less divergence (which is equivalent to much higher antenna gain). Such beams can create wireless connections at much higher link power budget and spatial density, thus also avoiding the need for capacity sharing among closely spaced devices. A significantly higher connection bandwidth per device can be realized as compared with radio-based systems such as the ones of the IEEE 802.11 family.

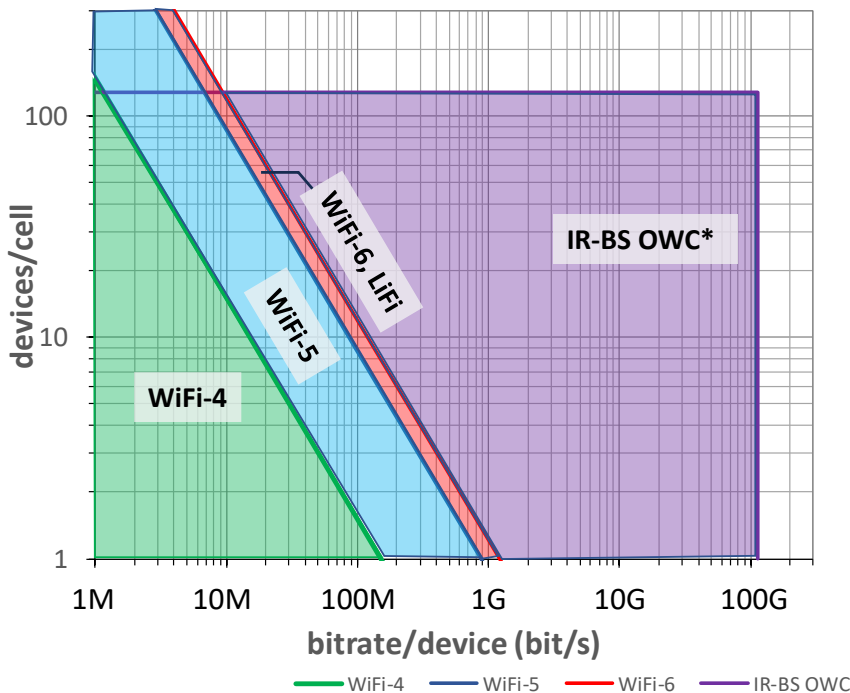


Fig. 3-18 Wireless connectivity using beam-steered OWC compared to using radio technologies (IEEE 802.11n a.k.a. WiFi-4, IEEE 802.11ac a.k.a. WiFi-5, IEEE 802.11ax a.k.a. WiFi-6; IR-BS OWC: infrared beam-steered optical wireless communication)

Fig. 3-18 illustrates how an OWC system using narrow infrared beams may outperform the various IEEE 802.11 systems, notably at higher data rates per device and higher device densities. In IEEE 802.11 systems, the product of bitrate per device \times number of devices per cell is limited by the sharing of the system's aggregate capacity. In the PHY layer, excluding multi-antenna MIMO techniques, the IEEE 802.11n (a.k.a. WiFi-4) offers 150Mbit/s per channel, IEEE 802.ac (a.k.a. WiFi-5) up to 867Mbit/s, and the latest IEEE 802.11ax (a.k.a. WiFi-6) up to 1201Mbit/s [57]. With 6 access points, WiFi-6 can offer up to 8×8 MIMO offering 9.6Gbit/s in theory, and 5.9Gbits in practice. LiFi-based OWC systems using a single luminary (as introduced in the market, with PHY rates of around 250Mbit/s typically) also employ capacity sharing. These are based on the Gigabit Home Networking (G.hn) specification developed in ITU for wired home networks (telephone lines, coaxial cables, power lines, and plastic optical fiber) which also supports the WiFi standards [58]; it limits the data rate to 1.6Gbit/s. Bi-directional point-to-point VLC systems are offered with 1Gbit/s capability [17], and according to the IEEE 802.11bb standard [20] LiFi in an 8×8 configuration may offer data rates up to 9.6Gbit/s, comparable to WiFi-6.

In contrast, an infrared beam-steered OWC (IR-BS OWC) system principally can offer a very high bandwidth per device, independent of the number of devices, where this number is only constrained by the maximum number of cells which can be addressed [59]. A capacity of up to 112Gbit/s per beam has been demonstrated using PAM-4 modulation [60], and an ability of steering 128 beams individually [61].

3.10.3 Latency

In machine-to-machine communications, the latency in the link should be minimized to ensure timely and reliable operation of robots individually and their interaction. In comparison with wired fiber-optic connections, wireless connections made through radio or optical waves have less propagation delay as the signals propagate at the speed of light in free space, whereas in fiber the speed of light is reduced by the refractive index of its material ($n \approx 1.5$). Therefore, typically the latency in free space is 33% less than in fiber, which may make a difference in the performance of high-speed machine-to-machine bidirectional communication, such as in data center rack-to-rack interconnects. Optical beams offer a much larger bandwidth than a radio link: each nm in the $1.5\mu\text{m}$ wavelength range corresponds to 125GHz of bandwidth wherein many multi-GHz channels can be accommodated. In the WiFi family, within an overall bandwidth of 645MHz in the 5GHz band (5.180-5.825GHz) multiple channels with bandwidths up to some 160MHz can be used. In the mm-wave 60GHz domain, overall a bandwidth of 7GHz (57 to 64GHz) is available; up to 4 channels of 2.16 GHz

each can be bundled in one channel according to IEEE 802.11ay reaching 20 to 40Gbit/s. Due to the restricted bandwidth available, radio systems have to apply comprehensive signal modulation techniques (e.g., OFDM with high-level QAM) in order to compress the signal's spectrum and to enable high data rate transport. Such modulation techniques need sizable digital signal processing both at the transmit and receive ends of the link, which adds to the latency. Moreover, the capacity sharing requires careful MAC processing, adding to the latency too. E.g., in the CSMA/CA (Carrier-sense multiple access with collision avoidance, [62]) protocol the latency is due to the waiting time for a free channel in the listen-before-talk procedure.

In LiFi systems considerable signal processing time is needed also for compressing the signal spectrum within the limited bandwidth available of the light sources and for overcoming the low SNR due to a low received signal intensity. The system's latency is increased further by the time needed for the MAC processing due to the beam sharing among the users' devices.

In an OWC system using narrow infrared beams, however, each beam offers a huge bandwidth and high link budget, and it does not need to be shared with other devices. This significantly relaxes the signal modulation efforts, avoids comprehensive MAC protocols, and thus minimizes the associated latency.

3.10.4 Energy efficiency

Next to raising the capacity sharing constraint among a number of devices, the beams of RF (radio-based) wireless systems cover cells with a relatively large footprint, and therefore the signal energy which is captured per device by its limited aperture cannot be very large. The same holds for LiFi systems. This results in a lower SNR and therefore in addition to the sharing constraint puts a limit on the capacity which per device can be reached. Moreover, the beam's intensity decreases at least with the square of the distance to the receiver, thus restricting the reach and further tightening the achievable capacity. By means of a phased array antenna, RF beams can be shaped to much lower divergence and hence higher intensity, which alleviates the reach issue, but at the expense of a comprehensive multi-element antenna design with many power-consuming RF phase shifters and amplifiers [64] . The gain G_A of an antenna is the product of its directivity D_A and its radiation efficiency η_A [63] . E.g., for an antenna gain of 30dBi (i.e., dB with respect to an isotropic antenna uniformly radiating into all directions), no less than 1000 hypothetical isotropic antenna elements are needed. A half-wave dipole antenna can be almost 10% efficient and have a gain of 2.15dBi; for 30dBi antenna gain about 600 dipole antennas would be needed. Passive horn antennas may also deliver narrow RF beams, but are relatively large and may achieve gains up to 25dBi [65] . The radiation efficiency η_A is defined

as the total power radiated by the antenna divided by the net power fed to the antenna by its transmitter [66] . It depends on the transfer efficiency of the interface and may depend on frequency. The directivity D_A is the ratio of the radiation intensity in a certain direction and the radiation averaged over all directions; for a hypothetical isotropic antenna, it is 1, so 0 dBi [67] . If the direction is not specified, the directivity refers to the axis of maximum radiation intensity. In a simplified far-field analysis, assuming a point source P emitting an omnidirectional uniform power density (such as an ideal isotropic antenna does) as shown in Fig. 3-19, the directivity D_A of a directional antenna may be interpreted as the ratio of the power emitted over the full sphere divided by the power emitted by the antenna in its angular aperture with half-angle θ_0 ; so

$$\begin{aligned} D_A &= \frac{A_{tot}}{\Delta A} = \frac{4\pi R^2}{\int_{\theta=0}^{\theta_0} 2\pi R^2 \sin \theta \, d\theta} = \frac{4\pi R^2}{4\pi R^2 \sin^2\left(\frac{\theta_0}{2}\right)} \\ &= \frac{1}{\sin^2\left(\frac{\theta_0}{2}\right)^2} \end{aligned} \quad (3-5)$$

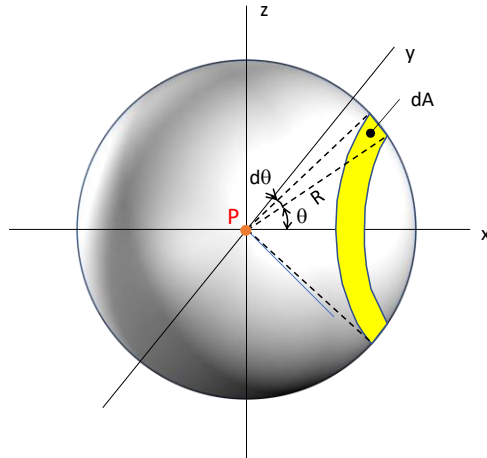
In contrast to the RF wireless scenario where narrow beams require sophisticated antenna designs and/or comprehensive phased-array antenna structures, in the OWC scenario narrow beams are readily created by employing a relatively simple single lens. Thus, when creating narrow dynamically-steered infrared beams each device can get an individual beam with a small footprint, which does not need to be shared and by which the reach is extended. By using just a single passive lens adequately corrected for spherical aberration, a highly collimated beam can be obtained, which has a very large equivalent antenna gain. No power-hungry electronics like in an RF phased array antenna are needed. E.g., in the 2D optical beam steerer based on an AWGR and a 2D fiber array reported in section 5.3 and in [61] we used a lens in slightly defocused ($p=21\%$) operation, which yields beams with a small divergence angle θ_0 (see eq. (5-27))

$$\tan \theta_0 = 2p \frac{\lambda}{\pi w_0} \quad (3-6)$$

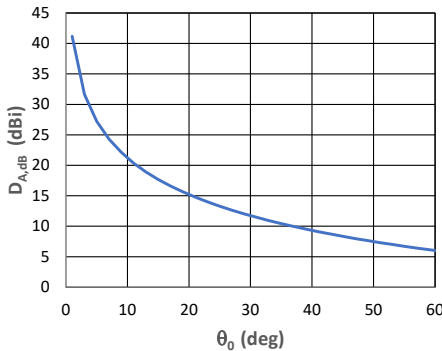
where w_0 is the SMF's mode field radius and λ the beam's wavelength. Hence, the beam steerer provides an equivalent antenna directivity

$$D_A \approx \frac{1}{p^2} \left(\frac{\pi w_0}{\lambda}\right)^2 \quad (3-7)$$

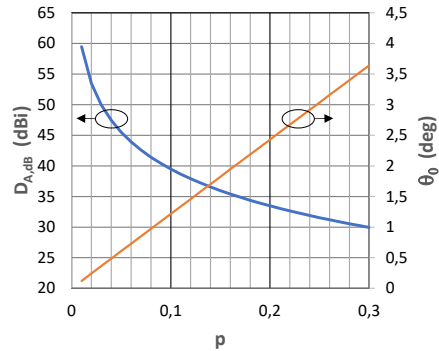
A high antenna directivity can easily be realized by only deploying a passive lens. E.g., for typical values $w_0=4.5\mu\text{m}$ and $\lambda=1.5\mu\text{m}$, with $p=0.21$ a $D_{A,dB}=33.0\text{dBi}$ is readily achieved (where $D_{A,dB} = 10 \log(D_A)$).



a) Modelling antenna directivity



b) Antenna directivity $D_{A,dB}$ of RF antenna vs. its aperture half-angle θ_0



c) Antenna directivity $D_{A,dB}$ of lensed optical beam steerer vs. defocusing parameter p

Fig. 3-19 Antenna directivity

Virtually, the capabilities of a narrow optical beam are much like the ones of a fiber, but without needing a fiber. In indoor applications without atmospheric disturbances, the loss in the link which conveys the signal energy from the OWC transmitter to a device (and vice-versa) is therefore less than in an RF wireless link, hence the SNR can be better and the attainable capacity much higher. Or reversely, for a specific capacity needed much less energy is needed. Moreover, the beams can be pinpointed to the respective devices only where and when

needed, and no signal energy is wasted, thus further improving the energy efficiency of a beam-steered OWC system. In radio systems, also measures have been introduced to improve energy efficiency by directing radio beams. In WiFi standard IEEE 802.11ba, the wake-up radio protocol has been introduced in which the user device is equipped with a primary connectivity radio (PCR) chain handling the high data rate and a low-power companion connectivity radio (CCR) chain waking up the PCR as soon as it detects data arriving [68]. In IEEE 802.11ax the target wake time (TWT) is introduced where access devices can determine when and how frequently they will wake up to send or receive data, thus reducing their power consumption [69].

3.11 Photonic integrated circuits for optical wireless communication⁷

The fast increase of demand for wireless connectivity, fueled by the growing bandwidth needed by mobile services as well as by the staggering numbers of wireless devices to be connected, is driving radio wireless networks into saturation. Optical wireless communication (OWC) has shown to have a great potential to solve this imminent congestion. It can offer huge amounts of additional bandwidth; the visible domain (400-700nm) brings an extra 320THz, and the fiber-optic infrared domain (1500-1600nm) an extra 12.5THz. Moreover, when using narrow optical beams very small picocells can be created, which enables dense high-capacity coverage by spatial division multiplexing (SDM). SDM is uniquely capable to meet exponentially growing capacity demand [74].

Two major directions in OWC may be discerned: using very wide beams which do not need extra steering, and narrow beams which need to be pinpointed to users accurately [75]. LiFi systems which are typically built on top of illumination systems (using LED-based luminaires) belong to the first direction. Because such wide beams typically cover multiple users, these users will need to share the capacity of the luminaire with its limited bandwidth, and thus can be provided only with modest capacity. By means of MIMO (multiple input multiple output techniques, like those known in advanced radio wireless systems) applied at the transmitter and receiver ends, the capacity per user may be increased. The second direction encompasses systems which typically use narrow infrared light beams, which are steered to users individually. Such systems may be considered as ‘LiFi 2.0’. Each user gets his own beam, a ‘virtual fiber’, and thus can get very high capacity without sharing and with high privacy, while no signal energy is wasted, and optimum system energy efficiency is achieved.

⁷ This section is largely based on Ton Koonen, Zizheng Cao, “Photonic integrated circuits for optical wireless communication,” *Proc. ACP 2021*, tutorial paper M5D1.

First commercial introduction of LiFi systems is already taking place. True mass deployment of OWC systems in the direct environment of users will be largely dependent on scalable manufacturability, power efficiency (in particular for battery-fed mobile devices), and cost-effectiveness. Photonic integration circuit (PIC) technologies play a crucial role in this. In this section, we will focus on PIC structures for OWC transmitters and OWC receivers.

3.11.1 Photonic integrated OWC transmitters

Wide-beam LED-based OWC systems are typically limited in reach and data capacity per user, as intensity scales with the squared inverse of the distance between user and liminary. Illumination LEDs have been optimized for light efficiency, not for modulation bandwidth. Hence several groups have studied dedicated LED technologies for OWC, notably gallium-nitride (GaN) micro-LEDs which due to their small active area operate at high current density, and can offer high modulation bandwidth as well as high output power density [76]. Such μ -LEDs can be made in large arrays, and thus jointly provide increased total output power. Moreover, such array structures can also enable to drive μ LEDs individually, and thus multiply the data capacity. The array can be mounted on top of an array of CMOS driver circuits, and thus optical signals from the individual μ LEDs can be directly generated from digital electrical input signals; see Fig. 3-20. With $10\mu\text{m}$ blue (450nm) μ LEDs a modulation bandwidth of 1.8GHz was reported. Using DCO-OFDM modulation with bit and power loading up to 256-QAM, a data rate of 7.7Gbit/s was achieved [77]. Operation in larger arrays of beyond 10000 μ LEDs is foreseen (which will bring associated management complexity issues).

Such arrayed μ LEDs approach opens the way towards effective OWC MIMO systems. As a mixture of the signals from the individual μ LEDs will arrive at each photodiode at the receiver side, additional signal processing is required both at the system's transmitter and receiver end to do the channel separation. Up to 7Gbit/s transmission was shown with a 3×3 array of $39\mu\text{m}$ μ LEDs [77] (see Fig. 3-20).

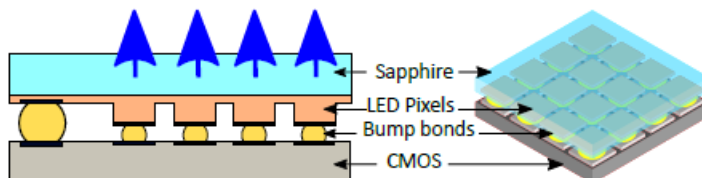


Fig. 3-20 μ -LED array bump-bonded to CMOS control chip [76]

Alternatively, in a beam-steered OWC system typically many narrow infrared beams are emitted, and each provide high data capacity to an individual user [59]. Each beam is pointed to a user who has been localized before (with e.g. a passive optical retroreflector array at the user device, and upstream power detector [18], or visible LED tags and upstream video camera [79]). 2D beam steering by using passive diffractive modules and remote wavelength-tunable laser diodes has been demonstrated, e.g., with a high port count arrayed waveguide grating router of which the output ports were arranged in a 2D fiber matrix positioned in front of a large aperture lens [61] (see section 5.3). A laboratory demonstrator has been built which can provide up to 128 beams. Real-time streaming of high-definition video signals embedded in 10Gbit/s data has been shown. Also, optical phased arrays (OPAs) have been reported for beam-steering and -shaping, in conjunction with phase tuning in the OPA’s arms and wavelength tuning of the laser diodes. Next to OWC, they also find applications in LiDAR. In [81] an OPA-based hybrid silicon PIC is reported which hosts 164 optical components (tunable laser diodes, optical amplifiers, photodiodes, phase tuners, and a photonic crystal lens; see Fig. 3-21). It can steer a beam over $23^\circ \times 3.6^\circ$ with beam divergence of $1^\circ \times 0.6^\circ$.

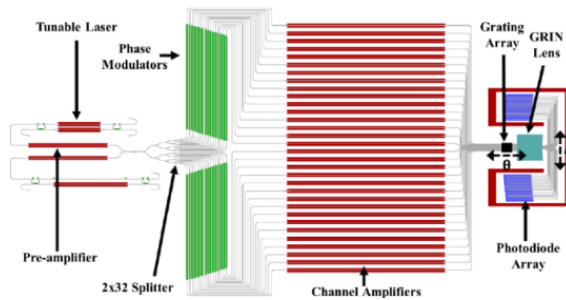


Fig. 3-21 OPA-based hybrid silicon PIC for 2D beam steering [81]

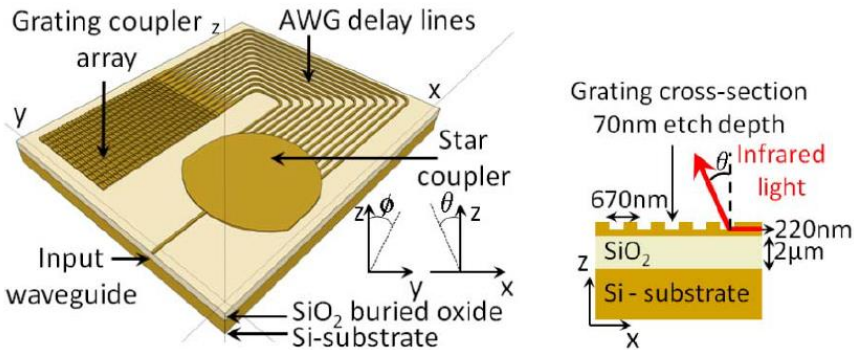


Fig. 3-22 2D beam steering photonic integrated circuit using λ -tuning [79]

A compact photonic integrated circuit (PIC) which can provide 2D beam steering using the cascaded-gratings concept has been reported in [82] ; see Fig. 3-22. An arrayed waveguide grating was co-integrated with an array of waveguide grating couplers in a passive silicon-on-insulator technology; input-to-free-space losses were 8.9 to 10dB. 2D steering was achieved over $15^\circ \times 50^\circ$ by wavelength tuning over 100nm; with a beam width of 4° , 50 resolvable spots could be generated in 2D. In [83] , 2D beam steering by means of an active PIC implemented in InP technology has been reported. While using an on-chip SG-DBR laser diode with a wavelength tuning range beyond 30nm, by tuning the wavelength as well as tuning electro-optically the local phase in the branches of an arrayed waveguide grating router 2D steering of a single beam over $3.5^\circ \times 10^\circ$ was achieved.

3.11.2 Photonic integrated OWC receivers

An OWC receiver needs to fulfill an ambitious range of criteria: it should have a large bandwidth in order to handle high data rates, and it should have a large aperture in order to catch maximum optical power, as well as a wide Field-of-View (FoV) in order to avoid delicate alignment with respect to the beam. It should consume only little power (as it is typically used at a battery-fed mobile device), and it should be cheap (so be simple and easy to manufacture). A large aperture may be created by using a large-diameter lens system which focuses the incoming beam on the photodiode (PD). However, the basic physics law of etendue states that a large aperture will imply a small FoV. A large diameter PD can help, but typically a large active area also brings a high junction capacitance, hence a reduced bandwidth. By using multiple PDs which jointly perform the photodetection the total active area is effectively increased.

Two ways have been reported to circumvent the increased capacitance which would be associated with this: an angular diversity receiver (ADR), and a receiver deploying a 2D matrix constellation of photodiodes. In an ADR, multiple PDs are used, where each one is looking into a different direction and thus the PDs jointly cover a larger FoV. Each PD is followed by a separate electrical transimpedance amplifier, and the outputs of these amplifiers are summed. As shown in Fig. 3-12 [84] , a 7-channels ADR has been reported, having InGaAs MSM PDs followed by separate CMOS preamplifiers, which can handle 5Gbit/s. In [85] an ADR is analyzed for visible light communication in conjunction with MIMO techniques. In [86] , a densely integrated 19×32 2D array of 20-30 μm pixels was reported which offered a bandwidth of over 10GHz. In a 6×6 array of 30 μm PDs, a bandwidth of 20GHz was reached, and a free space 10Gbit/s optical link over 1.5m with relaxed alignment was demonstrated [87] .

Increasing the receiver's aperture may also be achieved by separating the light collection and light detection functions. The waveguide outputs from multiple surface grating couplers (SGC-s) may be combined, and co-integrated with a

waveguide-fed UTC PD in InP technology [88] as shown for a single SGC in Fig. 3-23. In WDM operation with 5 wavelengths, a 200Gbit/s free-space link was demonstrated.

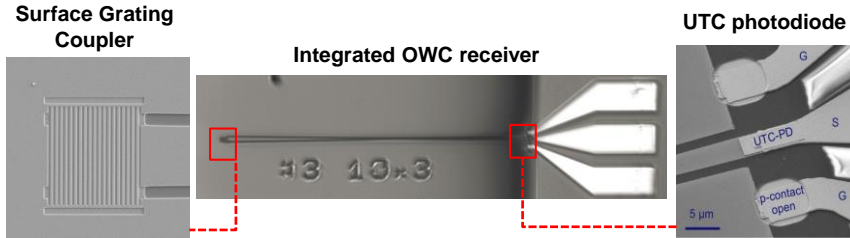
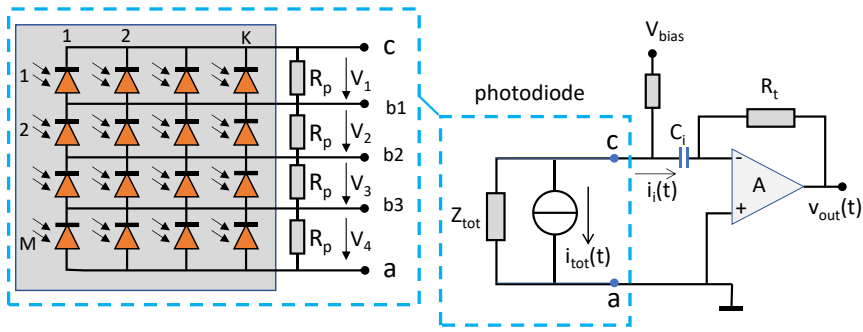


Fig. 3-23 Integrated cascaded aperture optical receiver [88]

As an alternative for the ADR approach, a 2D constellation of a matrix of PDs in combination with a single lens having a large numerical aperture has been proposed [89] (see Fig. 3-24; discussed in full detail in chapter 7). Such matrix has only a single output, so requires only a single preamplifier, and a single lens. This alternative considerably simplifies the receiver design. It can be shown that a 2D constellation of $M \times M$ PDs yields a capacitance which equals the capacitance of a single PD, whereas it has an M^2 times larger area and generates M times larger photocurrent (assuming that junction capacitance is dominant, and the fill factor is large) [90].



a) circuit diagram of TIA receiver with PD matrix [90]

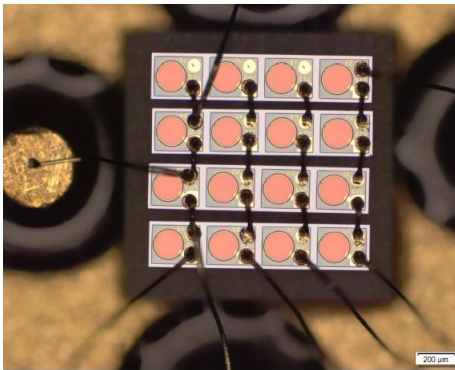
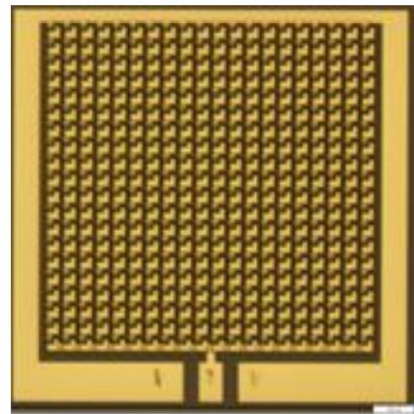
b) 4×4 matrix of photodiodes, each $\varnothing 150\mu\text{m}$ active area, by wire-bonding four 1×4 PD arrays [90]c) 20×20 matrix of $\varnothing 30\mu\text{m}$ photodiodes, by integration on III-V substrate [92]

Fig. 3-24 OWC receiver with large FoV employing a 2D matrix of photodiodes [90] [91]

A FoV of more than $\pm 10^\circ$ (half-angle) has been demonstrated with a 4×4 array of $\varnothing 150\mu\text{m}$ PDs. In a laboratory system demonstrator, real-time optical wireless streaming of Gbit/s Ethernet video signals to an OWC receiver module connected to a laptop was shown [91]. The 2D photodiode matrix concept is well scalable while retaining the bandwidth of a single PD. With a 20×20 matrix with $\varnothing 30\mu\text{m}$ PDs transmission of 25Gbit/s NRZ modulated signals over an OWC link of 20 m has been demonstrated [92]. The photodiode matrix configuration may also be extended in a 3rd dimension by a multi-stacked PIN photodiode structure, as shown in Fig. 3-25 [93]. Vertical pinholes with a diameter of $5\mu\text{m}$ were applied,

yielding a fill factor of 50%. Operation in an OWC link up to 20m at 20Gbit/s NRZ modulation has been shown.

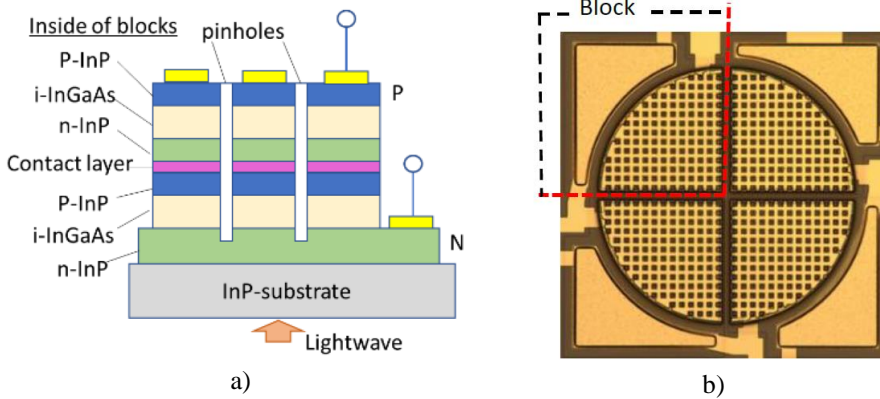


Fig. 3-25 Multi-stacked PIN photodiode; a) two-stacked PIN photodiode block, b) 4 two-stacked PD blocks interconnected in series (overall diameter 0.3mm) [93]

As briefly introduced in section 3.7, the light collection function may be separated from the light detection function, which enables to optimize both functions independently. Using InP photonic integration technology, a wide-area surface grating coupler (SGC) collecting the incident light has been monolithically integrated with an InP waveguide feeding a fast photodiode. A $10 \times 10 \mu\text{m}^2$ SGC was coupled via a narrow waveguide to a $3 \times 10 \mu\text{m}^2$ UTC photodiode which had an electrical bandwidth exceeding 67GHz (see Fig. 3-23) [88]. With this integrated SGC-waveguide-PD device, free-space 40Gbit/s NRZ-OOK data transmission has been demonstrated, as well as operation at 200Gbit/s in WDM operation at 5 wavelengths. Without compromising the bandwidth, the light collecting aperture can be increased further by enlarging the SGC by means of apodization, and by creating an array of SGCs plus an on-chip light combiner.

3.12 Concluding remarks

Optical Wireless Communication techniques hold a great potential to resolve the imminent exhaustion of indoor radio-based wireless communication resources. The optical spectrum, both in the visible and in the infrared domain, offers ample extra bandwidth without licensing issues, and thus great opportunities for carrying large volumes of wireless traffic. Optical wireless communication systems can take away much load from radio wireless systems, e.g., by offloading much of the heavy burden by broadband data transport in these networks. It will not fully replace radio wireless communication (e.g., it cannot support services without line-of-sight), but it will complement and co-exist with it. First VLC/LiFi

products are entering the market in appealing applications [72] [73]. Beam-steered infrared communication techniques have shown their ability to offer ultra-high data rates (beyond 100Gbit/s per beam), with high energy efficiency, and at high user densities with high privacy. Considerable work is still to be done to bring these techniques to market maturity, e.g., research on robust beam-steering OWC transmitters, compact low-cost OWC receivers, symmetric bi-directional OWC systems, scaling of the coverage area and reach, efficient localization, and co-existence scenarios with radio-based wireless technologies. Photonic integration is a key technology to achieve cost-effective high-performance OWC systems.

As OWC technologies have not matured yet, cost comparisons are hard to make. From a general viewpoint, VLC/LiFi systems may be preferred regarding CapEx (capital expenditures) due to their lower infrastructure costs, whereas beam-steered OWC systems may be more beneficial regarding OpEx (operational expenditures) due to their lower energy consumption.

3.13 References

- [1] Coopers law [on-line]. Available: <http://www.arraycomm.com/technology/coopers-law/>
- [2] The photophone of Alexander Graham Bell [on-line]. Available: <https://en.wikipedia.org/wiki/Photophone> , <https://www.loc.gov/item/today-in-history/june-03>
- [3] D.C. O'Brien, "Optical wireless communications: current status and future prospects," *Proc. IEEE Summer Topicals*, Newport Beach, 2016.
- [4] H. Haas, L. Yin, Y. Wang, and C. Chen, "What is LiFi?," *J. Lightw. Technol.*, vol. 34, no. 6, pp. 1533-1544, Mar. 2016.
- [5] Laser safety [on-line]. Available: https://en.wikipedia.org/wiki/Laser_safety
- [6] Photodiode responsivity [on-line]. Available: <https://en.wikipedia.org/wiki/Responsivity>
- [7] V. Jungnickel, "Optical Wireless in 5G," *IEEE Summer Topicals*, tutorial, Jul. 11, 2016, Newport Beach, CA.
- [8] J. Grubor, S.C. Jeffrey Lee, K.-D. Langer, A.M.J. Koonen, and J.W. Walewski, "Wireless high-speed data transmission with phosphorescent white-light LEDs," *Proc. ECOC 2007*, Sep.16-20, 2007, Berlin, paper PD3.6.
- [9] X. Huang, S.Chen, Z. Wang, J.Shi, Y. Wang, J. Xiao, N. Chi, "2.0-Gb/s Visible light link based on adaptive bit allocation OFDM of a single phosphorescent white LED," *IEEE Phot. J.*, vol. 7, no. 5, Oct. 2015, DOI: 0.1109/JPHOT.2015.2480541.
- [10] G. Cossu, A.M. Khalid, P. Choudhury, R. Corsini, and E. Ciaramella, "3.4 Gbit/s visible optical wireless transmission based on RGB LED," *Optics Express*, vol. 20, no. 26, Dec. 2012, p. B501-B506.
- [11] Y. Wang, L. Tao, X. Huang, J. Shi, and N. Chi, "8-Gb/s RGBY LED-Based WDM VLC System Employing High-Order CAP Modulation and Hybrid Post

- Equalizer,” *IEEE Phot. J.*, vol. 7, no. 6, Dec. 2015, <https://doi.org/10.1109/JPHOT.2015.2489927>.
- [12] S. Rajagopal, R.D.Roberts, S.-K. Lim, "IEEE 802.15.7 visible light communication: modulation schemes and dimming support," *IEEE Comm. Mag.*, vol. 50, no. 3, Mar. 2012, pp. 72-82.
- [13] R. Singh, T. O’Farrell, and J.P.R. David, "An enhanced color shift keying modulation scheme for high-speed wireless visible light communications," *J. Lightw. Technol.*, vol. 32, no.14, Jul. 2014, pp. 2582-2592.
- [14] A.E. Aziz, K. Th. Wong, and J.-C. Chen, "Color-shift keying—how its largest obtainable “minimum distance” depends on its preset operating chromaticity and constellation size," *J. Lightw. Technol.*, vol. 35, no. 13, Jul. 2017, pp. 2724-2733.
- [15] R.X.G. Ferreira, E. Xie, J.J.D. McKendry, S. Rajbhandari, H. Chun, G. Faulkner, S. Watson, A. E. Kelly, E. Gu, R.V. Penty, I.H. White, D.C. O’Brien, and M.D. Dawson, “High bandwidth GaN-based micro-LEDs for multi-Gb/s visible light communications,” *Phot. Technol. Lett.*, vol.28, no. 19, Oct. 2016, pp. 2023-2026.
- [16] S. Rajbhandari, A.V.N. Jalajakumari, H. Chun, G. Faulkner, K. Cameron, R. Henderson, D. Tsonev, H. Haas, E. Xie, J.J.D. McKendry, J. Herrnsdorf, R. Ferreira, E. Gu, M.D. Dawson, and D.C. O’Brien, “A multi-Gigabit/sec integrated Multiple-Input Multiple-Output VLC demonstrator,” *J. Lightw. Technol.*, vol. 35, no. 20, Oct. 2017, pp. 4358-4365.
- [17] 1 Gbit/s VLC system of Fraunhofer HHI [on-line]. Available: <https://www.hhi.fraunhofer.de/en/departments/pn/products-and-solutions/1-gbit-s-lifi-system.html>
- [18] LiFi-XC of Purelifi, <http://purelifi.com/lifi-products/lifi-x/>
- [19] Trulifi of Signify, <https://www.signify.com/global/innovation/trulifi>
- [20] IEEE 802.11bb LiFi standard, https://www.ieee802.org/11/Reports/tgbb_update.htm
- [21] Spatial light modulators [on-line]. Available: <https://holoeeye.com/products/spatial-light-modulators/>
- [22] N. A. Riza, "Reconfigurable optical wireless," *Proc. LEOS 12th Annual Meeting*, vol. 1, 1999, paper MH4, pp. 70-71.
- [23] J. Xu, M. Cua, E.H. Zhou, Y. Horie, A. Faraon, C. Yang, "Wide-angular-range and high-resolution beam steering by a metasurface-coupled phased array," *Opt. Lett.*, Vol. 43, No. 21, Feb. 2018, pp. 5255-5258.
- [24] A. Gomez, K. Shi, C. Quintana, M. Sato, G. Faulkner, B.C. Thomsen, and D.C. O’Brien, “Beyond 100-Gb/s indoor wide field-of-view optical wireless communications,” *Phot. Technol. Lett.*, vol. 27, no. 4, Feb. 2015, pp. 367-370.
- [25] A. Gomez, C. Quintana, G. Faulkner, and D.C. O’Brien, “Point-to-multipoint holographic beamsteering techniques for indoor optical wireless communications”, *Proc. of SPIE vol. 9772*, Broadband Access Comm. Techn. X, 2016, 7 p.
- [26] K. Wang, A. Nirmalathas, C. Lim, K. Alameh, and E. Skafidas, "Full-duplex gigabit indoor optical wireless communication system with CAP modulation," *IEEE Photon. Technol. Lett.*, vol. 28, no. 7, Apr. 2016, pp. 790-793.

- [27] M.D. Soltani, H. Kazemi, E. Sarbazi, A.A. Qidan, B. Yosuf, S. Mohamed, R. Singh, B. Berde, D. Chiaroni, B. Béchadergue, F. Abdeldayem, H. Soni, J. Tabu, M. Perrufel, N. Serafimovski, T.E.H. El-Gorashi, J. Elmirghani, R. Penty, I.H. White, H. Haas, M. Safari, "Terabit Indoor Laser-Based Wireless Communications: LiFi 2.0 for 6G," *arXiv:2206.10532*, June 2022.
- [28] M.Z. Chowdhury, M.K. Hasan, Md. Shahjalal, Md. Tanvir. Hossan, Y.M. Jang, "Optical Wireless Hybrid Networks: Trends, Opportunities, Challenges, and Research Directions," *IEEE Communications Surveys & Tutorials*, vol. 22, no. 2, Jan. 2020, pp. 930-966.
- [29] A.M.J. Koonen, C.W. Oh, K. Mekonnen, Z. Cao, and E. Tangdiongga, "Ultra-High Capacity Indoor Optical Wireless Communication using 2D-Steered Pencil Beams," *J. Lightw. Technol.*, vol. 34, no. 20, Oct. 2016, p. 4802-4809.
- [30] T. Mullane, D. McDonald, T. Farrell, J. Dunne, "Full Coverage microsecond wavelength switching of a monolithic widely tunable laser, from any channel to any channel, over the entire C band on the ITU G.682 ITU grid," Opto-Ireland 2002: Optics and Photonics Technologies and Applications, *Proc. of SPIE*, Vol. 4876, 2003, p. 260-265, [on-line].
Available: <https://www.spiedigitallibrary.org/conference-proceedings-of-spie>
- [31] M. Born and E. Wolf, Principles of Optics: Electromagnetic Theory of Propagation, Interference and Diffraction of Light, 7th ed., 1999, Cambridge University Press, ISBN 0521642221.
- [32] P.M. van den Berg, "Diffraction theory of a reflection grating," *Applied Scientific Research*, Dec. 1971, pp. 261-293
- [33] Z. Yaqoob, A.A. Rizvi, and N.A. Riza, "Free-space wavelength-multiplexed optical scanner," *Applied Optics*, vol. 40, no. 35, Dec. 2001, pp. 6425-6438.
- [34] C.W. Oh, E. Tangdiongga, and A.M.J. Koonen, "Steerable pencil beams for multi-Gbps indoor optical wireless communication," *Optics Letters*, vol. 39, no. 18, Sep. 2014, pp. 5427-5430.
- [35] Z. Yaqoob, M.A. Arain, and N.A. Riza, "High-speed two-dimensional laser scanner based on Bragg gratings stored in photothermorefractive glass," *Applied Optics*, vol. 42, no. 26, Sep. 2003, p. 5251-5262.
- [36] A.M.J. Koonen, C.W. Oh, and E. Tangdiongga, "Reconfigurable free-space optical indoor network using multiple pencil beam steering," *Proc. OECC/ACOFT 2014*, Melbourne, paper Tu3F-1.
- [37] C.W. Oh, E. Tangdiongga, and A.M.J. Koonen, "42.8 Gbit/s Indoor Optical Wireless Communication with 2-Dimensional Optical Beamsteering", *Proc. OFC 2015*, Los Angeles, paper M2F.3.
- [38] M. Shirasaki, "Large angular dispersion by a virtually imaged phased array and its application to a wavelength demultiplexer," *Optics Letters*, Vol. 21, No. 5, Mar. 1996, pp. 366-368.
- [39] T. Chan, E. Myslivets, and J.E. Ford, "2-Dimensional beamsteering using dispersive deflectors and wavelength tuning," *Optics Express*, vol. 16, no. 19, Sep. 2008, p. 14617-14628.
- [40] A.M.J. Koonen, C.W. Oh, A.M. Khalid, K.A. Mekonnen, M. Torres Vega, Z. Cao, and Eduward Tangdiongga, "2D beam-steered high-capacity optical wireless

- communication," *Proc. IEEE Summ. Top. 2016*, Newport Beach, paper TuC2.2.
- [41] A.M. Khalid, A.M.J. Koonen, C.W. Oh, Z. Cao, K.A. Mekonnen, and E. Tangdionga, "10 Gbps indoor optical wireless communication employing 2D passive beam steering based on arrayed waveguide gratings," *Proc. IEEE Summ. Top. 2016*, Newport Beach, paper TuC2.3.
- [42] A.M.J. Koonen, A.M. Khalid, C.W. Oh, F. Gomez-Agis, and E. Tangdionga, "High-capacity optical wireless communication using 2-dimensional IR beam steering," *Proc. OECC 2017*, Singapore, Jul. 31 – Aug. 4, 2017, paper 1-4K-3.
- [43] Etendue [on-line]. Available: <https://en.wikipedia.org/wiki/Etendue>
- [44] Non-imaging optics [on-line]. Available: https://en.wikipedia.org/wiki/Nonimaging_optics
- [45] J. Zeng, V. Joyner, J. Liao, S. Deng, Z. Huang, "A 5Gb/s 7-channel current-mode imaging receiver front-end for free-space optical MIMO," *Proc. IEEE MWSCAS 2009*, Cancun, pp. 148-151.
- [46] S. Collins, D.C. O'Brien, and A. Watt, "High gain, wide field of view concentrator for optical communications," *Opt. Lett.*, vol. 39, no. 7, Apr. 2014, p. 1756-1759.
- [47] T.-H. Do and M. Yoo, "An in-depth survey of visible light communication based positioning systems," *Sensors*, vol. 16, no. 5, 2016, art. no. 678 [Online]. Available: <http://www.mdpi.com/1424-8220/16/5/678>.
- [48] N. Saha, M.S. Ifthekhar, N. Tuan Le, Y.M. Jang, "Survey on optical camera communications: challenges and opportunities," *IET Optoelectron.*, 2015, vol. 9, no. 5, pp. 172–183.
- [49] N. Tuan Le, M.A. Hossain, Y. Min Jang, "A survey of design and implementation for optical camera communication," *Elsevier Signal Processing: Image Communication*, vol. 53, 2017, pp. 95-109.
- [50] J. Herrnsdorf, M. J. Strain, E. Gu, R. K. Henderson, and M. D. Dawson, "Positioning and space-division multiple access enabled by structured illumination with light-emitting diodes," *J. Lightw. Technol.*, vol. 35, no. 12, Jun. 2017, pp. 2339-2345.
- [51] A.M. Khalid et al., "Bi-directional 35-Gbit/s 2D Beam Steered Optical Wireless Downlink and 5-Gbit/s Localized 60-GHz Communication Uplink for Hybrid Indoor Wireless Systems," *Proc. OFC 2017*, Los Angeles, Mar. 2017, paper Th1E.6.
- [52] K.A. Mekonnen, N. Calabretta, E. Tangdionga, and A.M.J. Koonen, "High-capacity dynamic indoor network utilizing optical wireless and 60-GHz radio techniques," *Proc. MWP 2017*, Beijing, Oct. 2017, paper We.2.3.
- [53] A. Gomez, K. Shi, C. Quintana, G. Faulkner, B. C. Thomsen, and D.C. O'Brien, "A 50 Gb/s transparent indoor optical wireless communications link with an integrated localization and tracking system," *J. Lightw. Technol.*, vol. 34, no. 10, May 2016, pp. 2510-2517.
- [54] N.Q. Pham, K.A. Mekonnen, E. Tangdionga, A. Mefleh, A.M.J. Koonen, "Accurate indoor localization for beam-steered OWC system using optical camera," in *Proc. ECOC2019*, Dublin, Sep. 22-26, 2019, paper P45.
- [55] C.W. Oh, Z. Cao, E. Tangdionga, and A.M.J. Koonen, "10 Gbps all-optical full-

- duplex indoor optical wireless communication with wavelength reuse”, *Proc. OFC 2016*, Anaheim, Th4A.6.
- [56] F. Gomez-Agis, S. van der Heiden, C.M. Okonkwo, E. Tangdiongga, and A.M.J. Koonen, “112 Gbit/s transmission in a 2-D beam steering AWG-based optical wireless communication system,” *Proc. ECOC 2017*, Gothenburg, paper Th.2.B.1.
- [57] WiFi IEEE 802.11 standards [Online]. Available: https://en.wikipedia.org/wiki/IEEE_802.11 .
- [58] Gigabit home networking specification G.hn [on-line]. Available: https://www.itu.int/dms_pub/itu-t/opb/tut/T-TUT-HOME-2021-3-PDF-E.pdf
- [59] A. M. J. Koonen, K. A. Mekonnen, Z. Cao, F. M. Huijskens, N.-Q. Pham, E. Tangdiongga, “Ultra-high capacity wireless communication by means of steered narrow optical beams,” *Philosophical Trans. Royal Soc. A*, Mar. 2020, 19 pp., <http://dx.doi.org/10.1098/rsta.2019.0192>
- [60] F. Gomez-Agis, S. P. van der Heide, C. M. Okonkwo, E. Tangdiongga, and A. M. J. Koonen, “112 Gbit/s transmission in a 2D beam steering AWG-based optical wireless communication system,” *Proc. ECOC 2017*, Göteborg, Sweden, Sep. 2017, Paper Th.2.B.1.
- [61] A. M. J. Koonen, F. Gomez-Agis, F. M. Huijskens, and K. A. Mekonnen, “High-capacity optical wireless communication using two-dimensional IR beam steering,” *J. Lightw. Technol.*, vol. 36, no. 19, pp. 4486–4493, Oct. 2018.
- [62] CSMA/CA protocol [on-line]. Available: https://en.wikipedia.org/wiki/Carrier-sense_multiple_access_with_collision_avoidance
- [63] Antenna gain [on-line]. Available: [https://en.wikipedia.org/wiki/Gain_\(antenna\)](https://en.wikipedia.org/wiki/Gain_(antenna))
- [64] P. Hannan, "The element-gain paradox for a phased-array antenna," *IEEE Trans. on Antennas and Propagation*, vol. 12, no. 4, pp. 423-433, July 1964.
- [65] Horn antenna, Wikipedia [Online]. Available: https://en.wikipedia.org/wiki/Horn_antenna
- [66] Radiation efficiency [on-line]. Available: https://en.wikipedia.org/wiki/Radiation_efficiency
- [67] Antenna directivity [on-line]. Available: <https://en.m.wikipedia.org/wiki/Directivity>
- [68] D.-J. Deng, S.-Y. Lien, C.-C. Lin, M. Gan, H.-C. Chen, "IEEE 802.11ba Wake-Up Radio: Performance Evaluation and Practical Designs," *IEEE Access*, Vol. 8, Aug. 2020, pp. 141547-141557
- [69] Target wake time in IEEE 802.11ax protocol [on-line]. Available: <https://www.commscope.com/blog/2018/802.11ax-fundamentals-target-wake-time-twt/>
- [70] K. Wang, A. Nirmalathas, C. Lim, K. Alameh, and E. Skafidas, “Full duplex gigabit indoor optical wireless communication system with CAP modulation,” *Photon. Technol. Lett.*, vol. 28, no. 7, pp. 790–793, Apr. 2016.
- [71] A. Gomez, K. Shi, C. Quintana, M. Sato, G. Faulkner, B.C. Thomsen, and D. C. O’Brien, “Beyond 100-Gb/s indoor wide field-of-view optical wireless communications,” *Phot. Technol. Lett.*, vol. 27, no. 4, Feb. 2015, pp. 367-370.
- [72] Signify’s Trulifi, a new range of LiFi systems. [Online]

- Available: <https://www.signify.com/en-in/innovation/trulifi>
- [73] pureLiFi's LiFi@Home product family [Online] Available: <https://www.purelifi.com/products/lifihome/>
- [74] Ton Koonen, "Optical technologies to disclose the spatial diversity dimension in systems and networks," *Proc. ACP 2020*, Beijing, 26 Oct. 2020, plenary talk, paper M1A1.
- [75] A.M.J. Koonen, "Indoor optical wireless systems: Technology, trends, and applications," *J. Lightw. Technol.*, vol. 36, no. 8, pp. 1459–1467, Apr. 2018.
- [76] A.D. Griffiths, J. Herrnsdorf, J.J.D. McKendry, M.J. Strain, M.D. Dawson, "Gallium nitride micro-light-emitting diode structured light sources for multi-modal optical wireless communications systems," *Philosophical Trans. Royal Soc. A*, Mar. 2020, 15 pp., <https://doi.org/10.1098/rsta.2019.0185>
- [77] Luc Mareta, Alexandre Lagrangea, Ludovic Dupré, "Ultra-High Speed Optical Wireless Communications with gallium-nitride microLED," *Proc. of SPIE*, 5 Mar. 2021); doi: 10.1117/12.2576092
- [78] A.M.J. Koonen, K.A. Mekonnen, F.M. Huijskens, N.-Q. Pham, Z. Cao, E. Tangdiongga, "Fully passive user localization for beam-steered high-capacity optical wireless communication system," *J. Lightw. Technol.*, vol. 38, no. 10, pp. 2842-2848, May 2020.
- [79] Ngoc Quan Pham, Ketemaw Mekonnen, Eduward Tangdiongga, Ali Mefleh, Ton Koonen, "User localization and upstream signaling for beam-steered infrared light communication system," *Phot. Techn. Lett.*, vol. 33, no. 11, June 2021, pp. 545-548.
- [80] Martijn J.R. Heck, "Highly integrated optical phased arrays: photonic integrated circuits for optical beam shaping and beam steering," *Nanophotonics*, vol. 6, no. 1, pp. 93–107, 2017.
- [81] J. C. Hulme, J. K. Doyle, M. J. R. Heck, J. D. Peters, M. L. Davenport, J. T. Bovington, L. A. Coldren, J. E. Bowers, "Fully integrated hybrid silicon two dimensional beam scanner," *Optics Express*, vol. 23, no. 5, 9 Mar 2015.
- [82] K. Van Acoleyen, W. Bogaerts, and R. Baets, "Two-Dimensional Dispersive Off-Chip Beam Scanner Fabricated on Silicon-On-Insulator," *Phot. Technol. Lett.*, vol. 23, no. 17, Sep. 2011, p. 1270-1272.
- [83] W. Guo, P.R.A. Binetti, C. Althouse, L.A. Johansson, and L.A. Coldren, "InP photonic integrated circuit with on-chip tunable laser source for 2D optical beam steering," *Proc. OFC 2013*, Los Angeles, paper OTh3I-7.[82]
- [84] J. Zeng, V. Joyner, J. Liao, S. Deng, Z. Huang, "A 5 Gb/s 7-channel current-mode imaging receiver front-end for free-space optical MIMO," *Proc. IEEE MWSCAS*, 2009, Cancun, pp. 148–151.
- [85] Cuiwei He, Stefanie Cincotta, Mohammed M. A. Mohammed, Jean Armstrong, "Angular Diversity Aperture (ADA) Receivers for Indoor Multiple-Input Multiple-Output (MIMO) Visible Light Communications (VLC)," *IEEE Access*, vol. 7, pp. 145282-145301, Oct. 2019.
- [86] Toshimasa Umezawa, Yuki Yoshida, Atsushi Kanno, Naokatsu Yamamoto, Tetsuya Kawanishi, "Integrated high-speed photodetector array for SDM

- communications,” *Proc. ACP 2019*, paper M3H.4.
- [87] Toshimasa Umezawa , Yuki Yoshida , Atsushi Kanno , Atsushi Matsumoto, Kouichi Akahane, Naokatsu Yamamoto, Tetsuya Kawanishi , “FSO Receiver With High Optical Alignment Robustness Using High-Speed 2D-PDA and Space Diversity Technique,” *J. Lightw. Technol.*, vol. 39, no. 4, pp. 1040–1047, Feb. 2021.
- [88] Z. Cao, L. Shen, Y. Jiao, X. Zhao, A.M.J. Koonen, “200 Gbps OOK transmission over an indoor optical wireless link enabled by an integrated cascaded aperture optical receiver,” *Proc. OFC2017*, Los Angeles, post-deadline paper Th5A.6.
- [89] A.M.J. Koonen, K.A. Mekonnen, F.M. Huijskens, Z. Cao, E. Tangdiongga, “Novel Broadband OWC Receiver with Large Aperture and Wide Field of View”, *Proc. ECOC 2020*, Brussels, Dec. 2020, paper Tu2G.6.
- [90] Ton Koonen, Ketemaw Mekonnen, Zizheng Cao, Frans Huijskens, Ngoc Quan Pham, Eduward Tangdiongga, "Beam-Steered Optical Wireless Communication for Industry 4.0," *IEEE J. of Selected Topics in Quantum Electronics*, Vol. 27, No. 6, Nov./Dec. 2021, 10 pp.
- [91] Ton Koonen, Ketemaw Mekonnen, Frans Huijskens, Ngoc Quan Pham, Zizheng Cao, Eduward Tangdiongga, "Optical Wireless GbE Receiver with Large Field-of-View," *Proc. ECOC 2021*, Bordeaux, 13-16 Sep. 2021, paper Th1B.6.
- [92] T. Umewaza, A.Q. Matsumoto, K. Akahane, A. Kanno, N. Yamamoto, “400-pixel high-speed photodetector for high optical alignment robustness FSO receiver,” *Proc. OFC 2022*, San Diego, Mar. 2022, paper M4I.3.
- [93] T. Umezawa, S. Nakajima, A. Bekkali, M. Hattori, A. Matsumoto, A. Kanno, K. Akahane, N. Yamamoto, “Multi-Stacked Large-Aperture High-Speed PIN-Photodetector for Mobile-FSO Communication,” *Proc. ECOC 2023*, Glasgow, Oct. 1-5, 2023, paper We.D.2.

4 Beam-steered indoor OWC system⁸

Much research effort has been reported in visible light communication (VLC), which can piggy-back on existing LED illumination systems [1][2]. VLC systems are typically omni-directional, implying capacity-sharing of the light source by multiple user terminals. Also, the light intensity at the receiver inherently goes down with the square of the distance to the source, which after the opto-electrical conversion in the photodetector implies that the electrical signal-to-noise ratio (SNR) at the receiver decreases with the fourth power of the distance to the source, and thus the link reach is quite limited.

Links with a larger reach can be realized with directional collimated optical beams. Accurate agile two-dimensional (2D) beam steering is needed in order to address the (moving) user terminals; the concepts for this approach were introduced by Riza in [3]. Optical beam 2D steering systems have been reported using actively controlled devices such as micro-electro-mechanical system (MEMS)-actuated mirrors [4] [5], spatial light modulators (SLMs) [3] [6], and an optical switch for coarse steering followed by an SLM for fine steering [7]. Each beam may require a separate steering device, which makes scaling to many beams challenging. It has been shown that by operating an SLM in a spatial division mode, multiple beams can be supported in a point-to-multipoint scheme [8]. Also beam steering systems which use static diffractive devices have been reported, where the steering is controlled through changing the wavelength of the light beam fed to the device via fiber by remotely located tunable laser diodes. The steering is determined by the wavelength of the channel carrying the data; thus, no separate control channel for the steering is needed, which eliminates the need for tedious book-keeping of which control channel belongs to which signal channel. The wavelength is actually serving as an embedded control channel. 1D steering by means of a plane reflection grating was introduced in [9]. This concept was demonstrated with high-speed free-space communication for the first time in [10], showing transmission at 1Gbit/s over 2m reach using on-off keying (OOK) modulation. Similarly, transmission at 2.5 Gbit/s OOK over 60cm was shown in [11], and at 10Gbit/s OOK over 2.5m in [12]. Steering of multiple beams is

⁸ This chapter is largely based on A.M.J. Koonen, C. W. Oh, K. Mekonnen, Z. Cao, and E. Tangdiongga, "Ultra-high capacity indoor optical wireless communication using 2D-steered pencil beams," *IEEE/OSA J. Lightw. Technol.*, vol. 34, no. 20, pp. 4802–4809, Oct. 2016, and also on US patent 9246589 B2, WO patent 2013107853, priority date Jan. 20, 2012, "Two-dimensional optical beam steering module," by Antonius Marcellus Jozef Koonen, Peter G.M. Baltus, and Antonio Liotta.

supported by using multiple wavelengths. A system using multiple narrow-band Bragg gratings stored in photo-thermo-refractive (PTR) glass volumes was reported in [13]; the number of beams supported equals the number of Bragg gratings. Here, multi-beam generation via a single aperture was proposed using multi-wavelength selection. The speed of the beam steering can be considerably faster than when using actively controlled devices, as the wavelength tuning time of a laser diode (with wavelength settling times less than $1\mu\text{s}$) can be much smaller than the electro-mechanical tuning time of a MEMS mirror or the tuning time of an SLM (both in the ms-range). 2D optical beam steering solutions by means of a photonic integrated circuit have been reported in [14] and [15]. These circuits showed relatively high losses and no free-space data transmission was applied.

In this chapter, we introduce in section 4.1 an indoor optical wireless communication system according to the BROWSE concept proposed by us in [16] - [20], and discuss its design boundaries which define functional details of the key OWC modules to be elaborated in chapters 5 to 8. Via an indoor fiber network, in every room 2D steering of directional narrow optical infrared pencil beams is deployed for the wireless paths, which are each aimed at a specific user terminal. Thus, the full ultra-high capacity of such a beam is available to that terminal, and neither congestion nor interference with other terminals occurs. Each beam actually may be regarded as a ‘virtual fiber’, offering the connectivity power of as single fiber (and even more than that, as its latency is 50% less, and waveguide dispersion is absent). In section 4.2, the 2D beam steering function is discussed using a novel concept deploying wavelength tuning in combination with a pair of crossed diffraction gratings. Adding wavelengths results in additional beams for steering; thus, the system can readily be scaled to many beams. To the best of the authors’ knowledge, this has been the first wavelength-controlled 2D beam-steered system demonstrated for ultra-high speed multi-beam communication. The pencil beam’s directivity effectively alleviates the reach limitations of VLC and saves energy by spatial allocation of capacity on demand, offering capacity only when and where it is needed. The upstream wireless paths from the terminals in a bidirectional wireless system may implemented in a hybrid optical/RF fashion by high-capacity radio wireless channels in the 60GHz band, which are transported over the indoor backbone fiber network by means of radio-over-fiber techniques employing recovery of the unmodulated optical carrier from a downstream channel, as described in section 4.3. The upstream RF paths may be impacted by external EMI, and/or induce crosstalk to other users when not sufficiently confined. Alternatively, fully building on the key strengths of optical wireless communication, the bi-directional system may be implemented as an all-OWC system by also establishing the upstream links with optical beams; see chapter 8. The chapter is concluded with summarizing the main research

directions for the key beam-steered OWC modules to be elaborated in chapters 5 to 8.

4.1 The BROWSE system concept

As discussed in chapter 3, OWC by means of 2D-steered infrared beams is an attractive technique to provide broadband services wirelessly to users individually even at high user densities. We have proposed the system concept shown in Fig. 4-1 (see [17] and [4]) which we have investigated in the project ‘BROWSE - Broadband Beam-steered Reconfigurable Optical-Wireless System for Energy-efficient communication’, funded by the European Research Council within the Advanced Investigator program. Inside a building, each room is equipped with one or more pencil radiating antennas (PRAs). Each PRA can emit multiple optical pencil beams, and contains passive diffractive optics. The capacity foreseen per beam is at least 1Gbit/s, and capacities of 10-s of Gbit/s are within reach. Multiple PRAs per room are foreseen in order to provide full coverage of the room, and to enable circumvention of possible line-of-sight path blockings. The circumvention is enabled by re-routing the optical signal to another PRA by means of the optical cross-connect (OXC). Inside a PRA, a passive diffractive module steers a beam in two angular dimensions (i.e., 2D steering), by just varying the wavelength of the beam. The wavelength of each beam thus acts as an embedded control channel, which simplifies the management of the indoor traffic flows as it avoids the need of implementing a separate control network and the need for tedious bookkeeping of which control channel belongs to which signal channel. We have proposed two options for realizing such a diffractive module: one using on a pair of crossed diffraction elements [18], or an alternative one using an arrayed waveguide grating router with its output ports grouped in a 2D matrix [19]; full design details are given in sections 5.2 and 5.3, respectively.

For the diffractive module using a pair of crossed diffraction elements, we propose to deploy two elements (e.g. reflection gratings, see Fig. 4-2.a) where one element has a relatively low diffractive power, and the other one a high diffractive power. These elements together form a fully passive PRA module, which steers a beam in two dimensions according to its wavelength. The beam is continuously swept in one dimension by changing the wavelength over less than the large free spectral range (FSR) of the low-dispersive element, whereas it is swept multiple times in the orthogonal dimension when it traverses multiple small FSR-s of the other highly dispersive element. As a result, an area is scanned in 2 dimensions line by line, by just varying a single parameter, namely the wavelength λ of the beam. The wavelength of the beam thus also acts as a control channel of the beam steering, embedded in the data channel; hence a separate control channel is avoided, which relaxes network management and control.

For the diffractive module using an arrayed waveguide grating router with its output fibers arranged in a 2D matrix, wavelength-tuning of the input signal yields steering of the beam in both of the two dimensions with discrete steps (Fig. 4-2.b, see section 5.3).

We propose to use infrared wavelengths beyond $1.4\mu\text{m}$, where eye safety regulations allow higher beam powers than in the visible range; up to 10mW is allowed according to ANZI Z-136 and IEC 60825 standards [21]. Moreover, beyond $1.5\mu\text{m}$ there are already many mature devices readily available, designed for optical fiber communication systems. Multiple beams can be handled individually by just adding wavelengths, making this concept readily scalable to large numbers of beams. The wavelength-tunable sources are hosted jointly in the Central Communication Controller (CCC; see Fig. 4-1), and are dynamically connected upon demand to the PRAs in the respective rooms by means of an optical cross-connect switch (OXC) and the point-to-point (P2P) fiber feeder backbone network. Optionally, one may share fiber lines in a point-to-multipoint (P2MP) topology by band-multiplexing multiple wavelength channels at the OXC and demultiplexing these near the PRAs (cf. a WDM-PON). However, in order to assure that this wavelength-partitioning leaves enough wavelength tuning range per PRA, this would require an ultra-wide wavelength tuning range per tunable source. E.g., 30nm wide tuning by an integrated sampled-grating distributed Bragg reflector (SG-DBR) laser diode has been reported in [15]. Conceptually, wider tuning may be achieved by putting multiple tunable lasers each covering a distinct range in parallel. To limit the wavelength tuning requirements, we have chosen the P2P fiber network topology in our system concept.

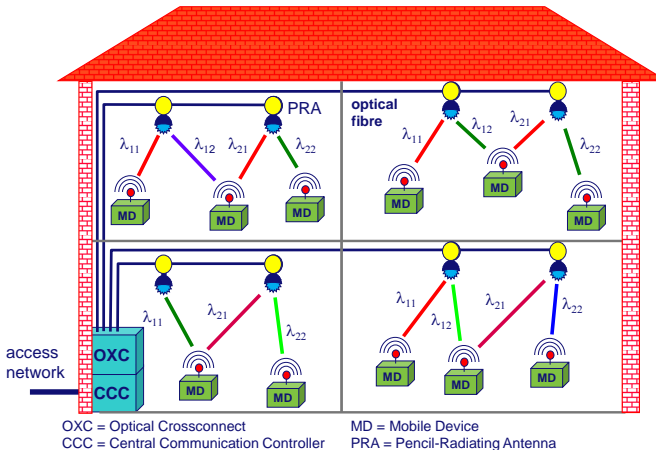


Fig. 4-1 Free-space indoor optical communication by pencil beams

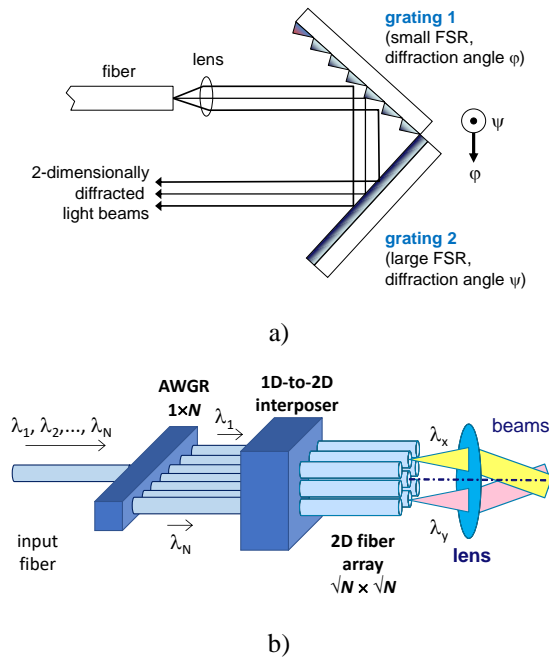


Fig. 4-2 2-dimensional diffractive optical beam steering module using
 a) a pair of crossed gratings (FSR: Free Spectral Range), or
 b) arrayed waveguide grating router with output ports in a 2D matrix.

The indoor OWC system concept using 2D-steerable IR beams we propose is shown in Fig. 4-1. In each room, multiple pencil-beam radiating antennas (PRAs) are installed. A PRA contains passive diffractive optics and can emit multiple beams of which each is 2D steered under control of its wavelength. The wavelength of each beam thus acts as an embedded control channel, which simplifies the management of the indoor traffic flows as it avoids the need of implementing a separate control network. By using multiple PRA-s per room, line-of-sight blocking can be circumvented, as one PRA can take over the duties of another one. Each PRA is fully passive; it contains no moving parts and does not need electrical powering nor electrical control signals. Its optical data signals are fed remotely via the indoor fiber backbone network from a central site in the building, where all network management and control functions are located. This co-location also eases management, maintenance and upgrading of the whole network. At this central communication controller (CCC), tunable transceivers together with a transparent optical cross-connect (OXC) module take care that the user data streams are each dynamically routed to the appropriate PRA in the appropriate room with the appropriate wavelength. For bi-directional operation, the return path for each user may be established by RF techniques such as 60GHz

radio-over-fiber techniques, or alternatively may be established by optical wireless links too, as is described in detail in chapter 8.

4.2 2D beam steering using diffractive means

For specifying the functionality of the PRA, we assume that it has to cover an area of $L \times L$ while it is positioned at a height H with respect to that area. It has to address the area by means of 2-dimensional steering of a beam having a diameter D_{beam} (see Fig. 4-3). The number of steering steps needed is $N=(L/D_{beam})^2$. Given that for diffractive steering of a beam a wavelength tuning range $\Delta\lambda$ is available, the wavelength tuning step size is $\delta\lambda=\Delta\lambda/N=\Delta\lambda \cdot (D_{beam}/L)^2$. Hence a lower bound for the beam diameter is given by

$$D_{beam} > L \sqrt{\frac{\delta\lambda}{\Delta\lambda}} \tag{4-1}$$

When assuming that the PRA is launching (nearly) collimated beams out of a circular aperture, the beam spot projected in the user plane is also circular. The receiver at the user may be tilted over an angle ε_{rx} with respect to the user plane, and the angle of beam incidence α on the receiver is

$$\alpha = \varphi_c + \varepsilon_{rx} \tag{4-2}$$

where φ_c is the angle at which the beam is launched from the PRA, see Fig. 4-3.b.

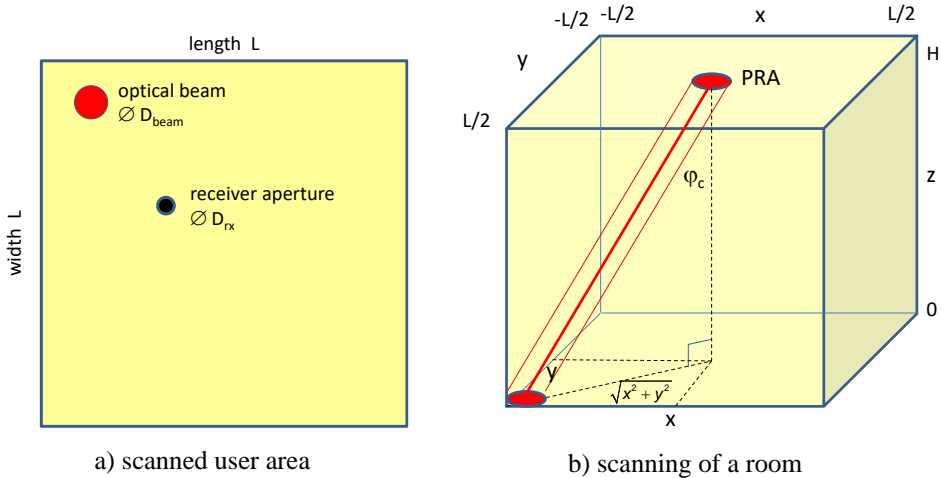


Fig. 4-3 Scanning the room with a collimated optical beam

The maximum incidence angle α_{max} which the receiver can handle is specified as its Field of View (FoV) α_{FoV} . The required FoV of the receiver α_{FoV} for the coverage area is

$$\alpha_{FoV} \geq \text{atan} \left(\frac{L}{H \sqrt{2}} \right) + \varepsilon_{rx} \quad (4-3)$$

In a first-order analysis, we assume that the field of view (FoV) of the receiver exceeds the maximum incidence angle α_{max} , and thus the received power is not restricted by the FoV. Such an approximation holds for a lensless receiver where the received light is incident directly on the active area of a photodiode. When the receiver in the user terminal has an aperture with diameter D_{rx} , the PRA is fixed in the middle of the ceiling at height H , and the power intensity in the beam is uniform across its diameter D_{beam} , the fraction T of the beam's power P_{beam} which is captured by the receiver with aperture diameter D_{rx} is

$$T = \frac{P_{rx}}{P_{beam}} = \begin{cases} \left(\frac{D_{rx}}{D_{beam}} \right)^2 \cos \varepsilon & \text{if } D_{rx} \leq D_{beam} \\ 1 & \text{if } D_{rx} > D_{beam} \end{cases} \quad (4-4)$$

where P_{rx} is the power captured by the receiver, which implicitly gives an upper bound to the beam diameter D_{beam} in order to guarantee an adequate minimum received power level $P_{rx,min}$. Fig. 4-4 shows how D_{beam} can be determined as a compromise between a minimum wavelength tuning step and a minimum receiver sensitivity. If the beam-to-receiver power coupling fraction T_{eq} should be at least -20dB (so for a beam power of +10dBm at least -10dBm is captured by the receiver's aperture), and if an area with $L=1.5\text{m}$ should be covered with a total available wavelength tuning range $\Delta\lambda=100\text{nm}$, the beam diameter should be $D_{beam} \leq 10\text{mm}$ and the tuning step size $\delta\lambda=4.4\text{pm}$ when the receiver's aperture diameter $D_{rx}=1\text{mm}$. The tuning step size limits the bandwidth BW of the OWC link, as $BW \ll \delta\lambda c_0 / \lambda^2$. Therefore, a narrow beam not only complicates the required accuracy for the beam steering, the required stability of the wavelength tuning, and the user localization process, but also limits the link's bandwidth. E.g., with $\delta\lambda=4.4\text{pm}$ the bandwidth $BW \ll \delta\lambda c_0 / \lambda^2 \approx 587\text{MHz}$ in the $1.5\mu\text{m}$ wavelength window. When a smaller beam-to-receiver power coupling fraction T_{eq} is allowed, the system requirements are relaxed. E.g., a $T_{eq} > -30\text{dB}$ is achieved with $D_{beam} \leq 10\text{mm}$ and $\delta\lambda=46\text{pm}$, allowing a bandwidth $BW \ll 6.1\text{GHz}$. The system requirements are significantly relaxed further when the receiver's aperture is increased: e.g., at $T_{eq} > -30\text{dB}$ an aperture $D_{rx}=10\text{mm}$ enables a beam diameter $D_{beam} \leq 314\text{mm}$ and tuning step size $\delta\lambda=4.4\text{nm}$ (i.e., a bandwidth $BW \ll 584\text{GHz}$).

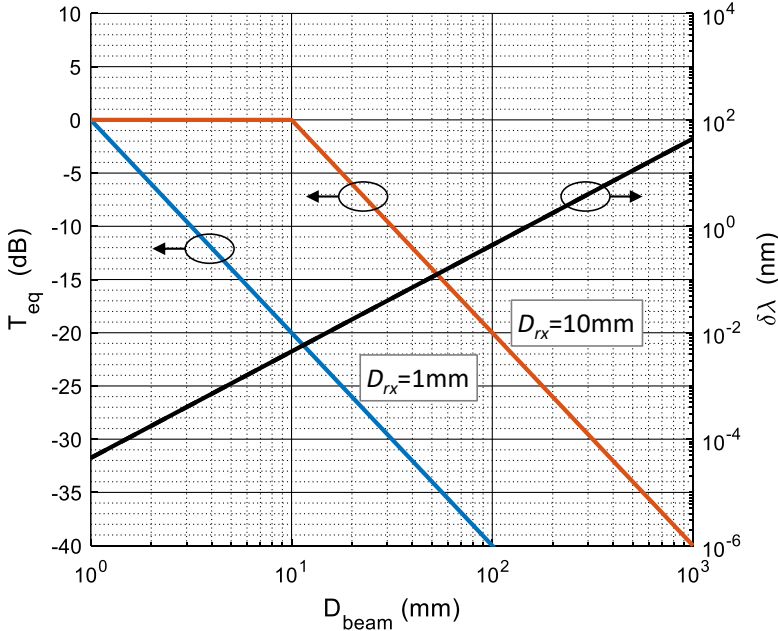


Fig. 4-4 Choosing the beam diameter D_{beam} for a lensless receiver (with $L=1.5\text{m}$, and $D_{rx}=1\text{mm}$ or $D_{rx}=10\text{mm}$)

However, increasing the receiver's aperture by increasing the photodiode leads to reduction of the receiver's bandwidth as the junction capacitance of a photodiode scales with its active area. Alternatively, while maintaining the photodiode's size, the aperture may be increased by applying intermediate optics, such as a compound parabolic concentrator (CPC), a condenser lens, etc. Unfortunately, due to the basic physics law of the conservation of etendue, these aperture-enlarging optics inevitably also restrict the FoV α_{FoV} of the receiver. In chapter 7, it is analyzed how the FoV can be increased by applying a certain degree of defocusing, i.e. by putting the photodiode not in the focal plane of the lens but somewhat closer to it by a distance x .

When assuming a uniform beam and ideal thin lens without any lens aberrations, the FoV of the receiver if the incident beam diameter D_{beam} exceeds the diameter D_{lens} of the lens with focal length f is (cf. eq. (7-38))

$$\alpha_{FoV} = \text{atan} \left(\frac{|p D_{lens} - D_{PD}|}{2 f (1 - p)} \right) \quad (4-5)$$

where D_{PD} is the diameter of the active area of the photodiode, and the defocusing parameter $p=x/f$ ($0 \leq p < 1$). Enlarging p enables to increase the FoV, but also reduces the fraction of the beam power coupled to the photodiode power.

According to eq. (4-3), given the area to be covered and assuming a negligible tilt of the receiver (i.e., $\varepsilon_{rx}=0$), , for the required defocusing p follows

$$p \geq \frac{D_{PD} + \frac{L}{H} f \sqrt{2}}{D_{lens} + \frac{L}{H} f \sqrt{2}} \quad (4-6)$$

As introduced in chapter 7, a large photodetector area can be created by building a matrix of photodiodes while preserving the bandwidth of the individual small photodiodes This allows to increase the defocusing p and thus to increase the FoV, but is accompanied by a decrease of the beam-to-photodetector power coupling. A suitable compromise between the FoV and the received optical power needs to be defined, depending on the system's requirements. According to eq. (4-6), the required defocusing p implies an equivalent beam-to-photodiode power coupling fraction T_{eq} (cf. eq. (7-39))

$$\begin{aligned} T_{eq} &= \frac{\eta}{M} \left(\frac{D_{PDmatrix}}{p D_{beam}} \right)^2 \\ &\leq \frac{\eta}{M} \left(\frac{D_{lens}}{D_{beam}} \frac{1 + \frac{L}{H} \frac{f}{D_{lens}} \sqrt{2}}{1 + \frac{L}{H} \frac{f}{D_{PDmatrix}} \sqrt{2}} \right)^2 \end{aligned} \quad (4-7)$$

In eq. (4-7), a matrix configuration of $M \times M$ photodiodes is assumed, which has a fill factor η (i.e., the aggregate active area of all the photodiodes in the matrix divided by the total area within the circle circumscribing the matrix; see section 7.2.1).

Similarly, when the beam diameter D_{beam} is smaller than the lens diameter D_{lens} , the FoV of the receiver is

$$\alpha_{FOV} = \text{atan} \left(\frac{|p D_{beam} - D_{PDmatrix}|}{2 f (1 - p)} \right) \quad (4-8)$$

and the required defocusing p is

$$p \geq \frac{D_{PDmatrix} + \frac{L}{H} f \sqrt{2}}{D_{beam} + \frac{L}{H} f \sqrt{2}} \quad (4-9)$$

which yields an equivalent beam-to-photodetector power coupling

$$T_{eq} = \frac{\eta}{M} \left(\frac{D_{PDmatrix}}{p D_{beam}} \right)^2 \leq \frac{\eta}{M} \left(\frac{1 + \frac{L}{H} \frac{f}{D_{beam}} \sqrt{2}}{1 + \frac{L}{H} \frac{f}{D_{matrix}} \sqrt{2}} \right)^2 \quad (4-10)$$

Fig. 4-5 shows how the beam diameter D_{beam} may be chosen in order to cover the $L \times L$ user area when a lensed receiver is applied. It also shows the optical spectral bandwidth $\delta\lambda$ available per beam, which corresponds with a maximum link bandwidth available for communication $BW_{max} \approx \delta\lambda c_0 / \lambda^2$. Two lenses have been assumed: an ideal thin lens with a diameter of $\varnothing 25\text{mm}$ and focal length $f=5\text{mm}$, and an ideal thin lens with diameter $\varnothing 50\text{mm}$ and $f=10\text{mm}$. Fresnel lenses (which can have a large D/f number, so a large aperture/focal length ratio and thus a large FoV; see chapter 7) with these parameters have been used in our OWC laboratory testbed. With the Fresnel lenses, the beam-to-PD matrix coupling has been numerically analyzed by means of ray tracing in section 7.2.2, wherein a 4×4 PD matrix is assumed with $\varnothing 150\mu\text{m}$ photodiodes spaced at $17\mu\text{m}$, yielding a PD matrix diameter $D_{PDmatrix}=0.859\text{mm}$. By increasing the beam diameter, the required wavelength step size $\delta\lambda$ is increased and thus the maximum available bandwidth $BW_{max} \approx \delta\lambda c_0 / \lambda^2$ grows. When a beam-to-PD matrix power coupling factor $T_{eq} > -30\text{dB}$ is needed, without a lens the beam diameter should be $D_{beam} < 9.5\text{mm}$, and the wavelength tuning step $\delta\lambda = 4.0\text{pm}$ ($BW_{max} \approx 0.53\text{GHz}$). With the lenses, the beam diameter can be significantly larger, and thus the wavelength tuning step $\delta\lambda$ larger, which eases the beam steering process. With the $\varnothing 25\text{mm}$ lens, $D_{beam} < 54\text{mm}$ and $\delta\lambda = 0.13\text{nm}$ ($BW_{max} \approx 17\text{GHz}$), and with the $\varnothing 50\text{mm}$ lens $D_{beam} < 60\text{mm}$ and $\delta\lambda = 0.16\text{nm}$ ($BW_{max} \approx 21\text{GHz}$). Fig. 4-5 also shows that the power received by a lensless receiver equipped with the same PD matrix is significantly less for the same beam diameter.

It may therefore be concluded that for a practical robust OWC indoor system based on diffractive 2D steering of relatively narrow beams by means of wavelength tuning, it is preferred to maximize the diameter of these steered beams, and to facilitate this by using lensed receivers at the user which can provide an adequate field-of-view while also capturing a sufficiently large fraction of the incident optical beam to enable high-capacity communication. Such receiver design approach is elaborated in more detail in chapter 7.

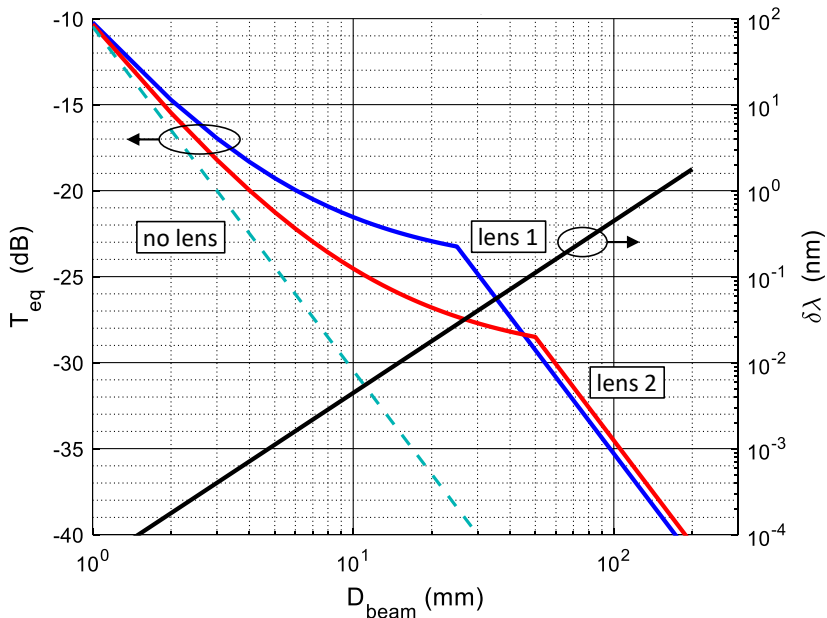


Fig. 4-5 Choosing the beam diameter D_{beam} for a lensed receiver with lens 1 (blue curve; a thin lens with diameter $\varnothing 25\text{mm}$ and $f=5\text{mm}$), and lens 2 (red curve; thin lens $\varnothing 50\text{mm}$ and $f=10\text{mm}$), and for a lensless receiver (dashed curve). Assumptions: area size $L=1.5\text{m}$, height $H=2.5\text{m}$, and a 4×4 PD matrix with overall diameter $D_{PDmatrix}=0.86\text{mm}$ and fill factor $\eta=49\%$.

4.3 The indoor fiber backbone network

A fiber backbone network is foreseen throughout the building in order to connect the PRAs located in the various rooms, as shown in Fig. 4-1. A point-to-point fiber link connects each PRA to the Central Communication Controller (CCC), where the tunable laser diodes are located. By means of an optical cross-connect (OXC), according to actual traffic demands these laser diodes are mapped to the appropriate PRAs in the appropriate rooms. At the CCC, autonomic network management is located to intelligently locate and track the (roaming) users' mobile devices (MDs), and to control the OXC settings and the wavelength tuning accordingly. Machine learning techniques can be applied which gather user behavior characteristics, in order to speed up localization, tracking and beam steering processes.

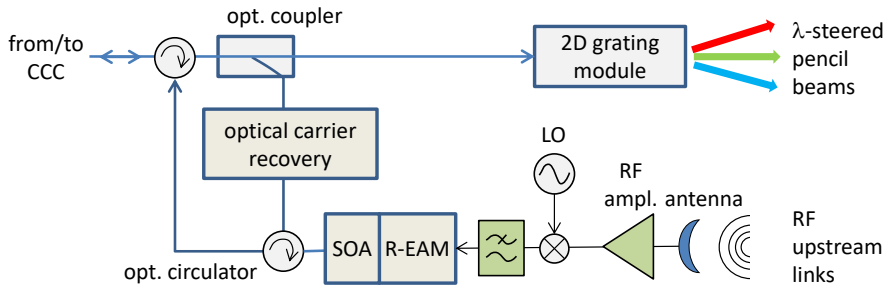


Fig. 4-6 Radio-over-fiber upstream path at PRA site, with optical carrier recovery

In a hybrid optical/TRF wireless bi-directional communication system, for the upstream path from the MD to the CCC, RF links in the 57-64GHz band can be foreseen, to be picked up by an antenna at the PRA and carried over the fiber network to the CCC using radio-over-fiber techniques. As illustrated in Fig. 4-6, at the PRA site a nearly clean optical carrier can be recovered from the downstream intensity-modulated optical signal (the received steerable pencil beam). This carrier recovery can be done by erasing the modulation by an SOA operated in the gain-saturated regime [22], or an injection-locked Fabry-Pérot laser diode [23]. Subsequently, a reflective modulator, composed of an SOA plus reflective electro-absorption modulator (R-EAM) [24][25], is used to modulate the downshifted upstream RF signal onto this clean carrier.

By means of a phased-array antenna at the PRA providing distinctive tunable nulls in the antenna pattern, also localization and tracking of the active MDs can be supported for aiding the optical pencil beam steering. Alternatively, localization and tracking may be done by means of a wide-view camera at the ceiling observing near-IR LED tags at the MD [26]; more details are discussed in Ch. 6.

4.3.1 Hybrid OWC downstream/RF upstream system

A preliminary system experiment for assessing the feasibility of upstream transmission employing radio-over-fiber (RoF) techniques was carried out using the setup shown in Fig. 4-7. Optical carrier recovery was implemented by using a semiconductor optical amplifier (SOA) working in its saturation region. The radio upstream signal was emulated by an arbitrary waveform generator (AWG) operating in baseband followed by up-conversion using a local oscillator at 7 GHz. The resulting signal emulates the down-converted 60 GHz radio signal (with 7 GHz bandwidth) received from the mobile device. This radio signal then modulates the intensity of the recovered optical carrier (at $\lambda=1550$ nm) using a 10 GHz bandwidth REAM-SOA. The upstream RoF signal is launched into the 1 km fiber link with 0 dBm power. Rate-adaptive DMT modulation was used. At

the CCC, the optical signal was received by a 10 GHz receiver and captured by a digital phosphor oscilloscope for signal processing.

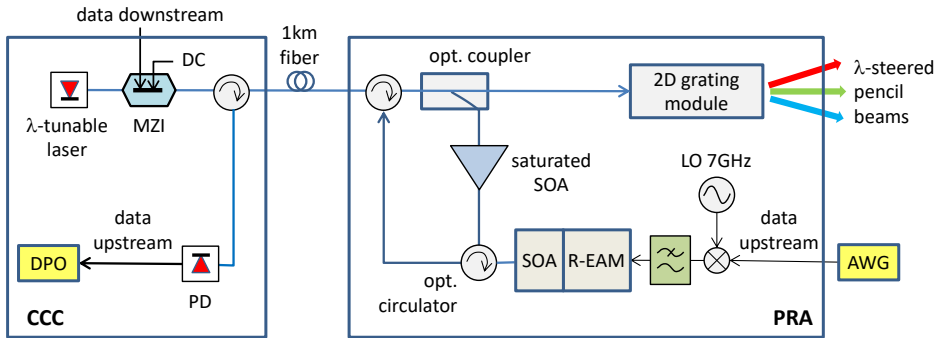


Fig. 4-7 Radio-over-fiber upstream system experiment

Fig. 4-8 depicts the waveforms at the input and output of the SOA at a bias current of 350 mA and optical input power of -1 dBm. In this operating condition the SOA was in deep saturation and erased the modulation from 300 mV (peak-to-peak) to less than 20 mV. The influence of the SOA bias current and input power on the upstream performance is illustrated in Fig. 4-8. It was possible to achieve >10 Gbit/s transmission when the input optical power was > -5 dBm. Increasing the SOA bias current and input optical power further improved the performance as the SOA was able to erase the downlink modulation even better.

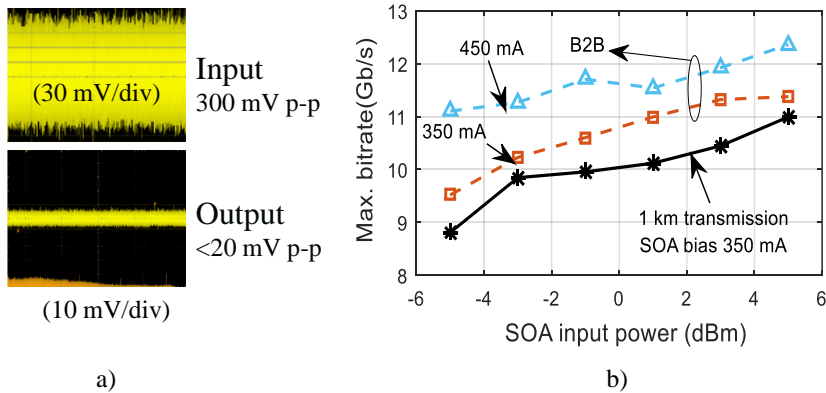


Fig. 4-8 Optical carrier recovery by the saturated SOA; a) waveforms at the input and output of the SOA at bias current 350 mA and input optical power -1 dBm; b) maximum upstream bitrate achievable

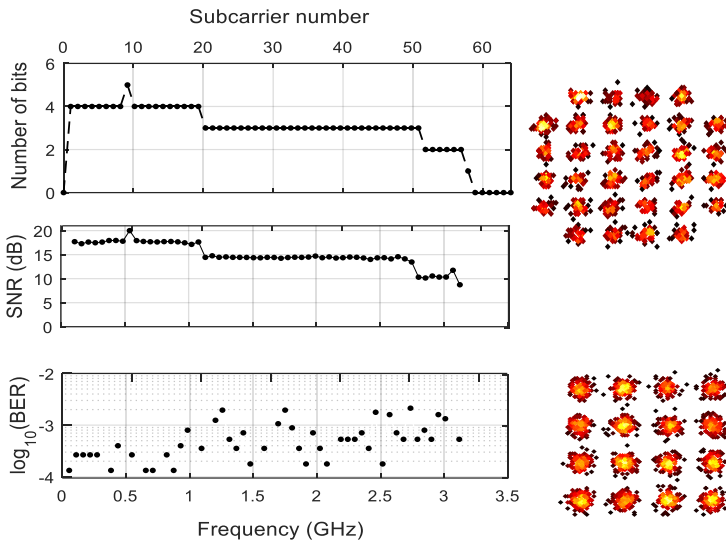


Fig. 4-9 DMT bit-loading profile and BER per subcarrier for the received upstream radio signal

Fig. 4-9 shows the adaptive DMT bit loading and BER performance for the radio signal after 1 km fiber transmission when the SOA was biased at 350 mA and the input optical power was -2 dBm. A maximum bit rate of 10 Gbit/s was achieved at an average BER 10^{-3}. Up to 32-QAM was utilized for the DMT subcarriers modulation.

4.4 Concluding remarks

Free-space optical communication deploying 2D steerable narrow optical pencil beams can offer the ultimate wireless capacity per user device. Diffractive beam steering techniques enable to emit multiple beams from a single ceiling unit (typically located at the ceiling in an indoor scenario), while each beam is individually steerable by changing its wavelength. Moreover, the optical signals which create the beams can be generated remotely, not at the ceiling unit, which facilitates maintenance, upgrading and upscaling of the system. The proposed concept which was introduced in the ERC Advanced Grant BROWSE project employs a pair of passive crossed diffractive elements which enables scaling to large numbers of pencil beams, each individually steerable by tuning its wavelength in the 1.5 μ m infrared regime. Angular beam steering over a 6 $^{\circ}$ ×12 $^{\circ}$ area (i.e., an area of 32×64cm 2 at 3m distance) was achieved by wavelength tuning from 1505 to 1630nm. Further careful design of the diffractive stages augmented by angular magnification using a lens system can increase the area coverage. Downstream delivery of 32Gbit/s per optical pencil beam in the

1.5-1.6 μm range over 3m reach using PAM-4 modulation with a simple free-space receiver has been demonstrated. With adaptive DMT modulation using 512 tones, a 42.8Gbit/s gross bitrate has been achieved. In the return path, by using radio-over-fiber techniques, DMT modulation and recovery of the downstream optical carrier, upstream delivery of 10Gbit/s per upstream 60GHz radio signal has been demonstrated.

Within the BROWSE project, we also explored an alternative diffractive 2D beam-steering technique based on an arrayed waveguide grating router (AWGR) and 2D arrangement of its fiber output ports. This technique employs readily available AWGR modules which are widely used in optical fiber communication networks and do not involve the delicate alignment needed for the crossed-gratings technique. As discussed in section 5.3, an indoor area coverage of $17^\circ \times 17^\circ$ is readily feasible, and a data capacity of up to 112Gbit/s per beam with PAM-4 modulation has been achieved.

For aligning the receiver aperture, automated electromechanical alignment measures can be applied which maximize the received power but need extra alignment time. Alternatively, the alignment effort can be relaxed by increasing the Field of View of the receiver by means of a novel photodiode matrix constellation as will be discussed in chapter 7.

4.5 References

- [1] D. O'Brien, R. Turnbull, H. Le Minh, G. Faulkner, O. Bouchet, P. Porcon, M. El Tabach, E. Gueutier, M. Wolf, L. Grobe, J. Li, "High-Speed Optical Wireless Demonstrators: Conclusions and Future Directions," *IEEE/OSA J. Lightw. Technol.*, Vol. 30, No. 13, pp. 2181-2187, Jul. 2012.
- [2] H. Haas, "Visible Light Communication," in *Proc. of OFC 2015*, Los Angeles, March 22-26, 2015, paper Tu2G.5.
- [3] N. A. Riza, "Reconfigurable optical wireless." in *Proc. LEOS'99 12th Annual Meeting*, Vol. 1, 1999, pp. 70-71.
- [4] A.D. Yalcinkaya, H. Urey, D. Brown, T. Montague, and R. Sprague, "Two-axis electromagnetic microscanner for high resolution displays," *IEEE J. Microelectromech. Syst.*, Vol. 15, No. 4, Aug. 2006, pp. 786-794.
- [5] K. Wang, A. T. Nirmalathas, C. Lim, E. Skafidas, "Experimental Demonstration of Full-Duplex Optical Wireless Personal Area Communication System with 16-CAP Modulation," in *Proc. of OFC 2015*, Los Angeles, March 22-26, 2015, paper M2F-7.
- [6] A. Gomez, K. Shi, C. Quintana, M. Sato, G. Faulkner, B.C. Thomsen and D. O'Brien, "Beyond 100-Gb/s indoor wide field-of-view optical wireless communications," *IEEE Phot. Technol. Lett.*, 27(4), pp.367-370, 2015.
- [7] N.A. Riza, Z. Yaqoob, "Space-multiplexed optical scanner," *Applied Optics*, Vol. 43, No. 13, May 2004, pp. 2703-2708.
- [8] A. Gomez, C. Quintana, G. Faulkner, D.C. O'Brien, "Point-to-multipoint holographic beamsteering techniques for indoor optical wireless

- communications”, in *Proc. SPIE 9772, Broadband Access Communication Technologies X*, Feb. 2016, 7 p.
- [9] Z. Yaqoob, A.A. Rizvi, N.A. Riza, “Free-space wavelength-multiplexed optical scanner,” *Applied Optics*, Vol. 40, No. 35, Dec. 2001, pp. 6425-6438.
- [10] K. Liang, H. Shi, S.J. Sheard, D.C. O’Brien, “Transparent optical wireless hubs using wavelength space division multiplexing,” in *Proc. SPIE 5550 Free-Space Laser Comm. IV*, Oct. 2004, 8 p.
- [11] C.W. Oh, F.M. Huijskens, Z. Cao, E. Tangdiongga, A.M.J. Koonen, “Toward multi-Gbps indoor optical wireless multicasting system employing passive diffractive optics,” *Optics Letters*, Vol. 39, No. 9, May 2014, pp. 2622-2625.
- [12] C.W. Oh, E. Tangdiongga, A.M.J. Koonen, “Steerable pencil beams for multi-Gbps indoor optical wireless communication,” *Optics Letters*, Vol. 39, No. 18, Sep. 2014, pp. 5427-5430.
- [13] Z. Yaqoob, M.A. Arain, N.A. Riza, “High-speed two-dimensional laser scanner based on Bragg gratings stored in photothermorefractive glass,” *Applied Optics*, Vol. 42, No. 26, Sep. 2003, pp. 5251-5262.
- [14] K. Van Acoleyen, W. Bogaerts, R. Baets, “Two-Dimensional Dispersive Off-Chip Beam Scanner Fabricated on Silicon-On-Insulator,” *IEEE Phot. Technol. Lett.*, vol. 23, no. 17, Sep. 2011, pp. 1270-1272.
- [15] W. Guo, P.R.A. Binetti, C. Althouse, L.A. Johansson, L.A. Coldren, “InP photonic integrated circuit with on-chip tunable laser source for 2D optical beam steering,” in *Proc. of OFC 2013*, Los Angeles, March 19-21, 2013, paper OTh3I-7.
- [16] A.M.J. Koonen, C.W. Oh, and E. Tangdiongga, “Reconfigurable free-space optical indoor network using multiple pencil beam steering,” *Proc. OECC/ACOFT 2014*, July 2014, Melbourne, paper Tu3F-1.
- [17] A.M.J. Koonen, C.W. Oh, K. Mekonnen, E. Tangdiongga, “Ultra-high capacity indoor optical wireless communication using steered pencil beams,” in *Proc. MWP 2015*, Paphos, Oct. 25-29, 2015, paper WeC-5.
- [18] A.M.J. Koonen, C.W. Oh, K.A. Mekonnen, Z. Cao, E. Tangdiongga, “Ultra-high capacity indoor optical wireless communication using 2d-steered pencil beams,” *IEEE/OSA J. Lightw. Technol.*, Vol. 34, No. 20, pp. 4802– 4809, Oct. 2016. (doi:10.1109/JLT.2016.2574855)
- [19] A.M.J. Koonen, F. Gomez-Agis, F.M. Huijskens, K.A. Mekonnen, Z. Cao, E. Tangdiongga. “High-capacity optical wireless communication using two-dimensional IR beam steering,” *IEEE/OSA J. Lightwave. Technol.*, Vol. 36, No. 19, pp. 4486–4493, Oct. 2018. (doi:10.1109/JLT.2018.2834374)
- [20] A.M.J. Koonen, K.A. Mekonnen, F.M. Huijskens, E. Tangdiongga, “Bi-directional all-optical wireless Gigabit Ethernet communication system using automatic self-aligned beam steering,” *J. of Lightw. Technol.*, Vol. 41, No. 11, June 2023, pp. 3446-3454. (<https://doi.org/10.1109/JLT.2022.3231438>)
- [21] See e.g. https://en.wikipedia.org/wiki/Laser_safety
- [22] H. Takesue, and T. Sugie, “Wavelength Channel Data Rewrite Using Saturated SOA Modulator for WDM Networks With Centralized Light Sources,” *IEEE/OSA J. Lightw. Technol.*, Vol. 21, No. 11, pp. 2546 – 2556, Nov. 2003.

-
- [23] H. D. Kim, S.-G. Kang, and C.-H. Lee, "A low-cost WDM source with an ASE injected Fabry–Pérot semiconductor laser," *IEEE Photon. Technol. Lett.*, Vol. 12, No. 8, Aug. 2000, pp. 1067–1069.
 - [24] N. Dupuis, J. Décobert, C. Jany, F. Alexandre, A. Garreau, N. Lagay, F. Martin, D. Carpentier, J. Landreau, and C. Kazmierski, "10-Gb/s AlGaInAs colorless remote amplified modulator by selective area growth for wavelength agnostic networks," *IEEE Photon. Technol. Lett.*, Vol. 20, No. 21, pp. 1808–1810, Nov. 2008.
 - [25] K. Ławniczuk, O. Patard, R. Guillaumet, N. Chimot, A. Garreau, C. Kazmierski, G. Aubin, and K. Merghem, "40-Gb/s Colorless Reflective Amplified Modulator," *IEEE Photon. Technol. Lett.*, Vol. 25, No. 4, pp. 341–343, Feb. 2013.
 - [26] A. Gomez, K. Shi, C. Quintana, G. Faulkner, B.C. Thomsen, D.C. O'Brien, "A 50 Gb/s transparent indoor Optical Wireless communications link with an integrated localization and tracking system," *IEEE/OSA J. Lightw. Technol.*, Vol. 34, No. 10, May 2016, pp. 2510-2517.

5 Beam steering techniques for indoor OWC

5.1 Introduction

An essential task of the indoor optical wireless network as introduced in section 3.6 is to provide independent accurate steering in two dimensions of each optical beam. At the ceiling unit, multiple beams need to be steered. In literature, steering by tunable little mirrors employing micro-electrical mechanical system (MEMS) techniques has been proposed [16]. Another solution proposed is based on spatial light modulator (SLM) techniques employing programmable reflection or transmission gratings [17][18]. Both solutions need a steering element per beam, with its separate control signal. Scaling to many beams hence leads to a complex steering module with comprehensive control needs. Moreover, the steering is done by active elements, so local powering and maintenance of the steering modules is required. These modules typically are mounted on the ceiling and may not be readily accessible.

Steering an infrared beam with fully passive devices may be done by tuning the wavelength of the light in combination with wavelength-diffractive functions. For steering the downstream beams, as proposed in the BROWSE system architecture (see section 4.1) the optical transmitters hosted in the central site can be equipped with tunable laser diodes which readily generate the optical signals at the wavelengths needed and feed these signals via an indoor fiber backbone network to passive diffractive beam steerers in the respective rooms. Laser diode tuning speed is typically much faster than the speed with which MEMS and SLM devices can be tuned. Beam steering has been reported by means of multiple tilted Bragg gratings embedded in a holographic photo-thermo-refractive glass volume [19] ; each grating is designed to diffract a specific wavelength into a specific direction. The number of beams which can be steered is limited by the number of gratings. We propose to use diffractive beam steerer concepts: one based on crossed diffraction gratings in section 5.2, or alternatively in section 5.3 one based on an arrayed waveguide grating router (AWGR) as is already widely deployed in multi-wavelength optical fiber networks. In combination with wavelength tuning, these concepts are readily scalable to handle many beams individually by just a single steering module.

To establish the upstream link in a bi-directional OWC system, from each user module a single beam has to be steered accurately towards the upstream receiver in the ceiling unit. Diffraction-based upstream beam steering is not preferred for cost reasons, hence 2D beam steering by mechanical means using a laser diode with arbitrary-wavelength is considered in section 5.4.

The chapter is concluded in section 5.5 with comparing the characteristics of the various beam steering methods.

5.2 2D diffractive beam steerer using crossed gratings⁹

As outlined in Ch. 4.2, our proposed line-by-line 2D scanning technique implies that $M=L/D_{\text{beam}}$ lines need to be scanned in order to fully cover the $L \times L$ area.

5.2.1 Beam steerer design

The 2D beam-steering module may deploy a pair of diffractive elements, one being highly diffractive with a small FSR, and the other one being mildly diffractive with a large FSR which comprises multiple of the small FSR-s; e.g., the crossed-grating module shown in Fig. 4-2.a. Scanning one line is equivalent to passing through one FSR of the highly diffractive element, so the total wavelength tuning over $\Delta\lambda$ should go across M orders (FSR-s) of this element. When a diffractive element based on interference among a number of beams is used, interference maxima occur when neighbouring beams are in-phase, so have an optical path length difference ΔL equal to an integer multiple m (i.e. the interference order) of the wavelength λ [1]. The FSR of order m covers the wavelength range $[\lambda_m, \lambda_m + \Delta\lambda_{FSR,m}]$ and is found from the relation $\Delta L = m \cdot \lambda_m = (m-1)(\lambda_m + \Delta\lambda_{FSR,m})$ (cf. Fig. 5-2), hence

$$\Delta\lambda_{FSR,m} = \frac{\lambda_m}{m-1} \quad \text{for } m \geq 2 \quad (5-1)$$

Extrapolating, the tuning range $\Delta\lambda_{\text{tun}}$ which is needed to cover M orders and starts at λ_{min} in the highest order m_{max} is

$$\Delta\lambda_{\text{tun}} = \sum_{i=m_{\text{max}}-M}^{m_{\text{max}}} \Delta\lambda_{FSR,i} = \lambda_{\text{min}} M / (m_{\text{max}} - M) \quad (5-2)$$

Hence, the highest order at which the highly diffractive element needs to operate is

⁹ This section is largely based on A.M.J. Koonen, F. Gomez-Agis, F.M. Huijskens, and K.A. Mekonnen, "High-capacity optical wireless communication using two-dimensional IR beam steering," *IEEE/OSA J. Lightw. Technol.*, vol. 36, no. 19, pp. 4486–4493, Oct. 2018. Related patent: US patent 9246589 B2, WO patent 2013107853, priority date Jan. 20, 2012, "Two-dimensional optical beam steering module," by Antonius Marcellus Jozef Koonen, Peter G.M. Baltus, and Antonio Liotta.

$$m_{max} = (L/D_{beam}) (1 + \lambda_{min}/\Delta\lambda_{tun}) \quad (5-3)$$

E.g., for the $D_{beam}=3\text{cm}$ derived above, $\Delta\lambda_{tun}=100\text{nm}$ and $\lambda_{min}=1500\text{nm}$, with $L=1.5\text{m}$ we find $m_{max}=800$. Such a high order is far beyond the capabilities of regular diffraction gratings and needs specific multi-beam diffraction elements.

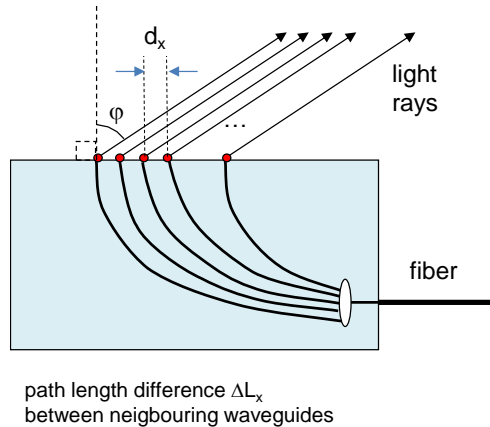


Fig. 5-1 Highly dispersive arrayed waveguide grating

An element with high diffractive power operating in high order (and thus having a small FSR) is the arrayed waveguide grating (AWG) shown in Fig. 5-1. Neighbouring waveguides have an optical path length difference ΔL_x , and are spaced at the end facet by d_x . Multi-beam interference maxima occur in direction φ if

$$\Delta L_x + d_x \sin \varphi = m \lambda \quad (5-4)$$

which implies that the order m is bounded by

$$\frac{\Delta L_x - d}{\lambda} \leq m \leq \frac{\Delta L_x + d}{\lambda} \quad (5-5)$$

Typically, $\Delta L_x \gg d > \lambda$, hence $m \gg 1$ and a high angular dispersion $d\varphi/d\lambda$ can be achieved as

$$\frac{d\varphi}{d\lambda} = \frac{m}{d_x \cos \varphi} \quad (5-6)$$

From Fig. 5-1 follows that (with $m \geq 2$)

$$\Delta\lambda_{FSR,m} = \frac{\lambda}{m-1} = \frac{\lambda^2}{\Delta L_x + d_x \sin \varphi - \lambda} \quad (5-7)$$

Hence, by designing the AWG with a large internal optical path length difference ΔL_x a small FSR $\Delta\lambda_{FSR,m}$ and a high order m can be achieved. The angular dispersion characteristics for various orders m are illustrated in Fig. 5-2.

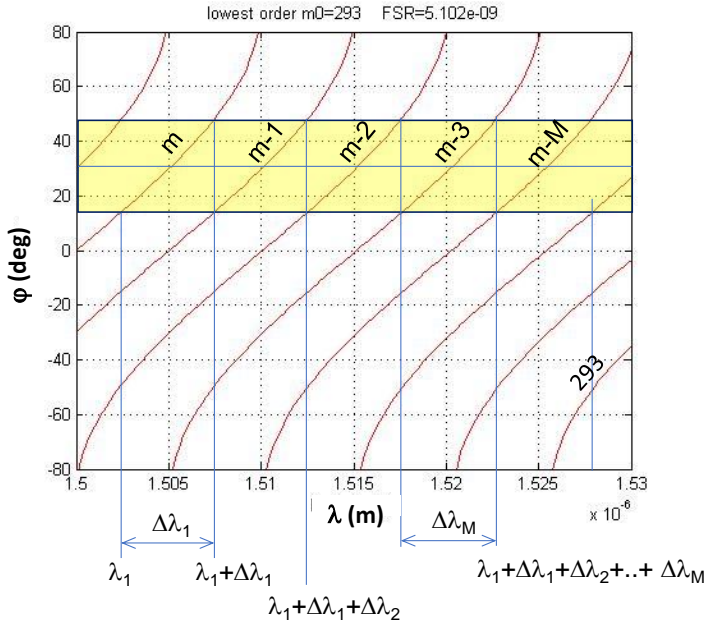


Fig. 5-2 Diffraction angle φ vs. wavelength for arrayed waveguide grating operating in high orders (with $\Delta L_x=450\mu\text{m}$, $d_x=3.3\mu\text{m}$)

The angular tuning range $\Delta\varphi_m$ which is achieved in order m when tuning over one FSR from λ to $\lambda+\Delta\lambda_{FSR,m}$ is

$$\begin{aligned} \Delta\varphi_m &= \varphi(\lambda + \Delta\lambda_{FSR,m}) - \varphi(\lambda) \\ &= \arcsin\left(\frac{1}{d_x} \left(m\lambda \frac{m}{m-1} - \Delta L_x\right)\right) \\ &\quad - \arcsin\left(\frac{1}{d_x} (m\lambda - \Delta L_x)\right) \end{aligned} \quad (5-8)$$

$\Delta\varphi_m$ is largest when $\varphi(\lambda+\Delta\lambda_{FSR,m})=\pi/2$, which yields

$$\cos \Delta\varphi_{m,max} = 1 - \frac{1}{m} \left(1 + \frac{\Delta L_x}{d_x} \right) \tag{5-9}$$

E.g., with $\Delta L_x=450\mu\text{m}$, $d_x=3.3\mu\text{m}$ and $\lambda=1.5\mu\text{m}$, an order $m\approx 300$ is achieved and an FSR $\Delta\lambda_{FSR,m} \approx 5\text{nm}$ with a maximum angular tuning range $\Delta\varphi_{m,max} \approx 56.9$ deg.

An alternative solution for obtaining a small FSR and high order m is the VIPA – Virtually Imaged Phased Array [2][3], which relies on multi-beam interference generated by two reflective sides of a parallel plate as shown in Fig. 5-3. Interference maxima occur in the angular direction φ_o which satisfies the VIPA equation [2]

$$m \lambda = 2 n_v t \cos(\varphi_i - \varphi_o) \tag{5-10}$$

where φ_i is the angle of incidence on the VIPA and n_v the refractive index of the medium in the VIPA cavity. The interference order m is approximately equal to twice the optical thickness of the plate (i.e. $2n_v t$) divided by the wavelength λ , hence a high order m can be achieved at reasonable plate thickness.

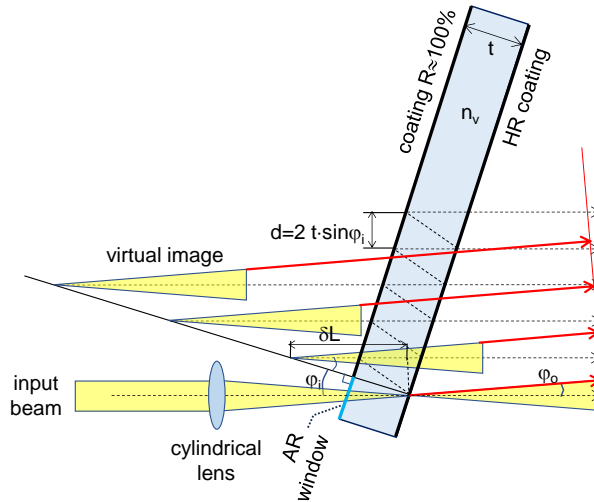


Fig. 5-3 Virtually Imaged Phased Array (HR: coating with high reflection (≥95%); AR: anti-reflection coating)

The angular tuning range $\Delta\varphi_o$ when tuning in order m over one FSR from λ to $\lambda+\Delta\lambda_{FSR,m}$ is (with $m \geq 2$)

$$\begin{aligned}\Delta\varphi_{o,m} &= \varphi_o(\lambda + \Delta\lambda_{FSR,m}) - \varphi_o(\lambda) \\ &= \arccos\left(\frac{\lambda}{2n_v t} \cdot m\right) - \arccos\left(\frac{\lambda}{2n_v t} \frac{m^2}{m-1}\right)\end{aligned}\quad (5-11)$$

The maximum $\Delta\varphi_o$ in order m is achieved when $m^2\lambda = 2n_v t (m-1)$, i.e. when $\varphi_o(\lambda + \Delta\lambda_{FSR,m}) = \varphi_i$, and is

$$\Delta\varphi_{o,m_max} = \arccos\left(1 - \frac{1}{m}\right)\quad (5-12)$$

Hence the maximum angular tuning range decays for large order m , e.g. for $m=300$ we find $\Delta\varphi_{o,m_max}=4.68^\circ$, and for $m=800$ $\Delta\varphi_{o,m_max}=2.87^\circ$.

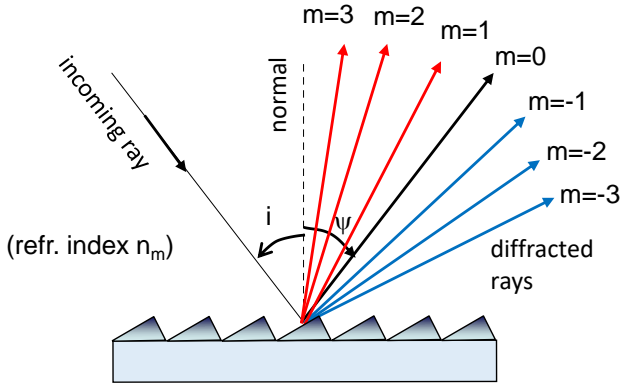


Fig. 5-4 Reflection grating operating in various orders m

For the element with low diffractive power and large FSR (larger than the total wavelength tuning range $\Delta\lambda_{tun}$), a diffraction grating operating in a lower order can be used as shown in Fig. 5-4. According to the well-known grating equation (see [1], and section 3.6.2)

$$\sin\psi + \sin i = \frac{m\lambda}{n_m d}\quad (5-13)$$

where d is the groove spacing and n_m the refractive index of the outside medium, the achievable order m (an integer) is bounded by (where for $x>0$ the function $\lceil x \rceil$ rounds x up to the largest integer smaller than x , and the function $\lfloor x \rfloor$ rounds $x>0$ down to the smallest integer larger than x)

$$\left\lceil \frac{n_m d}{\lambda} (\sin\theta_i - 1) \right\rceil \leq m \leq \left\lfloor \frac{n_m d}{\lambda} (\sin i + 1) \right\rfloor\quad (5-14)$$

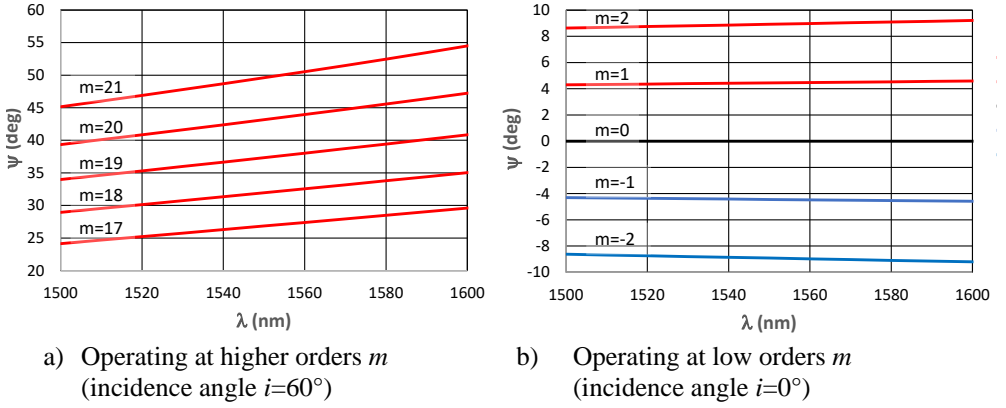


Fig. 5-5 Diffraction angle ψ vs. wavelength λ for reflection grating operating in various orders m (grating with 50 grooves/mm)

The Free Spectral Range (FSR) in order m is the wavelength range $\Delta\lambda_{FSR,m}$ with which at incident angle i the wavelength λ can be increased to arrive in the neighbour order $m-1$ at the same diffraction angle ψ . Hence, as illustrated in Fig. 5-5.a it follows with eq. (5-13)

$$\begin{aligned} m\lambda &= (m-1)(\lambda + \Delta\lambda_{FSR}) \\ \Delta\lambda_{FSR} &= \frac{\lambda}{m-1} \quad \text{for } m \geq 2 \end{aligned} \quad (5-15)$$

For $m \leq -1$ holds (cf. Fig. 5-5.b)

$$\Delta\lambda_{FSR} = \frac{\lambda}{|m-1|} \quad (5-16)$$

The angular tuning range $\Delta\psi_m$ achieved when tuning over one FSR in order m (with $m \geq 2$) from λ to $\lambda + \Delta\lambda_{FSR,m}$ is

$$\begin{aligned} \Delta\psi_m &= \psi(\lambda + \Delta\lambda_{FSR,m}) - \psi(\lambda) \\ &= \arcsin\left(\frac{m(\lambda + \Delta\lambda_{FSR,m})}{nd} - \sin i\right) - \arcsin\left(\frac{m\lambda}{nd} - \sin i\right) \end{aligned} \quad (5-17)$$

$\Delta\psi_m$ is maximum when $\psi_m(\lambda + \Delta\lambda_{FSR,m}) = \pi/2$, which implies

$$\cos \Delta\psi_{m,max} = 1 - \frac{m}{m-1} \frac{\lambda}{d} \quad (5-18)$$

Moreover, $\psi_m(\lambda + \Delta\lambda_{FSR,m}) = \pi/2$ also implies $\sin \theta_t = \lambda/d (m^2/(m-1)) - 1$. As $\sin \theta_t \leq 1$, this yields an upper bound for the attainable $\Delta\psi_{m,max}$ given by

$$\cos \Delta\psi_{m,max} \geq 1 - \frac{2}{m} \quad (5-19)$$

To satisfy the two bounds for $\cos \Delta\psi_{m,max}$ yields for the maximum order m_{max}

$$m_{max} = \left\lfloor \frac{d}{\lambda} \left(1 - \sqrt{1 - \frac{2\lambda}{d}} \right) \right\rfloor \quad (5-20)$$

where the function $\lfloor x \rfloor$ rounds $x > 0$ down to the largest integer smaller than x . As shown in Table 5-1, when deploying a maximum wavelength tuning range $\Delta\lambda_{tun} = 100\text{nm}$ (from $\lambda=1.5$ to $1.6\mu\text{m}$), the maximum attainable angular tuning range $\Delta\psi_{max}$ is 28.36° , which can be achieved with a reflection grating of $N=75$ grooves/mm at a large incidence angle of $i = 66.93^\circ$.

Table 5-1 Maximum angular tuning range $\Delta\psi_{m,max}$ using a reflection grating with N grooves/mm, achieved at $\lambda=1500\text{nm}$ over a tuning range $\Delta\lambda_{tun}$ for the maximum order m_{max} and incidence angle i

N (gr/mm)	$\Delta\psi_{m,max}$ (deg)	order m_{max}	tuning range $\Delta\lambda_{tun}$ (nm)	i (deg)	$\Delta\psi_{m,max}$ bound (deg)
50	22,80	25	63	72,39	23,07
55	23,97	23	68	79,66	24,07
60	25,11	21	75	79,90	25,21
65	26,22	19	83	72,83	26,53
70	27,32	17	94	63,71	28,07
75	28,36	16	100	66,93	28,96
80	29,37	15	107	68,21	29,93

For the overall crossed-gratings structure, using the proposed arrayed waveguide structure for grating 1, it can be derived that the two-dimensional angular diffracted intensity pattern I as a function of wavelength λ and the orthogonal angles φ and ψ when assuming a 2D AWG matrix of isotropically radiating apertures is [4]

$$I(\varphi, \psi, \lambda) = I_0 \left[\frac{\sin \left(M \frac{\pi d_y}{\lambda} (\sin \psi - \sin i) \right)}{\sin \left(\frac{\pi d_y}{\lambda} (\sin \psi - \sin i) \right)} \right]^2 \left[\frac{\sin \left(N \frac{\pi}{\lambda} (d_x \sin \varphi + \Delta L_x) \right)}{\sin \left(\frac{\pi}{\lambda} (d_x \sin \varphi + \Delta L_x) \right)} \right]^2 \quad (5-21)$$

where i is the angle of incidence on the reflection grating 2, d_y is the groove spacing and M is the effective number of grooves of this grating; N is the effective number of waveguides in the arrayed waveguide grating 1, and d_x is the spacing

between the emitting endfaces of the waveguides in this grating. Fig. 5-6 shows by simulation results how the pencil beam can be steered across a (x,y) -plane on the floor of the room, where x and y are expressed in units as fraction of the height H of the room (assuming that the PRA is mounted on the ceiling; $x/H=\tan \psi$ and $y/H=\tan \varphi$, see Fig. 4-3). The parameters assumed for the waveguide grating 1 are $N=50$, $d_x=6\mu\text{m}$, and $\Delta L_x=450\mu\text{m}$ (yielding a $\Delta\lambda_{\text{FSR1}}=5\text{nm}$). For grating 2 we choose a ruled Echelle grating (in Littrow mount) with $i=75\text{deg.}$, $M=50$, and $d_y=12.05\mu\text{m}$ (83 grooves/mm). The wavelength λ of the pencil beam was stepwise tuned from $\lambda=1.504\mu\text{m}$ to $1.574\mu\text{m}$, with a step size of 0.2nm , so over a wavelength range covering 14 times $\Delta\lambda_{\text{FSR1}}$. Fig. 5-6 illustrates how area coverage by 2D beam steering deploying only simple λ -tuning can be achieved: angular coverage over $21^\circ\times 20^\circ$, which with $H=2.5\text{m}$ corresponds to a room area of $0.96\times 0.92\text{m}^2$ in the (x,y) plane. The beam spots are elliptical with a longer axis in the ψ -direction than in the φ -direction, which is due to the higher angular dispersion $d\varphi/d\lambda$ of the AWG.

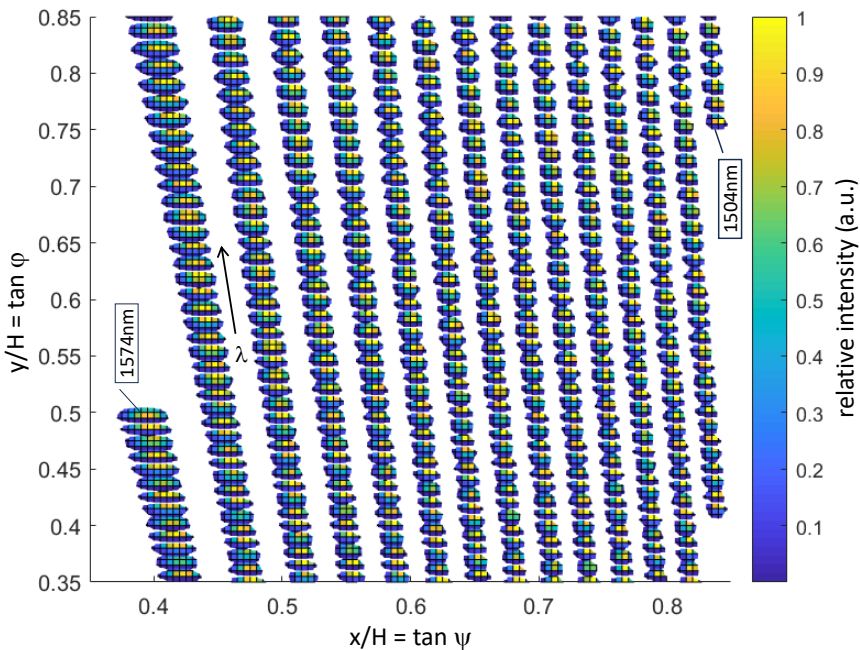


Fig. 5-6 2D scanning by λ -tuning of the room area (λ -step size 0.2 nm)

5.2.2 System experiments

As shown in Fig. 5-7, a laboratory system setup has been built for 2D beam steering deploying an echelle reflection grating with 13.3 grooves/mm operating in order $m=95$ at an incidence angle of 80.7° and wavelength $\lambda=1550\text{nm}$, followed by a transmission grating with 1000 grooves/mm operating in $m=1$ and incidence angle of 49.9° . The optical carrier is generated by a Keysight laser providing 13dBm output power tunable from $\lambda=1505\text{nm}$ to 1630nm . It is followed by an MZI external modulator having 6 to 8dB loss driven by a Keysight 20GHz bandwidth 65GS/s arbitrary waveform generator (AWG). After a polarization controller, via a triplet lens collimator with focal length $f=18.4\text{mm}$ a pencil beam with 3.3mm beam waist diameter and up to 6dBm power is launched onto the crossed grating pair. Three silver-coated mirrors are used to fold the path of 3m total length. At the receiver side, a second lens collimator captures the beam, and signal analysis takes place with a real-time oscilloscope to observe the eye pattern and to analyze the BER. This second lens collimator needs to be aligned very carefully with respect to the first one in two angular dimensions, due to its very small field of view (only 0.034 degrees full angle). Total path losses in the link between the lens collimators are measured to be $\leq 6.15\text{dB}$ for $\lambda=1518$ to 1600nm , which is 9.85dB less than in our previous setups with two reflection gratings reported in [4] and [6]. These path losses are mainly due to the losses of the two gratings; the three silver-coated mirrors contribute a reflection loss of only 0.11dB each.

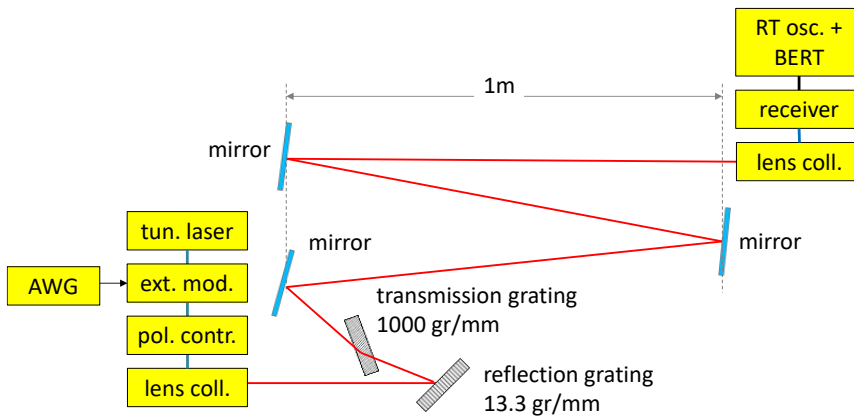


Fig. 5-7 2D beam-steered system experiment

Fig. 5-8 shows the calculated 2D-steered beam positions when λ is varied from 1505 to 1630nm, for which the order of the echelle grating varies from $m=98$ to 90, corresponding to the 9 scanning lines shown. Received optical powers measured in the encircled spots were between -0.15 and 1.2dBm. Angular

tuning over 6° in the φ -range and 12° in the ψ -range is achieved. The dispersion of the two gratings together with the limited aperture of the receiver collimator sets the spectral passband of the pencil beam channel. Using the broadband ASE of an EDFA, the -3dB passband width was found to be 10.35GHz , as shown in Fig. 5-9.

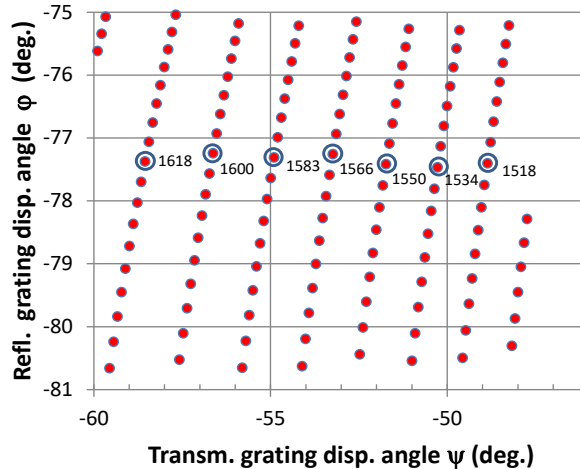


Fig. 5-8 2D beam scanning (simulated; encircled spots were measured at the wavelengths indicated)

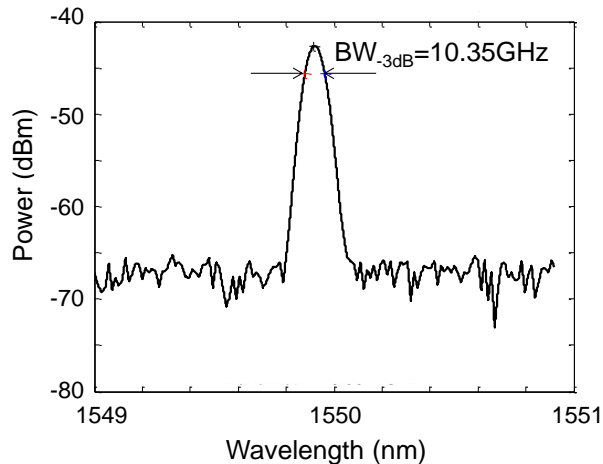


Fig. 5-9 Spectral characteristics of the 2D-steered pencil beam channel

System BER measurements were done at $\lambda=1520\text{nm}$ and $\lambda=1550\text{nm}$. With PAM-4 modulation, we have achieved 32Gbit/s transmission at $\text{BER} < 4 \times 10^{-3}$ (i.e. below the HD-FEC (Hard-Decision Forward Error Correction) limit [5]). A simple

10GHz bandwidth receiver without extra equalization is used. Pre-distortion is applied at the AWG to spectrally shape the overall transmission channel. The BER performances of the link at $\lambda=1520\text{nm}$ and $\lambda=1550\text{nm}$ are shown in Fig. 5-10 for PAM-4 symbol rates from 12 to 16GBaud, both for the back-to-back scenario (i.e. connecting the fiber of the transmitting lens collimator directly to the fiber after the receiving lens collimator) and for the scenario including the free-space beam link. With respect to back-to-back measurements, at 16GBaud power penalties were 1.21dB at $\lambda=1520\text{nm}$ and 2.07dB at $\lambda=1550\text{nm}$. The respective eye patterns are shown in Fig. 5-11.

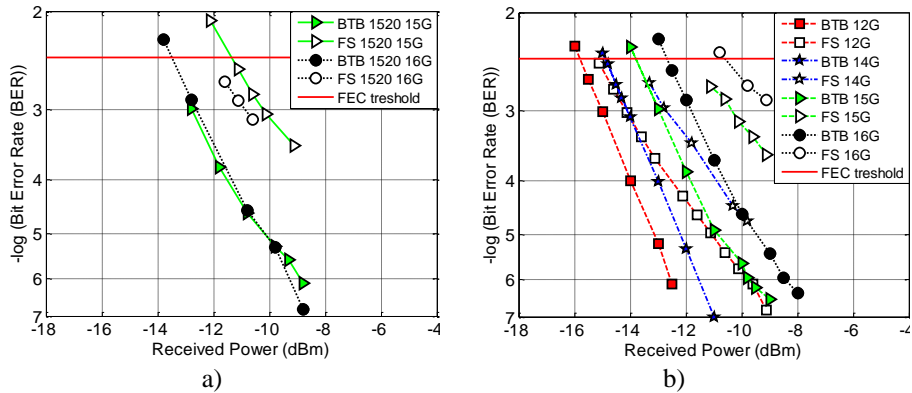


Fig. 5-10 BER performance of back-to-back and free-space link at a) $\lambda=1520\text{nm}$ for 15 and 16GBaud PAM-4, and at b) $\lambda=1550\text{nm}$ for 12 to 16GBaud PAM-4

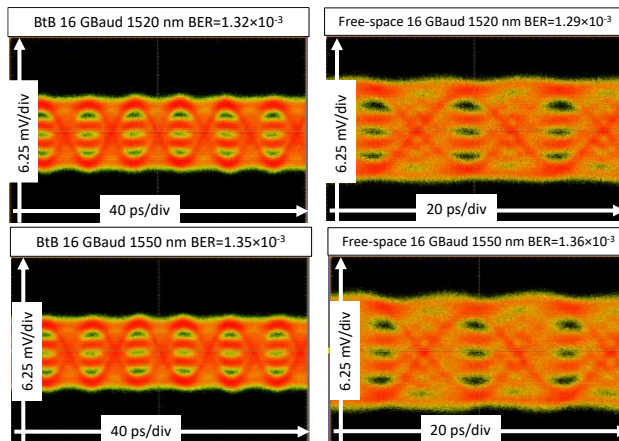


Fig. 5-11 Received PAM-4 eye patterns at 16GBaud, measured in back-to-back and in the free-space pencil beam link at $\lambda=1520\text{nm}$ (top row) and $\lambda=1550\text{nm}$ (bottom row)

In our previous system setup with two reflection gratings [6], we achieved transmission of 42.8Gbit/s using discrete multitone modulation (DMT) with 512 tones and adaptive bitloading per tone. A maximum loading of 7 bits/symbol (QAM-128) was observed, decreasing to 1 bit/symbol at the edge of the passband of the pencil beam channel. Excluding DMT overhead, the net transmitted data rate was 37.3Gbit/s. With respect to the DMT solution, the PAM-4 solution requires much less signal processing and thus offers the benefit of a much simpler receiver structure at the user's device. It also offers less power consumption and lower latency [7].

5.2.3 Concluding remarks

Free-space optical communication deploying 2D steerable narrow optical pencil beams can offer the ultimate wireless capacity per user device. The proposed concept employs a pair of passive crossed diffractive elements which enables scaling to large numbers of pencil beams, each individually steerable by tuning its wavelength in the 1.5 μ m infrared regime. Angular beam steering over a 6 $^\circ$ x12 $^\circ$ area (i.e. an area of 32x64cm² at 3m distance) was achieved by wavelength tuning from 1505 to 1630nm. Further careful design of the diffractive stages augmented by angular magnification using a lens system is needed to increase the area coverage. The efficiency of a reflection grating typically depends on the polarization state of the incident light; hence, some polarization control of the light carried by the input fiber (or the use of polarization-maintaining fiber in the feeder network) may be needed.

Downstream delivery of 32Gbit/s per optical pencil beam in the 1.5-1.6 μ m range over 3m reach using PAM-4 modulation with a simple free-space receiver has been demonstrated. With adaptive DMT modulation using 512 tones, a 42.8Gbit/s gross bitrate has been achieved.

5.3 2D diffractive beam steerer using an AWGR and 2D fiber array¹⁰

In section 5.2, we have proposed and explored an arrangement with two cross-aligned diffraction gratings, which provides 2D beam steering by wavelength tuning [4] [20]. The beam steering follows a line-by-line scanning process, where by increasing the wavelength the beam's footprint runs smoothly along a horizontal line, but at the end of that line makes a stepwise jump to the next line. For this, one of the gratings needs to operate in multiple high interference orders, and the other one in a single low order. The full wavelength tuning range

¹⁰ This section is largely based on A.M.J. Koonen, F. Gomez-Agis, F.M. Huijskens, and K.A. Mekonnen, "High-capacity optical wireless communication using two-dimensional IR beam steering," *J. Lightw. Technol.*, vol. 36, no. 19, pp. 4486–4493, Oct. 2018. It is also based on patent PCT/EP2017/080716, priority date Nov. 29, 2016, "Two-dimensional optical beam steering module," by A.M.J. Koonen.

comprises several orders (each covering the so-called free spectral range, FSR) of the high-order grating, but at most only one order of the low-order grating. This setup requires highly efficient gratings with low polarization dependency, and careful highly stable mechanical adjustment of these gratings.

As an alternative approach which requires less alignment effort and does not have a dependency on the polarization state of the incoming signals, we propose the beam steering module concept shown in Fig. 5-12 [23][24]. It uses arrayed waveguide grating router (AWGR) modules which are readily available commercially, primarily for deployment in fiber-based communication networks. The $N \times M$ output fibers of the AWGR are arranged in an $N \times M$ 2D fiber array, which is put in the object plane of a lens. The position of a fiber in the object plane determines in which 2D direction its corresponding beam is emitted after the lens. For operation with a wide Field-of-View (FoV), the lens should have a small f/D number and should be well corrected for having minimal off-axis lens aberrations and thus well-defined beams (e.g., a $f/0.95$ multi-element camera lens with $f=50\text{mm}$ is used in the laboratory setup; see section 5.3.2).

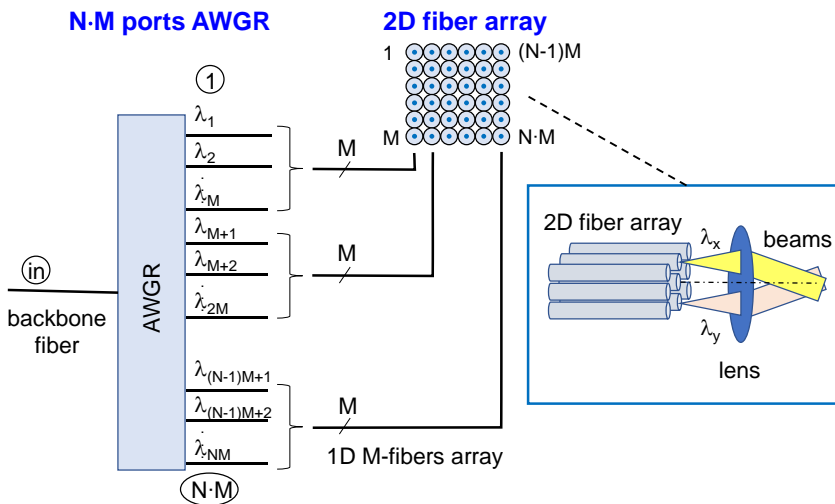


Fig. 5-12 2D steering of IR beams using a high port-count AWGR

5.3.1 Beam steerer design

By putting the fiber array in the focal plane of the lens, collimated beams will be emitted with diameter $D_0 = 2f \tan \alpha$ where $\tan \alpha = \lambda / (\pi w_0)$ with mode field radius w_0 of the single mode fiber. In the analysis paraxial geometric optics are used assuming an ideal aberration-free lens, i.e., with no Petzval field curvature. Each collimated beam creates a spot in the image plane with diameter $D_{beam} = D_0$. To cover a square image area of size $L \times L$ with no spacing between adjacent spots,

$N=M$ and the number of AWGR ports needed is $N M= M^2 = (L/D_{beam})^2$. The spacing Δy of the fibers in the 2D array needs to be $\Delta y = L / [M(b/f - 1)]$ where $f = \pi w_0 L / (2\lambda M)$ is the lens focal length, and b is the distance between the image plane and the lens. E.g., for $D_{beam} = 3\text{cm}$, $\lambda = 1.5\mu\text{m}$, $w_0 = 4.5\mu\text{m}$ (so $\tan\alpha = 0.106$), $L = 1.5\text{m}$ and room height $b = 2.5\text{m}$, we need an array of $M \times M = 2500$ fibers with $\Delta y = 1.80\text{mm}$ and $f = 14.1\text{cm}$. For a given image area, a larger spot size D_{beam} will reduce the AWGR port count needed; but obviously also requires a larger aperture at the receiver in order to assure that enough power is detected to handle the large data rate. Commercially available AWGR-s operating in C-band are typically offered with port counts up to 96. In previous experiments [23], we used an AWGR with 80 ports, so $M=9$. To cover an area of only $0.75 \times 0.75\text{m}^2$ using a spot size $D_{beam} = 8.3\text{cm}$, a large condenser lens was needed with $f = 39.3\text{cm}$ and diameter $D_{lens} = 21\text{cm}$, and fiber spacing $\Delta y = 15.5\text{mm}$ which yielded a 2D fiber array with a total size of $12.4 \times 12.4\text{cm}^2$.

The size of such rather bulky setups can be reduced significantly by a defocusing approach: when putting the fiber array out of focus and closer to the lens, the emitted beams are slightly diverging and the spot diameter D_{beam} increases. Conversely, for a given coverage area and a given acceptable spot diameter D_{beam} , defocusing results in a significantly smaller focal length f and diameter of the lens D_{lens} , and smaller spacing Δy between the fibers in the array, and thus to a significant reduction of the size of the beam steering module. The relative defocusing parameter p (with $0 \leq p < 1$) can be defined by

$$p = 1 - \frac{v}{f} \quad (5-22)$$

where the object distance between the array and the lens is given by v ; by defocusing the fiber array is moved closer to the lens by pf . In order to cover an $L \times L$ area at distance b_0 from the lens by beam spots with equal diameter D_{beam} while the spots are contiguous (so with zero spacing between them), from Fig. 5-13 using paraxial geometric optics it can be shown that the required lens focal length f , lens diameter D_{lens} , fiber spacing Δy , beam spot diameter D_{beam} as a function of distance b , beam divergence dD_{beam}/db and spacing between the centers of the spot Δy_{spot} are

$$f = \frac{1}{1-p} \left(\frac{L}{M} \frac{1}{2 \tan \alpha} - p b_0 \right) \quad (5-23)$$

$$D_{lens} = (M-1) |\Delta y| + 2f(1-p) \tan \alpha \quad (5-24)$$

$$\Delta y = 2f \tan \alpha \left(\frac{f}{b_0 - f} + p \right) = \frac{L}{M} \frac{L - 2pb_0 M \tan \alpha}{-L + 2b_0 M \tan \alpha} \quad (5-25)$$

$$D_{beam}(b) = 2 \tan \alpha \{f + p(b - f)\} \quad (5-26)$$

$$\frac{d D_{beam}(b)}{d b} = 2 p \tan \alpha \quad (5-27)$$

$$\Delta y_{spot} = \Delta y \left(\frac{b}{f} - 1 \right) \quad (5-28)$$

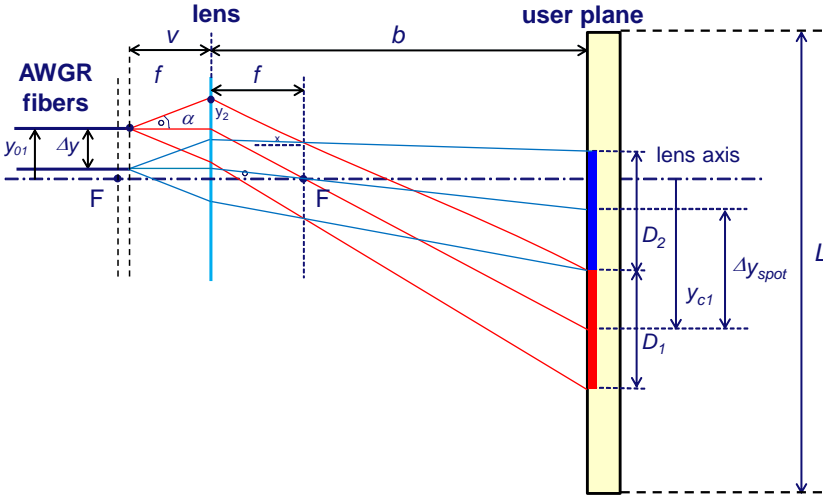


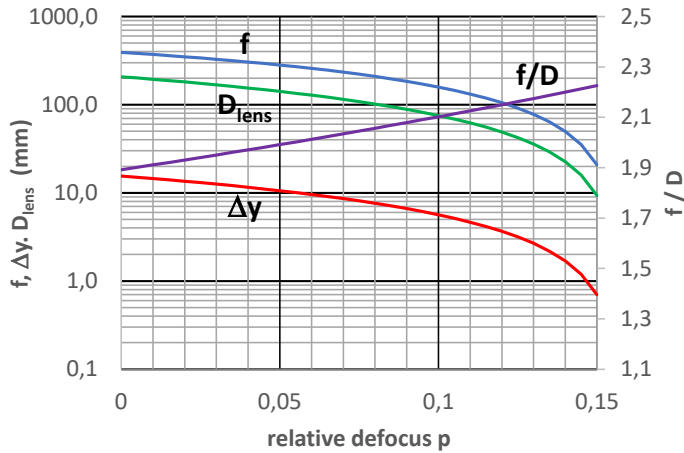
Fig. 5-13 Reducing the size of the beam steering module by defocusing the fiber array ($D_1=D_2=D_{beam}$)

In order to have well-defined spots in the user plane, the lens should have minimal field curvature errors (a.k.a. Petzval curvature [25]), hence should be well-corrected over a wide FoV. E.g., in our OWC laboratory setup we deployed a fast $f/0.95$ camera lens with $f=50\text{mm}$ having 10 elements in 7 groups, optimized for portrait photography [31].

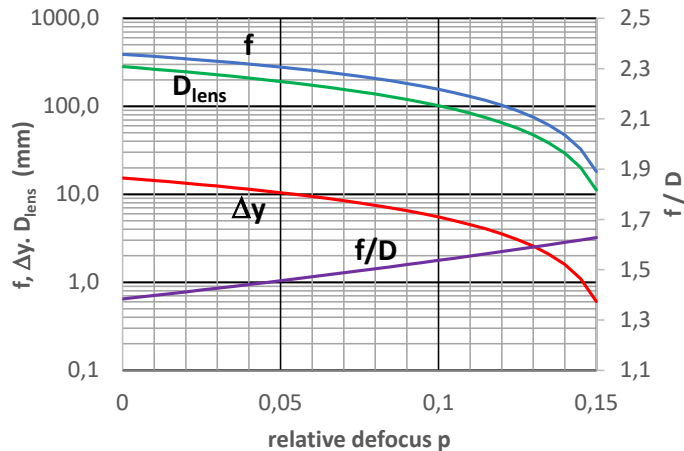
Fig. 5-14 illustrates the impact of the defocusing on the module's size. As shown in Fig. 5-14.a, for an 81 ports AWGR and coverage area of $0.75 \times 0.75\text{m}^2$ with room height $b_0=2.5\text{m}$, no defocusing (so $p=0$) yields a lens focal length $f=39.3\text{cm}$, fiber spacing $\Delta y=15.5\text{mm}$ and lens diameter $D_{lens}=20.8\text{cm}$ for a beam spot size $D_{beam}=8.3\text{cm}$ (which was used in [23] and [26] to realize a beam supporting up to 35Gbit/s OOK data transmission). However, using a defocusing of 12% (so $p=0.12$), we find $f=10.5\text{cm}$, $\Delta y=3.67\text{mm}$, and $D_{lens}=4.90\text{cm}$ only, while the spot size stays the same and hence the transmission capacity also. Clearly, defocusing can reduce the size of the beam steering module considerably without affecting the system's performance. A larger defocusing also decreases

the lens speed needed, so increases the f-number f/D : it increases from $f/D=1.83$ for no defocusing ($p=0$) to $f/D=2.15$ for $p=0.12$.

Similarly, for an AWGR with a larger port count, the coverage area can be increased while the defocusing keeps the module compact. As shown in Fig. 5-14.b: when adopting the same beam spot size $D_{beam}=8.3\text{cm}$, for a 196 ports AWGR ($M=14$) at room height $b_0=2.5\text{m}$, a $1.16\times 1.16\text{m}^2$ area can be covered with a defocusing factor $p=0.135$ yielding $f=61.2\text{mm}$, $\Delta y=2.08\text{mm}$ and $D_{lens}=3.83\text{cm}$.



a) $M=9, L=0.75\text{m}$



b) $M=14, L=1.16\text{m}$

Fig. 5-14 Reducing the module size by defocusing, when opting for a beam diameter $D_{beam}=8.3\text{cm}$ and applying a) AWGR with 81 ports ($M=9$), or b) AWGR with 196 ports ($M=14$)

Experiments in our laboratory setup with 9.5dBm transmitted beam power and at the receiver a Keplerian telescopic 10× beam compressor with an aperture diameter of 5cm have shown that a spot size $D_{beam} = 12.0\text{cm}$ allows a data transmission rate of more than 10Gbit/s in OOK modulation format. For this spot size, with $M = 14$ and $b_0 = 2.5\text{m}$ an area of $1.68 \times 1.68\text{m}^2$ (equivalent with an angular coverage of $18.6^\circ \times 18.6^\circ$) can be covered with $p = 0.21$ yielding $f = 51.2\text{mm}$, $\Delta y = 2.51\text{mm}$, and $D_{lens} = 4.12\text{cm}$ (implying an $f/D = 1.24$ number of the lens, which is readily available, e.g., for camera lenses).

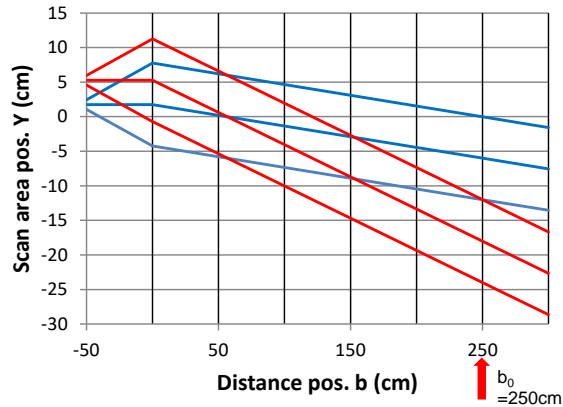
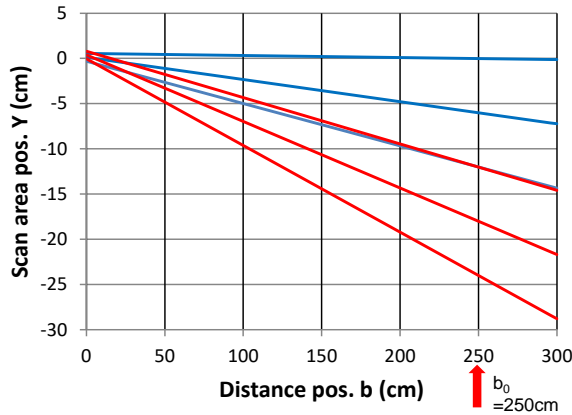
a) $p=0$ b) $p=0.21$

Fig. 5-15 Impact of defocusing on the beam profiles a) without defocusing ($p=0$) and b) with defocusing $p=0.21$. Assumption: room height $H=b_0=2.5\text{m}$.

Another advantage of the defocusing approach is the better fill factor of the covered area. Fig. 5-15 shows how the beams from two neighboring fibers each diverge when defocusing is introduced and the distance b between the lens and

the image plane increases. Without defocusing ($p = 0$) the beams are collimated and do not diverge. If the lens focal length f and fiber spacing Δy values have been set according to the equations given before for a given lens-to-image plane distance b_0 , the spots will exactly touch each other in the image plane where the distance b to the lens equals b_0 . E.g., for $b_0 = 250\text{cm}$ and spot size $D_{\text{beam}} = 12\text{cm}$, this is shown in Fig. 5-15.a for $p = 0$ where the beam's divergence $dD_{\text{beam}}/db = 0$, and in Fig. 5-15.b for $p = 0.21$ where $dD_{\text{beam}}/db = 0.0445$ (i.e. a divergence half-angle of 1.28°).

Fig. 5-16 shows how the spots are covering the image plane; herein the e^{-2} intensity contours of the Gaussian spot footprints are shown. The spots exactly touch each other when $b = b_0$, as shown in Fig. 5-16.a. In more detail, Fig. 5-17.a and .b show the coverage by beams with a uniform and with a Gaussian intensity profile, respectively, for $b = b_0$. When the image plane is moved to a larger distance from the lens (so when $b > b_0$), the spacing between the spot centers Δy_c increases ($\Delta y_c = \Delta y (b/f - 1)$). Without defocusing (i.e. $p = 0$), the beam spot diameter D_{beam} stays constant and becomes smaller than the spot spacing Δy_{spot} , hence the fill factor η (i.e. the summation of the footprint areas of all spots divided by the total coverage area) decreases when b increases (see Fig. 5-16.b). For $b < b_0$, overlap between the spots occurs (see Fig. 5-16.c). Fig. 5-17 illustrates the coverage of the user plane with a 12×12 matrix of spots from uniform beams and from Gaussian beams for $b = b_0$.

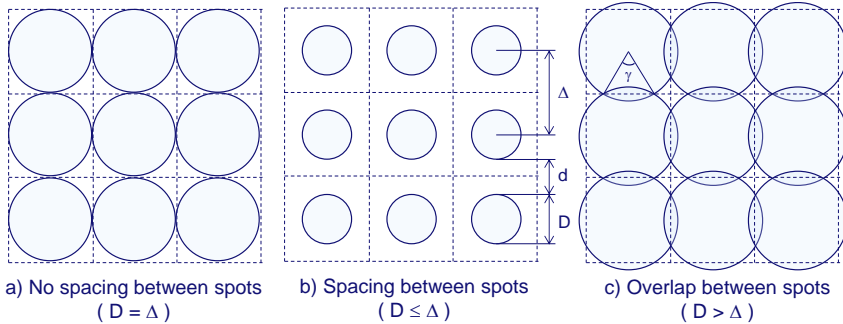


Fig. 5-16 Filling the image area by the beam spots

Fig. 5-18 shows how the beam spot diameter D_{beam} , the spacing between the beam spots Δy_{spot} , and the fill factor η evolve for a hexagonal stacking of the fibers in the 2D array when the distance b of the image plane to the lens is increased, both for the collimated-beams case ($p = 0$) and the defocused case ($p = 0.21$). The design assumptions for this were a spot diameter $D_{\text{beam}} = 12\text{cm}$ at room height $b_0 = 2.5\text{m}$, and $M = 144$ ports. Clearly by means of defocusing the dependency of the fill factor on the distance b to the lens is reduced.

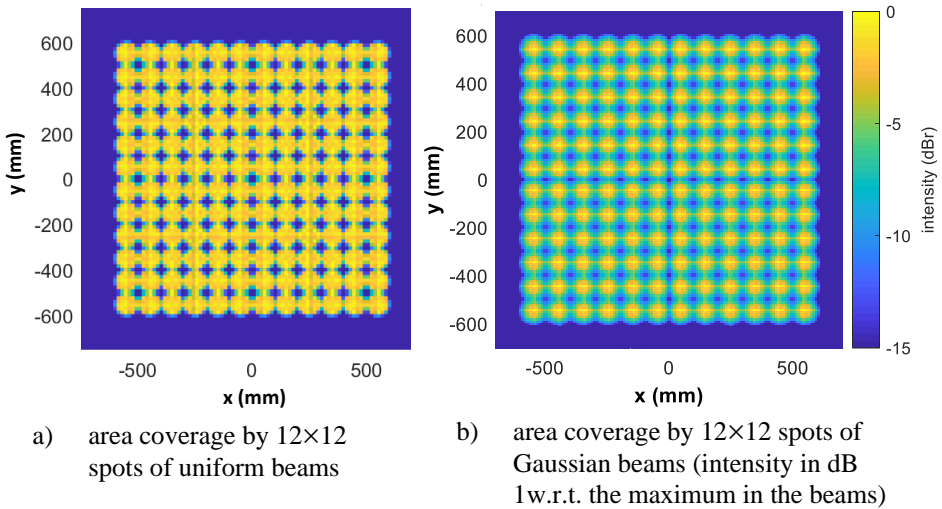


Fig. 5-17 Covering the user area by 144 beams ($\varnothing 100\text{mm}$ beam footprint, ideal aberration-free thin lens $f=50\text{mm}$, room height $H=2500\text{mm}$ (i.e., $b = b_0$; beam patterns by ray tracing, 1519 rays per beam). Note that the beams have different wavelengths.

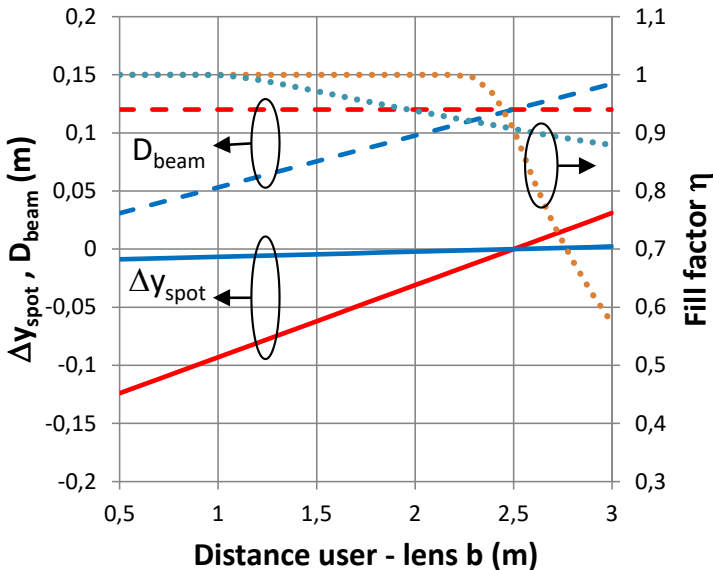


Fig. 5-18 Improving the area fill factor η by defocusing (with 12×12 uniform spots, and hexagonal fiber stacking; for beam diameter $D_{beam}=12\text{cm}$ at $b=b_0=2.5\text{m}$; beam spot spacing Δy_{spot} ; red curves: $p=0$; blue curves: $p=0.21$)

5.3.2 System experiments

Experimental demonstrations of the AWGR-based beam steering concept have shown its versatility to provide ultra-high wireless data transmission to devices individually, with capacities per beam using OOK ranging from 10Gbit/s [23] up to 35Gbit/s OOK [26], and using PAM-4 up to 112Gbit/s [27].

The first AWGR-based beam steering laboratory experiment applying defocusing is shown in Fig. 5-19 [24]. It uses a laser diode tunable from 1525 to 1580nm and emitting 0dBm optical power, a PRBS 2^{23} -1 generator of NRZ-OOK data driving a Mach Zehnder modulator (MZM), a variable optical attenuator followed by an EDFA, and a Gemfire 1×80 ports AWGR with channel center wavelengths from 1529.10 to 1569.80nm, spaced by 50GHz and -3dB channel bandwidth of 0.28nm (35GHz). For the focused case (i.e. $p = 0$), a condenser lens was needed with focal length $f = 40$ cm, diameter $D_{lens} = 20$ cm and a fiber array pitch $\Delta y = 15.0$ mm. The emitted power was 9.5dBm, i.e. below the 10dBm eye safety limit for $\lambda > 1.4\mu\text{m}$. At the receiver side, a telescopic lens system with 6cm aperture was used for beam narrowing, followed by a mid-IR filter which suppresses ambient light and passes the IR beams, and subsequently a 6mm aperture fiber collimator feeding the APD-TIA receiver via a $50\mu\text{m}$ core MMF. For the defocused case, we took $p = 0.12$, allowing a much smaller achromatic doublet lens with $f = 10.0$ cm and $D_{lens} = 50.2$ mm, and smaller fiber array with pitch $\Delta y = 3.7$ mm. NRZ-OOK data transmission at 10Gbit/s and at 20Gbit/s over 2.5m in free-space were realized, and the performance was measured for a central spot (HS-1) and a next-neighbor spot (HS-2). As shown in Fig. 5-20, the BER curves measured at 20Gbit/s for both HS-1 and HS-2 show nearly identical system performance for the focused and defocused cases, with a penalty of about 2dB with respect to back-to-back operation (due to lens aberrations and slight misalignments). Hence it can be concluded that the system performance is not reduced by the defocusing, whereas the system has become much more compact.

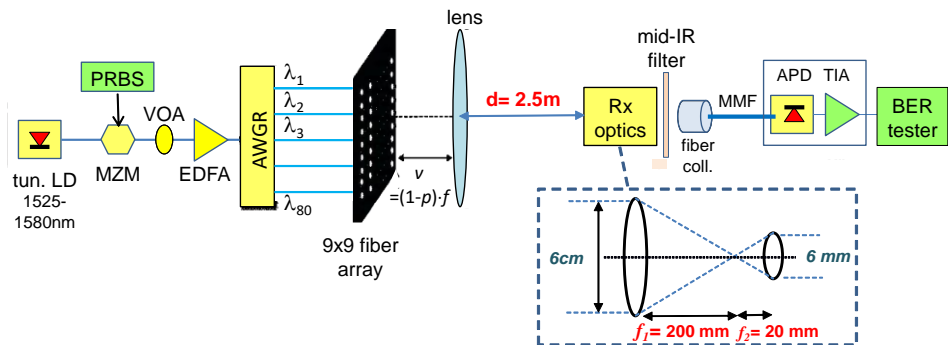


Fig. 5-19 Experimental setup applying the defocusing technique

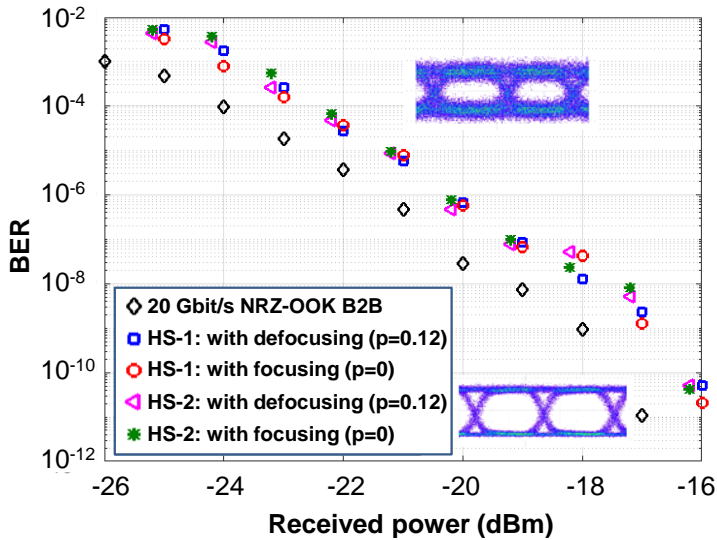


Fig. 5-20 20Gbit/s performance without and with defocusing

In a second laboratory experiment, shown in Fig. 5-21, by deploying the same AWGR 112Gbit/s transmission per beam could be achieved using PAM-4 signal modulation [27]. In order to overcome the bandwidth limitations of the AWGR (with a -3dB bandwidth of 35GHz) and of the driver electronics, digital signal processing (DSP) was applied which provided spectrum compression by coding the data into a PAM-4 format as well as further equalization. PAM-4 signals with raised-cosine 0.2 roll-off waveforms at 42GBaud and at 56GBaud were digitally generated using 19 taps and a 9-taps pre-compensation filter, and uploaded into a Keysight M8196A arbitrary waveform generator operating at 84GS/s. The output of a tunable laser was modulated by the PAM-4 signals in a single-drive 40GHz Mach-Zehnder modulator. After amplification in an EDFA, the signal is fed into the 80-ports AWGR and via the 9×9 2D fiber array and an $f = 40\text{cm}$ focal length lens with diameter of 20cm launched into free-space as a collimated beam (without defocusing, so with $p = 0$). The beam's power was +10dBm, so below the eye safety threshold. The beam's diameter was 8.5cm, and it was coupled into a receiver at a distance of 3.4m. The receiver's lens system has an aperture of 50mm and consists subsequently of a first lens with $f=50\text{mm}$, a second lens with $f=5\text{mm}$, and a third lens with $f=4.51\text{mm}$ which couples the light into a $10\mu\text{m}$ core single-mode fiber (SMF). The received power was -9.5dBm. Further optical amplification was done by a linear semiconductor optical amplifier (SOA), providing a gain of 10dB. Subsequently the signal was detected by a 70GHz PIN photodiode followed by a 35GHz RF amplifier. Alternatively, we demonstrated

recently a compact photonic integrated circuit where the light collection function by means of surface gratings was separated from the high-bandwidth detection function using a UTC photodiode with bandwidth $>67\text{GHz}$ [29]. The detected signal was digitized by an 80GS/s Keysight MSOV334A oscilloscope, followed by off-line DSP.

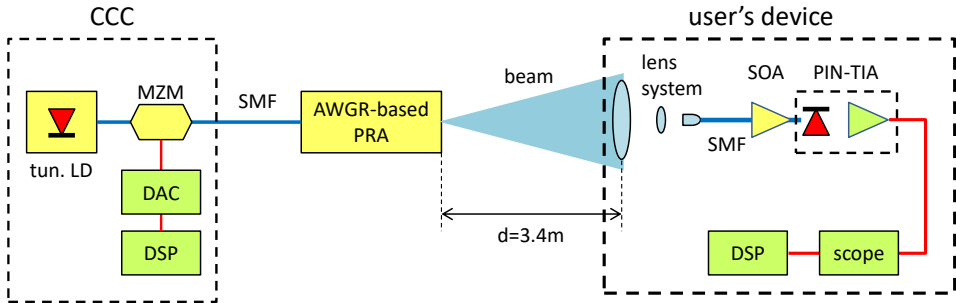


Fig. 5-21 AWGR-based beam-steered OWC system transmitting up to 112Gbit/s PAM-4 per beam

The BER performance was measured for 42GBaud PAM-4 signals (84Gbit/s) and 56Gbit/s PAM-4 signals (112Gbit/s; 100Gbit/s net after removing 12% HD-FEC overhead). The measured BER curves are shown in Fig. 5-22. At 42GBaud, for a received power of -7.5dBm the BER was $1.7 \cdot 10^{-3}$ (below the HD-FEC limit), and at 56GBaud the BER was below the HD-FEC limit for a received power of -4.5dBm (with an error floor appearing due to bandwidth limitations). In the insets of Fig. 5-22 also the clearly open PAM-4 eye patterns can be observed.

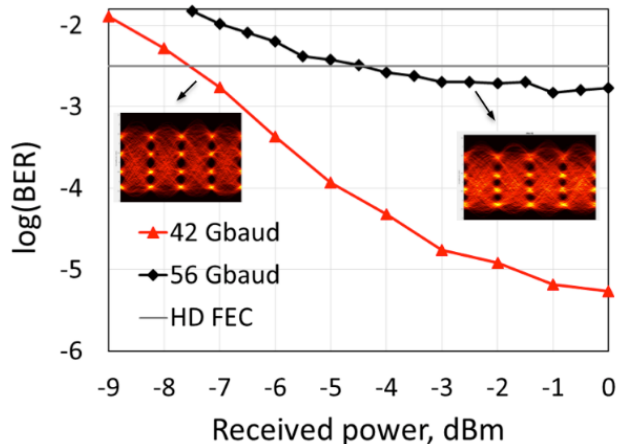


Fig. 5-22 BER performance of the received PAM-4 signals at 42 and 56GBaud

Thirdly, a demonstrator setup as shown in Fig. 5-23 has been built in our laboratory in order to provide a proof-of-concept of our AWGR-based beam-steered optical wireless communication system for the simultaneous wireless delivery of high-speed video streams. We have shown before in a bidirectional system setup 35Gbit/s NRZ-OOK downstream transmission with an 80-ports AWGR (without defocusing, so $p=0$, using a large $f=40\text{cm}$ condenser lens with 20cm diameter), and 5Gbit/s ASK upstream transmission by means of 60GHz UWB radio technology [26]. We also showed real-time 10G Ethernet transmission in TCP/IP sessions before [30]. The setup, shown in Fig. 5-23, demonstrates in downstream the delivery of two steerable IR beams each transporting a 10Gbit/s OOK signal, and in upstream a ultra-wideband (UWB) 60GHz radio channel for user localization and signalling. The IR beam-steering PRA was designed according to the design equations given in Section III for a 14×14 2D fiber array, a ceiling-to-table distance $b_0=2.5\text{m}$, and spot diameter at the table of 12cm. By choosing a defocusing parameter $p=0.21$, these design constraints yield a lens focal length $f=51.2\text{mm}$, lens diameter $D_{\text{lens}} = 41.2\text{mm}$ (so $f/D = 1.24$), and fiber spacing $\Delta y = 2.51\text{mm}$. A C-band AWGR with 96 ports was combined with an L-band AWGR with 48 ports, where the output ports have an ITU grid channel spacing of 50GHz, and a -3dB bandwidth of 35GHz and 24GHz, respectively. The output fibers were assembled into a honeycomb matrix array of 129 fiber ferrules spaced at a $\Delta y = 2.6\text{mm}$ pitch which fits into the aperture of a commercial high-speed $f=50\text{mm}$ camera lens with $f/D = 0.95$ [31]. The table area covered by the PRA when doing the 2D beam steering amounted to $1.6\times 1.6\text{m}^2$. Two optical beam receivers were employed, each equipped with a lensed collimator ($f=37.1\text{mm}$, $NA=0.24$) feeding the received signal with a power of about -16dBm via a single-mode fiber to an SFP+ transceiver capable of 10G Ethernet transmission. For the ease of use, future work will aim to create a compact dongle-type receiver equipped with a surface-illuminated photodiode directly followed by the receiver electronics, and with adequate optics to create a large angle-of-view as well as a sufficiently large aperture. The SFP+ transceivers were hosted in network interface cards (NICs) and were streaming high-definition video from two servers. One transceiver emitted at a fixed $\lambda=1559.92\text{nm}$ and thus provided a beam out of port #65 of the 2D fiber array, whereas the other transceiver was tunable across the C-band and thus provided a second steerable beam.

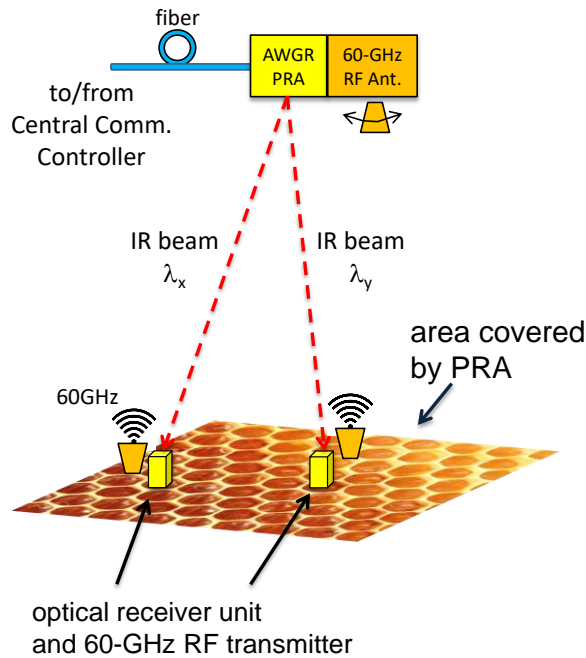


Fig. 5-23 Beam-steered OWC laboratory demonstrator

For the upstream 60GHz UWB link, the user's terminal was equipped with a horn antenna with 30dBi gain which emits towards a steerable similar horn antenna of a 60GHz RF receiver mounted next to the PRA at the ceiling (see Fig. 5-23). At this receiver, half of the received power is monitored by an RF power meter which serves as a sensor for the user localization. For this, the horn antenna is steered by a mechanical pan/tilt system, controlled by a Raspberry Pi 3 board. This board thus determines the user's coordinates and communicates these to the central communication controller (emulated on a laptop) which controls the tunable transceiver and thus closes the loop for controlling the 2D beam steering.

A photograph of this laboratory demonstrator setup is shown in Fig. 5-24, indicating the PRA, the steerable 60GHz horn antenna near the PRA, and the optical beam receiving cells on the table's surface. Fig. 5-25 shows the realized 2D array of 129 fibers, and the assembly of the fiber array with the $f = 50\text{mm}$ wide aperture camera lens. This commercially available multi-element camera lens has a high speed of $f/0.95$ [31]. It was designed basically for portrait photography, hence has very low lens aberrations and thus provides that the shape of the spots is retained even in the outer parts of the covered area. In the setup simultaneous independent transmission by two IR beams of two high-definition video streams was successfully demonstrated, each embedded in a 10G Ethernet connection and running at a video data rate of about 4.6Gbit/s.

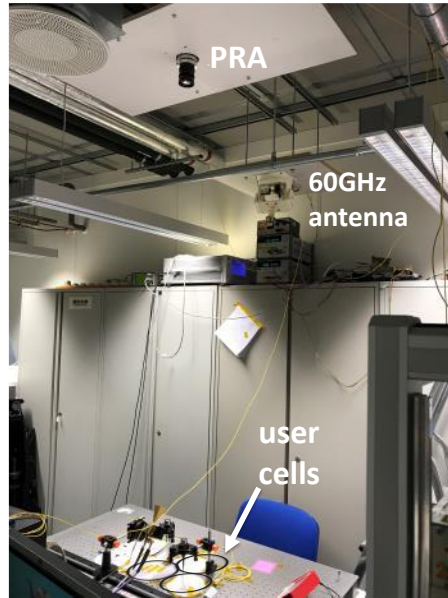


Fig. 5-24 Photo of the laboratory demonstrator

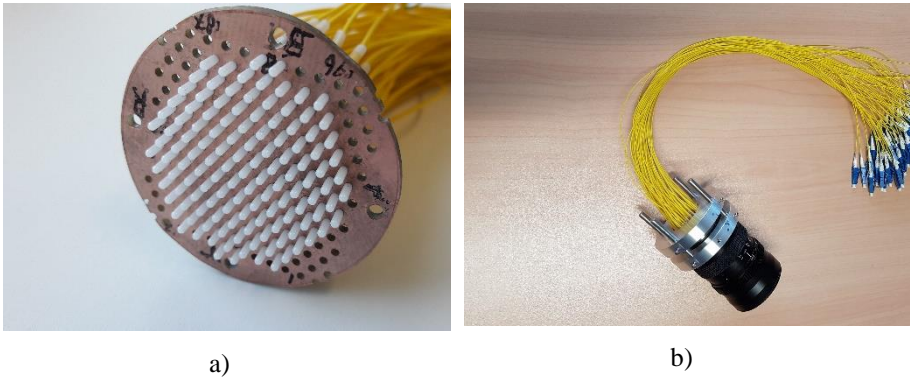


Fig. 5-25 Photos of a) 2D fiber array, and b) assembly of fiber array and camera lens

5.3.3 Concluding remarks

Based on a high port-count arrayed waveguide grating router with its output fibers arranged in a 2D array and a high-speed lens, individual wavelength-controlled 2D steering of narrow infrared beams can be realized. Thus many ultra-high capacity wireless links for high-bandwidth wireless services can be created. Capacities up to 35Gbit/s NRZ-OOK and 112Gbit/s PAM-4 per beam with a reach beyond 2.5m have been shown. With an 80-ports C-band AWGR, a total

wireless system throughput beyond 8.9Tbit/s can be achieved. By extension to a 192 ports (=96+48+48) 3-elements composite AWGR operating in C- and L-band, throughput volumes beyond 21Tbit/s become feasible. The number of ports may be doubled by operating two AWGR-s in a polarization diversity mode wherein one AWGR is fed from the feeder fiber by light signals in one linear polarization state and the other by light signals in the orthogonal linear polarization state (cf. [32]); note, however, that the polarization states in the feeder fiber need to be accurately controlled. By applying a defocusing technique, the size of the passive beam steering module is decreased considerably without affecting the system's performance. Wireless delivery of multiple high-speed ultrahigh-definition video streams by means of multiple narrow infrared beams has been shown in a laboratory proof-of-concept demonstrator. Autonomic localization of the user's devices is aided by a 60GHz UWB radio return path.

5.4 2D beam steering by mechanical translators¹¹

For establishing the upstream (US) link from each user device in a bi-directional OWC system, the use of a narrow low-power beam is preferred in order to minimize the depletion of the user's battery and to provide adequate eye safety for the (nearby) user. Moreover, preferably an arbitrary wavelength should be used for the upstream link and no diffraction-based techniques for the beam steering, in order to avoid a costly wavelength-tunable laser and associated control circuitry in the cost-sensitive user module. To capture the full power of the beam within the aperture of the US receiver, the beam should fit closely to the aperture, and continuous accurate beam steering is required. Hence, for the US beam steering we opted for a 2D translator stage which moves the output fiber of the US transmitter laterally over Δx and/or Δy with respect to the axis of the US lens 1, as shown in Fig. 5-26 ([33]; more details are given in chapter 8).

The (x,y) translator stage uses stepper motors (in linear actuator stages, e.g., [34]), driven by a controller board. It may be noted that stepper motors do not need to stay activated after the US beam alignment has been completed; this minimizes power consumption at the (typically battery-operated) user site. The effective lens aperture of the lens limits the displacement Δx to $\Delta x_{max} = \frac{1}{2} D_{lens} - f_1(1-p_1) \tan \alpha$. The achievable maximum US steering angle φ_{max} is

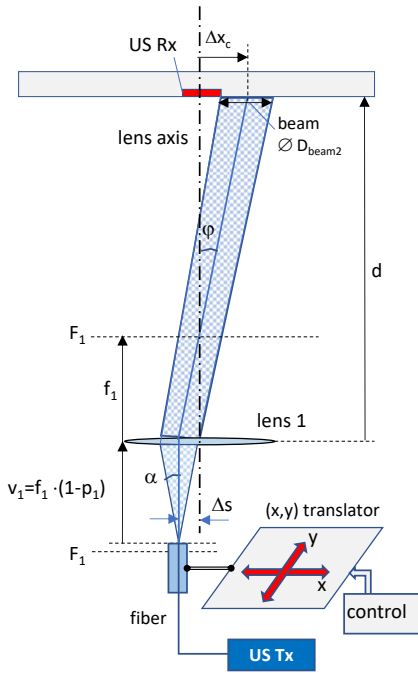
$$\varphi_{max} = \text{atan} \left[\frac{D_{lens}}{2 f_1} - (1 - p_1) \tan \alpha \right] \quad (5-29)$$

and the lateral steering resolution δx_c at the US Rx site at the ceiling is

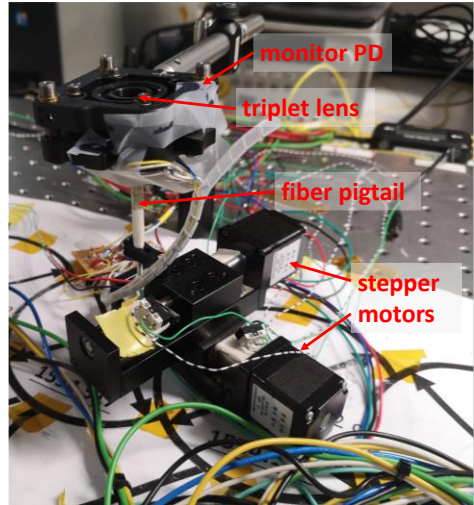
¹¹ This section is largely based on Ton Koonen, Ketemaw Addis Mekonnen, Frans Huijskens, Eduward Tangdionga, "Bi-directional all-optical wireless Gigabit Ethernet communication system using automatic self-aligned beam steering," *J. of Lightwave Technology*, Vol. 41, No. 11, June 2023, pp. 3446-3454, <https://doi.org/10.1109/JLT.2022.3231438>.

$$\delta x_c = \varepsilon_x \left(\frac{d}{f_1} - 1 \right) \tag{5-30}$$

where ε_x is the resolution of the (x,y) stepper motor stage, and d is the user-to-ceiling distance. For instance, when $d=2\text{m}$ and when using a triplet lens having a lens aperture with diameter $D_{\text{lens}1}=11.5\text{mm}$ and effective focal length $f_1=20\text{mm}$ with $p_1=0.0271$ for a US beam diameter $D_{\text{beam}2}=15\text{mm}$, and stepper resolution $\varepsilon_x=30\mu\text{m}$, the steering resolution $\delta x_c=2.97\text{mm}$ and maximum US steering angle $\varphi_{\text{max}}=10.8^\circ$ which exceeds the maximum DS steering angle of 10° as required (see section 8.3).



a) 2D US beam steerer



b) Laboratory module for 2D US beam steering, with NEMA-11 stepper motors and triplet lens $f=20\text{mm}$

Fig. 5-26 2D angular steering of US beam by means of (x,y) translator

5.4.1 Concluding remarks

By 2D mechanical translation, continuous 2D beam steering can be achieved which enables to position the upstream beam tightly within the US receiver's aperture. The upstream wavelength can be arbitrarily chosen, which allows the use of a cost-effective laser diode at the user.

5.5 Summarizing conclusions

In Table 5-2 the beam steering technologies discussed in this chapter are compared qualitatively.

Table 5-2 Comparison of beam steering technologies

Technology	Scalability of number of beams	FoV coverage	Steering speed	Active/passive module	Ref.
MEMS mirrors	low	20°×20°	low	active	[16]
SLM	low	3°×3° *	medium	active	[17][18]
2D stepper motor translator stage	not scalable	10.8°×10.8°	low	active	[33]
2D grating	high	6°×12°	high	passive	[2][20][21]
AWGR+2D fiber array	medium	17°×17°	high	passive	[23] - [28]

* 18° with lens-based angle magnifier

When using MEMS-based mirrors or an SLM, the scalability towards many beams is limited as each beam needs a separate steering element. The Field-of-View for covering the user area is relatively large when using MEMS mirrors, and small when using an SLM (but can be increased with an angular magnifier, at the expense of narrowing the beam). Both for the MEMS-based and the SLM-based steering, active electronic control at the steering module is needed, which requires a separate control line, and facilitates steering of the beam at slow/medium speed (in the order of several milliseconds).

When using the diffractive 2D grating-based concept, by remotely tuning the wavelength continuous steering of a beam is feasible in one direction and stepwise steering in the orthogonal direction. The number of beams is limited only by the resolving power of the gratings, which can be high. When the beams are carrying high-bandwidth signals, the dispersive nature of the gratings may noticeably stretch the beam spots, which may decrease the received power of a beam and cause some crosstalk with neighbouring beams. Moreover, reflection gratings may exhibit a performance dependent on the polarization of the incident light, in particular at larger incidence angles and smaller groove spacings, which requires control of the polarization state of the multiple light signals fed by the fiber feeder network.

When using the AWGR+2D fiber array, by remotely tuning the wavelength the beam is steered stepwise in both directions. The number of beams is limited by the number of output ports of the AWGR, which can be beyond 100. The beam steering speed is determined by the wavelength tuning speed of the laser diode.

This tuning time may be no more than a few nanoseconds for the laser diode itself; the tuning control electronics may increase that to a few microseconds. The modules according the 2D grating concept as well as the AWGR+2D fiber array concept are both passive, so do not require local powering nor maintenance. Their beam steering control is done by tuning the wavelength of a remote laser diode and does not need a separate control line (as the wavelength also carries the data signal). The polarization dependence of the performance an AWGR is typically small (polarization-dependent loss PDL<0.5dB), hence no polarization state control in the fiber feeder network is needed.

For individually steering the multiple downstream beams we have preferred the wavelength-tuned diffractive beam-steering techniques using 2D gratings or an AWGR+2D fiber array, given their high steering speed by using fast tunable laser diodes, their easy scaling and passive maintenance-free nature. Moreover, the AWGR+2D fiber array technique is not noticeably impacted by polarisation state fluctuations in the optical input signal (the polarization dependent loss (PDL) of an AWGR is typically <0.5dB; in contrast, these fluctuations can yield noticeable signal intensity variations in the 2D grating concept).

For steering the single upstream beam from each user device, diffractive beam steering is less attractive as it would need a relatively costly tunable laser diode and associated control circuitry at the cost-sensitive user module. We have preferred a 2D mechanical translator stage which moves the fiber pigtail of a laser diode with arbitrary wavelength with respect to the optical axis of a lens, and which is able to steer the upstream beam at an angle exceeding the FoV of the DS receiver (ca. $\pm 10^\circ$ half-angle, see section 7.4).

5.6 References

- [1] M. Born, E. Wolf, Principles of Optics, Pergamon Press, 1970.
- [2] T. Chan, E. Myslivets, J.E. Ford, "2-Dimensional beamsteering using dispersive deflectors and wavelength tuning," *Optics Express*, Vol. 16, No. 19, Sep. 2008, pp. 14617-14628.
- [3] M. Shirasaki, "Large angular dispersion by a virtually imaged phased array and its application to a wavelength demultiplexer," *Optics Letters*, Vol. 21, No. 5, Mar. 1996, pp. 366-368.
- [4] A.M.J. Koonen, C.W. Oh, E. Tangdionga, "Reconfigurable free-space optical indoor network using multiple pencil beam steering," in *Proc. OECC/ACOFT 2014*, Melbourne, July 2014, paper Tu3F-1.
- [5] Forward Error Correction (FEC): a primer on the essential element for optical transmission interoperability [on-line] Available: <https://www.cablelabs.com/blog/forward-error-correction-fec-a-primer-on-the-essential-element-for-optical-transmission-interoperability>
- [6] C.W. Oh, E. Tangdionga, A.M.J. Koonen, "42.8 Gbit/s indoor optical wireless communication with 2-dimensional optical beamsteering", in *Proc. of OFC 2015*, Los Angeles, March 22-26, 2015, paper M2F.3.

-
- [7] J.L. Wei, J.D. Ingham, D.G. Cunningham, R.V. Penty, I. White, I. (2012). "Performance and Power Dissipation Comparisons Between 28 Gb/s NRZ, PAM, CAP and Optical OFDM Systems for Data Communication Applications," *IEEE/OSA J. Lightw. Technol.*, vol. 30, no. 20, Sep. 2012, pp. 3273–3280.
- [8] A.M.J. Koonen, "Indoor optical wireless systems: technology, trends, and applications," *J. Lightw. Technol.*, vol. 36, no. 8, Apr. 2018, pp. 1459-1467. DOI 10.1109/JLT.2017.2787614.
- [9] A.M.J. Koonen, "Optical wireless systems: technology, trends and applications," webinar IEEE Phot. Soc., Feb. 21, 2018, <https://www.photonicsociety.org/education-careers/webinars/optical-wireless-communication-webinar>
- [10] H. Haas, "Visible light communication," in *Proc. OFC2015*, Los Angeles, March 22-26, 2015, paper Tu2G.5.
- [11] A.M. Khalid, et al., "1-Gb/s transmission over a phosphorescent white LED by using rate-adaptive discrete multitone modulation," *IEEE Photon. J.*, vol. 4, no. 5, pp. 1465–1473, Oct. 2012.
- [12] X. Huang, S.Chen, Z. Wang, J.Shi, Y. Wang, J. Xiao, N. Chi, "2.0-Gb/s Visible light link based on adaptive bit allocation OFDM of a single phosphorescent white LED," *IEEE Phot. J.*, vol. 7, no. 5, Oct. 2015, DOI: 0.1109/JPHOT.2015.2480541.
- [13] Nan Chi, et al., "High speed LED based visible light communication for 5G wireless backhaul," in *Proc. IEEE Summer Top.*, Newport Beach, CA, USA, Jul. 11, 2016, paper MC1.2.
- [14] A.M.J. Koonen, F. Gomez-Agis, Z. Cao, K.A. Mekonnen, F.M. Huijskens, E. Tangdiongga, "Indoor ultra-high capacity optical wireless communication using steerable infrared beams," in *Proc. MWP2017*, Beijing, Oct. 2017, keynote paper.
- [15] 2017. [Online]. Available: https://en.wikipedia.org/wiki/Laser_safety
- [16] K. Wang, A. Nirmalathas, C. Lim, K. Alameh, and E. Skafidas, "Full-duplex gigabit indoor optical wireless communication system with CAP modulation," *IEEE Photon. Technol. Lett.*, vol. 28, no. 7, Apr. 2016, pp. 790-793. (doi:10.1109/LPT.2015.2514102)
- [17] A. Gomez, K. Shi, C. Quintana, M. Sato, G. Faulkner, B.C. Thomsen, and D.C. O'Brien, "Beyond 100-Gb/s indoor wide field-of-view optical wireless communications," *Phot. Technol. Lett.*, vol. 27, no. 4, Feb. 2015, pp. 367-370. (doi:10.1109/LPT.2014.2374995)
- [18] A. Gomez, C. Quintana, G. Faulkner, D.C. O'Brien, 2016 "Point-to-multipoint holographic beamsteering techniques for indoor optical wireless communications," *Proc. of SPIE 9772*, paper no. 97720Q. Bellingham,WA. (doi:10.1117/12.2213252)
- [19] Yaqoob Z, Arain MA, Riza NA. 2003 High-speed two-dimensional laser scanner based on Bragg gratings stored in photothermorefractive glass. *Appl. Opt.* Vol. 42, 5251–5262. (doi:10.1364/AO.42.005251)
- [20] A.M.J. Koonen, C.W. Oh, K. Mekonnen, Z. Cao, E. Tangdiongga, "Ultra-high capacity indoor optical wireless communication using 2D-steered pencil beams," *IEEE/OSA J. of Lightw. Technol.*, vol. 34, no. 20, Oct. 2016, pp 4802-4809. (doi:10.1109/JLT.2016.2574855)

- [21] C.W. Oh, E. Tangdiongga, A.M.J. Koonen, “42.8 Gbit/s indoor optical wireless communication with 2-dimensional optical beamsteering”, in *Proc. OFC2015*, Los Angeles, March 22-26, 2015, paper M2F.3.
- [22] K.A. Mekonnen et al, “PIC-enabled dynamic bidirectional indoor network employing optical wireless and millimeter-wave radio techniques,” in *Proc. ECOC2015*, Düsseldorf, Sep. 2016, paper W.1.E.3.
- [23] A.M. Khalid et al, “10 Gbps indoor optical wireless communication employing 2D passive beam steering based on arrayed waveguide gratings,” in *Proc. IEEE Summ. Top. 2016*, Newport Beach, July 2016, paper TuC2.3.
- [24] A.M.J. Koonen et al., “High-capacity optical wireless communication using AWG router for 2-dimensional IR beam steering,” in *Proc. OECC2017*, Singapore, July 31 – Aug.4, 2017, paper 1-4K-3.
- [25] Petzval field curvature [on-line]. Available: https://en.wikipedia.org/wiki/Petzval_field_curvature
- [26] A.M. Khalid, P. Baltus, R. van Dommele, K.A. Mekonnen, Z. Cao, C.W. Oh, M. Matters, A.M.J. Koonen, “Bi-directional 35-Gbit/s 2D beam steered optical wireless downlink and 5-Gbit/s localized 60-GHz communication uplink for hybrid indoor wireless systems,” in *Proc. OFC2017*, Los Angeles, Mar. 2017, paper Th1E.6.
- [27] F. Gomez-Agis, S. P. van der Heide, C. M. Okonkwo, E. Tangdiongga and A. M. J. Koonen, “112 Gbit/s transmission in a 2D beam steering AWG-based optical wireless communication system”, in *Proc. ECOC2017*, Göteborg, Sweden, Sept. 17-21, 2017, paper Th.2.B.1. (doi:10.1109/ECOC.2017.8346059)
- [28] A.M.J. Koonen, F. Gomez-Agis, F.M. Huijskens, and K.A. Mekonnen, “High-capacity optical wireless communication using two-dimensional IR beam steering,” *IEEE/OSA J. of Lightw. Technol.*, vol. 36, no. 19, pp. 4486–4493, Oct. 2018. (doi:10.1109/JLT.2018.2834374)
- [29] Z. Cao, et al., “200 Gbps OOK transmission over an indoor optical wireless link enabled by an integrated cascaded aperture optical receiver,” in *Proc. OFC2017*, Los Angeles, Mar. 2017, paper PDP Th5A.6.
- [30] A.M. Khalid, M. Torres Vega, K.A. Mekonnen, Z. Cao, A. Liotta, A.M.J. Koonen, “Real time 10Gb-ethernet transmission over 2D indoor passive beam steered optical wireless system based on high port arrayed waveguide gratings”, in *Proc. ECOC2016*, Düsseldorf, Sep. 2016, paper W.4.P1.SC4.40.
- [31] Fast $f/0.95$ camera lens with $f=50\text{mm}$ [on-line]. Available: <https://www.slrmagic.com/product-page/hyperprime-50mm-t0-95>
- [32] X. Zhang, C. Li, Y. Jiao, H. v. d. Boom, E. Tangdiongga, Z. Cao, and A.M.J. Koonen. “Crosstalk-mitigated AWGR-based 2-D IR beam-steered indoor optical wireless communication system with a high spatial resolution.”, *J. of Lightw. Technol.*, Vol. 37, No. 15, Aug. 2019 , pp. 3713-3722(2019).
- [33] Ton Koonen, Ketemaw Addis Mekonnen, Frans Huijskens, Eduward Tangdiongga, “Bi-directional all-optical wireless Gigabit Ethernet communication system using automatic self-aligned beam steering,” *J. of Lightw. Technol.*, Vol. 41, No. 11, June 2023, pp. 3446-3454. (<https://doi.org/10.1109/JLT.2022.3231438>)

- [34] <https://www.helixlinear.com/Products/Linear-Actuators/PRA-Linear-Actuators/Profile-Rail-Linear-Actuator-PRA-11S-039~PRA-11S-039> [online]

6 User localization

6.1 Introduction ¹²

A powerful option for short-reach optical wireless communication is to use narrow infrared optical beams, as introduced in Ch. 2. These beams need to be accurately steered to the users and give each user an unshared personal wireless channel which can readily carry multiple Gbit/s [2]. Systems have been reported which steer the beams with MEMS mirrors [16] or other mechanical translator stages such as (x,y) steppers moving the optical source in combination with a lens system [4], or with spatial light modulators [5]. In these systems, each beam needs a separate steering element which has to be controlled over a control channel. We reported the steering of narrow IR beams by means of a passive diffractive module based on a pair of crossed gratings, or on an arrayed waveguide router with 2-dimensionally arranged output fiber array [2]. Each beam is two-dimensionally steered by just changing its wavelength remotely in the associated transmitter. Thus, the beam's wavelength acts as both the carrier of the data and as the control channel, so the control channel is embedded in the data channel and no separate control channel is needed.

For appropriately directing the narrow IR beams, the location of the user device needs to be known accurately. Various device localization techniques employing RF signals emitted or processed by the user have been reported, using triangular algorithms such as RSS (received signal strength), AoA (angle of arrival), and TDoA (time difference of arrival) [7]. Also, device localization techniques employing VLC signals have been reported, using multiple luminaires and signal processing at the user device [8]. Localization by means of a camera which determines the position of user devices by observing active LED tags on them has been reported in [9]. High localization accuracies within a few mm have been achieved. However, in each of these techniques there is a need for active functions in the user device, which draws extra power from the mobile device and thus compromises its battery lifetime.

In this chapter, we first propose a novel concept for localization of the users' devices and accordingly align the downstream beams to them while building on

¹² Sections 6.1 to 6.3 are largely based on A.M.J. Koonen, K.A. Mekonnen, F.M. Huijskens, N.-Q. Pham, Z. Cao, E. Tangdionga, "Fully passive user localization for beam-steered high-capacity optical wireless communication system," *J. Lightw. Technol.*, vol. 38, no. 10, pp. 2842-2848, May 2020.

our high-capacity IR beam-steered OWC system [10][11]. The concept is based on optical retro-reflectors, which are passive means reflecting incident light in the direction it came from. The 2D downstream beam steering is done by diffractive means and wavelength tuning of each beam's signal, and the steering takes place in discrete steps (cf. the AWGR beam steerer, section 5.3). The downstream beams typically have a footprint exceeding considerably the aperture of the user's device, in order to enable the coverage of a large area with a limited number of discretely steerable beams. The concept only requires a simple fully passive function at each user's device (namely a ring of miniature retro-reflectors), thus not draining the device's battery.

Second, we propose a novel concept for localizing the upstream receiver in the ceiling unit in order to accurately align the upstream beams. It also is based on applying passive retro-reflector means at the object to be localized, i.e. the upstream receiver. The 2D upstream beam steering is done with (x,y) stepper motor stages which enable analog beam steering. These beams preferably have a footprint smaller than the upstream receiver's aperture, which allows low-power upstream beams in order to save the user's battery and to provide adequate eye safety near to the user.

The use of retro-reflection means provides calibration of the localization which is inherently aligned with the steering of the signal beam, as we use the beam for localization as well. This avoids bookkeeping of the localization information versus the steering information, and avoids parallax errors which may occur when localization and steering are separated. We have validated both localization concepts in laboratory system experiments in which multiple high-definition video streams were carried by narrow infrared beams.

6.2 Localization in an indoor beam-steered system

Our indoor beam-steered OWC system concept has been introduced in Ch. 4, and is shown in Fig. 6-1. The (Fiber-to-the Home, FttH) access network is terminated at the entry of the house in a central communication unit, and from there the services are routed to the individual rooms by a fiber network. At the ceiling of each room, pencil beam radiating antennas (PRAs) launch the narrow IR beams to the respective mobile devices. A PRA is fully passive and contains optical diffractive elements which two-dimensionally direct each beam into a direction determined by the signal's wavelength. We have explored two options for implementing such a PRA, as introduced in section 3.6 [2]: by means of a pair of orthogonally-crossed diffraction gratings (see Fig. 4-2.a), and alternatively by means of an arrayed waveguide grating router (AWGR) with a high number of output fiber ports arranged in a 2D fiber array which is put in front of a lens (see Fig. 4-2.b). Both options use diffraction techniques to map the one-dimensional tuning of the beams' wavelengths to the two-dimensional positions in the area

where the user devices are located. This 1D-to-2D mapping implies discrete steps in the beam steering. In the crossed-gratings beam steerer, there is continuous beam steering when steering along a line by tuning the wavelength within a period of the small-FSR grating, and the steering makes discrete steps to the next lines when tuning to the next one of the FSR periods (see section 5.2). In the AWGR-based beam steerer, each incoming wavelength is by the AWGR routed to a specific fiber in this array, with its specific position with respect to the lens, and therefore after the lens is emitted as a beam into a specific direction (see section 5.3, and [10]). As shown in Fig. 5-13, the 2D fiber array is preferably positioned closer to the lens than the lens' focal plane, which yields slightly diverging beams ([10], section 5.3.1). This defocusing yields a more compact PRA module, and a coverage of the user plane which is less dependent on the user's distance to the lens. From the design condition that neighbouring beam spots in the image plane should touch each other for optimum coverage of the user area, and given a desired spot diameter required for adequate received power by the detector's optical aperture, the lens' focal length f and the fiber pitch Δy in the 2D fiber array can be calculated.

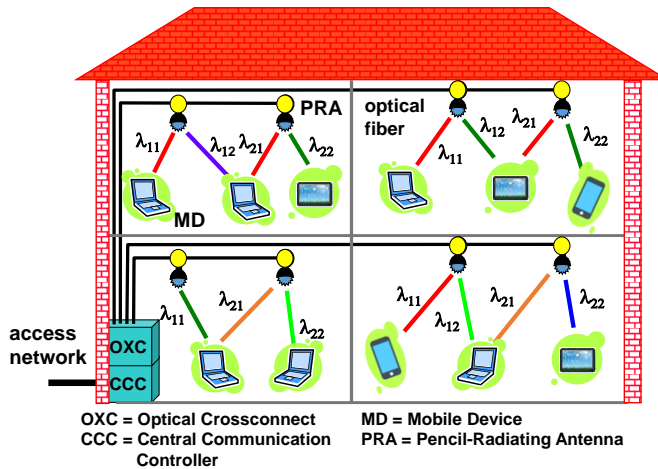


Fig. 6-1 Beam-steered indoor OWC system

In our hybrid OWC system demonstrator with downstream optical wireless links and upstream RF wireless links reported in [10], we deployed the AWGR-based PRA. Device localization was done by means of a 60GHz beam which was sent by the mobile device and was found by a scanning horn antenna positioned next to the PRA. Reading the mechanical 2D angular coordinates of this scanning antenna enabled to discover the (x,y) position of the user device, and subsequently the IR beam's wavelength was tuned such that the beam was pinpointed accurately to the device. Obviously, sending of the 60GHz beam draws power from the device's battery.

We also have reported device localization by means of a camera mounted at the ceiling which can observe the room and localize multiple user devices simultaneously [12]. Each user device has four visible LED tags surrounding its receiving optical aperture. These tags blink in a specific sequence which acts as the ID of that device, and for this operation have to draw some power from the battery of the user’s device. After processing the images captured by the camera and subsequently having determined the position coordinates of the devices, these positions have to be mapped and calibrated to the specific wavelengths which direct the beams to those locations. A localization accuracy of less than 5mm over a reach of 3m was achieved.

6.3 Localization when using discrete diffractive beam steering

To enable localization of the user’s device without drawing power from it, we explored how to equip the device with passive means for that, in particular a passive retroreflector based on an optical corner cube (CC) [11]. A CC reflects light rays in the same direction as they came from, but there is a displacement between incoming and reflected rays, as is analysed for the 2-dimensional case in Fig. 6-2 The magnitude of this displacement Δ is dependent on the entry point of the incoming ray into the CC, and on the incident angle α with respect to the main axis of the CC. The maximum displacement Δ_{max} is proportional to the entry aperture D of the CC; for the 2D case shown in Fig. 6-2, it follows that

$$\begin{aligned} \Delta &= 2h = 2L \sin(\pi/4 - \alpha) \leq D \sqrt{2} \sin(\pi/4 - \alpha) \\ &= \Delta_{max} \end{aligned} \tag{6-1}$$

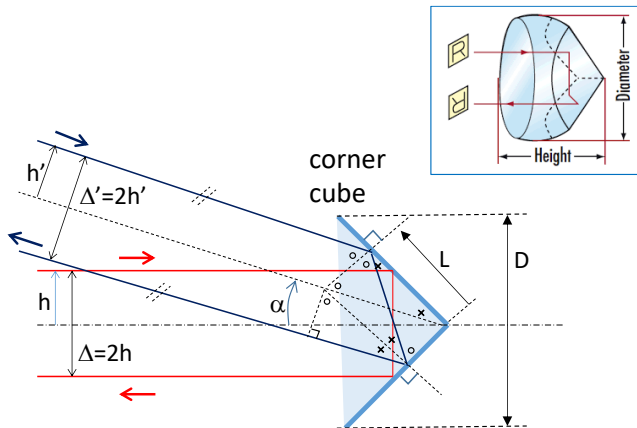


Fig. 6-2 Ray paths in optical corner cube reflector (inset: 3D view)

For the 3-dimensional case, a similar but more complicated analysis also shows a displacement which depends on the ray's entry point, and which decreases linearly with the CC's aperture D .

As illustrated in Fig. 6-3, a retro-reflecting CC mounted on the user device's OWC receiver will direct part of the incoming narrow IR beam back to the PRA, into the AWGR output port it came from. From the AWGR's input port, the reflected signal is subsequently returned to the central site, where via an optical circulator it is monitored in the localization processor. This processor is controlling the wavelength of the tunable laser diode. The device localization process begins by a command from the localization processor to the tunable laser diode to start scanning the room with an IR beam by sweeping its wavelength. As soon as the processor detects a returning reflected signal, it halts and stores the actual wavelength of the tunable laser, and thus has found and stored the location of the user device. The laser is then set to this wavelength, and by the correspondingly steered IR beam the system has established a high-speed wireless communication link to the user. In this way, the localization is self-calibrating: the device position is directly mapped to the wavelength needed for directing the beam, and no separate calibration is needed.

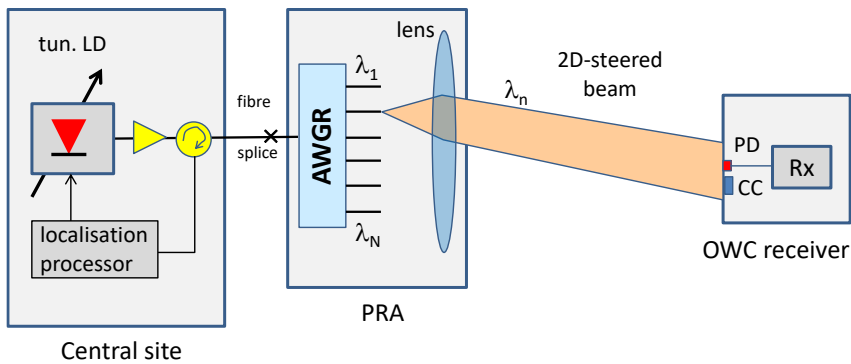


Fig. 6-3 Localising the user's OWC receiver by means of a retro-reflecting corner cube (CC)

6.3.1 Matrix of miniature corner cubes

As reported before [10], to achieve a compact design of the PRA it is required to position the 2D fiber array of the AWGR outputs not in the focal plane of the lens, but a bit closer to it; i.e. to introduce an amount of defocusing $p=1 - v/f > 0$ (see Fig. 5-13). Next to a reduction of the PRA's size, this defocusing yields a slight divergence of the beams, which improves the coverage of the user plane and makes the coverage less dependent on the actual distance to the lens; this relaxes the device mobility requirements. But the defocusing makes that the displaced beam returning from the CC may not end in the same fiber port as where

it came from. In a 2D analysis according to Fig. 6-4 and assuming an ideal thin lens (hence without field curvature), at the fiber plane this lateral offset δ of the returning beam is

$$\delta = \frac{f - v}{f} \frac{\Delta}{\cos \alpha} \leq p D_{CC} (1 - \tan|\alpha|) \quad (6-2)$$

To minimize this offset issue, it is preferred that the displacement Δ is minimized, and therefore the aperture D_{CC} of the CC is minimized. But this implies that only a very small fraction of the beam is retro-reflected, which compromises the detection process. We therefore opted to apply not a single small CC, but a matrix of many miniature CC-s. Such CC arrays are readily available in retro-reflecting foils; these are commercially available and are widely used already, e.g. for road signage. We acquired such a foil containing a fine pattern of miniature molded CC-s (from Orafol [13]); Fig. 6-5 shows a microscopic view of its structure; the diameter of a CC in it is about $100\mu\text{m}$.

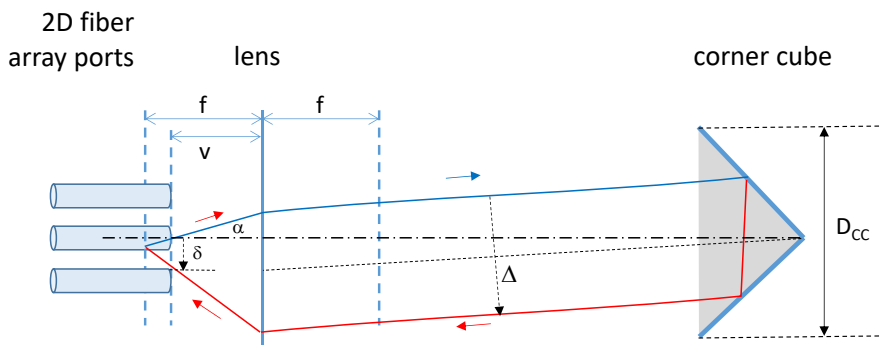


Fig. 6-4 Operating the retro-reflecting CC with a defocused PRA

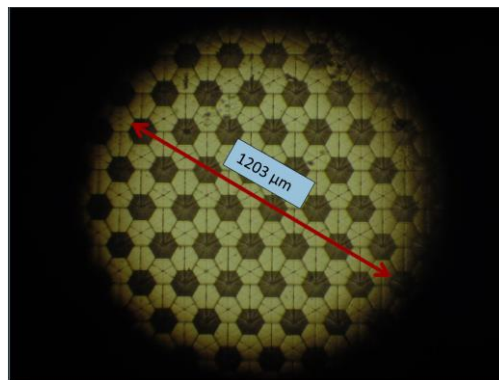
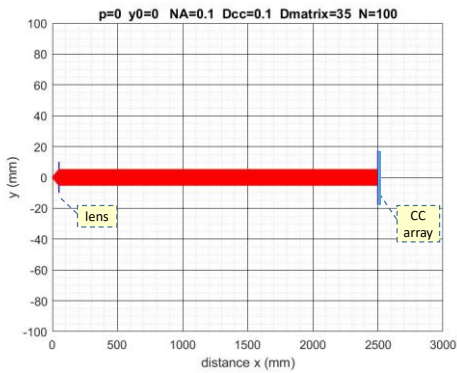
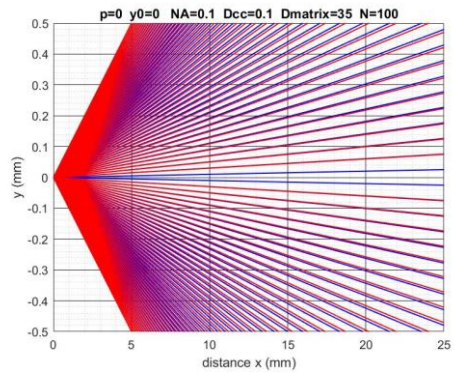


Fig. 6-5 Foil with many miniature corner cubes, each with a diameter of $100\mu\text{m}$ (from Orafol)

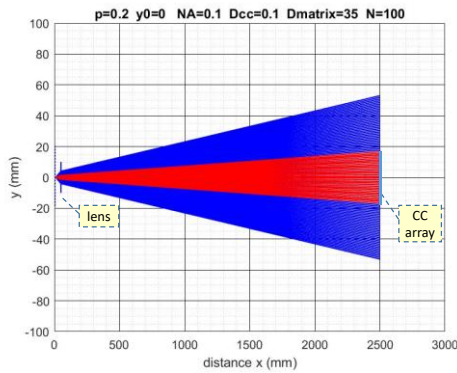
With 2D ray tracing implemented in MATLAB, the impact of defocusing on the lateral offset δ when applying a matrix of CC-s has been assessed. A lens with focal length $f=50\text{mm}$ and negligible aberrations was assumed, and a CC matrix foil with diameter of 35mm . In the system design for indoor application, a distance lens-CC matrix $b=2.5\text{m}$ was assumed. With a fiber $NA=0.1$, the beam diameter at the CC matrix was about 10mm when the 2D fiber array is in focus (so $p=0$), and 108mm when the 2D fiber array is 20% defocussed ($p=0.2$). Fig. 6-6 shows the ray tracing results; the blue rays are running towards the CC matrix, and the red rays are returning from the CC matrix. The impact of the CC diameter has been analysed by considering CC-s with diameter $D_{CC}=100\mu\text{m}$ and $=1\text{mm}$. No lateral offset occurs when the 2D fiber array is in focus ($p=0$); Fig. 6-6.a shows the collimated beam for the whole lens-to-CC matrix link, and Fig. 6-6.b the situation at the endface of a fiber in the 2D array. But when defocussing is introduced, e.g. $p=0.2$, a lateral offset δ occurs which is about 20% of the CC's diameter. Fig. 6-6.c shows the diverging beam for the lens-to-CC matrix link for $D_{CC}=100\mu\text{m}$. Only a part of the beam falls onto the CC matrix (with diameter 35mm) and is returned (red rays); the remainder of the beam is not returned. Fig. 6-6.d shows the lateral offset of the returning rays at the fiber endface in a zoomed-in view. Fig. 6-6.e and Fig. 6-6.f show similar ray tracings, but for $D_{CC}=1\text{mm}$. These show the clear increase in the lateral offset of the returning rays when the diameter of a CC is increased, and thus underline the need for a matrix array of miniature CC-s.



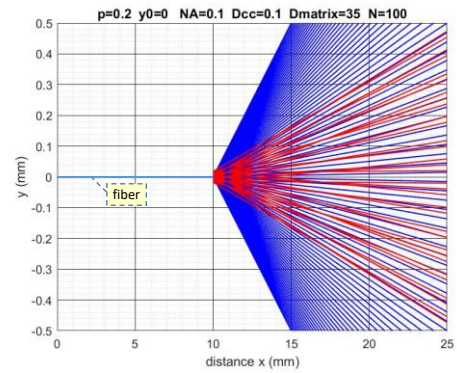
a) Focused ($p=0$), CC aperture $D_{CC}=100\mu\text{m}$



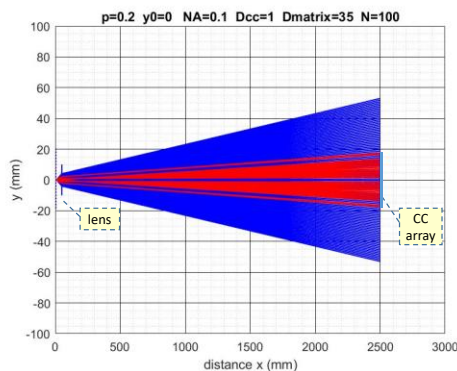
b) Focused ($p=0$), $D_{CC}=100\mu\text{m}$; zoomed-in at fiber in array



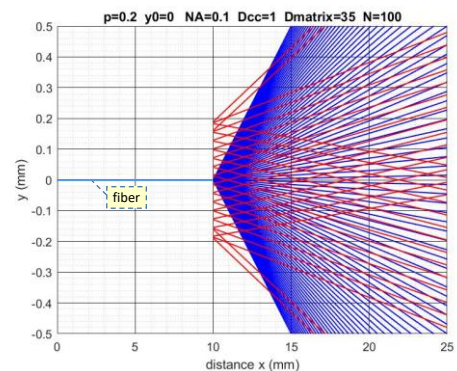
c) Defocused ($p=0.2$), CC aperture $D_{CC}=100\mu\text{m}$



d) Defocused ($p=0.2$), $D_{CC}=100\mu\text{m}$; zoomed-in at fiber in array



e) Defocused ($p=0.2$), CC aperture $D_{CC}=1\text{mm}$



f) Defocused ($p=0.2$), $D_{CC}=1\text{mm}$; zoomed-in at fiber in array

Fig. 6-6 Ray tracing with $N=100$ rays when the 2D fiber array: in a) and b) is in focus; in c) and d) is 20% defocused w.r.t. lens and CC diameter $D_{CC}=100\mu\text{m}$; in e) and f) is 20% defocused w.r.t. lens and $D_{CC}=1\text{mm}$. Blue rays are running towards the corner cube array; red rays are returning from the CC array; lens $f=50\text{mm}$, CC matrix diameter $D_{matrix}=35\text{mm}$, distance lens-to-user area $b=2.5\text{m}$.

6.3.2 System experiments

Our laboratory demonstrator setup is shown in Fig. 6-7.

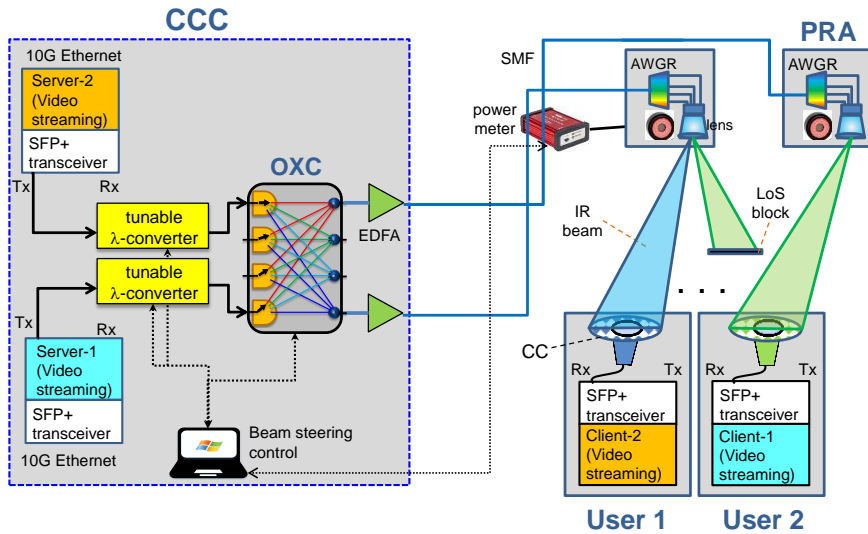


Fig. 6-7 Laboratory system demonstrator

In order to extend the area of coverage, and also in order to circumvent possible line-of-sight blockings, it features two PRA-s which can be selected by the optical cross-connect (OXC) in the central site (CCC). Equipped with a C+L band AWGR with channels spaced at 50GHz and -3dB bandwidths of 35GHz and 24GHz in the C-band and L-band, respectively, a PRA can launch up to 129 beams, each with diameter $\varnothing 10\text{cm}$, and cover a user area of about $\varnothing 1.3\text{m}$ at a reach of 2.5m. The OXC is composed of a 4x4 MEMS switch, with insertion losses of 7.0dB. In the demonstrator two user terminals are included, each equipped with a lens-based free-space optical receiver with $\varnothing 3\text{cm}$ aperture. A $\varnothing 4\text{cm}$ CC foil with a central hole of $\varnothing 3\text{cm}$ is mounted around this aperture. The physical details of the setup are shown by the photo in Fig. 6-8.

Two high-definition video streams are transmitted from the CCC, each embedded in a 10 Gbit/s Ethernet stream. The video servers are equipped with SFP+ transceivers which are operated at a fixed wavelength. The tunable wavelength converters translate these video streams to the wavelengths appropriate for the 2D beam steering to the respective user terminals by the PRAs. Each user terminal is connected to a client for receiving the video stream and displaying it on a monitor. Good real-time transmission of both video streams was achieved, with $\text{BER} < 3 \cdot 10^{-12}$ at transmitted beam power of 6.0dBm and received power levels of -19 to -23dBm.

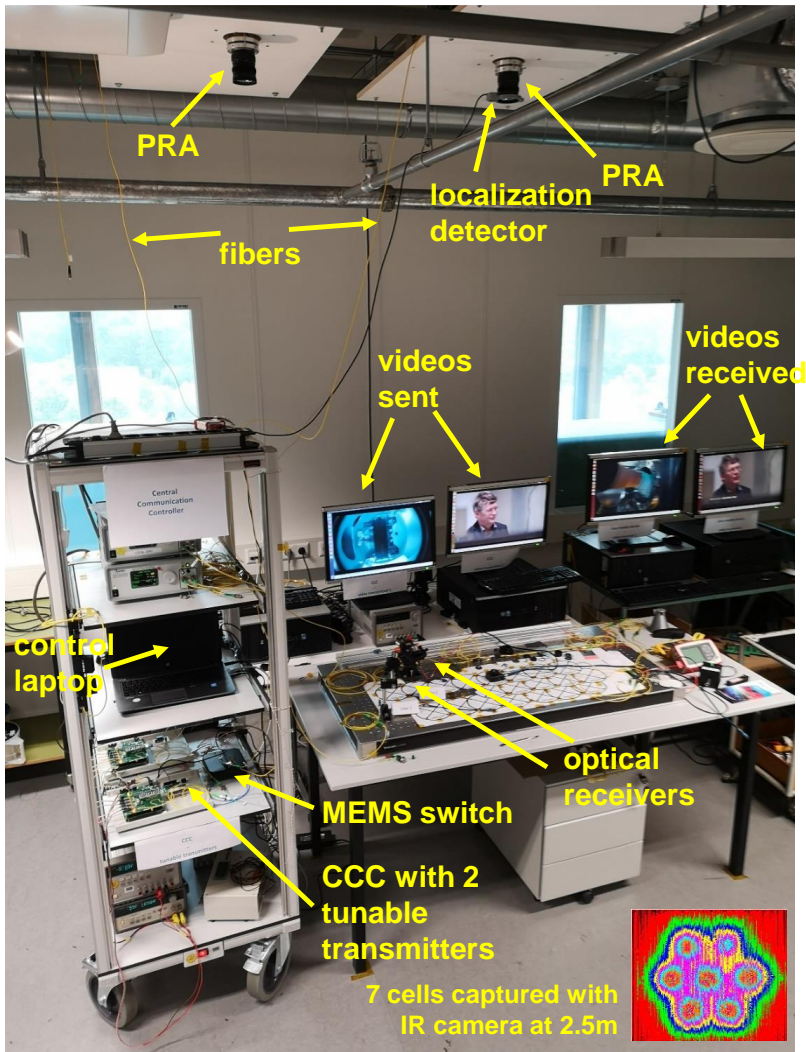


Fig. 6-8 Photo of laboratory demonstrator setup

We included the passive localization function by attaching a circular piece of Orafol foil containing the miniature CC-s on an OWC receiver, as depicted in Fig. 6-7. The photos in Fig. 6-9 show how this CC ring is retro-reflecting light in the direction it came from also when the CC ring is illuminated sideways. Due to internal optical reflections in the PRA (we used a commercial 50mm F/0.9 camera lens which was not anti-reflection coated for the $\lambda=1.5\mu\text{m}$ window, and connector joints between the 2D fiber array and the AWGR output fibers), we had to catch the returning rays by a small $\varnothing 1\text{cm}$ power detector next to the lens. The optical power launched into the wireless channel was 6dBm in all the measurements.

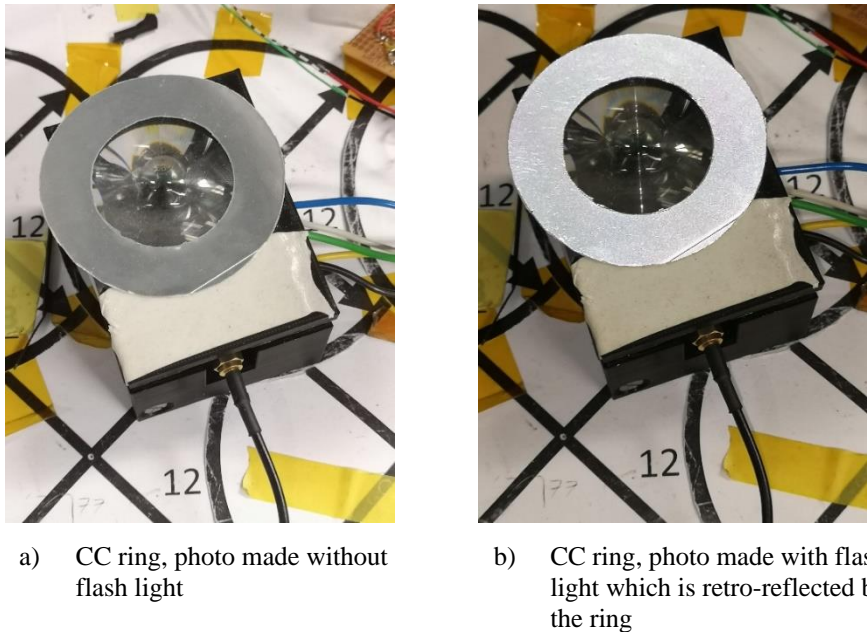


Fig. 6-9 The CC ring mounted around the lens aperture of the user's receiver

When the beam is scanning the user plane by tuning its wavelength, Fig. 6-10 shows the reflected power received by the localization detector for the case of two users, one equipped with a CC sheet with a diameter of 4cm and the other of 5cm. There is a 1-to-1 relation between the beam's wavelength and the device's position; hence the power peaks in Fig. 6-10 indicate the pico-cells where the devices are located. The height of the power peaks is related to the size of the CC sheet, as shown in Fig. 6-11. An adequate SNR > 5dB for the localization requires a CC foil diameter > 4cm. Background noise contributions are coming from the room illumination and from spurious reflections of the demonstrator table's surface. SNR values up to 15dB have been achieved, which enabled localization clearly within the required resolution of a single pico-cell (diameter 10cm). Scanning the whole user area takes about 15 s; the scan time is limited by the communication links between the power meter and the LABVIEW program running in the laptop which acts as localization processor and performs the beam steering control. The localization time is intrinsically constrained by the time needed to tune the wavelength of a laser diode over the full range for scanning the PRA's whole area, which can be done within a few milliseconds. However, the scanning process involves additional steps: the stepwise tuning to each cell consecutively, deciding whether there is retro-reflected power from that cell exceeding the background noise level, and subsequently moving to the next cell. Per cell 115ms is needed for all this, of which only a few ms is needed for the

actual laser tuning, and the majority is taken by the LabVIEW software running in the laptop controller, by the Arduino board which controls the laser tuning, and by the readout time of the localization power meter. Scanning the 129 cells in the area covered by the PRA thus takes about 15 seconds; this time may be reduced considerably by deploying more efficient algorithms implemented in embedded software.

The CC foil preferably surrounds the detector of the lens-based OWC receiver, which has an aperture of $\varnothing 3\text{cm}$. Hence, we also measured the returned localization power for a $\varnothing 4\text{cm}$ CC foil with a central hole of $\varnothing 3\text{cm}$ hosting the receiver’s detector, and a $\varnothing 4\text{cm}$ foil without hole. As shown in Fig. 6-12, the central hole caused a reduction of returned power of about 3.2dB (theoretically 3.6dB when uniformly illuminated).

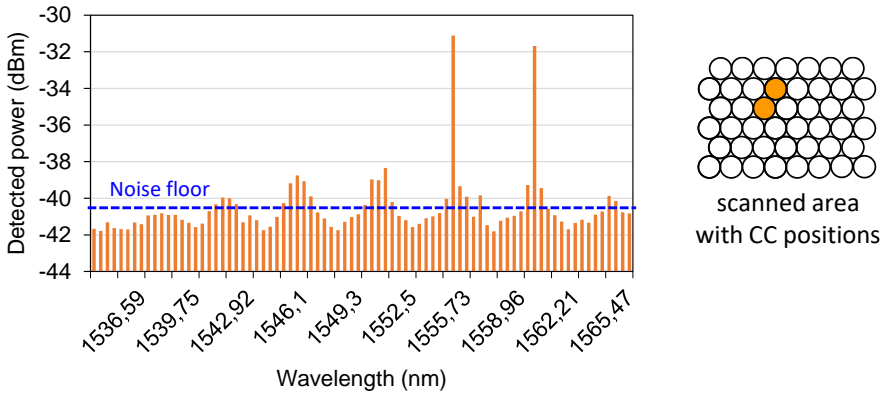


Fig. 6-10 Power received by localization detector when scanning across the system’s pico-cells (for CC sheet diameter $\varnothing 4\text{cm}$)

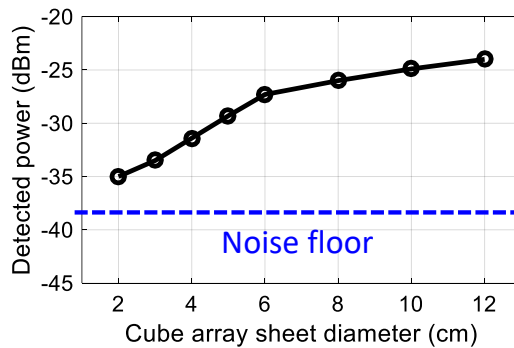


Fig. 6-11 Detected peak localization power vs. diameter of circular CC sheet

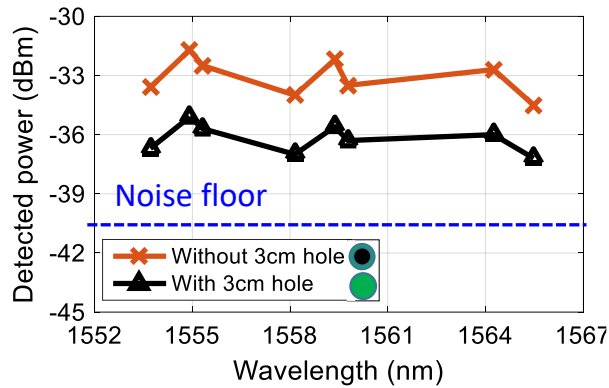


Fig. 6-12 Detected peak power vs. wavelength, for \varnothing 4cm CC foil with \varnothing 3cm hole, and \varnothing 4cm CC foil without hole

6.3.3 Concluding remarks

By means of narrow infrared optical beams on-demand, wireless links to individual users offering high capacity, high energy efficiency as well as strongly protected privacy can be established. This technology may enable highly-demanding broadband applications such as 8K ultra-high definition wireless video streaming, real-time virtual reality gaming or training without being hampered by wires, tele-presence meetings, Distinct advantages can be obtained in environments such as exhibition halls with frequently changing constellations of independent booths (which do not like capacity sharing), conference halls (where delegates want to download the proceedings instantly), electromagnetic radiation-sensitive areas (such as intensive care and surgery rooms in hospitals, inside airplanes, ...), airport waiting areas near the gate (where people want to do fast downloading or other voluminous internet things before getting on board), inside data centers between racks (where it provides minimum latency, as light travels 50% faster in air than in silica fiber), business meeting rooms requiring high privacy, etc., etc.

Efficient device localization is required in order to direct the beams on-demand and instantly to the user. Applying passive retro-reflection by means of a foil containing many miniature corner cubes has enabled device localization within the pico-cell resolution of our 2D beam-steered high-capacity optical wireless system setup. Real-time 10GbE video streaming to mobile devices has been demonstrated.

6.4 Localization when using analog mechanical beam steering^{13 14}

For upstream communication, i.e. from the user device to the ceiling unit, 2D analog beam steering by e.g. 2D electro-mechanical transducer stages has been explored [4]; see section 5.4. The upstream beam power is restricted in order to save battery power consumption in the user's device and for eye safety at the user as well. For obtaining sufficient power budget in the upstream link, it is therefore preferred to capture the full power of the upstream beam within the aperture of the receiver at the ceiling. Alignment of the beam can then be achieved by means of an RR (retro-reflective) ring surrounding the receiver aperture and can be automated by scanning the US beam spot over this RR ring in the search for the receiver's aperture.

6.4.1 Center-of-gravity algorithm

Provided that the user is within the coverage area of the PRA, initially the relatively large RR ring is to be found by taking coarse scanning steps of several cm-s (see also the spot scanning mechanism described in detail in Chapter 8). As soon as the RR ring has been found, the fine scanning in order to find the US Rx aperture is started. Fig. 6-13 illustrates the fine scanning in x- and y-direction.

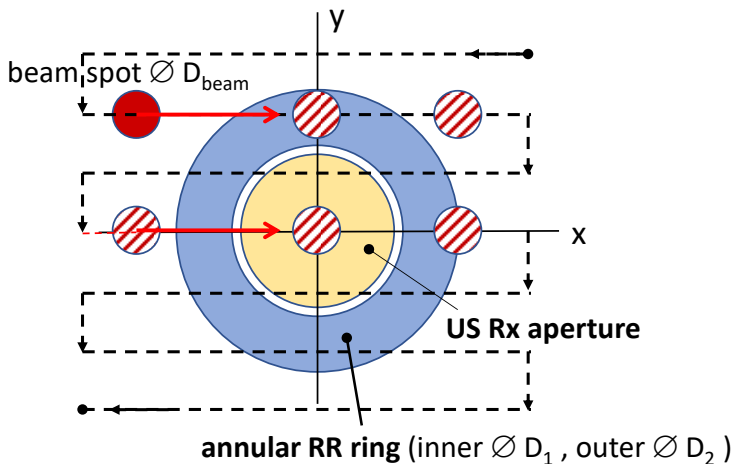


Fig. 6-13 Scanning the RR ring at the US receiver

¹³ This section is largely based on Ton Koonen, Ketemaw Addis Mekonnen, Frans Huijskens, Eduward Tangdionga, "Bi-directional all-optical wireless Gigabit Ethernet communication system using automatic self-aligned beam steering," *J. of Lightwave Technology*, Vol. 41, No. 11, June 2023, pp. 3446-3454, <https://doi.org/10.1109/JLT.2022.3231438>

¹⁴ Dutch patent application N2032214 "Bi-directional all-optical wireless communication system with autonomous optical beam steering," inventor A.M.J. Koonen, filed June 17, 2022

When assuming a uniform power profile of the beam, at every position of the scanning beam the power reflected by the RR ring can be analytically derived. It is proportional to the area of overlap between the beam and the RR ring, which is

$$A_{\text{overlap beam-RR}} = A_{RR}(R_1) - A_{RR}(R_2) \quad (6-3)$$

where if $R_n - R_{\text{beam}} < |D| < R_n + R_{\text{beam}}$

$$A_{RR}(R_n) = A\left(\frac{R_{\text{beam}}^2 - (R_n - D)^2}{2D}, R_n\right) + A\left(\frac{R_n^2 - (R_{\text{beam}} - D)^2}{2D}, R_{\text{beam}}\right) \quad (6-4)$$

and wherein the area overlap function $A(d,R)$ is

$$A(d,R) = R^2 \left\{ \frac{\pi}{2} + \arcsin\left(\frac{d}{R} - 1\right) + \left(\frac{d}{R} - 1\right) \sqrt{1 - \left(\frac{d}{R} - 1\right)^2} \right\} \quad (6-5)$$

with distance D between the beam center and the center of the RR ring (which has an outer radius R_1 and inner radius R_2). The beam spot should preferably be not very small in order to get sufficient power reflected from the RR ring, but should be smaller than the ring's width in order to obtain a good resolution, so $R_{\text{beam}} \leq \frac{1}{2}(R_1 - R_2)$. For $R_2 + R_{\text{beam}} < |D| < R_1 - R_{\text{beam}}$ the beam has full overlap with the RR ring, so then $A_{\text{overlap beam RR}} = \pi R_{\text{beam}}^2$. For $|D| < R_2 - R_{\text{beam}}$ or $|D| > R_1 + R_{\text{beam}}$ there is no overlap, so $A_{\text{overlap beam-RR}} = 0$.

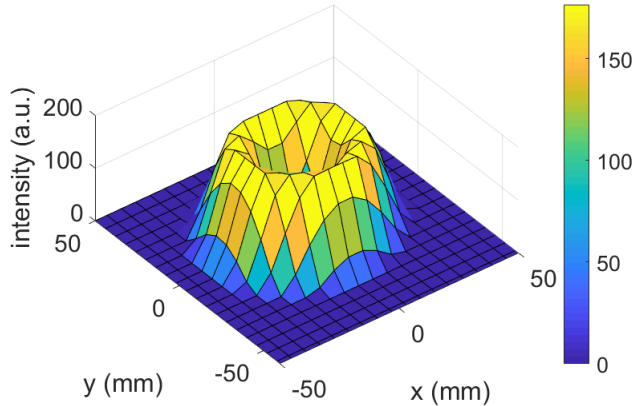


Fig. 6-14 Reflected power profile when scanning the RR ring with a uniform beam (scan step size 6mm, beam diameter $\varnothing 15$ mm, RR ring inner diameter $\varnothing 25$ mm, outer diameter $\varnothing 62$ mm; color bar: optical intensity, in arbitrary units)

Based on this analysis, Fig. 6-14 shows the analytically calculated reflected power profile which can be monitored at the US Tx site, when the RR ring is scanned with a uniform beam. From the power results $\{p_i\}$ obtained at vector positions $\bar{r}_i = \begin{pmatrix} x_i \\ y_i \end{pmatrix}$, the center of gravity (CoG) vector position of the RR ring can be calculated as (cf. [14])

$$\overline{CoG} = \begin{pmatrix} x_{CoG} \\ y_{CoG} \end{pmatrix} = \frac{1}{P_{tot}} \sum_{i=1}^N p_i \begin{pmatrix} x_i \\ y_i \end{pmatrix} \quad \text{with} \quad P_{tot} = \sum_{i=1}^N p_i \quad (6-6)$$

As the US Rx aperture is centered inside the RR ring, localizing the CoG by scanning also yields the localization of this aperture and thus the automatic alignment of the US beam into this aperture can be achieved.

6.4.2 Impact of lens aberrations on beam alignment accuracy

The accuracy of the CoG algorithm depends on the diameter of the scanning beam, the start position of the scan, and the scan step size. For a uniform beam profile and beam diameters of $\varnothing 15\text{mm}$ and $\varnothing 25\text{mm}$, Fig. 6-15.a and Fig. 6-15.b respectively show how much the estimated CoG location deviates from its exact value when the scan start position and the scan step size are varied. These graphs were calculated with the analytical approach introduced above. As expected, they have a periodicity equal to the scan step size. With arbitrary start position of the scanning, a beam diameter $\varnothing 15\text{mm}$ and a scan step size of 6mm in the plane of the RR ring, the accuracy of the beam alignment with respect to the US Rx aperture of $\varnothing 25\text{mm}$ is better than $40\mu\text{m}$, which is well within the required precision. With a larger beam diameter and same scan step size, the accuracy even improves as the reflected power received during the scanning is larger; for a diameter of $\varnothing 25\text{mm}$ (the maximum value which just fits the US Rx aperture) and step size of 6mm, the accuracy is better than $4\mu\text{m}$. As expected, it can be seen that the accuracy clearly degrades for a larger step size and degrades slightly further when the beam diameter increases. When doubling the step size from 6mm to 12mm, for the $\varnothing 15\text{mm}$ beam diameter the accuracy degrades from $40\mu\text{m}$ to $150\mu\text{m}$; for the $\varnothing 25\text{mm}$ diameter, it degrades from $4\mu\text{m}$ to $200\mu\text{m}$.

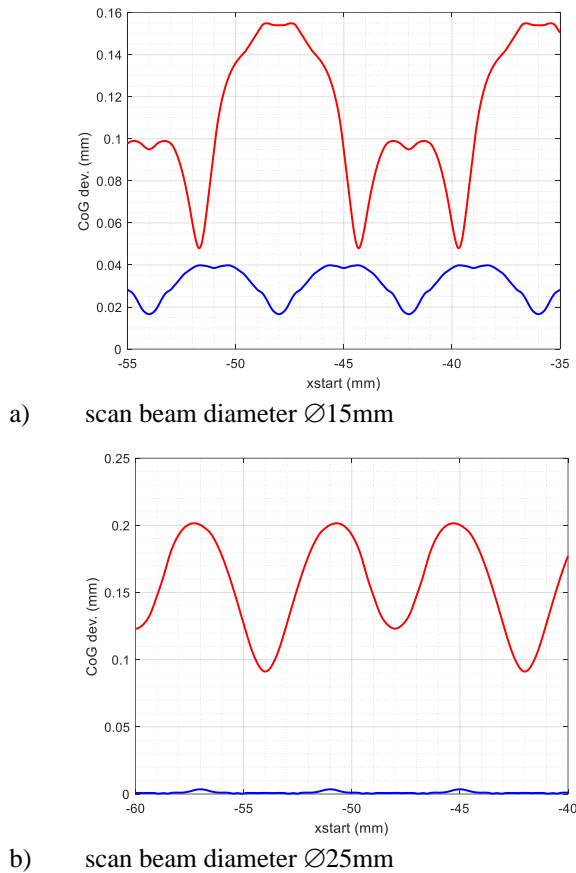
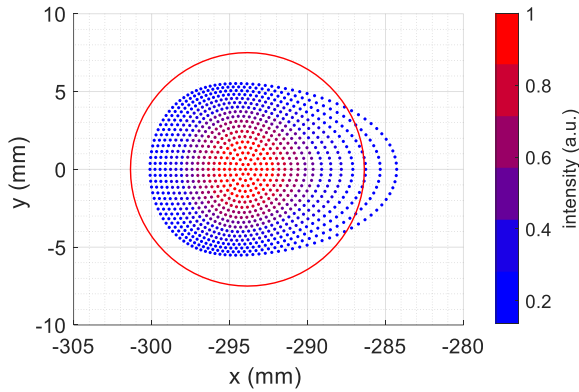
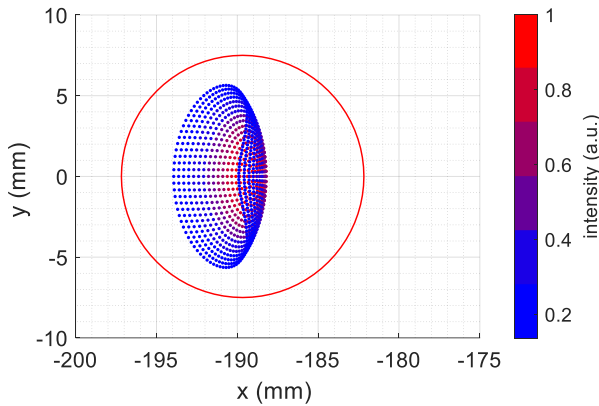


Fig. 6-15 Accuracy of the CoG algorithm versus start position of scan, for uniform scanning beam, with a) beam diameter $\varnothing 15\text{mm}$, and b) beam diameter $\varnothing 25\text{mm}$ (blue curve: scan step size 6mm, red curve: step size 12mm; RR ring inner diameter $\varnothing 25\text{mm}$, outer diameter $\varnothing 62\text{mm}$)

To achieve high localization precision, the CoG algorithm requires that the beam spot preserves its circular shape during the RR scanning. Hence the US lens should have minimal off-axis aberrations. Ray tracing with a self-built MATLAB-based program applied on several commercially available lens types shows that a Hastings triplet lens with $f=20\text{mm}$ [16] gives much lower aberrations than e.g. a commonly used plano-convex lens with the same focal length [17]; see Fig. 6-16.



a) triplet lens $f=20\text{mm}$: $\varphi_x=8.4\text{deg.}$, $\eta=98\%$, $\beta=12\%$



b) planoconvex lens $f=20\text{ mm}$: $\varphi_x=5.4\text{deg.}$, $\eta=100\%$, $\beta=50\%$

Fig. 6-16 US beam spot at the RR ring, using a) triplet lens, and b) plano-convex lens (by ray tracing, with 1027 Gaussian beams from US Tx; red circle: $\varnothing 15\text{mm}$; color bars: optical intensity, in arbitrary units)

Here η is the fraction of power captured by a $\varnothing 15\text{mm}$ aperture (red circle), and β the ellipticity of the spot, which indicates spot deformation and can be determined by the ray tracing as (cf. [15])

$$\beta = 1 - \frac{\sigma_x}{\sigma_y} \quad (6-7)$$

where σ_x and σ_y are the rms values of half the short and half the long axis of the deformed spot, respectively, which are calculated from the ray tracing results (assuming the spot is elongated in the y-direction) by

$$\sigma_x = \frac{1}{P_{tot}} \sqrt{\sum_{k=1}^K P_k^2 (x_k - x_{CoG})^2} \quad (6-8)$$

$$\sigma_y = \frac{1}{P_{tot}} \sqrt{\sum_{k=1}^K P_k^2 (y_k - y_{CoG})^2} \quad (6-9)$$

Here K rays are traced, P_k is the power in ray k , and P_{tot} is the total power of the K rays, so the power in the beam spot. For the triplet lens at a beam incident angle of $\varphi=8.4\text{deg}$. (see Fig. 6-16) we find $\beta=12\%$, whereas for the plano-convex lens $\beta=45\%$ already at a smaller $\varphi=5.4\text{deg}$. Note also that the ellipticity β must be low for efficient lens coupling of the US beam to the PD in the US Rx.

Fig. 6-17 shows how due to off-axis lens aberrations the spot is changing when scanning across the RR ring. The changes with the plano-convex lens are clearly larger than with the triplet lens, and this is affecting the accuracy of the CoG algorithm.

Fig. 6-18 illustrates the impact of these aberrations on the accuracy of the CoG algorithm. For both the triplet lens and the plano-convex lens, it shows the deviations in the estimated CoG position from its exact position when the scan start position is varied. These deviations and their spreading are presented for various positions of the RR ring, i.e., for various FoV positions φ . Each marker represents the results of scanning across the whole RR ring (outer diameter \varnothing 62mm) with a Gaussian beam spot of \varnothing 15mm waist and with a scan step size of 6mm. Each marker involves ray tracing of $K=469$ rays for 15×15 scan positions, so of more than 150000 rays. As Fig. 6-18 presents, the localization errors made by the CoG algorithm depend somewhat on the position where the scanning starts. This trend agrees with the results shown in Fig. 6-15 obtained from the analytical calculations with a uniform beam. As shown in Fig. 6-18 also, the localization errors in general increase at larger FoV angles φ , which is due to the increasing off-axis lens aberrations. The localization errors and the spreading in the errors when the scan start position is varied are larger when the plano-convex lens is used than when the triplet lens is used. This underlines once more the preference for applying a low-aberration lens, such as a triplet lens. Over a FoV φ -range up to 10deg ., it can be seen in Fig. 6-18 that the localization accuracy of the CoG algorithm is better than $180\mu\text{m}$ with the $f=20\text{mm}$ triplet lens, whereas the accuracy is within $760\mu\text{m}$ with the $f=20\text{mm}$ plano-convex lens.

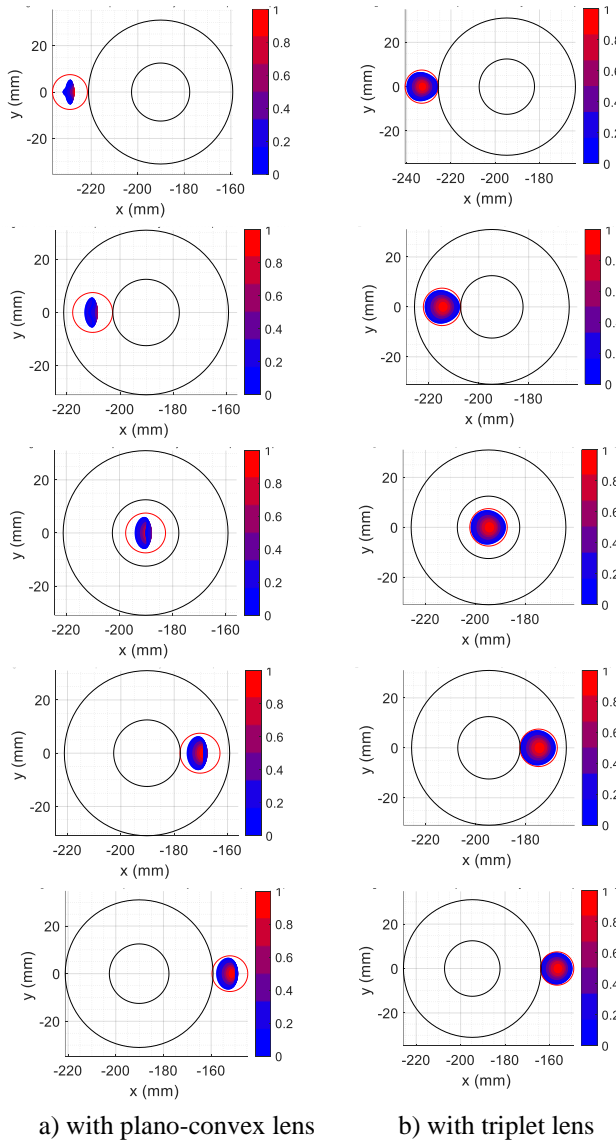


Fig. 6-17 Scanning with the US beam across the RR ring at the US receiver, for FoV position $\varphi \approx 5.5^\circ$. (left column: with a plano-convex lens, $f=20\text{mm}$ lens, right column: with a triplet lens, $f=20\text{mm}$; RR ring inner diameter $\varnothing 25\text{mm}$, outer diameter $\varnothing 62\text{mm}$; red circle: $\varnothing 15\text{mm}$, color bars: optical intensity, in arbitrary units)

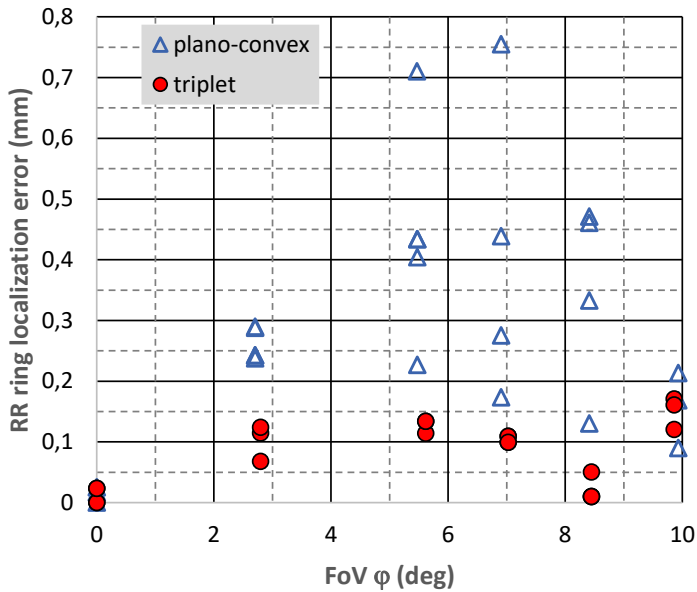


Fig. 6-18 Accuracy of the CoG algorithm versus the upstream beam incident angle φ when using a plano-convex lens $f=20\text{mm}$ (blue triangles) and using a triplet lens $f=20\text{mm}$ (red dots) (system parameters: beam spot $\varnothing 15\text{mm}$ at incident angle $\varphi=0$, scan step size 6mm , RR ring inner diameter $\varnothing 25\text{mm}$, outer diameter $\varnothing 62\text{mm}$)

Based on these simulation results, for the upstream link in our system demonstrator a beam diameter $\varnothing 15\text{mm}$, a scan step size of 6mm and an RR ring with outer diameter $\varnothing 62\text{mm}$ and inner diameter $\varnothing 25\text{mm}$ have been selected.

6.4.3 System experiments

The localization technique has been implemented in the bi-directional OWC laboratory setup shown in Fig. 8-1 and described in full detail in Ch. 8. The OWC receivers can handle GbE data speeds, and have a wide FoV $\approx \pm 10$ deg., which eases beam alignment and provides some tolerance to tilt of the user's device. The downstream (DS) beam alignment procedure uses the AWGR-based 2D steering of $+10\text{dBm}$ beams wider than the user's DS receiver aperture ($\varnothing 10\text{cm}$ Gaussian beams vs. $\varnothing 50\text{mm}$ Fresnel lens) by means of wavelength tuning controlled by LabVIEW running on a laptop computer, as discussed in section 6.3.

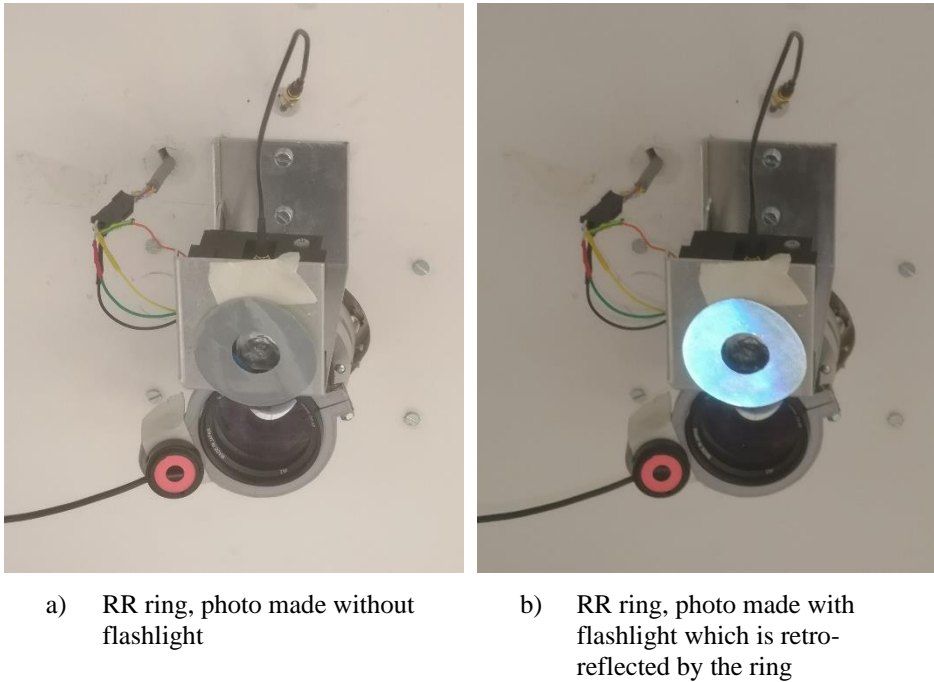


Fig. 6-19 The RR ring mounted around the lens aperture of the ceiling's upstream receiver

The upstream (US) beam alignment procedure uses 2D beam steering by means of an (x,y) stepper motor stage controlled by the CoG algorithm which is implemented in an Arduino board and is fed by a power detector (PD) monitoring the power reflected from the RR ring mounted around the $\varnothing 25\text{mm}$ Fresnel lens of the US receiver at the ceiling. Fig. 6-19 shows the RR ring and how it retro-reflects the light incident sideways. The US beams are narrower than the lens aperture ($\varnothing 15\text{mm}$ vs. $\varnothing 25\text{mm}$) as the US beam power has to be relatively low (only +2dBm) in order save battery power at the user's device, and also for enhanced eye safety while being close to the user. The results of monitoring the reflected power when scanning the narrow US beam across the RR ring are shown in Fig. 6-20. The shape of the 3D intensity graph is similar but a bit less smooth than the theoretical one in Fig. 6-14, due to noise fluctuations in the monitored power. These measured results serve as the inputs for the CoG algorithm.

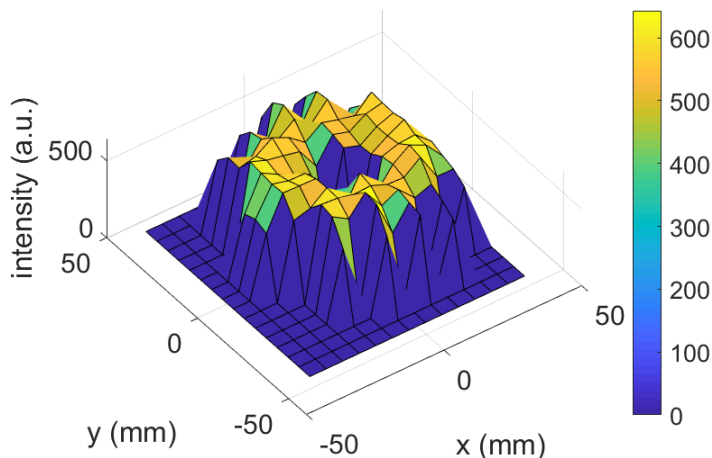


Fig. 6-20 Experimental results of monitoring the reflected power from the RR ring around the US receiver (upstream Gaussian beam $\varnothing 15\text{mm}$, RR ring with inner diameter $\varnothing 25\text{mm}$ and outer diameter $\varnothing 62\text{mm}$ (color bar: optical intensity, in arbitrary units)

Upon the user's request, the bidirectional OWC connection is set up by first establishing the upstream link. The US receiver is localized by scanning with the US beam in coarse steps until a first hit with the RR ring is found. Subsequently, the scanning continues in smaller steps (about 6mm each), and the results as gathered in Fig. 6-20 are fed into the CoG algorithm. The experimental surface plot of Fig. 6-20 approximates but is less smooth than the analytically derived surface plot shown in Fig. 6-14, due to noise in monitoring the reflected power levels. The measured plot may be smoothed by introducing a pilot tone on the scanning beam and applying synchronous detection techniques which improve the monitoring sensitivity. The scanning is finished when the whole RR ring has been scanned, and the CoG algorithm has converged. The total US beam alignment time takes about 10 seconds, which is mainly limited by the speed of the two stepper motors. This time may be shortened by increasing the step size (doubling the step size reduces the number of steps by a factor of 4), but at the cost of less accuracy (see Fig. 6-15).

After the US beam has been aligned and the upstream link has been established, the DS beam is aligned by scanning the user area using wavelength tuning and monitoring the power reflected by the RR ring at the user's receiver, as described in section 6.3. The downstream beam alignment takes less than 15 seconds, which is mainly limited by the LabVIEW control program running on a laptop at the headend site. Adequate alignment of both the upstream and downstream beam is confirmed by a good bidirectional TCP test results showing

about 940 Mbit/s in DS and about 939 Mbit/s in US direction, without packet loss; see section 8.4.

6.4.4 Concluding remarks

Automatic self-calibrated alignment of the upstream beam by means of a novel steering control protocol using the center-of-gravity (CoG) algorithm as well as automatic self-calibrated alignment of the downstream beam has been designed, realized, implemented and validated in a laboratory testbed. Broadband GbE receivers with a wide FoV $\approx\pm 10$ deg. were employed, which ease the required beam alignment accuracy. With low-aberration triplet lenses, a good accuracy of the CoG algorithm and hence adequate upstream beam steering has been achieved within 200 μ m accuracy and within 10 seconds alignment time, mainly limited by the stepper motors. The automatic downstream beam alignment takes less than 15 seconds, mainly limited by the wavelength-tuning control by means of LabVIEW. TCP measurements show 940Mbit/s transfer speeds per user within the FoV $\approx\pm 10$ deg.

6.5 Summarizing conclusions

Accurate self-calibrating steering of the downstream and upstream beams in bi-directional indoor systems without pre-establishing communication links between the ceiling unit and the user devices has been achieved by using passive retro-reflector techniques at the unit to be localized. By beam scanning and monitoring the reflected power, the beam is directly brought into the well-aligned position without needing calibration and without parallax errors, and the upstream and downstream links be established without requiring active functions at the unit to be localized. Being able to do downstream and upstream localization separately and independently enables to set up the OWC link upon an initiative from the user as well as upon an initiative from the central ceiling site, thus enlarging the flexibility to operate the system. The time consumed by the beam steering limits the system's suitability for mobile users. Its major benefits are for delivery of dense high-capacity services to nomadic users.

6.6 References

- [1] H. Haas, L. Yin, Y. Wang, and C. Chen, "What is LiFi?," *J. Lightw. Technol.*, vol. 34, no. 6, pp. 1533-1544, Mar. 2016.
- [2] A.M.J. Koonen, 'Indoor optical wireless systems: Technology, trends, and applications,' *J. Lightw. Technol.*, vol. 36, no. 8, pp. 1459–1467, Apr. 2018, doi: 10.1109/JLT.2017.2787614.
- [3] K. Wang, A. Nirmalathas, C. Lim, K. Alameh, and E. Skafidas, "Full-duplex gigabit indoor optical wireless communication system with CAP modulation," *IEEE Photon. Technol. Lett.*, vol. 28, no. 7, Apr. 2016, pp. 790-793.

-
- [4] A.M.J. Koonen, K.A. Mekonnen, F. Huijskens, E. Tangdionga, "Bi-directional all-optical wireless Gigabit Ethernet communication system using automatic self-aligned beam steering," *J. Lightw. Technol.*, vol. 41, no. 11, June 2023, pp. 3446-3454
- [5] A. Gomez, K. Shi, C. Quintana, M. Sato, G. Faulkner, B.C. Thomsen, and D.C. O'Brien, "Beyond 100-Gb/s indoor wide field-of-view optical wireless communications," *Phot. Technol. Lett.*, vol. 27, no. 4, Feb. 2015, pp. 367-370.
- [6] 'Laser safety', https://en.wikipedia.org/wiki/Laser_safety, accessed Nov. 14, 2019.
- [7] H. Liu, H. Darabi, P. Banerjee, J. Liu, 'Survey of Wireless Indoor Positioning Techniques and Systems,' *IEEE Trans. on Systems, Man, and Cybernetics*, vol. 37, no. 6, pp. 1067-1080, Nov. 2007.
- [8] T.-H. Do and M. Yoo, 'An in-depth survey of visible light communication based positioning systems,' *Sensors*, vol. 16, no. 5, 2016, paper no. 678. On-line at <http://www.mdpi.com/1424-8220/16/5/678>, accessed Nov. 14, 2019.
- [9] A. Gomez, K. Shi, C. Quintana, G. Faulkner, B. C. Thomsen, and D. C. O'Brien, "A 50 Gb/s transparent indoor optical wireless communications link with an integrated localization and tracking system," *J. Lightw. Technol.*, vol. 34, no. 10, pp. 2510–2517, May 2016.
- [10] A.M.J. Koonen, F. Gomez-Agis, F.M. Huijskens, K. A. Mekonnen, 'High-Capacity Optical Wireless Communication Using Two-Dimensional IR Beam Steering,' *J. Lightw. Technol.*, vol. 36, no. 19, pp. 4486-4493, Oct. 2018.
- [11] A.M.J. Koonen, K.A. Mekonnen, F.M. Huijskens, E. Tangdionga, "Fully passive user localisation for beam-steered high-capacity optical wireless communication system," in *Proc. ECOC2019*, Dublin, paper Tu.3.C.4, Sep. 22-26, 2019.
- [12] N.Q. Pham, K.A. Mekonnen, E. Tangdionga, A. Mefleh, A.M.J. Koonen, "Accurate Indoor Localization for Beam-Steered OWC System Using Optical Camera," in *Proc. ECOC2019*, Dublin, Sep. 22-26, 2019, paper P45.
- [13] Photoelectric acrylic reflector material, <https://www.orafol.com/en/europe/products/oralite-photoelectric-sheeting>, accessed Nov. 14, 2019.
- [14] <https://www.sciencetopia.net/physics/center-gravity> [online]
- [15] <https://math.stackexchange.com/questions/537115/what-are-definitions-of-ellipticity> [online]
- [16] <https://www.edmundoptics.com/f/hastings-triplet-achromatic-lenses/11968/> [online]
- [17] <https://www.edmundoptics.com/p/200mm-dia-x-200mm-fl-uncoated-plano-convex-lens/5719/> [online]

7 Broadband OWC receiver with wide Field-of-View¹⁵

A crucial element in a beam-steered OWC system, in particular in settings where devices may move, is a receiver which can capture a large part of the optical beam without requiring tedious alignment of the device regarding the position and the angle of incidence of the beam. The receiver hence should have a large aperture as well as a wide Field-of-View (FoV) angle. High-speed photodiodes typically have a small active area in order to minimize their bandwidth-limiting electrical junction capacitance, so a quite small aperture. The receiving aperture can be increased by a lens system, but as stated by the fundamental optics law of conservation of etendue [1] this is compromised by a decrease of the FoV. In an angular diversity receiver [2][3], multiple photodiodes are used in parallel to jointly increase the active area, but each one needs to be followed by a separate high-bandwidth preamplifier and their outputs to be summed, which increases noise, requires careful phase synchronization among these amplifiers and complicates the receiver circuitry. Non-imaging optics such as a compound parabolic concentrator can also increase the receiving aperture, but still need to obey the law of conservation of etendue [4] [5]. This law may be broken by applying phosphorescence for wavelength-converting the optical signal received with a large aperture, which thus can be captured inside a doped slab waveguide [6] or doped fiber [7]. This process, however, has inherent bandwidth limits and requires a relatively high received power level. Yet another approach reported is to separate the functions of light collection and light detection and optimize them individually, e.g., by capturing the light into a waveguide by means of surface grating couplers (SGC-s) and subsequently use a fast waveguide-coupled photodiode for detection. With a $10 \times 10 \mu\text{m}^2$ SGC and $3 \times 10 \mu\text{m}^2$ 67GHz uni-traveling-carrier (UTC) photodiode, 40Gbit/s on-off-keyed transmission has been demonstrated [8]. A larger aperture can be achieved by apodization of the SGC and by multiple SGC-s of which the outputs are combined into a single waveguide (incurring power combining losses).

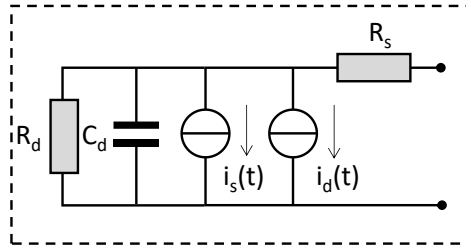
¹⁵ This chapter is an extended version of the chapter in paper “Beam-steered optical wireless communication for industry 4.0”, by Ton Koonen et al., *IEEE J. of Sel. Topics in Quantum Electron.*, Dec. 2021. It is also based on patent PCT/EP2020/080594, priority date Oct. 31, 2019, “Receiver for optical wireless communication with large aperture and wide angle of view,” by A.M.J. Koonen.

In this chapter, we propose an alternative concept which extends the receiver's aperture and its FoV while it requires only a single pre-amplifier, so avoiding high complexity and reducing power consumption which is particularly beneficial at the compact and (often) battery-operated user device [9]. Instead of a single photodiode, a 2D matrix of photodiodes is used to increase the active area while keeping its bandwidth equal to that of the single photodiode. This matrix constellation still has only a single signal output. The 2D photodiode matrix concept is introduced and theoretically analyzed in section 7.1, including its bandwidth characteristics, biasing conditions, and signal-to-noise ratio (SNR) performance of the receiver in comparison with single-PD receiver and a multi-PD angular diversity receiver (ADR). In section 7.2, it is studied both analytically and numerically by means of extensive ray tracing how the beam-to-photodiode coupling is improved by applying the PD matrix concept, including studies about the impact of the fill factor of the PD matrix, and about the impact on the receiver's performance when it is shifted within the footprint of the beam taking also into account the crosstalk power which may come in from neighbouring beams. Section 7.3 discusses the assembly of the PD matrix and its implementation into a transimpedance pre-amplifier circuit board. Section 7.4 reports on the experimental validation of the receiver's performance employing a 4×4 PD matrix, including the assessment of its BER performance and Field-of-View (FoV) at 1 and 1.25 Gbit/s (Gigabit Ethernet, GbE) data rates. Section 7.5 analyzes the scaling of the PD matrix to larger sizes and its impact on the attainable FoV, and the chapter concludes with some summarizing remarks in section 7.6.

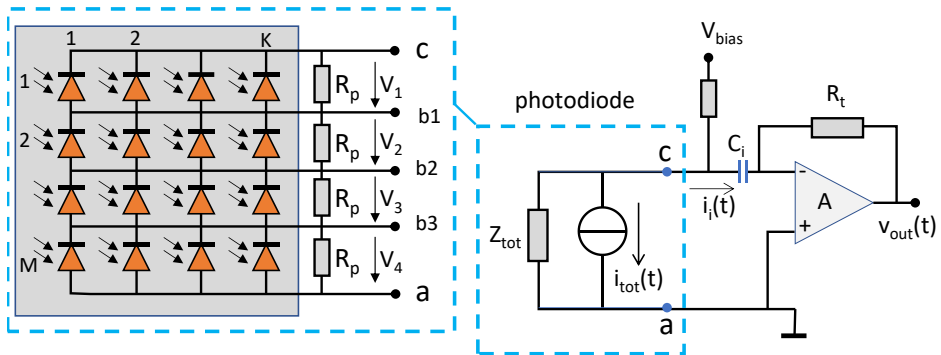
7.1 Receiver based on a matrix of photodiodes

A photodiode may electrically be modelled by the equivalent circuit shown in Fig. 7-1.a, where R_s represents the (typically small) resistance of the bond wires, R_d the (large) parallel resistance representing the leakage current, C_d the capacitance of the reverse-biased photodiode's junction, $i_d(t)$ the (small) dark current, and $i_s(t)$ the generated photocurrent where $i_s(t) = \mathcal{R} a P(t)$ in which \mathcal{R} is the photodiode's responsivity, and a is the fraction of the optical beam's power $P(t)$ reaching the photodiode's active area. By putting K photodiodes in parallel the total active area is increased K -fold, so the generated photocurrent as well, but also the capacitance increases K -fold and hence the bandwidth decreases K -fold. Putting photodiodes in series in order to increase the area is commonly not considered a viable option, as ideal current sources should not be cascaded. Assuming a non-infinite parallel resistance R_d , however, M photodiodes may be cascaded, and thus the capacitance of this cascade is decreased M -fold and the bandwidth increases M -fold. The generated photocurrent does not increase by the cascading. We combined the putting of photodiodes in K parallel columns with

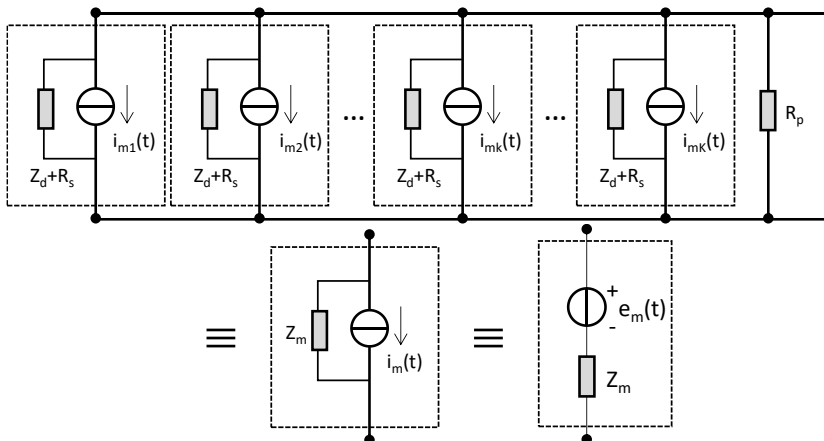
putting them in series in M rows, leading to a 2-dimensional $K \times M$ photodiodes matrix; using only two poles, this matrix can be applied in a transimpedance amplifier as shown in Fig. 7-1.b.



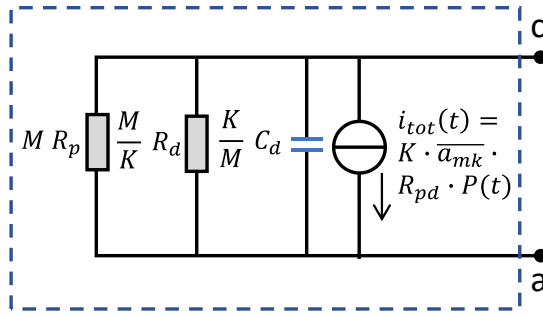
a) Equivalent circuit of single photodiode



b) 2D matrix of photodiodes applied in transimpedance amplifier



c) Putting K photodiodes in parallel



d) Equivalent circuit of 2D matrix of photodiodes (if $R_s \ll R_d$ and $i_d(t) \ll i_s(t)$)

Fig. 7-1 OWC receiver employing a two-dimensional matrix of photodiodes

Following Thevenin's and Norton's theorems (illustrated in Fig. 7-1.c), putting K identical photodiodes in parallel in the m^{th} row may be represented by a single current source $i_m(t)$ with parallel impedance Z_m , or equivalently a single voltage source $e_m(t)$ with serial impedance Z_m , where

$$i_m(t) = \sum_{k=1}^K i_{mk}(t) = \frac{Z_d}{Z_d + R_s} \{K i_d(t) + \mathcal{R} P_0(t) \sum_{k=1}^K a_{mk}\} \quad (7-1)$$

with $Z_d = R_d \parallel 1/j\omega C_d$, where $Z_1 \parallel Z_2$ denotes the connection of impedances Z_1 and Z_2 in parallel, and

$$Z_m = \left(\frac{Z_d + R_s}{K} \right) \parallel R_p \quad (7-2)$$

$$e_m(t) = i_m(t) Z_m = \left\{ \frac{Z_d}{K} \parallel \frac{R_p}{1 + R_s/Z_d} \right\} \left\{ K i_d(t) + \mathcal{R} P_0(t) \sum_{k=1}^K a_{mk} \right\} \quad (7-3)$$

Next, putting M rows in series each composed of K identical photodiodes yields for the overall $K \times M$ photodiodes matrix

$$\begin{aligned} e_{tot}(t) &= \sum_{m=1}^M e_m(t) \\ &= \left(\frac{Z_d + R_s}{K} \parallel R_p \right) \frac{Z_d}{Z_d + R_s} \left\{ M K i_d(t) + \mathcal{R} P_0(t) \sum_{m=1}^M \sum_{k=1}^K a_{mk} \right\} \end{aligned} \quad (7-4)$$

$$Z_{tot} = \sum_{m=1}^M Z_m = M \left\{ \left(\frac{Z_d + R_s}{K} \right) \parallel R_p \right\} \quad (7-5)$$

$$i_{tot}(t) = \frac{e_{tot}(t)}{Z_{tot}} = \frac{Z_d}{Z_d + R_s} \left\{ K i_d(t) + \frac{\mathcal{R} P_0(t)}{M} \sum_{m=1}^M \sum_{k=1}^K a_{mk} \right\} \quad (7-6)$$

$$i_{tot}(t) = \frac{K}{1+R_s/Z_d} \{ i_d(t) + \mathcal{R} P_0(t) \overline{a_{mk}} \} \quad (7-7)$$

where $\overline{a_{mk}} = \frac{1}{M \cdot K} \sum_{m=1}^M \sum_{k=1}^K a_{mk}$

Hence the photodiode matrix can be represented by the equivalent circuit shown in Fig. 7-1.d composed of a current source $i_{tot}(t)$ and impedance Z_{tot} as

$$i_{tot}(t) = \frac{K [i_d + \mathcal{R} \overline{a_{mk}} P(t)]}{1 + \frac{R_s}{R_d} (1 + j\omega R_d C_d)} \quad (7-8)$$

$$Z_{tot} = \frac{M R_p [R_d + R_s (1 + j\omega R_d C_d)]}{R_d + (R_s + K R_p) (1 + j\omega R_d C_d)} \quad (7-9)$$

where $\overline{a_{mk}} = \frac{1}{M \cdot K} \sum_{m=1}^M \sum_{k=1}^K a_{mk}$ is the average fraction of the beam's power which is incident on each photodiode, and Z_{tot} can be decomposed in a resistance $M(R_p \parallel (R_d + R_s)/K)$ in parallel with a capacitance $(K/M) C_d$.

7.1.1 Frequency characteristics

The photodiode matrix can be readily applied in the simple transimpedance amplifier configuration of Fig. 7-1.b, of which the transimpedance $Z_T = v_{out}(t) / i_{tot}(t)$ near DC and the -3dB bandwidth ω_{-3dB} for $R_s \ll R_d$ is

$$Z_T(\omega = 0) = \frac{A R_t}{1 + A + \frac{R_t}{M R_p} + \frac{K}{M} \frac{R_t}{R_d + R_s}} \quad (7-10)$$

$$\omega_{-3dB} \approx \frac{M}{K} \frac{1}{C_d} \left[\frac{1 + A}{R_t} + \frac{1}{R_p} \right] + \frac{1}{R_d C_d} \quad (7-11)$$

Hence the bandwidth for $R_p \gg R_t/(1+A)$ and $R_d \gg (K/M) \cdot R_t/(1+A)$ is given by

$$\omega_{-3dB} \approx \frac{M}{K} \frac{1 + A}{C_d R_t} \quad (7-12)$$

i.e. M/K times larger than with a single photodiode (for which $K=M=1$). The transimpedance near DC referenced to the generated photocurrent is

$$Z_{T,ref}(\omega = 0) = \frac{v_o(t)}{\bar{a} \mathcal{R} P(t)} \approx K \frac{A}{1 + A} R_t \quad (7-13)$$

and is therefore K times larger than with a single photodiode.

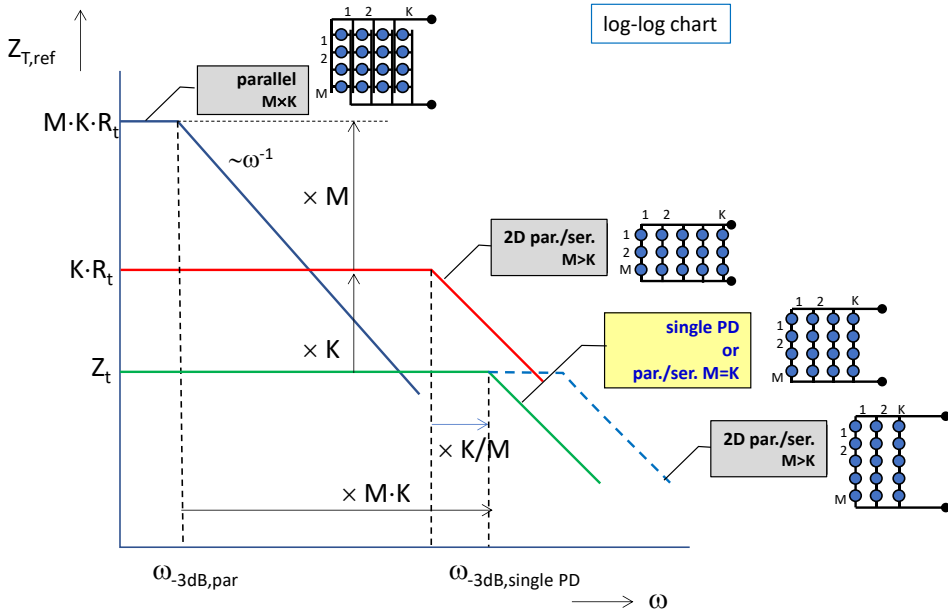


Fig. 7-2 Frequency characteristics of OWC receiver using a $K \times M$ matrix of photodiodes

Fig. 7-2 gives an overview of how the receiver characteristics will basically depend on the constellation of the photodiode matrix. When comparing a square $M \times M$ photodiode array to a single photodiode, it can be observed that the active detection area is M^2 times larger, the bandwidth is the same, and the output signal is M times larger.

7.1.2 Bias conditions in the photodiode matrix

The DC reverse-biasing voltages across the photodiodes in the matrix may get unbalanced when the photodiodes are unevenly illuminated, and this may impact the performance characteristics of the photodiodes. As shown in Fig. 7-1.b, the grouping of the photodiodes in the matrix consists of K columns and M rows. Fig. 7-3 illustrates how the overall bias voltage V_{bias} across the total matrix is built up by the bias voltages V_m across the m^{th} rows (with $m=1, 2, \dots, M$). As each row transports the same current I , for the individual photocurrents i_m holds

$$i_1 + \frac{V_1}{R_a} = i_2 + \frac{V_2}{R_a} = \dots = i_m + \frac{V_m}{R_a} = \dots = i_M + \frac{V_M}{R_a} = I \tag{7-14}$$

where $R_a = \left(\frac{R_d + R_s}{K} \right) \parallel R_p$

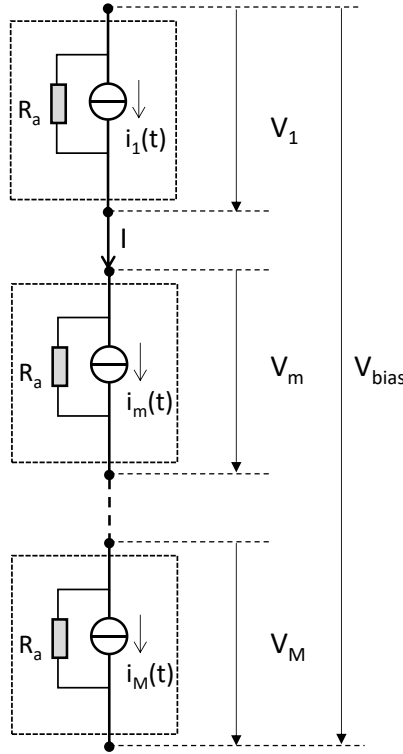


Fig. 7-3 DC bias conditions when cascading photodiodes

Thus

$$V_{bias} = \sum_{m=1}^M V_m = M R_a I - R_a \sum_{m=1}^M i_m \quad (7-15)$$

$$\begin{aligned} V_m = R_a (I - i_m) &= \frac{V_{bias}}{M} - R_a \left(i_m - \frac{1}{M} \sum_{m=1}^M i_m \right) \\ &= \frac{V_{bias}}{M} + R_a (\bar{i}_m - i_m) \end{aligned} \quad (7-16)$$

where $\bar{i}_m = \frac{1}{M} \sum_{m=1}^M i_m$ is the average of the photocurrents in the m rows.

The photocurrent i_m is composed of the contributions of each of the K photodiodes in that row, so when assuming identical photodiodes

$$i_m = \sum_{k=1}^K i_{mk} = \frac{R_d}{R_d + R_s} \left\{ K i_d + \mathcal{R} P_0 \sum_{k=1}^K a_{mk} \right\} \quad (7-17)$$

$$V_m - \frac{V_{bias}}{M} \approx \left(R_d \parallel (K R_p) \right) \mathcal{R} P_0 \left(\bar{a}_{mk} - \frac{1}{K} \sum_{k=1}^K a_{mk} \right) \quad (7-18)$$

where $\bar{a}_{mk} = \frac{1}{M K} \sum_{m=1}^M \sum_{k=1}^K a_{mk}$ is the average of the fraction a_{mk} of the optical beam's power P_0 which captured by the $(m,k)^{\text{th}}$ photodiode of the $M \times K$

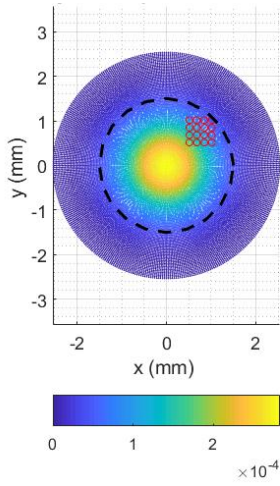
matrix. From eq. (7-18) it can be seen that the unbalance in the DC bias voltages V_m across the photodiode rows can be effectively reduced by applying a parallel resistance R_p which is considerably smaller than R_d / K .

In order to analyze the impact of uneven illumination of the photodiode matrix, the fractions a_{mk} have been calculated by numerical integration of the intensity profile of the beam when the beam is being shifted diagonally across the photodiode matrix. The active area of each photodiode is $\varnothing 150\mu\text{m}$, and they are spaced by $17\mu\text{m}$ ¹⁶. The beam is captured and projected onto the photodiode matrix by a lens system as shown in Fig. 7-7 in section 7.2.1.

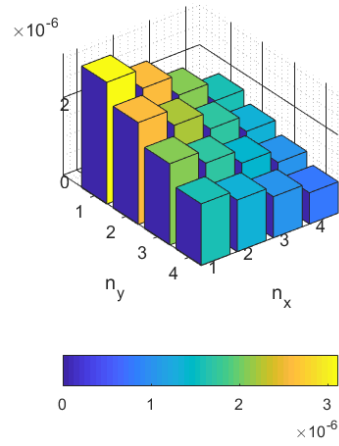
Firstly, the analysis has been done for a typical upstream transmission scenario, wherein a Gaussian beam is assumed with beam waist diameter of 15mm and a lens with $f=5\text{mm}$ focal length and aperture diameter of $D_{lens}=25\text{mm}$; see Ch. 8. Assuming an ideal thin lens which makes an image of the beam onto the matrix, Fig. 7-4.a and Fig. 7-4.b illustrate the received power per photodiode for a beam incidence angle α of 15 deg. and defocusing parameter $p=0.2$. The finite lens diameter is cropping the beam image to a diameter of $p \cdot D_{lens}$, so to $\varnothing 5\text{mm}$. As Fig. 7-4.c shows, the equivalent beam-to-matrix coupling factor T_{eq} for $\alpha=15\text{deg}$. is about -21.3dB ¹⁷. The DC bias voltages across the m^{th} row ($m=1, 2, \dots, 4$) calculated with eq. (7-18) versus the incidence angle α are shown in Fig. 7-4.d. When the photodiodes are evenly illuminated, their bias voltages are balanced at an equilibrium of $V_m=V_{bias}/M=2.5\text{V}$ (for $m=1, 2, \dots, 4$). At uneven illumination when shifting the beam across the PD matrix, the bias voltages deviate from this equilibrium by $+0.71\text{V}$ to -0.64V for a resistance effectively in parallel of every photodiode $R_{eff}=K \cdot R_p // R_d = K \cdot R_a = 1\text{M}\Omega$. With $R_{eff}=50\text{k}\Omega$, these deviations range only from $+36\text{mV}$ to -32mV . Clearly the bias voltage unbalances are effectively reduced by reducing the (external) parallel resistance R_p .

¹⁶ These physical dimensions are typical data for 2.5Gbit/s photodetectors (cf. Albis Optoelectronics [15])

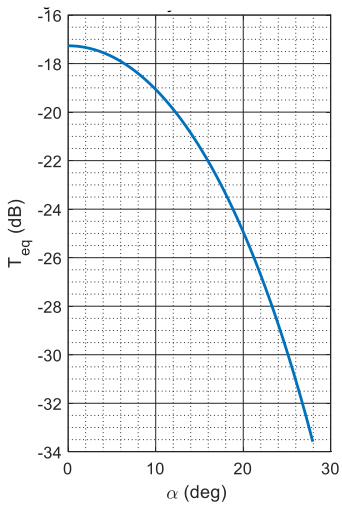
¹⁷ For upstream communication, a typical beam power $P_0=2\text{dBm}$ and receiver sensitivity of -20dBm for GbE transmission is assumed.



a) Gaussian beam image onto PD matrix at $\alpha=15$ deg. (defocusing $p=0.2$; dashed circle: imaged beam waist)



b) Received power per PD at $\alpha=15$ deg. (at $p=0.2$)



c) Equivalent coupling loss T_{eq} of beam to PD matrix vs. α

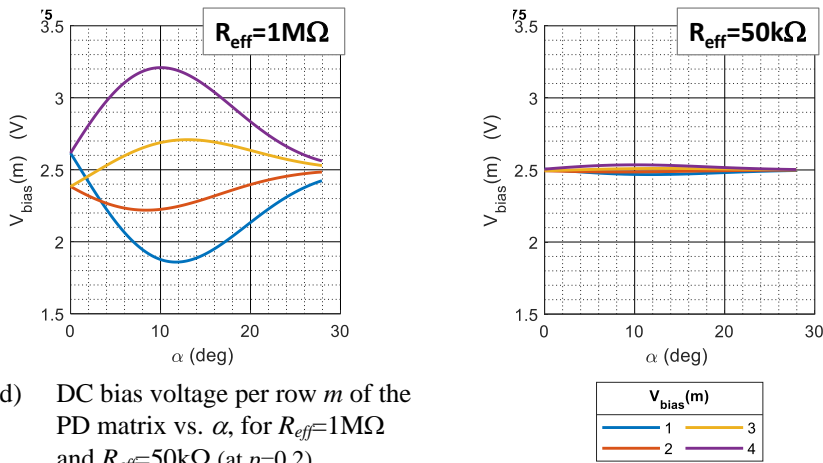
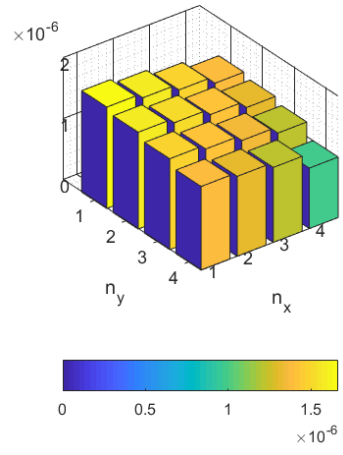
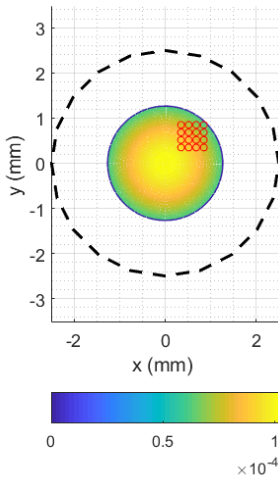
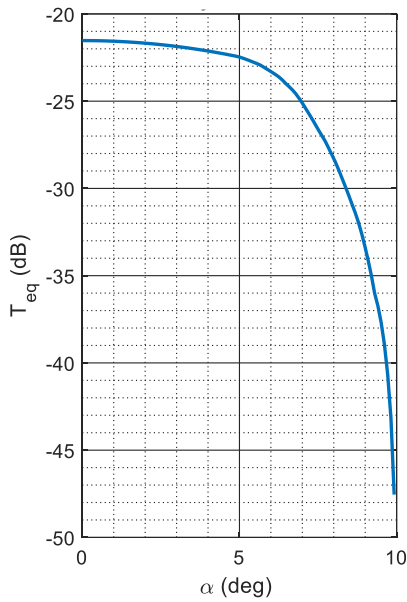


Fig. 7-4 DC bias conditions per photodiode in 4×4 PD matrix when beam incidence angle α is varied (for typical upstream scenario with Gaussian beam, waist $D_{\text{beam}}=\text{Ø}15\text{mm}$, and ideal thin lens with aperture $D_{\text{lens}}=\text{Ø}25\text{mm}$, $f=5\text{mm}$; bias voltage $V_{\text{bias}}=10\text{V}$)

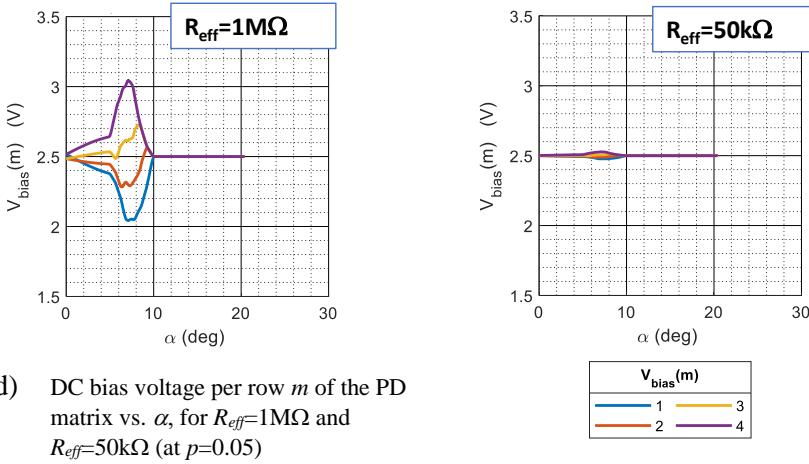
Secondly, a similar numerical analysis has been done for a downstream transmission scenario where typically the Gaussian incident beam has a waist which is larger than the lens' aperture. The results are shown in Fig. 7-5 when shifting the beam across the PD matrix, with a beam waist of 100mm , and a thin lens with $f=10\text{mm}$ and aperture diameter $D_{\text{lens}}=50\text{mm}$. The cropping of the beam's image by the limited lens' aperture results in a flatter intensity profile of the image than for the upstream case, yielding a slower decrease of T_{eq} versus α up to $\alpha\approx 7$ deg. (and a steep decline thereafter). The beam-to-matrix coupling factor T_{eq} for $\alpha=5$ deg. is about -22.5dB , with a defocusing parameter $p=0.05$ (i.e. cropped beam image of $\text{Ø}2.5\text{mm}$). In a typical downstream scenario with beam power $P_0=10\text{dBm}$, with this ideal thin lens, an α even up to 25 deg. would allow GbE transmission (at a typical GbE receiver sensitivity of -20dBm). As shown in Fig. 7-5.d, when shifting the beam the bias voltage deviations from the $V_m=2.5\text{V}$ equilibrium state range from $+0.55\text{V}$ to -0.46V for an effective parallel resistance $R_{\text{eff}}=K\cdot R_p // R_d=1\text{M}\Omega$. With $R_{\text{eff}}=50\text{k}\Omega$, the deviations range only from $+27\text{mV}$ to -23mV . Hence, also for this downstream scenario the effectiveness of reducing the parallel resistance R_p in order to reduce the voltage unbalances is clear.



- a) Gaussian beam image onto PD matrix at $\alpha=5$ deg. (dashed circle: imaged beam waist; defocusing $p=0.05$)
- b) Received power per PD at $\alpha=5$ deg. (at $p=0.05$)



- c) Equivalent coupling loss T_{eq} of beam to PD matrix vs. α



- d) DC bias voltage per row m of the PD matrix vs. α , for $R_{eff}=1M\Omega$ and $R_{eff}=50k\Omega$ (at $p=0.05$)

Fig. 7-5 DC bias conditions per photodiode in 4×4 PD matrix when beam incidence angle α is varied (for typical downstream scenario with Gaussian beam, waist $D_{beam} \varnothing 100\text{mm}$; ideal thin lens with aperture $D_{lens} = \varnothing 50\text{mm}$, $f=10\text{mm}$; bias voltage $V_{bias}=10\text{V}$)

On the other hand, the resistance R_p should remain large enough in order not to affect the frequency characteristics of the transimpedance receiver. If R_p is much larger than $R_t / (A+1)$, the bandwidth nor the amplitude characteristics of the receiver are noticeably affected (see eqs. (7-10) and (7-11)).

7.1.3 SNR performance

The SNR performance of the OWC receiver using an $M\times K$ photodiode matrix has been analyzed. Representing the intensity-modulated instantaneous power $P_0(t)$ by

$$P_0(t) = \overline{P_0} (1 + m_0(t)) \quad \text{with modulation index } |m_0(t)| \leq 1 \quad (7-19)$$

the average generated signal power $\overline{i_{tot}^2}$ according to eq. (7-7) when neglecting the dark current i_d is

$$\overline{i_{tot}^2(t)} = \overline{P^2(t)} \left(\frac{Z_d}{Z_d + R_s} K \mathcal{R} \overline{a_{mk}} \right)^2 = \left| \frac{Z_d}{Z_d + R_s} \right|^2 \overline{m_0^2} \left(\frac{A \mathcal{R} \overline{P_0}}{M} \right)^2 \quad (7-20)$$

where $A = K M \overline{a_{mk}}$ is the fraction of the average beam's power $\overline{P_0}$ which is captured by all $M\times K$ photodiodes.

The shot noise variance of the photocurrent $i_{mk}(t)$ generated in photodiode (m,k) in a bandwidth B is

$$\overline{\sigma_{i,mk}^2} = 2q I_{mk} B = 2q B \mathcal{R} \overline{P_0} a_{mk} \quad (7-21)$$

where q is the charge of an electron and B is the receivers' bandwidth. Hence, the shot noise variance of the photovoltage $e_{mk}(t)$ is

$$\overline{\sigma_{e,mk}^2} = |Z_d|^2 \overline{\sigma_{i,mk}^2} = |Z_d|^2 2q B \mathcal{R} \overline{P_0} a_{mk} \quad (7-22)$$

As the shot noise voltage in each photodiode is statistically independent of the shot noise in the other photodiodes, the shot noise power generated in the k^{th} column of the PD matrix is

$$\overline{\sigma_{i_tot,k}^2} = \frac{\overline{\sigma_{e_tot,k}^2}}{M^2 |Z_d + R_s|^2} = \frac{|Z_d|^2 2q B \mathcal{R} \overline{P_0}}{M^2 |Z_d + R_s|^2} \sum_{m=1}^M a_{mk} \quad (7-23)$$

and the shot noise power in the output current signal of the PD matrix is

$$\begin{aligned} \sigma_{i,shot}^2 &= \sum_{k=1}^K \overline{\sigma_{i_tot,k}^2} = \left| \frac{Z_d}{Z_d + R_s} \right|^2 \frac{2q B \mathcal{R} \overline{P_0}}{M^2} \sum_{k=1}^K \sum_{m=1}^M a_{mk} \\ &= \left| \frac{Z_d}{Z_d + R_s} \right|^2 \frac{2q B \mathcal{R} \overline{P_0}}{M^2} A \end{aligned} \quad (7-24)$$

The shot noise-limited SNR of a receiver using the PD matrix therefore is

$$SNR_{shot} = \frac{\langle i_{tot}^2 \rangle}{\sigma_{i,shot}^2} = \frac{\overline{m_0^2} A \mathcal{R} \overline{P_0}}{2 q B} \quad (7-25)$$

Similarly, when the receiver uses a single PD the shot noise power is

$$\overline{\sigma_{i,shot}^2} = 2q B I_{PD} = 2q B \mathcal{R} A \overline{P_0} \quad (7-26)$$

and the signal power is

$$\overline{i_{out}^2} = (\mathcal{R} A \overline{P_0})^2 \overline{m_0^2} \quad (7-27)$$

which yields a shot noise-limited SNR

$$SNR_{shot} = \frac{\overline{i_{out}^2}}{\sigma_{i,shot}^2} = \frac{\overline{m_0^2} A \mathcal{R} \overline{P_0}}{2 q B} \quad (7-28)$$

Hence, the shot noise-limited SNR of a receiver using the PD matrix is the same as when using a single PD.

Typically, the received power is low and thermal noise of the TIA electronics (with a white noise power density N_0 and bandwidth B) is dominating the shot noise from the photodiodes. The thermal noise-limited SNR is, assuming $R_s \ll Z_d$,

$$SNR_{therm} = \frac{\overline{i_{tot}^2}}{\sigma_{therm}^2} \cong \frac{\overline{m_0^2}}{N_0 B} (K \overline{a_{mk}} \mathcal{R} \overline{P_0})^2 \quad (7-29)$$

Thus, for the $M \times K$ PD matrix receiver the SNR is a factor K^2 better than for the single-PD receiver if the received optical power per photodiode is the same.

7.1.4 Comparison with angular diversity receiver

An angular diversity receiver (ADR) also deploys multiple photodiodes, but each photodiode is followed by an individual TIA, whereafter the outputs of all TIAs are summed [2][3]. When compared to an ADR, the proposed PD matrix receiver has the same bandwidth and a better SNR. Moreover, particularly at high frequencies the TIA-s of the ADR need to be phase-synchronous, which complicates their design.

As shown in Fig. 7-6, whereas an $N \times N$ PD matrix receiver needs only a single TIA, an ADR needs N^2 TIA-s plus a summation amplifier, hence is less compact and consumes more power.

Assuming that thermal receiver noise dominates, we find for the signal power at the output of the $N \times N$ PD matrix receiver

$$S_{out} = \overline{m_0^2} (N \overline{a_{mk}} \mathcal{R} P_o |Z_T|)^2 \quad (7-30)$$

where $\overline{a_{mk}}$ denotes the average fraction of the beam's power which is captured by a photodiode (m,k) in the matrix. For the noise power we find

$$N_{out} = F_1 N_0 B |Z_T|^2 \quad (7-31)$$

where the TIA has a transimpedance Z_T , input noise current i_{th} , and noise figure F_1 . The SNR at the output of the PD matrix receiver is

$$\left(\frac{S_{out}}{N_{out}} \right)_{PD \text{ matrix}} = \frac{\overline{m_0^2} (N \overline{a_{mk}} \mathcal{R} P_o)^2}{F_1 N_0 B} \quad (7-32)$$

For the ADR, the signal power after the summation amplifier (with power gain G_2 and noise figure F_2) is

$$S_{out} = G_2 \overline{m_0^2} \left(\sum_{n=1}^{N^2} a_n \mathcal{R} P_o |Z_T| \right)^2 = G_2 \overline{m_0^2} (N^2 \overline{a_n} \mathcal{R} P_o |Z_T|)^2 \tag{7-33}$$

where $\overline{a_n}$ is the average fraction of the beam’s power which is captured by photodiode n (with $n=1, 2, \dots, N^2$) in the ADR constellation. The thermal noise contributions of the TIAs are uncorrelated, and thus add incoherently, yielding a noise power after the summation amplifier

$$\begin{aligned} N_{out} &= G_2 F_2 \left(\sum_{n=1}^{N^2} N_0 B |Z_T|^2 F_1 \right) \\ &= F_2 G_2 N^2 F_1 N_0 B |Z_T|^2 \end{aligned} \tag{7-34}$$

The SNR at the output of the ADR is

$$\left(\frac{S_{out}}{N_{out}} \right)_{ADR} = \frac{G_2 \overline{m_0^2} (N^2 \overline{a_n} \mathcal{R} P_o |Z_T|)^2}{F_2 G_2 N^2 F_1 N_0 B |Z_T|^2} = \frac{\overline{m_0^2} (N \overline{a_n} \mathcal{R} P_o)^2}{F_1 F_2 N_0 B} \tag{7-35}$$

(note that the amplifier noise factors F_1 and F_2 are always larger than 1).

Thus, from eqs. (7-32) and (7-35) it can be seen that the output SNR of the ADR is worse (by a factor F_2) than that of the PD matrix receiver.

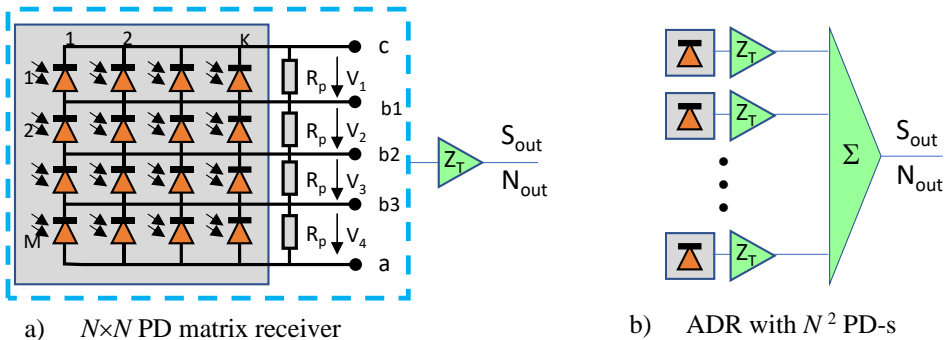


Fig. 7-6 Comparing the PD matrix receiver with an angular diversity receiver (ADR)

7.2 Capturing the optical beam by the photodiode matrix

In order to create a large aperture and thus to collect as much power of the incident optical beam onto the photodiode matrix as possible, an optical lens is used. For

minimizing the unbalance in the bias voltages of the photodiodes, the photodiodes should be illuminated as evenly as possible and therefore the spot projected onto the matrix should preferably cover the whole matrix. As shown in Fig. 7-7, this may be achieved by putting the matrix not in the focal plane of the lens, but slightly closer to it, so defocused over a distance x . This diminishes the captured power but increases the FoV angle.

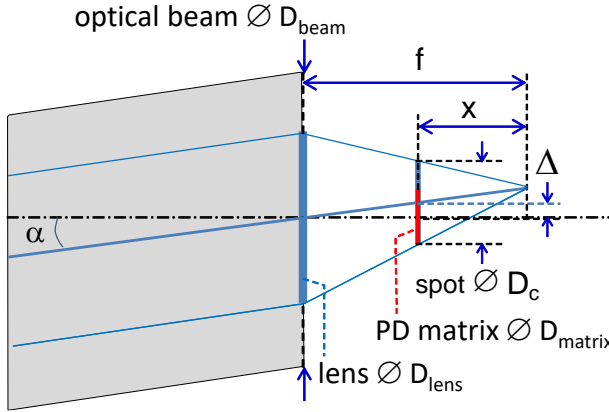


Fig. 7-7 Capturing the optical beam by the photodiode matrix in defocused position w.r.t. the lens (x : defocusing w.r.t. focal plane, Δ : displacement of spot w.r.t. center of PD matrix)

7.2.1 Theoretical analysis of the beam-to-photodiode matrix coupling

Fig. 7-7 illustrates how the optical beam is imaged by a lens system and captured by the photodiode matrix put in a defocused position with respect to the back focal plane of the lens. When assuming a beam with uniformly distributed intensity and diameter D_{beam} , and an aberration-free thin lens with diameter D_{lens} and focal length f , the diameter D_c of the beam's spot projected onto the matrix if the matrix is positioned with a defocusing factor $p = x/f$ (with $p < 1$) is

$$D_c = |p| \min(D_{beam}, D_{lens}) \quad (7-36)$$

When increasing the incidence angle α of the beam, the spot is moved away from the center of the photodiode matrix which is put on the axis of the lens. The displacement of the spot Δ w.r.t. the center of the PD matrix is

$$\Delta = (f - x) \tan \alpha = f(1 - p) \tan \alpha \quad (7-37)$$

The coupling of the beam to the PD matrix decreases as soon as the spot is no longer fully overlapping the PD matrix area. By defining the Field-of-View (FoV) α_{max} as the maximum incidence angle of the beam onto the lens for which the

spot is still fully overlaps the PD matrix area, i.e. for maintaining maximum coupling of the beam to the PD matrix, the FoV angle α_{max} is given by

$$\tan \alpha_{max} = \frac{|D_c - D_{matrix}|}{2f(1-p)} = \frac{|p| \min(D_{lens}, D_{beam}) - D_{matrix}|}{2f(1-p)} \quad (7-38)$$

Therefore, a lens with a small f is preferred in order to obtain a large FoV. It may be noted that putting the matrix beyond the focal plane, further away from the lens, i.e., at $p < 0$, will also increase D_c , but will yield a smaller FoV. Hence $0 \leq p < 1$ is the preferred defocusing range.

Typically, $D_{beam} \geq D_{lens}$. The maximum coupling fraction T_{max} of the beam's power P_{beam} onto all photodiodes of the matrix when $\alpha \leq \alpha_{max}$ is then

$$\begin{aligned} T_{max} &= \frac{P_{matrix}}{P_{beam}} \\ &= \cos \alpha \eta \left(\frac{D_{matrix}}{D_c} \right)^2 \left(\frac{D_{lens}}{D_{beam}} \right)^2 = \cos \alpha \cdot \eta \cdot \left(\frac{D_{matrix}}{p D_{beam}} \right)^2 \\ &\quad \text{for } D_{matrix}/D_{lens} < p < 1 \\ &= \cos \alpha \cdot \eta \cdot \left(\frac{D_{lens}}{D_{beam}} \right)^2 \quad \text{for } 0 \leq p \leq D_{matrix}/D_{lens} \end{aligned} \quad (7-39)$$

where D_{matrix} is the diameter of the circumscribing circle of the photodiode matrix, and η its fill factor (i.e. the sum of the active areas of all PDs divided by the total area of the circle). Assuming an $N \times N$ PD matrix where each photodiode has an active area with diameter D_0 and the spacing between the photodiodes is d , the diameter D_{matrix} of the matrix is (see Fig. 7-8)

$$D_{matrix} = 2R = \sqrt{2} (N-1)(D_0 + d) + D_0 \quad (7-40)$$

and the fill factor η of the matrix is

$$\eta = \left(\frac{N D_0}{D_{matrix}} \right)^2 = \left(\frac{N}{1 + \sqrt{2} (N-1) (1 + d/D_0)} \right)^2 \quad (7-41)$$

Typical data for commercially available 1×4 arrays of 2.5Gbit/s photodiodes [15] are $D_0 = 150 \mu\text{m}$ and a spacing which can be reduced to $d = 17 \mu\text{m}$, yielding a matrix diameter $D_{matrix} = 859 \mu\text{m}$ and fill factor $\eta = 48.8\%$. This implies an additional contribution of 3.11dB to the beam-to-PD matrix coupling loss when the matrix is uniformly illuminated.

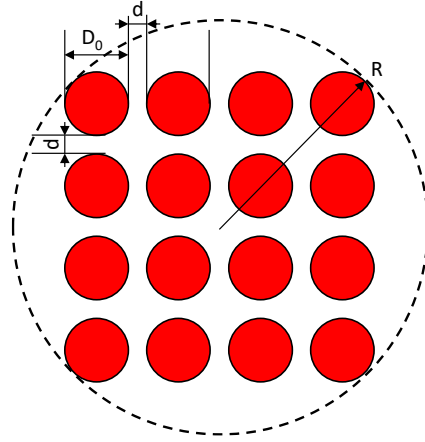


Fig. 7-8 $N \times N$ photodiode matrix (diameter PD active area D_0 , distance between PDs d , diameter of circumscribing circle of matrix $D_{matrix}=2R$)

By correcting for the current gain factor $1/N$ of the $N \times N$ photodiode matrix (see eq. (7-6)), an equivalent beam-to-photodiode matrix maximum power coupling factor $T_{max,eq}$ can be defined as

$$T_{max,eq} = T_{max}/N = \frac{\eta}{N} \left(\frac{D_{matrix}}{p D_{beam}} \right)^2 \cos \alpha$$

$$\text{for } D_{matrix}/D_{lens} < p < 1 \quad (7-42)$$

$$= \frac{\eta}{N} \left(\frac{D_{lens}}{D_{beam}} \right)^2 \cos \alpha \text{ for } 0 \leq p \leq D_{matrix}/D_{lens}$$

If $D_{beam} < D_{lens}$, the maximum coupling fraction T_{max} when $\alpha \leq \alpha_{max}$ is

$$T_{max} = \eta \left(\frac{D_{matrix}}{D_c} \right)^2 \cos \alpha = \eta \left(\frac{D_{matrix}}{p D_{beam}} \right)^2 \cos \alpha$$

$$\text{for } D_{matrix}/D_{beam} < p < 1 \quad (7-43)$$

$$= \eta \text{ for } 0 \leq p \leq D_{matrix}/D_{beam}$$

and the equivalent beam-to-photodiode matrix maximum power coupling factor $T_{max,eq}$ when corrected for the PD matrix current gain factor

$$T_{max,eq} = \frac{\eta}{N} \left(\frac{D_{matrix}}{p D_{beam}} \right)^2 \cos \alpha$$

$$\text{for } D_{matrix}/D_{beam} < p < 1 \quad (7-44)$$

$$= \frac{\eta}{N} \text{ for } 0 \leq p \leq D_{matrix}/D_{beam}$$

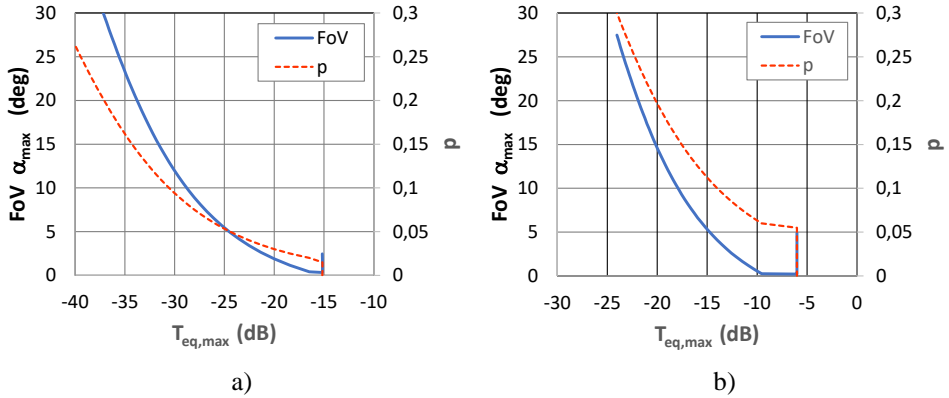
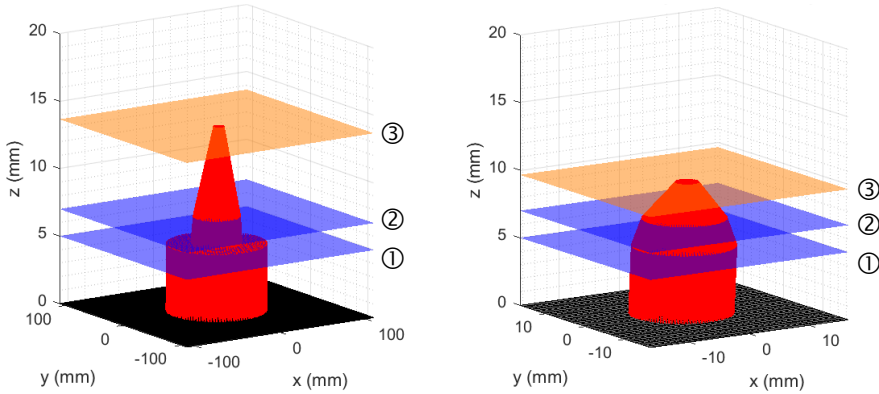


Fig. 7-9 Field-of-View α_{max} vs. beam-to-photodiode matrix coupling factor $T_{eq,max}$ with 4×4 PD matrix (single PD $D_0=150\mu\text{m}$, PD pitch $D_0+d=167\mu\text{m}$), when defocusing p is varied from 0 to 30%, for
 a) uniform beam $D_{beam}=100\text{mm}$, thin lens $D_{lens}=50\text{mm}$, $f=10\text{mm}$ (downstream)
 b) uniform beam $D_{beam}=15\text{mm}$, thin lens $D_{lens}=25\text{mm}$, $f=5\text{mm}$ (upstream)

Thus, the FoV of the receiver can be increased by defocusing the PD matrix, but at the expense of reducing the beam-to-PD matrix coupling. As an example, for a uniform beam and an ideal thin lens, and a 4×4 matrix of $\varnothing 150\mu\text{m}$ PIN photodiodes arranged at a pitch of $167\mu\text{m}$, by applying the equations (7-38), (7-42) and (7-44) Fig. 7-9 shows the compromise between FoV and beam-to-photodiode matrix coupling which can be set by adjusting the defocusing parameter p . In practice, the beam is not uniform and the lens is not ideal, hence a numerical analysis is needed by means of ray tracing.

7.2.2 Numerical analysis of the beam-to-photodiode matrix coupling

Typically, the beam diameter fills a significant part of (or is even considerably larger than) the lens diameter, hence lens aberrations will affect the imaging of the beam onto the photodiode matrix. Also, the beam does not have an ideal uniform intensity profile, but typically is assumed to have a Gaussian profile. We have developed a 3D ray tracing program in MATLAB, based on vector analysis according to the modelling described in the Appendix. With this program, we have assessed for a non-ideal lens and a non-uniform collimated beam how the equivalent beam-to-PD matrix power coupling factor T_{eq} depends on the beam incidence angle α when the defocusing p is varied.



- a) Downstream: Gaussian beam
 $D_{beam} = \varnothing 100\text{mm}$, Fresnel lens
 $D_{lens} = \varnothing 50\text{mm}$, $f = 10\text{mm}$, thickness
 2mm
- b) Upstream: Gaussian beam
 $D_{beam} = \varnothing 15\text{mm}$, Fresnel lens
 $D_{lens} = \varnothing 25\text{mm}$, $f = 5\text{mm}$, thickness
 2mm

Fig. 7-10 3D ray tracing for analyzing beam-to-PD matrix coupling (with 1027 rays, at defocusing $p=0.2$, and collimated beam incidence angle $\alpha=5\text{deg.}$; lens with Fresnel plane ① and flat plane ②; PD matrix plane ③)

Fig. 7-10 and Fig. 7-11 (calculated by ray tracing with 1027 rays for the downstream case) show how the collimated beam is projected onto the photodiode matrix, if the beam has a uniform profile or a Gaussian profile. With a Fresnel lens, a large light collection aperture D in combination with a short focal length f can be realized [12]. Its high D/f number enlarges the light collecting power of the OWC receiver. Its imaging properties are less good than those of well-corrected spherical lenses, but this is of less importance at the receiver site. When using an ideal thin lens and a Fresnel lens, both with $D_{lens} = 50\text{mm}$ and $f = 10\text{mm}$, Fig. 7-11 visualizes the impact of the lens aberrations introduced by the Fresnel lens for a defocusing $p=20\%$.

By high-resolution ray tracing with 25117 rays, we have analyzed the realistic case of a Gaussian beam with beam waist diameter $D_{beam} = 100\text{mm}$ and a Fresnel large aperture lens (optimized for minimum spherical aberration, and modeled for ray tracing according to the algorithms described in the Appendix section A.3) with effective focal length $f = 10\text{mm}$, thickness $d = 2\text{mm}$, and diameter $D_{lens} = 50\text{mm}$, as used in our laboratory experimental setup. We compared it with the theoretical case of a uniform beam with diameter $D_{beam} = 100\text{mm}$ and an ideal aberration-free thin lens with diameter $D_{lens} = 50\text{mm}$, as analyzed with eqs. (7-38) and (7-42). Examples of the modelling with 3D ray tracing are shown in Fig. 7-12. We have varied p from 0 to 30%, and derived by the ray tracing how the equivalent beam-to-photodiode coupling factor T_{eq} (including the fill factor η) depends on the beam incidence angle α and defocusing parameter p .

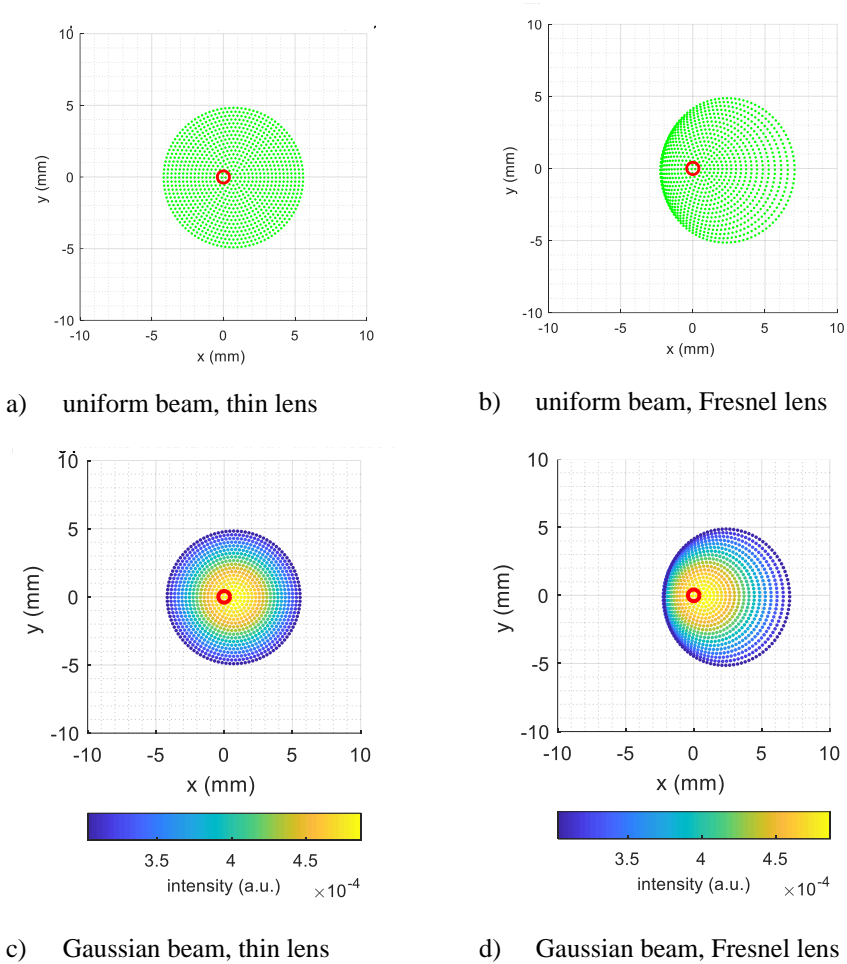


Fig. 7-11 Beam with width $D_{beam}=\varnothing 100\text{mm}$ projected onto photodiode matrix with diameter $D_{matrix}=859\mu\text{m}$ (red) for $\alpha=5\text{deg}$ and defocusing $p=20\%$ (both thin lens and Fresnel lens $D_{lens}=\varnothing 50\text{mm}$, $f=10\text{mm}$; 1027 rays traced)

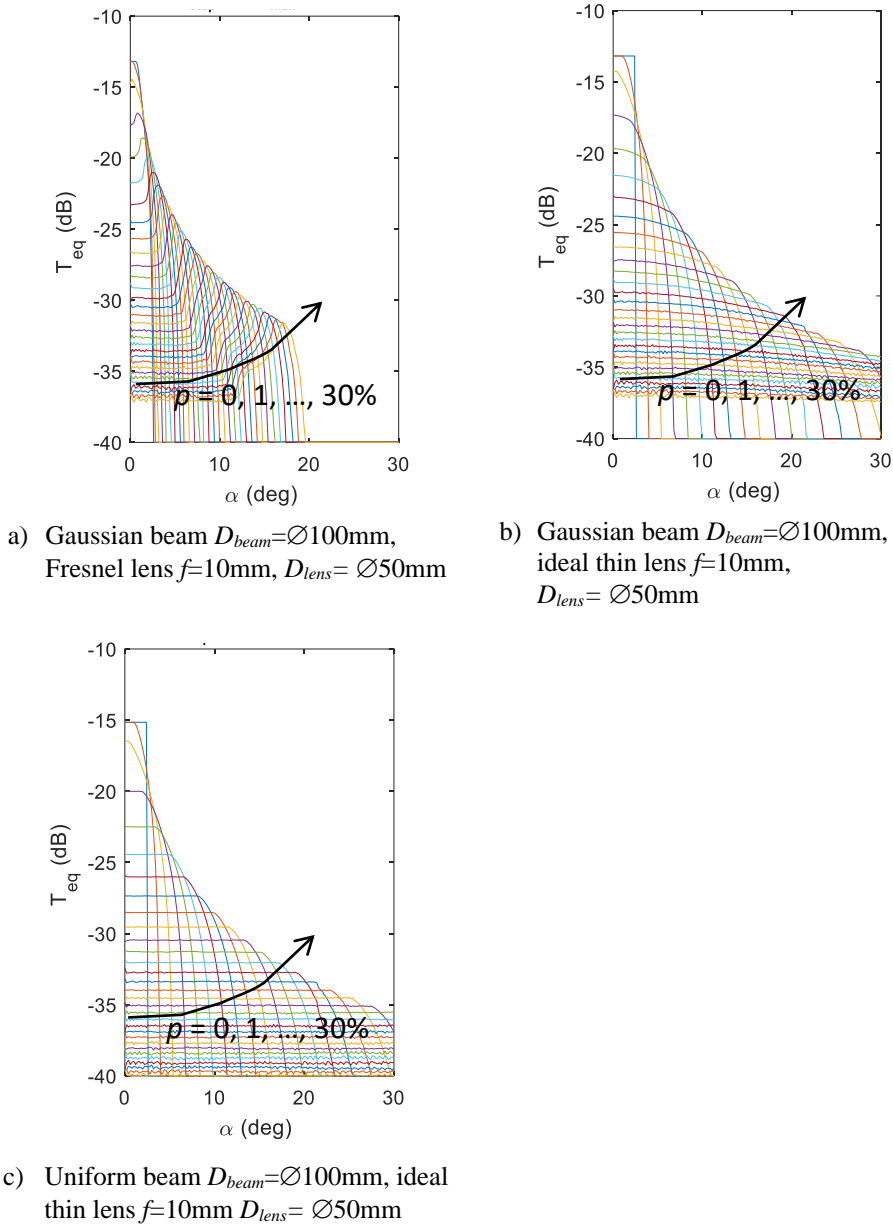
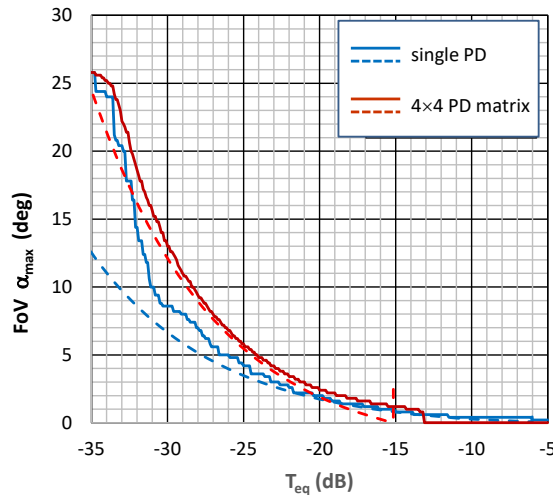


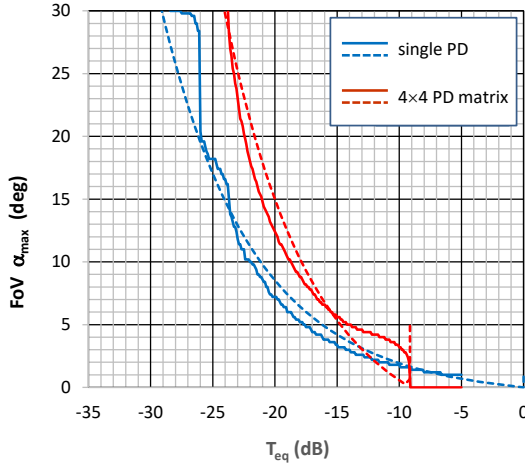
Fig. 7-12 Beam-to-photodiode power coupling factor T_{eq} versus beam incidence angle α of a beam with diameter $D_{beam}=\text{Ø}100\text{mm}$, using a 4×4 PD matrix ($D_{matrix}=859\mu\text{m}$, $\eta=48.8\%=-3.11\text{dB}$, $D_0=150\mu\text{m}$, $d=17\mu\text{m}$) and defocusing $p=0, 1, \dots, 30\%$. Calculated by ray tracing with 25117 rays.

The results in Fig. 7-12 calculated for a 4×4 PD matrix show how at a desired coupling factor T_{eq} typically the FoV maximum angle α_{max} can be increased by increasing the defocusing p . Increasing p also brings a decrease of T_{eq} at a given incidence angle α . The peaks which are observed in the T_{eq} -vs.- α curves of Fig. 7-12.a for the Fresnel lens and Gaussian beam at larger α and p are caused by lens aberrations. These peaks are absent for the aberration-free ideal thin lens with Gaussian beam in Fig. 7-12.b and with uniform beam in Fig. 7-12.c.

The FoV α_{max} decreases when the coupling T_{eq} has to be larger (and thus p smaller). In Fig. 7-13, the solid curves show the results from ray tracing (25117 rays, $p=0$ up to 30%; results are accurate up to $T_{eq}=-24$ dB) with the Gaussian beam and Fresnel lens for the 4×4 PD matrix and the single PD. These have been calculated for both the typical downstream case (in Fig. 7-13.a ; beam size $D_{beam}=\varnothing 100$ mm, lens $D_{lens}=\varnothing 50$ mm, $f=10$ mm) and the upstream case (in Fig. 7-13.b ; $D_{beam}=\varnothing 15$ mm, $D_{lens}=\varnothing 25$ mm, $f=5$ mm), as applied in our laboratory experiments. The dashed curves are from the analytically derived eqs. (7-38), (7-42) and (7-44) which hold for a uniform beam and an ideal thin lens. The results confirm that the FoV α_{max} obtainable with a 4×4 photodiode matrix ($D_{matrix}=0.86$ mm, $\eta=48.8\%$) is substantially higher than with a single photodiode ($D_0=150\mu\text{m}$).



a) Downstream: beam $D_{beam}=\varnothing 100$ mm, lens $D_{lens}=\varnothing 50$ mm with $f=10$ mm



b) *Upstream*: beam $D_{beam}=\text{Ø}15$ mm, lens $D_{lens}=\text{Ø}25$ mm with $f=5$ mm

Fig. 7-13 FoV α_{max} vs. beam-to-PD coupling T_{eq} for a single $\text{Ø}150\mu\text{m}$ PD (blue curves) and for a 4×4 matrix of $\text{Ø}150\mu\text{m}$ PDs spaced at $17\mu\text{m}$ (red curves) ; solid curves: by ray tracing with 25117 rays for Gaussian beam and Fresnel lens;dashed curves: by theoretical analysis with eqs. (7-38), (7-42) and (7-44), for uniform beam and ideal thin lens.

7.2.3 Impact of the fill factor of the photodiode matrix

For an $N\times N$ PD matrix, substituting from eq. (7-41)

$$D_{matrix} = \frac{N D_0}{\sqrt{\eta}} \quad (7-45)$$

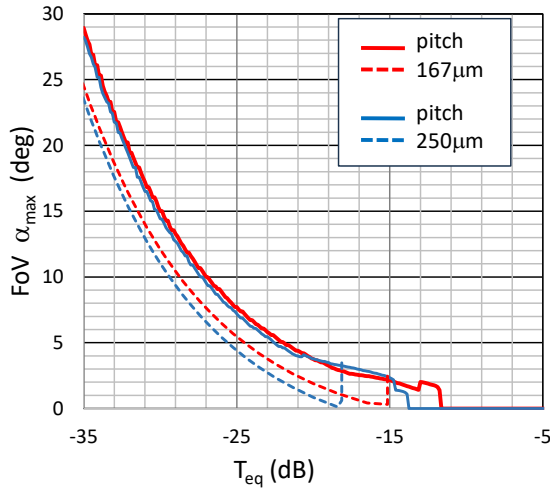
into eq. (7-42) yields if $D_c > D_{matrix}$ (i.e., if the beam spot fully overlaps the PD matrix)

$$\begin{aligned} T_{eq} &= \frac{\eta}{N} \left(\frac{D_{matrix}}{D_c} \right)^2 \cos \alpha = N \left(\frac{D_0}{D_c} \right)^2 \cos \alpha \\ &= N \left(\frac{D_0}{p D_a} \right)^2 \cos \alpha \end{aligned} \quad (7-46)$$

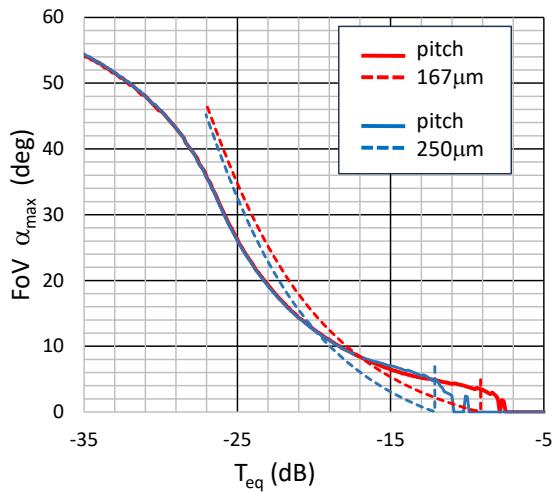
with $D_a = \min(D_{beam}, D_{lens}) = D_c/p$. From eq. (7-38) follows

$$\tan \alpha_{max} = \frac{D_0 N}{2 f \left(\sqrt{\frac{T_{eq}}{N \cos \alpha}} - \frac{D_0}{D_a} \right)} \left(1 - \sqrt{\frac{T_{eq}}{\eta N \cos \alpha}} \right) \quad (7-47)$$

Hence, for the theoretical case of a uniform beam and ideal thin lens and if the beam spot fully overlaps the PD matrix, it may be concluded that the fill factor η does not impact the equivalent beam-to-photodiode matrix power coupling factor T_{eq} , and hardly impacts the Field-of-View α_{max} when T_{eq} is small.



- a) *Downstream*: with Gaussian beam $D_{beam}=\varnothing 100\text{mm}$; thin lens $\varnothing 50\text{mm}$, $f=10\text{mm}$



- b) *Upstream*: with Gaussian beam $D_{beam}=\varnothing 15\text{mm}$; thin lens $\varnothing 25\text{mm}$, $f=5\text{mm}$

Fig. 7-14 Impact of fill factor η (in 4×4 PD matrix, with PD $\varnothing 150\mu\text{m}$, PD pitch $250\mu\text{m}$, $\eta=24.6\%$, PD pitch $167\mu\text{m}$, $\eta=48.8\%$; solid curves: by numerical integration, for Gaussian beam; dashed curves: by theoretical analysis, for uniform beam)

In the case of a Gaussian beam and ideal thin lens, the small impact of the fill factor η , in particular at small T_{eq} and thus at larger FoV, is confirmed by the results of a numerical integration analysis shown in Fig. 7-14.a when the beam is larger than the lens' aperture (the typical downstream case), and Fig. 7-14.b when it is smaller (the typical upstream case).

7.2.4 Shifting the receiver's aperture over the beam's footprint

In the analysis so far, it has been assumed that the lens aperture of the receiver was positioned in the center of the beam's footprint, i.e. the signal's cell. When the aperture is shifted, however, the power captured by the receiver will change, depending on the intensity profile of the beam and the diameter of the aperture. The power will decrease as part of the signal beam is lost. In addition, when the neighbouring cells are illuminated by beams as well, crosstalk from those cells into the signal's cell may occur. Moreover, the shape of the beam's spot reaching the photodetector may be deformed, which impacts the Field-of-View of the receiver.

7.2.4.1 Impact of crosstalk from neighbouring cells

For a uniform beam profile with diameter $D_{beam} = 2 R_{beam}$, the fraction of the beam's power captured by the receiver aperture with lens diameter $D_{lens} = 2 R_{lens}$ can be analytically calculated, as illustrated in Fig. 7-15. The position x_1 of the cord connecting the intersection points of the beam's circle and the lens' circle is for $R_{beam} - R_{lens} < x_{AP} < R_{beam} + R_{lens}$

$$x_1 = \frac{R_{beam}^2 - R_{lens}^2 + x_{AP}^2}{2 x_{AP}} \quad (7-48)$$

and the areas A_1 and A_2 are

$$A_1 = R_{beam}^2 \left\{ \frac{\pi}{2} - \arcsin\left(\frac{x_1}{R_{beam}}\right) - \frac{x_1}{R_1} \sqrt{1 - \left(\frac{x_1}{R_{beam}}\right)^2} \right\} \quad (7-49)$$

$$A_2 = R_{lens}^2 \left\{ \frac{\pi}{2} - \arcsin\left(\frac{x_{AP} - x_1}{R_{lens}}\right) - \left(\frac{x_{AP} - x_1}{R_{lens}}\right) \sqrt{1 - \left(\frac{x_{AP} - x_1}{R_{lens}}\right)^2} \right\} \quad (7-50)$$

For $x_{AP} \leq R_{beam} - R_{lens}$ there is a full overlap of the lens aperture by the beam, and for $x_{AP} \geq R_{beam} + R_{lens}$ there is no overlap. Using these equations, the fraction of the beam's power captured by the lens, i.e., the aperture coupling factor T_{AP} , versus the receiver shift x_{AP} for a uniform beam is

$$T_{AP} = \frac{P_{captured}}{P_{beam}} = \frac{A_1 + A_2}{\pi R_{beam}^2}$$

$$\text{for } R_{beam} - R_{lens} < x_{AP} < R_{beam} + R_{lens} \tag{7-51}$$

$$= 1 \text{ for } 0 \leq x_{AP} \leq R_{beam} - R_{lens}$$

$$= 0 \text{ for } x_{AP} \geq R_{beam} + R_{lens}$$

It may be noted that due to the (x,y) symmetry of the cell pattern, similar equations hold when the receiver moves in the -x direction, or the +y or -y direction.

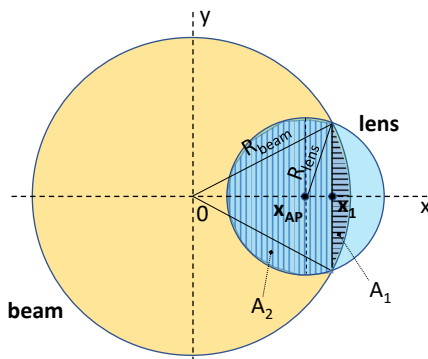


Fig. 7-15 Shifting the receiver's lens aperture with diameter $D_{lens} = 2 \cdot R_{lens}$ by a distance x_{AP} with respect to the beam's footprint with diameter $D_{beam} = 2 \cdot R_{beam}$

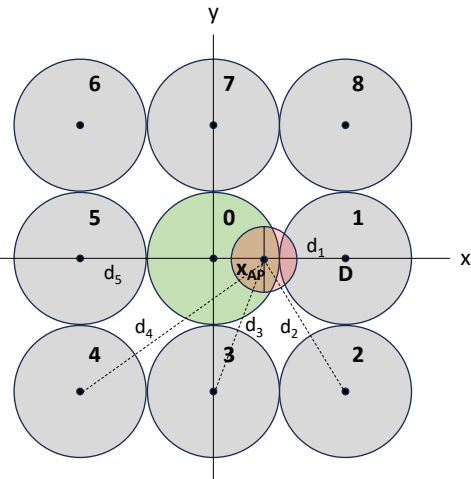


Fig. 7-16 Moving the receiver among multiple cells (cell 0: signal cell; cells 1-8: neighbour cells; red circle: lens aperture)

As illustrated in Fig. 7-16, the receiver may also capture power from neighbouring cells if these cells are receiving a beam as well. Thus, crosstalk from these cells into the signal cell may occur. Assuming that the cells are contiguous (in order to have optimum coverage of the user area) and receive identical power, the crosstalk coupling factor of the power from the closest adjacent neighbour cell (cell 1) into the receiver's signal cell (cell 0) is

$$XT_1(x_{AP}, D) = T_{AP}(d_1) = T_{AP}(D - x_{AP}) \tag{7-52}$$

where d_1 is the distance between the center of cell 1 and the center of the signal cell 0, and D is the spacing of the cells. Similarly, the crosstalk coupling factor from the other neighbour cells is given by

$$XT_n(x_{AP}, D) = T_{AP}(d_n) \text{ for } n = 2, \dots, 8 \quad (7-53)$$

where according to Fig. 7-16 the distances d_n are

$$\begin{aligned} d_2 &= \sqrt{d_1^2 + D^2} = \sqrt{D^2 + (D - x_{AP})^2} \\ d_3 &= \sqrt{x_{AP}^2 + D^2} \\ d_4 &= \sqrt{(D + x_{AP})^2 + D^2} \\ d_5 &= D + x_{AP} \end{aligned} \quad (7-54)$$

As the cells are contiguous, $D=D_{beam}$. Due to the symmetry around the x-axis, the shifting of the receiver along the x-axis implies $XT_6=XT_4$, $XT_7=XT_6$, $XT_8=XT_2$. The optical signal-to-crosstalk ratio $SXR_{1,opt}$ due to the crosstalk factor XT_1 from the closest cell 1 is

$$SXR_{1,opt}(x_{AP}, D) = \frac{T_{AP}(x_{AP})}{XT_1(x_{AP}, D)} = \frac{T_{AP}(x_{AP})}{T_{AP}(D - x_{AP})} \quad (7-55)$$

The crosstalk from the neighbouring cells can be regarded as incoherent interchannel crosstalk contributions w.r.t. the signal cell, and typically the crosstalk from the closest cell 1 is dominating the other crosstalk contributions from cells 2 to 8. The total crosstalk is the sum of all contributions, hence the signal-to-crosstalk ratio $SXR_{tot,opt}$ is given by

$$SXR_{tot,opt}(x_{AP}, D) = \frac{T_{AP}(x_{AP})}{\sum_{n=1}^8 XT_n(d_n)} \quad (7-56)$$

Following the analysis in [14], the bit error ratio BER when applying the optimum decision threshold in the receiver, assuming equally likely binary symbols “0” and “1” being sent, where P_0 is the power received for a “0” bit and P_1 for a “1” bit, is

$$BER = Q\left(\frac{\mathcal{R}(P_1 - P_0)}{\sigma_1 + \sigma_0}\right) \quad (7-57)$$

where \mathcal{R} is the responsivity of the photodiode, and σ_0 and σ_1 are the noise deviation for the “0” and the “1” bit, respectively. If the received signal is impaired by crosstalk with a crosstalk coupling ratio ε , and assuming that the noises are independent of the signal power (so no APD photodiode or optical amplifier is used) and the thermal noise of the receiver dominates, the power penalty incurred by single-neighbour crosstalk can be deduced from

$$P_1 - P_0 = P'_1 - P'_0 \quad (7-58)$$

where P_0' and P_1' represent the received powers in the “0” and “1” bit, respectively, including the crosstalk. Without crosstalk and assuming a perfect extinction ratio, $P_1 = P_s$ and $P_0 = 0$, where P_s is the peak received power per bit. The worst-case crosstalk impact occurs when $P_1' = P_s'$ and $P_0' = \varepsilon \cdot P_s'$, where ε is the crosstalk-to-signal ratio (so equivalently for the n^{th} crosstalk contributor $\varepsilon_n = XT_n/T_{AP}$). Hence the power penalty due to the crosstalk from a single neighbour is

$$PP = 10 \log \left(\frac{P'_s}{P_s} \right) = -10 \log(1 - \varepsilon) \quad (7-59)$$

With multiple interferers, their crosstalk power contributions in the worst case may be added. Hence, for M interferers with crosstalk ratios ε_n ($n=1, 2, \dots, M$) the power penalty PP is

$$PP = 10 \log \left(\frac{P'_s}{P_s} \right) = -10 \log \left(1 - \sum_{n=1}^M \varepsilon_n \right) \quad (7-60)$$

The power penalty incurred due to inter-channel crosstalk from a single interferer and from multiple ones (with equal ε_i) is shown in Fig. 7-17. For a crosstalk ratio $\varepsilon < -10\text{dB}$, the power penalty is less than 0.5dB with a single interferer, while it increases with multiple interferers, e.g., to 2.25dB for $M=4$ interferers.

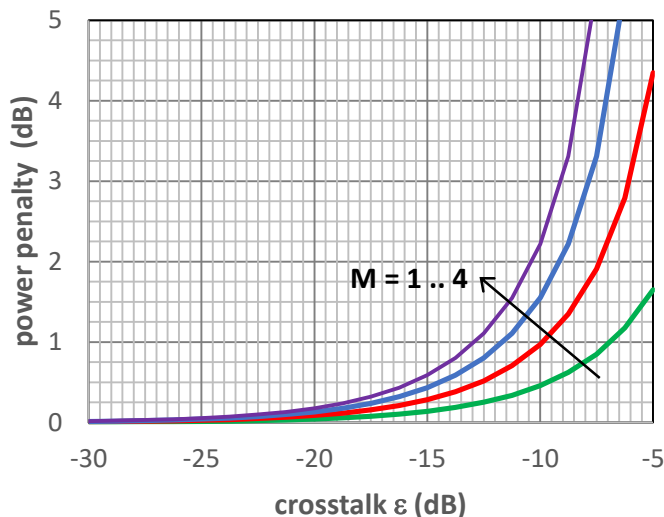


Fig. 7-17 Impact of inter-channel crosstalk vs. crosstalk ratio $\varepsilon=1/SXR$ per interferer (for $M=1, \dots, 4$ interferers with same ε)

For a uniform beam with a diameter $\varnothing 100\text{mm}$, $T_{AP}(x_{AP})$ and $XT_1(x_{AP}, D)$ have been calculated as a function of the receiver shift x_{AP} . It may be noted that due to the strictly confined beam profile only the closest neighbour cell 1 contributes crosstalk and the other cells 2-8 do not. The results are shown in Fig. 7-18 for lens apertures varying from $D_{lens}=20$ to $=50\text{mm}$. The aperture coupling factor T_{AP} will not change as long as the shift $|x_{AP}| \leq R_{beam} - R_{lens}$, but it will decrease for larger shifts. For smaller lens apertures, less power is captured and T_{AP} is smaller, but it will start to decrease only at larger shifts (i.e., for $|x_{AP}| > R_{beam} - R_{lens}$). The crosstalk factor XT_1 has been calculated for a cell spacing $D=100\text{mm}$, i.e. when the cells are contiguous. As all cells are identical, T_{AP} and XT_1 have opposite behaviour vs. x_{AP} . The resulting optical signal-to-crosstalk ratio SXR_{opt} vs. the shift x_{AP} is shown in Fig. 7-20.a. When $x_{AP}=D_{beam}/2=50\text{mm}$, i.e. when the receiver is at the edge of the signal cell, the receiver gets as much signal as crosstalk from the neighbouring interferer, hence $SXR_{opt}=0\text{dB}$. For a power penalty $<0.5\text{dB}$, using a lens diameter $D_{lens}=50\text{mm}$ a receiver shift $|x_{AP}|$ up to 32 mm is allowed, while for $D_{lens}=20\text{mm}$ the allowable shift $|x_{AP}|$ increases to 44mm.

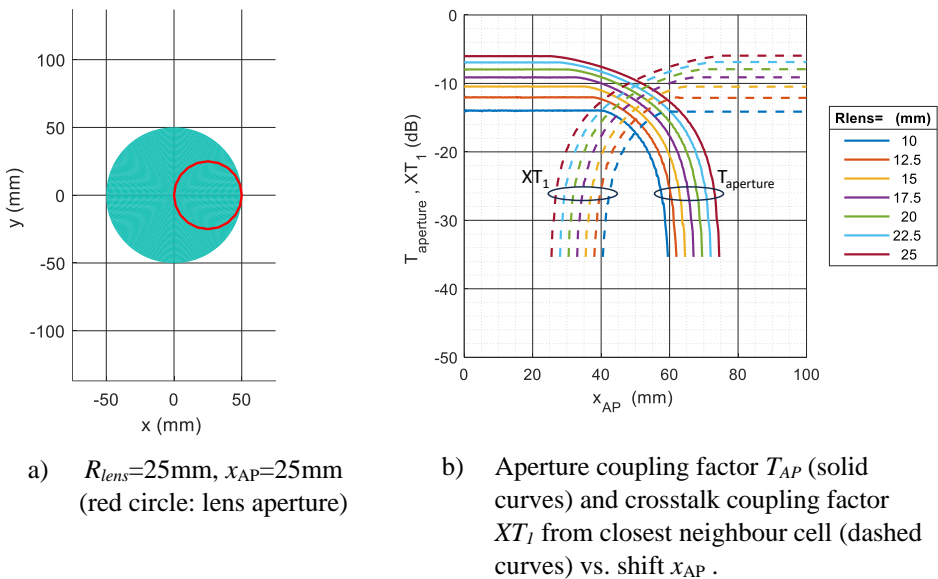


Fig. 7-18 Shifting the receiver’s lens aperture with diameter $D_{lens}=2 \cdot R_{lens}$ over a distance x_{AP} with respect to the center of the footprint of a uniform beam with beam diameter $D_{beam}=100\text{mm}$ (cell spacing $D=100\text{mm}$)

Similarly, for a Gaussian beam with waist $\varnothing 100\text{mm}$ and multiple interfering neighbour cells the aperture coupling factor $T_{AP}(x_{AP})$ and crosstalk coupling factors $XT_n(x_{AP}, D)$ vs. the receiver shift x_{AP} have been calculated by means of ray tracing, as shown in Fig. 7-19. The ray tracing is done by launching the rays from

an aperture with diameter equal to $3\times$ the beam waist, thus omitting only a fraction $1.5\cdot 10^{-8}$ of the Gaussian beam's power (see Table A- 1 in Appendix A). It can be observed that T_{AP} starts to decrease as soon as the receiver is shifted, but that it decreases slower when the lens aperture is larger. Hence, it is advantageous to maximize the lens aperture D_{lens} in order to reduce this decline.

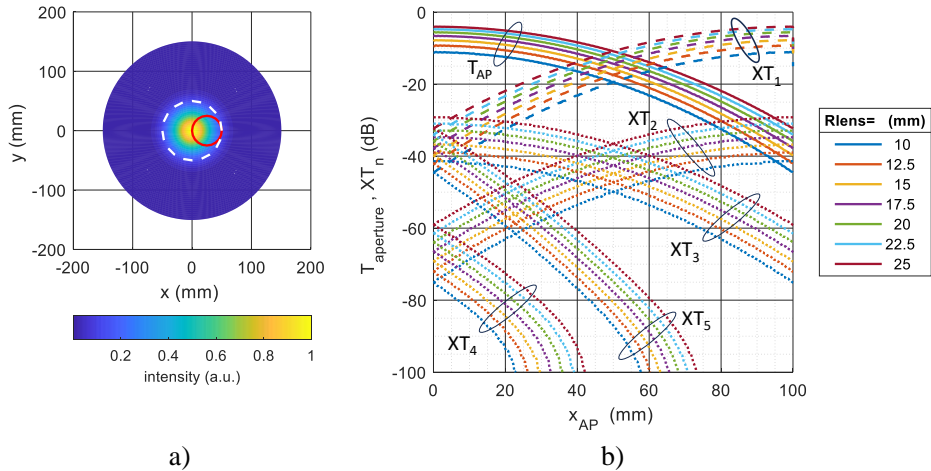
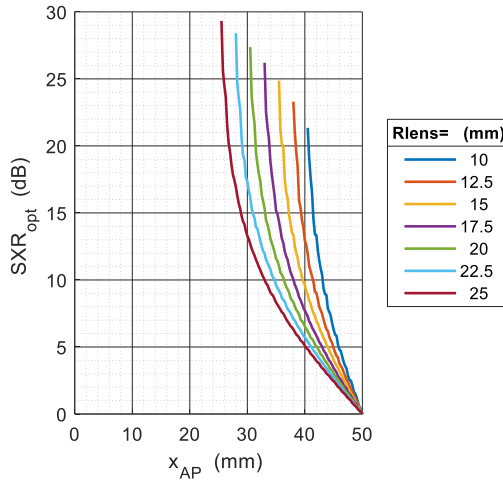


Fig. 7-19 Shifting the receiver's lens aperture with diameter $D_{lens}=2\cdot R_{lens}$ over a distance x_{AP} with respect to the center of the signal cell (no. 0 in Fig. 7-16) when using a Gaussian beam with beam waist diameter $D_{beam}=100\text{mm}$.

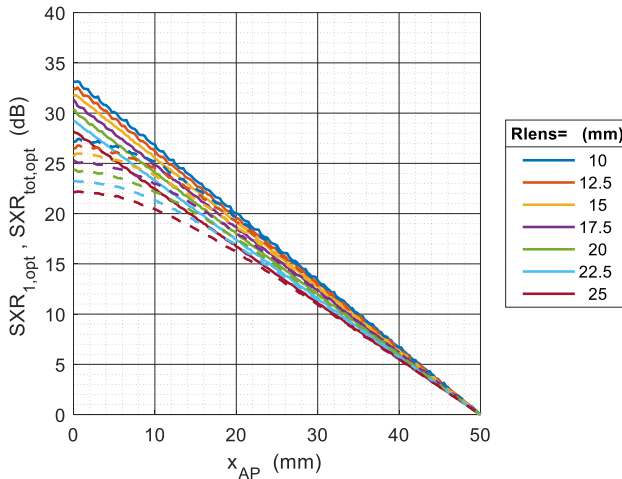
- a) Receiver aperture shifted by $x_{AP}=25\text{mm}$ w.r.t. the beam spot, (red circle: lens aperture, $R_{lens}=25\text{mm}$; white dashed circle: beam waist; ray tracing with 25117 rays)
- b) Aperture coupling factor T_{AP} (solid curves) and crosstalk coupling factors XT_n from neighbour cells (dashed curve XT_1 for closest neighbour; dotted curves XT_2 through XT_5) vs. shift x_{AP} . Lens apertures $D_{lens}=20 \dots 50\text{mm}$. Cell spacing $D=100\text{mm}$. Ray tracing with 50311 rays per beam.

It may be noted that crosstalk contributions XT_1 and XT_2 increase when T_{AP} decreases (so for increasing x_{AP}), but that XT_3 , XT_4 and XT_5 increase. Clearly the dominating crosstalk is XT_1 which comes from the closest neighbour cell 1. It may be noted that the lens aperture $D_{lens}=2\cdot R_{lens}$ should be minimized to minimize the crosstalk. The optical signal-to-crosstalk ratio $SXR_{J,opt}$ as well as the signal-to-crosstalk ratio $SXR_{Iob,opt}$ taking the crosstalk contributions from all neighbour cells into account are shown for a range of lens diameters in Fig. 7-20.b. The difference between both sets of curves is small, in particular for a larger receiver shift x_{AP} , which shows the strong dominance of the crosstalk from the closest cell 1 above the crosstalk contributions from the other cells. When the receiver is shifting to

the edge of the signal cell, so for x_{AP} approaching $D_{beam}/2=50\text{mm}$, the SXR curves converge towards $SXR_{opt}=0\text{dB}$. For a power penalty $<0.5\text{dB}$ with a single interferer, with a Gaussian beam $D_{beam}=100\text{mm}$ and a lens diameter $D_{lens}=50\text{mm}$ a receiver shift $|x_{AP}|$ up to 32 mm is allowed, while for $D_{lens}=20\text{mm}$ the allowable shift $|x_{AP}|$ increases somewhat to 35mm. The aperture coupling factor T_{AP} , however, is considerably reduced when D_{lens} decreases from 50 to 20mm.



a) for uniform beams (only crosstalk from cell 1)



b) for Gaussian beams (solid curves: crosstalk from cell 1; dashed curves: crosstalk from all neighbour cells)

Fig. 7-20 Optical signal-to-crosstalk ratio SXR_{opt} vs. receiver shift x_{AP} , for varying lens apertures (beam diameter $D_{beam}=100\text{mm}$)

It may be noted that in case of using the AWGR-based beam steerer (cf. section 5.3) crosstalk into the signal cell may also stem from adjacent wavelength channels in the AWGR which leak into the signal's output port of the AWGR; typically, such crosstalk is less than -20dB w.r.t. the signal and does not noticeably impact the system's performance.

7.2.4.2 Impact of cropping the beam's spot by the lens' aperture

Next to the decrease in captured power caused by the shift, the change in the intersection of the beam with the lens' aperture also affects the shape and intensity profile of the spot projected on the photodiode, and thus may affect the FoV of the receiver. By means of ray tracing, the impact of the shift on the equivalent beam-to-PD coupling efficiency T_{eq} as well as on the FoV of the receiver have been assessed. Fig. 7-21 shows how the shape and intensity profile of the spot change due to the shift.

The impact of the shift may be reduced by optimizing the defocusing parameter p at each new position of the receiver; this implies additional control complexity for adapting the position of the PD matrix with respect to the lens. Even when applying this re-optimization of p , the impact of the shift on the T_{eq} and the FoV is significant. For the 4×4 PD matrix receiver, the results of ray tracing in Fig. 7-22.a show that the FoV attainable for $T_{eq} = -30\text{dB}$ is reduced from 13 deg. to 2 deg. (half-angle) when the receiver is shifted away from the center over 50mm. For the single PD receiver, Fig. 7-22.b shows that the attainable FoV then declines a bit faster, from 12 deg. to less than 1 deg.

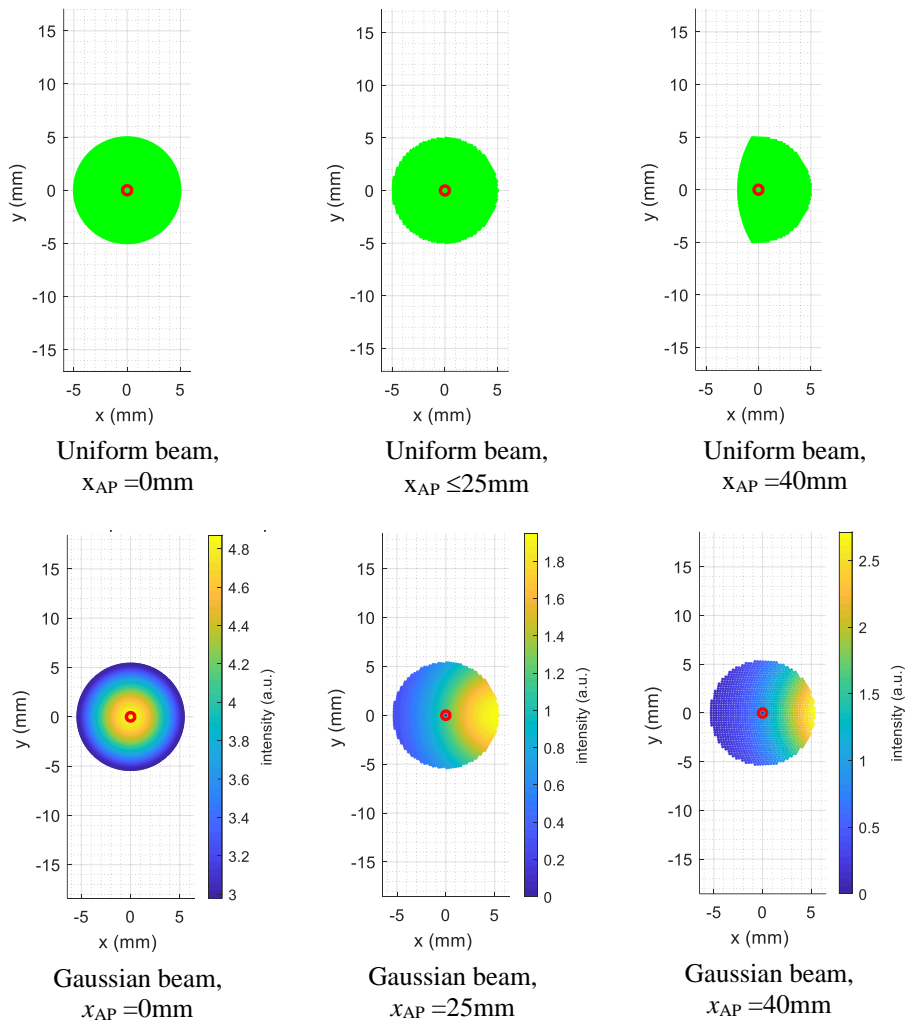


Fig. 7-21 Beam spot projected on PD matrix when receiver aperture shifts over distance x_{AP} from the center of the beam (for beam diameter $D_{beam} = \varnothing 100$ mm, and Fresnel lens with aperture $D_{lens} = \varnothing 50$ mm, $f = 10$ mm, with defocusing $p = 20\%$)

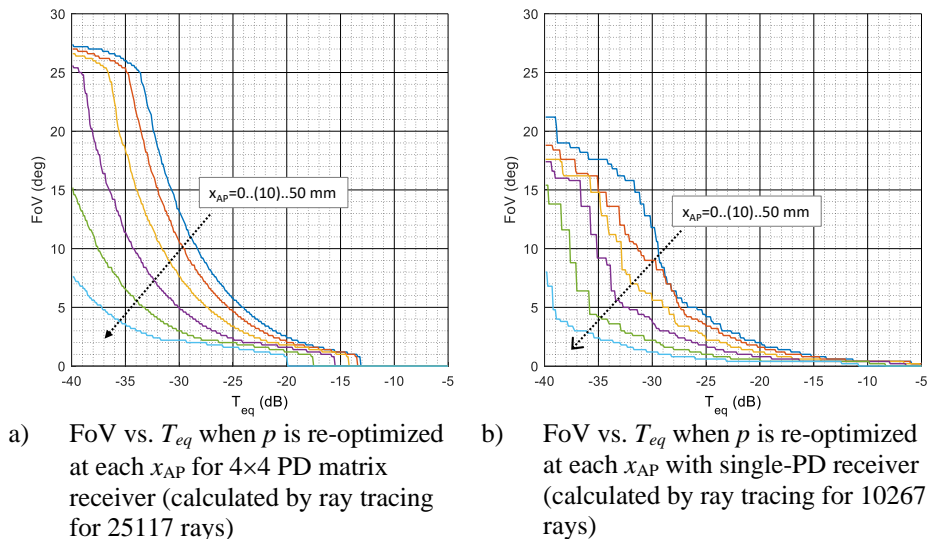
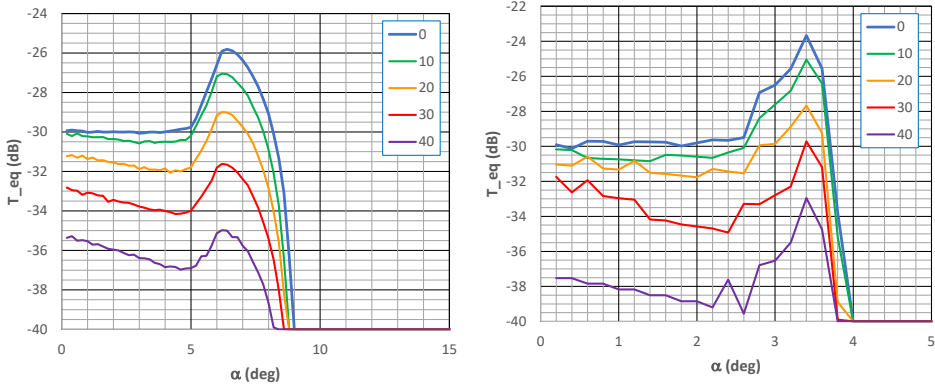


Fig. 7-22 Impact of shifting the receiver over a distance x_{AP} with respect to the center of the beam's footprint when applying a) the 4×4 PD matrix and b) a single PD. Assumptions: Gaussian beam, waist diameter $\varnothing 100$ mm, and receiver with Fresnel lens, aperture $\varnothing 50$ mm, $f=10$ mm.

To limit the complexity in the cost-sensitive receiver, it may be preferred to optimize and fix p in order to obtain a maximum FoV at an acceptable T_{eq} when the receiver is positioned in the center of the beam, and not to alter this defocusing p when the receiver is moved. By ray tracing, the dependence of T_{eq} on the beam incidence angle α for various settings of p when changing the shift x_{AP} has been assessed, similarly as done in the ray tracing analysis reported in section 7.2.2. For the 4×4 PD matrix receiver and shift $x_{AP}=0$, Fig. 7-23.a shows that a $T_{eq} > -30$ dB for α up to the FoV half-angle $\alpha_{max}=8.2$ deg. is achieved when adopting a fixed $p=13.5\%$. The table lists the reduction in T_{eq} and in the FoV half-angle α_{max} when the shift x_{AP} of the receiver with respect to the center of the Gaussian beam grows from 0 to 40mm, as illustrated in Fig. 7-21. Similarly, Fig. 7-23.b shows the impact of the shift for the single PD receiver, for which a fixed $p=7.0\%$ is adopted to guarantee a $T_{eq} > -30$ dB for α up to $\alpha_{max}=3.7$ deg.

It may be concluded that the impact of the receiver shift on the equivalent beam-to-PD coupling T_{eq} is approximately the same for the PD matrix receiver and the single-PD receiver, but that the FoV performance of the PD matrix receiver is clearly better.

If there are active neighbour beams, also crosstalk power from these beams may be captured by the receiver. Because the distances between the signal beam and these neighbour beams will be small with respect to the distant ceiling unit, the incidence angles of the neighbour beams are approximately equal to the incidence angle of the signal beam. Hence, the impact of such crosstalk on the receiver’s T_{eq} -vs.- α performance shown in Fig. 7-23 may be found by including the (typically small) power penalty due to the crosstalk (as analyzed in section 7.2.4.1 and shown in Fig. 7-20) into the beam-to-photodetector coupling efficiency T_{eq} .



x_{AP} (mm)	T_{eq} (dB)	FoV α_{max} (deg.)
0	>-30	8.2
<20	>-32	7.9
<30	>-34	7.6
<40	>-37	7.5

x_{AP} (mm)	T_{eq} (dB)	FoV α_{max} (deg.)
0	>-30	3.7
<20	>-32	3.65
<30	>-34	3.63
<40	>-37	3.8

a) with 4x4 PD matrix receiver, and fixed $p=13.5\%$

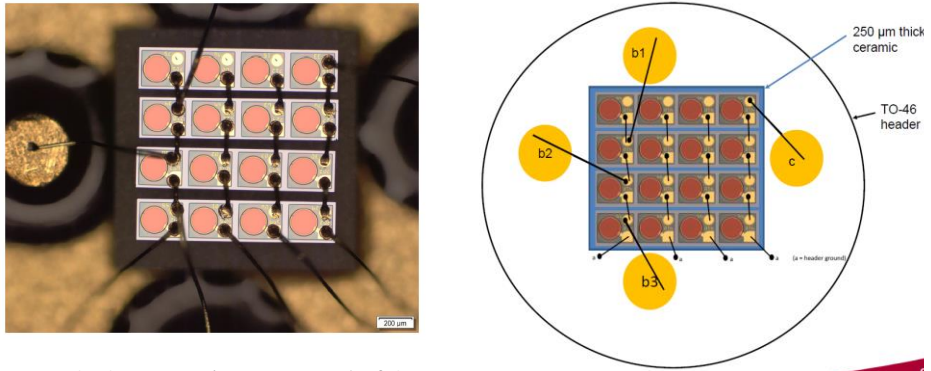
b) with single PD receiver, and fixed $p=7\%$

Fig. 7-23 Impact on the beam-to-PD coupling factor T_{eq} versus beam incidence angle α of shifting the receiver across the beam’s footprint (over a distance x_{AP} from 0 to 40mm), if the defocusing factor p is not re-optimized, but fixed: for a) the 4x4 PD matrix receiver with a fixed $p=13.5\%$, and b) the single PD receiver with a fixed $p=7.0\%$. Same assumptions as in Fig. 7-22.

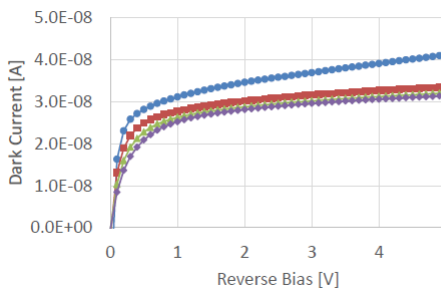
7.3 Implementing the receiver

We have designed a 4x4 PD matrix composed of four 1x4 arrays photodiodes which each have an active area diameter of $\varnothing 150\mu\text{m}$ and are spaced at a pitch of $250\mu\text{m}$. These arrays can support 2.5Gbit/s OOK-modulated data, and are

available from Albis Optoelectronics [15], who manufactured the photodiode arrays, interconnected them by wire bondings, and packaged them in a low-profile TO-46 can; see Fig. 7-24.a and .b

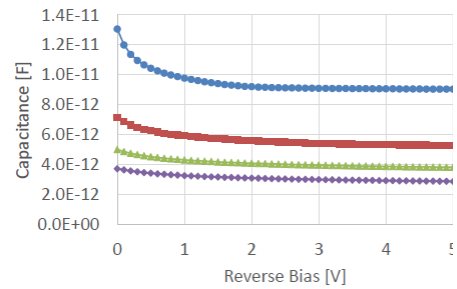


- a) 4×4 PD matrix, composed of 4 wire-bonded 1×4 arrays of $\varnothing 150\mu\text{m}$ 2.5Gbit/s photodiodes



- c) dark currents vs. reverse bias voltage on the PD matrix

- b) wiring diagram



- d) capacitances vs. reverse bias voltage on the PD matrix (a: anode side of the whole matrix, c: cathode side, b1-b3: the 3 intermediate levels; see Fig. 7-1.b)

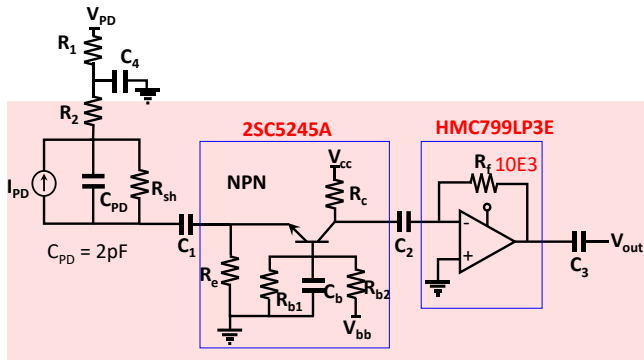
Fig. 7-24 4×4 PD matrix (assembled and characterized by Albis Optoelectronics)

The photodiode matrix is equipped with the taps according to the concept of Fig. 7-1.b for connecting external resistors and thus minimizing the bias voltage unbalances when the photodiodes are unevenly illuminated (as discussed in section 7.1). Measurements on the completed packaged PD matrix performed by Albis Optoelectronics confirmed the validity of our PD matrix concept. The results are shown in Fig. 7-24.c and Fig. 7-24.d. Fig. 7-24.c shows that the dark current gradually declines when more rows of the matrix are cascaded; for the whole matrix, it is $\sim 2.9\text{nA}$ at 5V reverse bias voltage. The measured cathode-to-

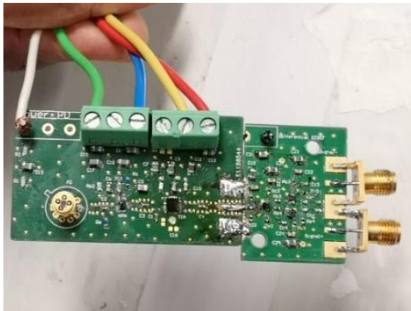
anode capacitance of the matrix (c-a curve in Fig. 7-24.d) was found to be $\sim 3\text{pF}$ for a matrix reverse bias voltage $>1.5\text{V}$, which is indeed equal to the specified capacitance of $\sim 2.3\text{pF}$ of a single PD plus a parasitic capacitance of $\sim 0.7\text{pF}$ added by the TO-46 can. It may also be noted that the capacitance is only weakly dependent on the reverse bias voltage beyond 1.5V . The other curves b1-a to b3-a illustrate how the capacitance indeed decreases by cascading more rows.

With the packaged 4×4 PD matrix we built the OWC receiver circuit of which the circuit diagram is shown in Fig. 7-25.a. A common-base transistor front-end amplifier stage was applied in order to minimize the impedance load to the PD matrix and thus maximize bandwidth, followed by a 700MHz bandwidth $10\text{k}\Omega$ commercially available transimpedance amplifier (TIA). Fig. 7-25.b shows the complete assembly, mounted on an epoxy printed circuit board. The measured frequency characteristics of this receiver are given in Fig. 7-25.c; the measured -3dB bandwidth is 670MHz , so just slightly reduced with respect to the bandwidth of the TIA. The OWC receiver module was equipped with a Fresnel lens with a large D/f ratio ($f=10\text{mm}$, $D_{\text{lens}}=\text{Ø}50\text{mm}$) in order to maximize its FoV; see Fig. 7-25.d. A commercial bidirectional GbE SMF-to-RJ45 media converter was adapted to incorporate our OWC receiver module; this combination has been successfully deployed in our laboratory system experiments showing optical wireless high-definition GbE video streaming to a laptop.

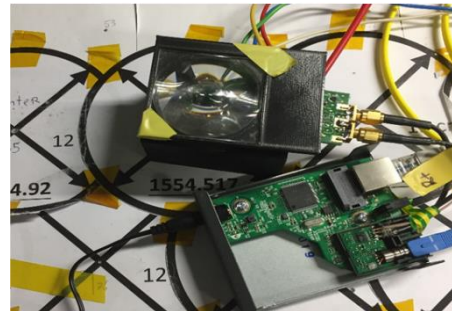
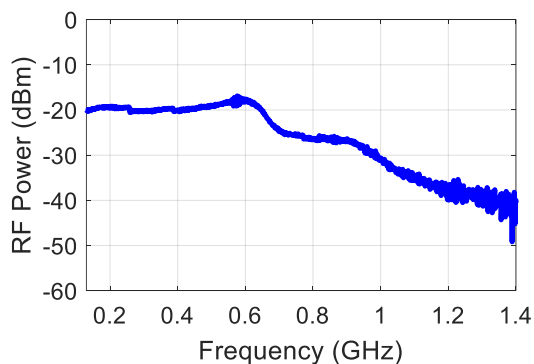
The performance of the PD matrix is impacted by the circuit parasitic impedances inherent to the wire bonding. This performance may be improved by additional on-chip integration steps, in particular by adding pre-defined tracks to the chip's metallization mask which add only minimal parasitic effects and interconnect the photodiodes instead of the external wire bondings used in our experiments.



a) OWC front-end receiver circuit



b) OWC receiver, assembled on a printed circuit board including packaged 4×4 PD matrix module with front-end receiver and a differential output stage

d) downstream OWC receiver module equipped with $\varnothing 50\text{mm}$ Fresnel lens and combined with GbE media converter module providing an RJ45 outlet

c) Measured frequency characteristics of the OWC receiver

Fig. 7-25 Prototype of OWC receiver with 4×4 photodiode matrix

7.4 Experimental validation

The performance of prototypes of the OWC receiver has been evaluated in our laboratory testbed outlined in Fig. 7-26 (which we also used for the localization experiments, see section 6.3.2).

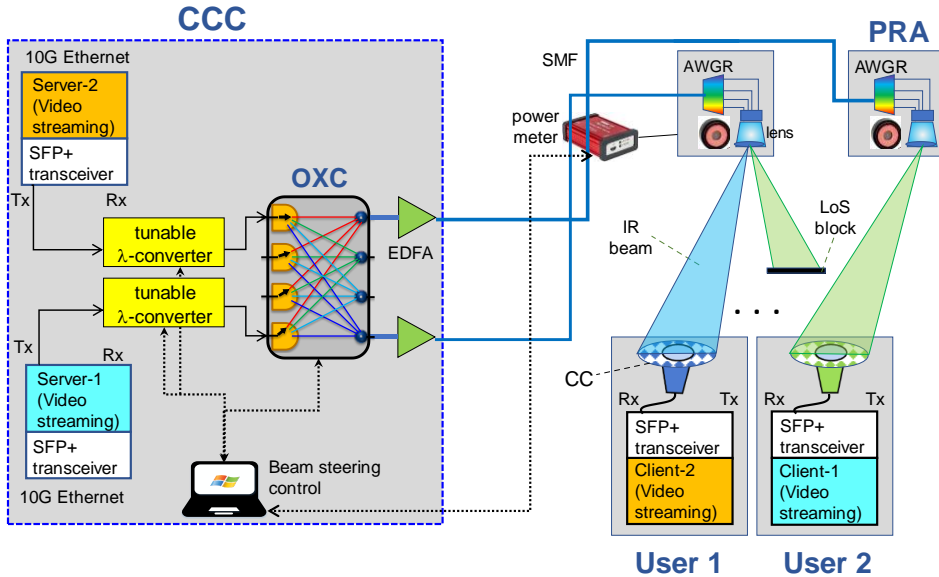


Fig. 7-26 Indoor OWC laboratory testbed

We added a single-input dual-output converter stage after our novel wide-FoV receiver and measured the BER performance at each output as well as at the combined differential output. A receiver sensitivity (per PD element) of -30.5dBm at 1Gbit/s and of -29.0dBm at 1.25Gbit/s (GbE, Gigabit Ethernet speed) was measured (see Fig. 7-27).

Equipped with a large aperture Fresnel lens ($\varnothing 50\text{mm}$, $f=10\text{mm}$), we measured the FoV in our laboratory setup. As shown in Fig. 7-28, error-free ($\text{BER} < 10^{-9}$) performance was achieved over a sizable area when moving the receiver, being more than 3.5 cells wide with a cell-to-cell center spacing of $\sim 9\text{cm}$ at a distance of $\sim 180\text{cm}$ from the beam-steerer (PRA). This corresponds to a FoV half-angle $\alpha \approx 10$ degrees, which is in line with the simulation results reported in Fig. 7-13.a.

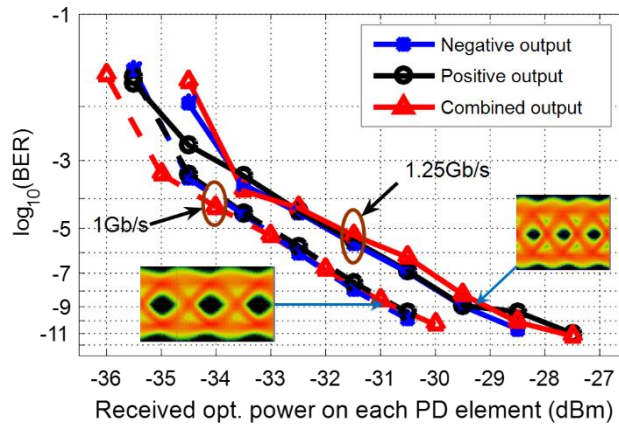


Fig. 7-27 BER performance for various OOK bitrates

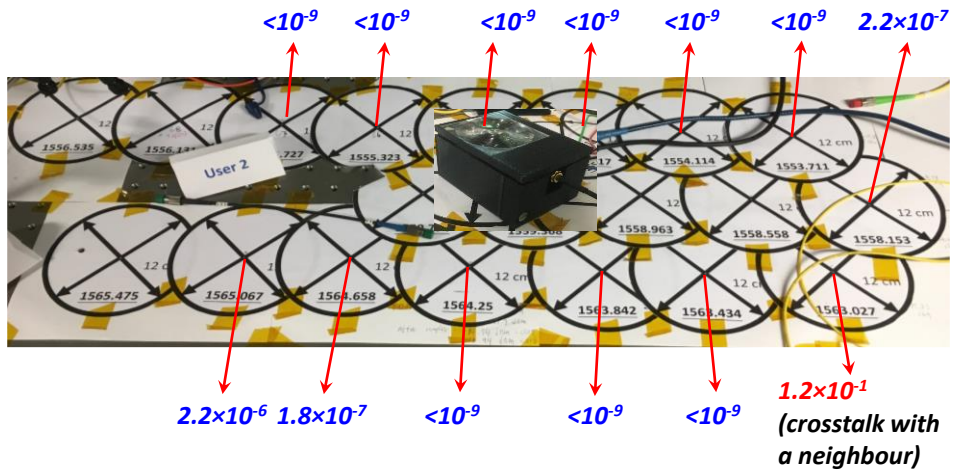


Fig. 7-28 FoV assessment at 1Gbit/s; error-free transmission found within 10 deg. from the center cell (cell diameter 10cm)

Moreover, we adapted a commercially available GbE fiber-to-RJ45 media converter in order to combine it with our OWC receiver. As shown in Fig. 7-29, we successfully demonstrated real-time high-definition GbE video streaming at a laptop computer using its RJ45 input.

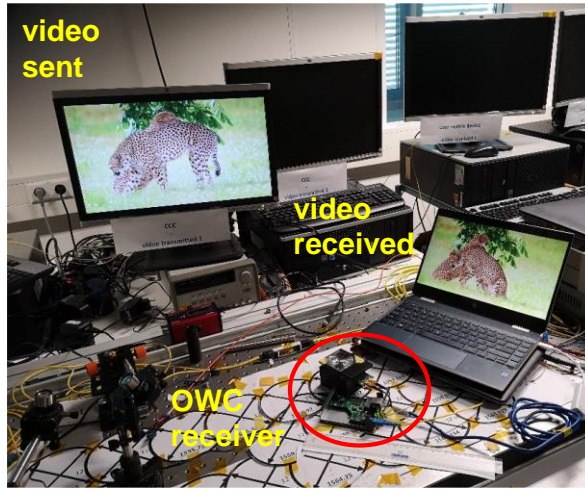
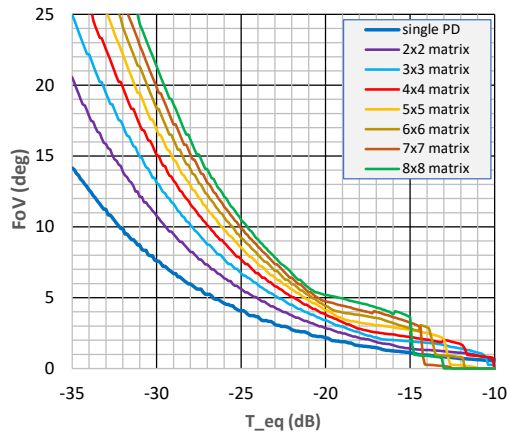


Fig. 7-29 GbE video streaming by OWC to laptop

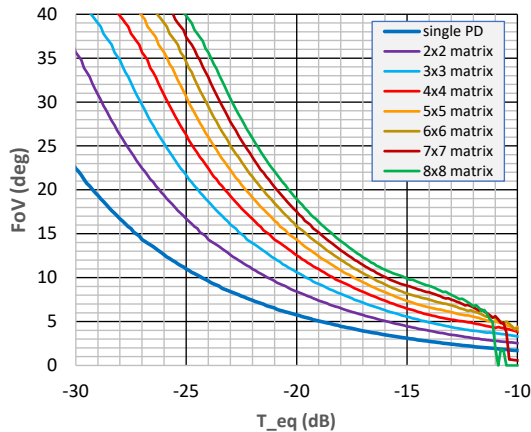
7.5 Scaling the PD matrix

The impact on the FoV of scaling the PD matrix to other $N \times N$ dimensions has been analyzed by numerical integration for the case of a Gaussian beam profile and an ideal aberration-free thin lens. For downstream (launching a Gaussian beam with waist $\varnothing 100\text{mm}$ and power $P_0=10\text{dBm}$ and using a thin lens with $D_{lens}=50\text{mm}$ and $f=10\text{mm}$), at a required $T_{eq}=-30\text{ dB}$ according to Fig. 7-30.a the attainable FoV is $\pm 7.5\text{ deg.}$ for a single PD and grows from $\pm 11\text{ deg.}$ to $\pm 21\text{ deg.}$ when the PD matrix is enlarged from 2×2 to 8×8 . For upstream (with a Gaussian beam of $+2\text{dBm}$ power and waist $\varnothing 15\text{mm}$, and a thin lens with $D_{lens}=25\text{mm}$ and $f=5\text{mm}$), at a required $T_{eq}=-22\text{ dB}$ an FoV $\approx \pm 11\text{ deg.}$ is attainable for a single PD. An FoV growing from $\pm 11\text{ deg.}$ to $\pm 26\text{ deg.}$ can be achieved when the PD matrix size is increased from 2×2 to $8 \times 8\text{ deg.}$

Upscaling the PD matrix thus increases the FoV performance, but this FoV improvement becomes less significant at larger matrix sizes. The scalability of our PD matrix concept has been validated at high data rates; 25Gbit/s NRZ modulated transmission over 20 m has been demonstrated with a 20×20 matrix of $\varnothing 30\ \mu\text{m}$ PD-s [13].



a) downstream (Gaussian beam $\varnothing 100$ mm, thin lens $\varnothing 50$ mm, $f=10$ mm)



b) upstream (Gaussian beam $\varnothing 15$ mm, thin lens $\varnothing 25$ mm, $f=5$ mm)

Fig. 7-30 Impact of scaling the PD matrix on the FoV

7.6 Concluding remarks

The photodiode matrix concept offers powerful solutions for realizing high-bandwidth receivers for optical wireless communication with an enlarged FoV and aperture. Thus, it eases optical beam alignment issues and increases the operational area.

Numerical ray tracing shows that with a 4×4 PD matrix a clearly better FoV vs. beam-to-photodetector coupling T_{eq} receiver performance can be achieved than with a single PD. It is found that the fill factor of the PD matrix has little

impact on this performance when the PD matrix is over-filled (which is the typical case in the large-FoV receiver design optimization).

Moreover, with respect to alternative solutions such as angular diversity receivers and receivers with adaptable optics, the PD matrix receiver can be less complex, consume less power, and achieve a better SNR performance. Shifting the receiver in the user plane will reduce its performance; it brings a power penalty and the FoV is reduced as well. According to numerical analysis, a shift within 70% of the beam cell radius does not seriously affect the receiver's performance.

Experimental validation of a front-end receiver built with a 4×4 PD matrix (assembled by wire-bonding commercial 1×4 linear arrays of $\varnothing 150\mu\text{m}$ photodiodes) and a commercially available TIA (750MHz bandwidth, 10k Ω transimpedance) has shown good receiver performance at 1.25Gbit/s.

Scaling the PD matrix to larger dimensions can further improve the receiver's FoV performance, albeit the improvement slows down at high dimensions.

7.7 References

- [1] Optics law of conservation of etendue [Online]. Available: <https://en.wikipedia.org/wiki/Etendue> .
- [2] J. Zeng, V. Joyner, J. Liao, S. Deng, Z. Huang, "A 5Gb/s 7-channel current-mode imaging receiver front-end for free-space optical MIMO," *Proc. IEEE MWSCAS2009*, Cancun, pp. 148-151.
- [3] Z. Zeng, M. Dehghani Soltani, M. Safari, H. Haas, "Angle Diversity Receiver in LiFi cellular networks," *Proc. ICC2019*, Shanghai, July 2019.
- [4] R. Winston, "Dielectric compound parabolic concentrators," *Appl. Opt.* , vol. 15, no. 2, Feb. 1976, pp. 291–292.
- [5] K. Wang, A. Nirmalathas, C. Lim, K. Alameh, and E. Skafidas, "Full duplex gigabit indoor optical wireless communication system with CAP modulation," *Photon. Technol. Lett.*, vol. 28, no. 7, pp. 790–793, Apr. 2016.
- [6] S. Collins, D. C. O'Brien, and A. Watt, "High gain, wide field of view concentrator for optical communications," *Opt. Lett.*, vol. 39, no. 7, Apr. 2014, p. 1756-1759.
- [7] A. Riaz and S. Collins, "A wide field of view VLC receiver for smartphones," *Proc. ECOC2020*, Brussels, Dec. 2020, paper Tu2G.4.
- [8] Z. Cao, L. Shen, Y. Jiao, X. Zhao, A. M. J. Koonen, "200 Gbps OOK transmission over an indoor optical wireless link enabled by an integrated cascaded aperture optical receiver," *Proc. OFC2017*, Los Angeles, post-deadline paper Th5A.6.
- [9] A. M. J. Koonen, K. A. Mekonnen, F. M. Huijskens, Z. Cao, E. Tangdiongga, "Novel Broadband OWC Receiver with Large Aperture and Wide Field of View", *Proc. ECOC2020*, Brussels, Dec. 2020, paper Tu2G.6.
- [10] A.M.J. Koonen, K.A. Mekonnen, F.M. Huijskens, N.-Q. Pham, Z. Cao, E. Tangdiongga, "Optical Wireless GbE Receiver with Large Field-of-View," *Proc. ECOC2021*, Bordeaux, Sep. 2021, paper Th1B.6.

-
- [11] A.M.J. Koonen, K.A. Mekonnen, Z. Cao, F.M. Huijskens, N.-Q. Pham, E. Tangdionga, “Beam-steered optical wireless communication for industry 4.0”, *IEEE J. of Sel. Topics in Quantum Electron.*, Vol. 27, No. 6, Nov./Dec. 2021, art. 6000510 (10 pp.). (doi: <https://doi.org/10.1109/JSTQE.2021.3092837>).
- [12] https://en.wikipedia.org/wiki/Fresnel_lens [online]
- [13] T. Umewaza, AQ. Matsumoto, K. Akahane, A. Kanno, N. Yamamoto, “400-pixel high-speed photodetector for high optical alignment robustness FSO receiver,” *Proc. OFC 2022*, San Diego, Mar. 2022, paper M4I.3.
- [14] R. Ramaswami, K. N. Sivarajan, G. H. Sasaki Ramaswami, Ch. 5 “Transmission System Engineering,” in “Optical Networks - A Practical Perspective,” 3rd ed., 2010, Elsevier Inc., <https://doi.org/10.1016/C2009-0-17339-7>
- [15] Albis Optoelectronics, Multi-Channel Top Illuminated Monitor Photodiode Array [Online]. Available: https://www.albisopto.com/albis_product/pd00jx-multi-channel-top-illuminated-monitor-photodiode-array/

8 Bidirectional all-optical OWC indoor system¹⁸

8.1 Introduction

Optical wireless communication by means of 2D-steered narrow infrared beams (BS-OWC) is a very promising technique for surmounting the bottlenecks of today's radio wireless systems, such as the heavy congestion which is often incurred in WiFi networks. The small footprint of each infrared beam enables users to be connected at high user densities while they do not need to share capacity (whereas in wide-coverage LiFi and WiFi systems users have to share capacity, by means of MAC protocols). Most beam-steered OWC systems reported so far have focused on downstream connectivity only. In [1], we showed GbE video streaming by downstream BS-OWC links covering a sizable user area without a need to carefully align the orientation of the user's device, thanks to the wide Field-of-View (FoV) of its receiver. Bidirectional beam-steered systems which were reported so far mostly employed hybrid links (i.e., optical beam downstream, mm-wave radio beam upstream) [7-9]. Hybrid links, however, do not preserve the key advantages of OWC, such as security against eaves-dropping and immunity against electro-magnetic interference (EMI). Alternatively, all-optical bidirectional systems reported simply duplicated the downstream link into an upstream one, e.g. using MEMS mirrors [5], or SLMs [9], or they covered very short distances only such as for docking systems [10]. It should be noted that in an indoor network, however, the downstream OWC links are typically emerging from a common point-to-multipoint (P2MP) multicasting unit, which is mounted at the room's ceiling, whereas the upstream links are MP2P links from each user device to the upstream receiver at the ceiling. Such asymmetry in the connectivity patterns is not optimally served by duplicating the downstream link into an upstream one.

To establish and control the accurate steering of beams in BS-OWC systems, various solutions have been reported which require additional active infrastructure elements. RF beacons may be used which enable triangular

¹⁸ This chapter is largely based on Ton Koonen, Ketemaw Addis Mekonnen, Frans Huijskens, Eduward Tangdionga, "Bi-directional all-optical wireless Gigabit Ethernet communication system using automatic self-aligned beam steering," *J. of Lightw. Technol.*, Vol. 41, No. 11, June 2023, pp. 3446-3454.

localization [7]. Solutions using active optical beacons have been reported in [12] and [13], where localization is done by camera observation of active LED tags at the user side, and in [14] and [15] where in a search-and-scan process a beam is deployed with variable divergence which sends localization messages to the user who then needs an active feedback channel for responding.

In this chapter, we in detail describe and demonstrate an all-optical bidirectional BS-OWC system which we briefly introduced in [16]. It expands our previous BS-OWC GbE downstream-only video streaming system [1] with a beam-steered GbE upstream link per user, established by automatic self-alignment of the upstream link next to the self-alignment of the downstream link. We propose passive optical retro-reflecting structures at the receiver which enable to automate the beam steering control without needing an active pre-existing feedback channel. In Section 8.2, our proposed architecture of the bidirectional OWC system is explained. The downstream path design has been introduced previously in [1][17][18]; Section 8.3 introduces the upstream path design; the upstream beam steering principle has been discussed in Section 5.4. The upstream beam alignment to the upstream receiver's aperture has been automated, by using the hole-seeking center-of-gravity algorithm as described in Section 6.4, wherein its performance has been analyzed by simulations when adopting the system's design choices, and experimentally validated in our OWC testbed. Section 8.4 describes the full experimental bidirectional OWC system which implements these choices and reports its performance for bidirectional TCP tests and GbE video transmission. Section 8.5 summarizes the results and draws conclusions about the application potential of our proposed system.

8.2 Bidirectional OWC system architecture

Fig. 8-1 shows the architecture of our proposed all-optical bidirectional OWC system. The ceiling central unit hosts the passive pencil-radiating antenna (PRA) unit which directs narrow downstream (DS) optical beams in 2 dimensions according to their wavelength; the DS data are fed from λ -tunable laser transmitters [17]. The PRA contains an arrayed waveguide grating router module acting as wavelength-demultiplexer, of which the output wavelength ports are arranged in a 2D fiber array. The position of each output fiber with respect to the axis of the subsequent lens determines the direction of the beam emitted at that wavelength. Thus, each user is DS-connected by his private λ -beam ($\lambda_1, \lambda_2, \dots$), and many users can be connected simultaneously.

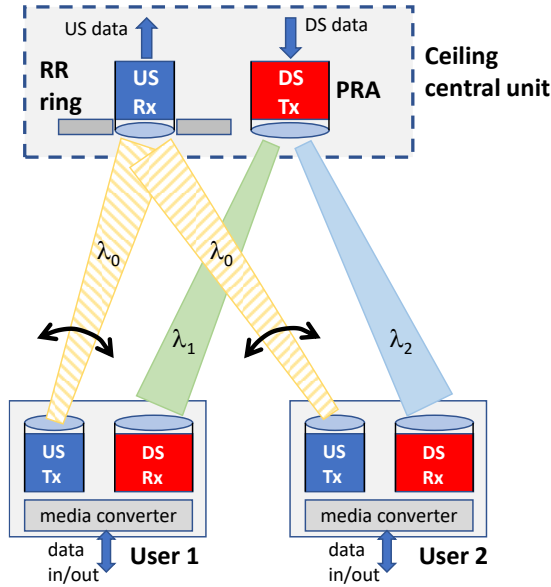


Fig. 8-1 Bidirectional BS-OWC system with automatic upstream beam self-alignment

For upstream, a beam with arbitrary wavelength (λ_0) is preferred, in order to avoid costly λ -tunable sources and their control circuitry at the user's site. Therefore, the upstream beam steering in 2 dimensions from the upstream transmitter (US Tx) towards the upstream receiver (US Rx) at the ceiling central unit is done by mechanical means. This typically requires a pre-existing optical feedback loop from the ceiling unit to each user to control the pointing of the upstream beam and to assist in establishing the upstream path; hence, it requires to set up the DS path first. To circumvent this bootstrapping issue, we propose to use a ring of retro-reflecting miniature corner cubes (RR ring) which surrounds the aperture of the upstream receiver (US Rx) at the ceiling. Such RR ring can be cut from commercially available RR foils commonly used for e.g., road signage; we have demonstrated passive user localization with such RR foil technology before [18]. At the user site, the US power reflected from the RR ring is monitored and enables automatically aligning the US beam to the US Rx, employing a dedicated RR hole-seeking algorithm. Multiple users can deploy the RR ring simultaneously for their US beam alignment, as the RR ring reflects an US beam to its originating user only. The US Rx at the ceiling will receive US beams from multiple users. Therefore, for establishing each US link an US medium access control protocol is needed, e.g., a TDMA protocol similar to the ones deployed in commercial TDMA PON systems [19].

It may be noted that our system uses two optical apertures in the ceiling central unit. Other BS-OWC system architectures, such as in [12], used bidirectional

single aperture configurations for fiber-to-fiber coupling via the free-space link. Although in such solutions the ceiling unit for a single user may be more compact, for multiple users multiple ceiling units are needed. In our proposed architecture the two-aperture ceiling unit is shared among multiple users, requires feeding by only a single fiber, and therefore may then be more compact and easier to install.

8.3 Upstream optical path design

Fig. 8-2 shows the design of the US optical path, starting at the user site and covering a distance d which ends at the PRA site at the ceiling.

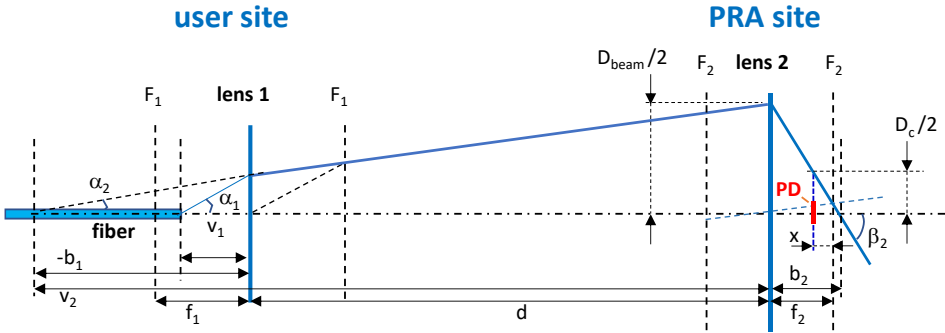


Fig. 8-2 Design of upstream optical path

Similar to the DS path design [17], we choose some defocusing of the fiber with respect to the user's lens 1 (with focal length f_1) in order to obtain a slightly diverging US beam which eases US alignment. Using thin lens analysis, the US beam diameter D_{beam} at the PRA site with defocusing $p_1=1-v_1/f_1$ is

$$D_{beam} = 2 p_1 \tan \alpha_1 \left[d + f_1 \left(\frac{1}{p_1} - 1 \right) \right] \quad (8-1)$$

where $\tan \alpha_1 = \lambda / (\pi w_0)$ represents the divergence of the Gaussian beam with waist radius w_0 launched from the SMF; for $\lambda = 1.5 \mu\text{m}$ and $w_0 = 4.5 \mu\text{m}$, $\tan \alpha_1 = 0.1$. The photodiode (PD) after lens 2 (with focal length f_2) at the US receiver in the PRA site is put slightly out of focus by some defocusing $p_2 = x/f_2 > 0$; this enlarges the receiving FoV α (see section 7.2). The spot diameter D_c at the PD and the FoV α are given by

$$D_c = 2 p_1 \tan \alpha_1 \left[f_2 + p_2 \left\{ d + f_1 \left(\frac{1}{p_1} - 1 \right) - f_2 \right\} \right] \quad (8-2)$$

$$\tan \alpha = \frac{|D_c - D_{PD}|}{2 f_2 (1 - p_2)} \quad (8-3)$$

where D_{PD} is the photodiode's diameter. For achieving a large FoV, the focal

length f_2 should be as small as possible, while the aperture of lens 2 should still be large enough to capture the full beam diameter. Assuming a uniform power profile in the beam, the beam-to-PD power coupling factor T at normal incidence at the PRA is

$$T = 1 \quad \text{if } D_c \leq D_{PD}$$

$$= \left(\frac{D_{PD}}{D_c}\right)^2 \quad \text{if } D_c > D_{PD} \quad (8-4)$$

For lens 2 at the PRA, a Fresnel lens is preferred, as such lens type is particularly suited for light collection and can combine a large aperture with a short focal length in order to realize a large FoV [12]. The imaging performance of a Fresnel lens is less good than that of conventional plano-convex or biconvex lenses, but for collecting light onto the PD this is not an issue. For lens 1 at the user, a triplet lens is preferred. A triplet lens is the least complicated lens which is able to eliminate a range of lens aberrations [21]; as will be discussed in Section V, this is of importance to attain adequate performance in the automated upstream beam steering alignment process without needing a costly complex lens at the user's device. In our system demonstrator, to be discussed in Section VI, a Fresnel lens is used with 25mm aperture and focal length $f_2=5\text{mm}$ [22], and a Hastings triplet lens with $f_1=20\text{mm}$ and aperture 11.5mm [23].

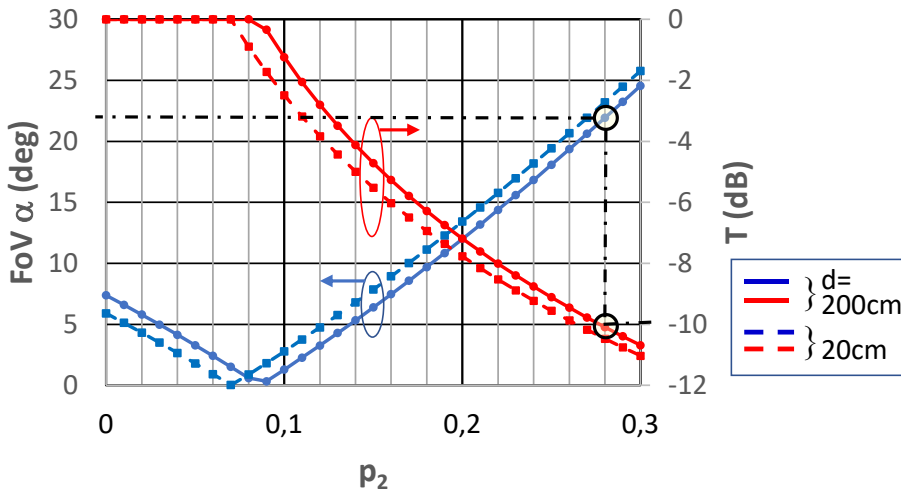


Fig. 8-3 Upstream beam coupling to US receiver (US beam spot $D_{\text{beam}}=15\text{mm}$; $f_1=20\text{mm}$, $f_2=5\text{mm}$, $D_{PD}=1.32\text{mm}$)

Neglecting lens aberrations, for $f_1=20\text{mm}$ and $f_2=5\text{mm}$ a US beam diameter $D_{\text{beam}2}=15\text{mm}$ needs a defocusing $p_1=2.78\%$ at a user-ceiling distance $d=200\text{cm}$, and $p_1=30.6\%$ at $d=20\text{cm}$. Fig. 8-3 shows how the beam-to-PD power coupling

factor T and the half-angle FoV α then depend on the defocusing p_2 . Note that T excludes the fill factor loss of the PD, which is about -7.2dB for the composite 4x4 photodiode matrix with active area diameter $D_{PD}=1.32\text{mm}$ adopted in our system (see [1]). Accepting $T > -10\text{dB}$ implies a defocusing at the US receiver $p_2 < 28\%$ and thus yields a FoV $\alpha < 22\text{deg.}$ half-angle which amply exceeds the FoV of the DS receiver (which is about 10deg., see [1]), as required in the bidirectional system. Note that the FoV of the bidirectional system determines the user area which can be covered; this FoV is given by the minimum of the FoV of the downstream link and the FoV of the upstream link (minus a possible tilt angle of the user device).

The analog 2D upstream beam steering by means of stepper motors moving the optical source (i.e., the fiber pigtail of a laser diode) at the user's device has been introduced in section 5.4, and enables accurate alignment of the upstream beam to the aperture of the upstream receiver mounted at the ceiling by means of the Center-of-Gravity algorithm as introduced in section 6.4.

8.4 System demonstrator

Fig. 8-4 shows the configuration of the bidirectional OWC laboratory system. It adds the US part to our previous DS GbE video streaming setup having a reach of 2m [1]. By λ -tuning, the 10dBm DS beams with footprint diameter $\varnothing 10\text{cm}$ are 2D steered by an AWGR-based diffractive unit. Using a 4x4 photodiodes matrix with diameter $\varnothing 1.32\text{mm}$ and a $\varnothing 50\text{mm}$ $f=10\text{mm}$ Fresnel lens, the DS-Rx has a FoV $\approx \pm 10\text{deg.}$ [1]. The automatic alignment of the DS beam to the DS-Rx has been achieved by monitoring the reflected power from an RR ring around the aperture of the DS-Rx at the user dongle, where this reflected power is monitored by a photodetector (PD) at the PRA site close to the lens which launches the DS beam. This monitored power is used for the λ -tuning control which drives the 2D DS beam steering as described in detail in [18]. Note that the DS beam is much wider than aperture of the DS-Rx, in order to achieve wide area coverage within a limited λ -tuning range. Hence the DS beam alignment is done by maximizing the monitored power, and the hole-seeking CoG algorithm is not used.

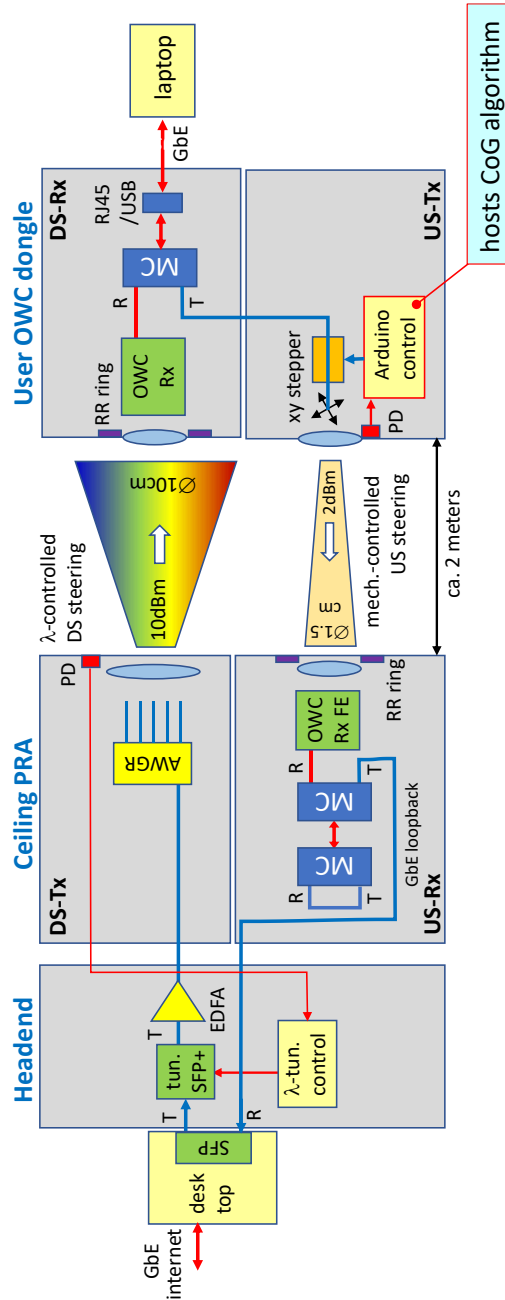


Fig. 8-4 Bi-directional OWC laboratory system, including both the downstream beam alignment and upstream automated beam alignment (blue: fiber; red: copper lines)

The demonstrator setup which has been realized in our laboratory is shown in Fig. 8-5, the ceiling site in Fig. 8-7, and the user site in Fig. 8-8.

In the DS link from the ceiling site two PRA-s are foreseen, with the possibility to switch between them in case there is a line-of-sight blockage for one of them; see Fig. 8-6. PRA1 is composed of a C-band AWGR from Kaiaam with 96 flat-top channels spaced at $\Delta\nu=50\text{GHz}$ having a bandwidth $BW=35\text{GHz}$, adjacent channel isolation $a_{ac} >24\text{dB}$, and polarization-dependent loss $\text{PDL}<0.5\text{dB}$, in combination with an L-band AWGR from Kylaia with 48 channels at $\Delta\nu=50\text{GHz}$ having a $BW=24\text{GHz}$, $a_{ac} >30\text{dB}$, and $\text{PDL}<0.4\text{dB}$; it provides 144 output ports of which 128 fit in the entry aperture of the $f/0.95$ $f=50\text{mm}$ camera lens; PRA1 can support 128 beams. PRA2 is equipped with a C-Band AWGR only from Usource with 96 channels at $\Delta\nu=50\text{GHz}$, $BW=35\text{GHz}$, $a_{ac} >21\text{dB}$, and $\text{PDL}<0.65\text{dB}$; it can support 96 beams.

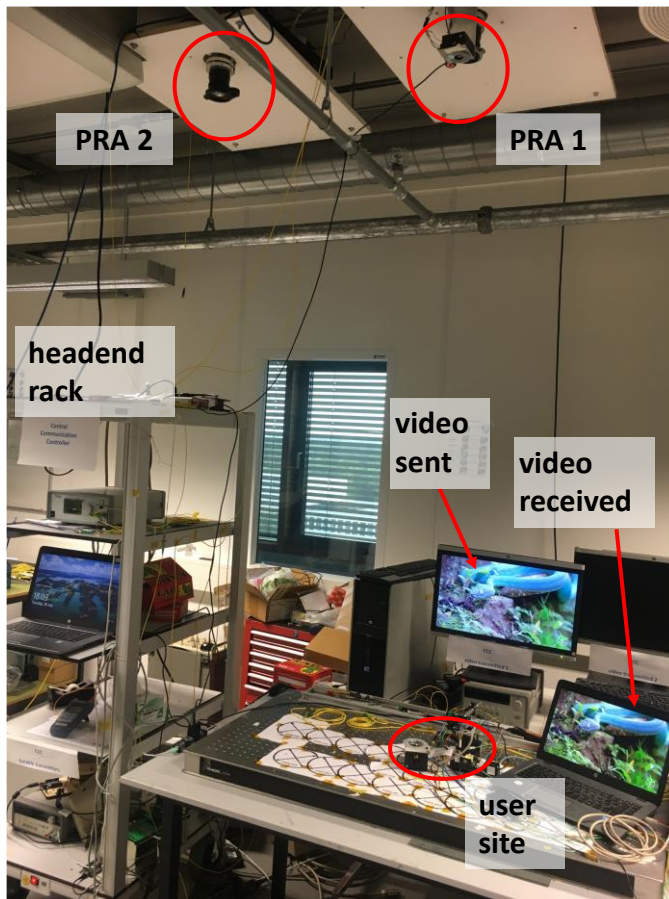


Fig. 8-5 Laboratory demonstration of GbE video streaming via bidirectional OWC link to a laptop computer

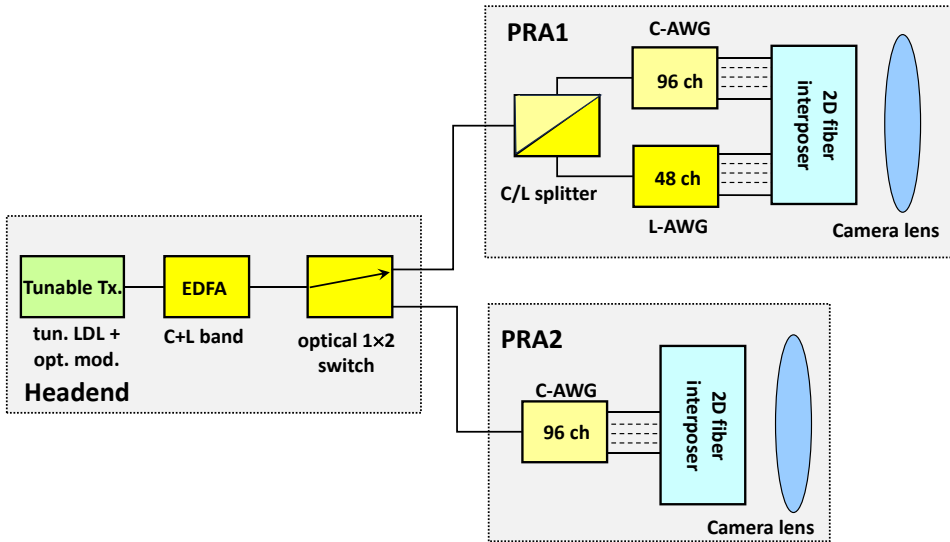


Fig. 8-6 Headend transmitter site with PRA selection switch and the two PRA-s

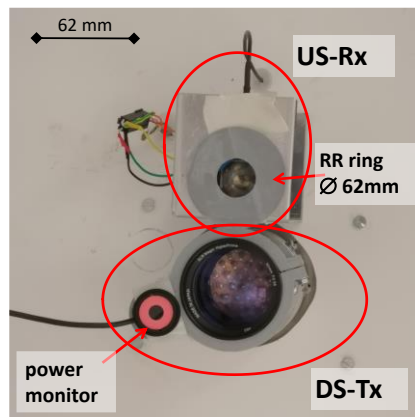


Fig. 8-7 PRA site: US-Rx with RR ring, and DS-Tx with power monitor PD

In the US link, a 2dBm $\varnothing 15\text{mm}$ US beam at $\lambda \approx 1.5 \mu\text{m}$ is launched using a triplet lens with $f=20 \text{ mm}$. Note that the US beam power is well below the eye safety threshold of 10dBm. Although the beam is slightly diverging, this safety aspect is particularly important as the user may be very close to his upstream unit. When well aligned, the US beam fits fully within the $\varnothing 25\text{mm}$ aperture of the US-Rx at the ceiling; thus, sufficient link budget for good GbE upstream connectivity is achieved, although the US beam power is only 2dBm. The beam is mechanically 2D steered by a NEMA11 xy stepper motor stage, which is controlled by an Arduino board. This board performs the CoG automatic beam alignment algorithm according to eq. (6-6) and gets its input from monitoring the

power reflected by the RR ring at the PRA by three low-bandwidth $\varnothing 1$ mm photodiodes at the user site. Fig. 6-20 shows the experimental results of monitoring this power. The 3D representation of the experimental data shows a similar shape as the analytical one shown in Fig. 6-14 which was calculated for a uniform scanning beam. The 3D shape of the experimental data is somewhat less smooth, due to the noise fluctuations in the monitored power.

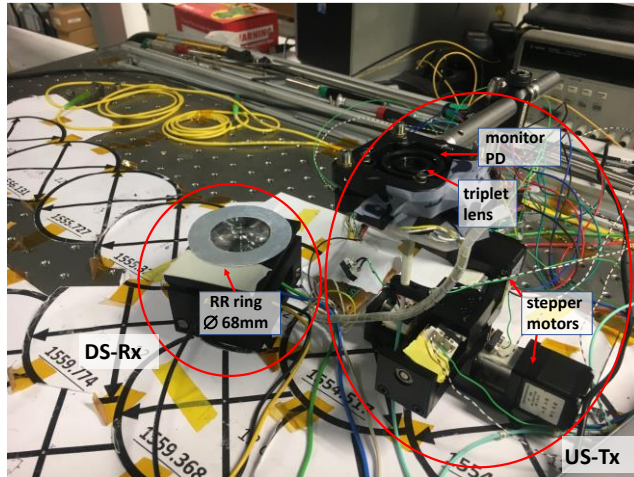


Fig. 8-8 User site: US-Tx with stepper motors, triplet lens, monitor PD, and DS-Rx with RR ring

The US-Rx has a $\varnothing 25$ mm Fresnel lens with $f=5$ mm, achieving a $\text{FoV} \approx \pm 12 \text{deg}$. (cf. [1]). Commercial GbE media converters (MCs) are used to convert the bidirectional GbE data from optical to electrical RJ45/USB signals. These MCs have SMF optical inputs and outputs. For operating as OWC receiver, the optical receiver SMF front-end of the first MC is replaced by our OWC receiver front-end (OWC Rx FE) with 4×4 photodiode matrix TIA receiver which has an enhanced FoV of about 10deg . (see [1]). Our CoG US beam alignment algorithm executed by the Arduino board successfully achieved US connectivity within 10 seconds for a step size of 6mm, and even within 4s for 7.5mm. Other localization techniques (such as using camera observation and active LED tags at the user device [12][13]) may need only a few tens of ms, but need a pre-calibration of the localization results to the beam steering coordinates, and a camera at the user device for upstream beam alignment. Moreover, measurement of the distance is needed in order to enable correction for the distance-dependent parallax shift between the camera observation unit and the beam steering unit [26]. Our retro-reflection-based localization technique, however, is self-calibrating the localization to the beam steering, requires only limited signal processing at the user device, and has no parallax issues. Within the FoV range,

bidirectional TCP test by Iperf measurements showed ~ 940 Mbit/s in DS and ~ 939 Mbit/s in US, without packet loss. Unidirectionally, Iperf in UDP test showed ~ 958 Mbit/s US with 0.18% packet loss.

The bidirectional connection is set up by firstly establishing the automatic alignment of the upstream beam upon the user's request. It starts with coarse localization of the US-Rx by large beam scanning steps. As the RR ring is much larger than the aperture of the US-Rx, the coarse search time is reduced remarkably with respect to using no RR ring. Next, fine localization is done with small steps of about 6mm using the CoG algorithm as proposed in section 6.4.1, which processes the monitored power reflected by the RR ring (as represented in Fig. 6-20). This US-Rx localization takes about 10 seconds, mainly limited by the stepper motor speed. When the scan step size is enlarged, the alignment time will decrease inversely proportional to the square of the step size, but the accuracy will remarkably degrade (cf. Fig. 6-15).

Secondly, the downstream link is aligned automatically by monitoring the retro-reflected power from the passive RR ring at the DS-Rx of the laptop and using the wavelength-tuning control procedure we have reported before in [18] and was discussed in section 6.3. The downstream alignment time is less than 15 seconds, and is mainly limited by the LabVIEW control program.

8.5 Conclusions

GbE bidirectional OWC transmission for high-density user connections using narrow infrared beams with automatic self-calibrated alignment of the upstream beam by means of a novel steering control protocol using the center-of-gravity (CoG) algorithm as well as automatic self-calibrated alignment of the downstream beam has been designed, realized, and implemented in a laboratory testbed. Broadband receivers with a wide FoV $\approx \pm 10$ deg. were employed, which ease the required beam alignment accuracy. With low-aberration triplet lenses, a good accuracy of the CoG algorithm and hence adequate upstream beam steering has been achieved within $200\mu\text{m}$ accuracy and within 10 seconds time, mainly limited by the stepper motors. The automatic downstream beam alignment takes less than 15 seconds, mainly limited by the wavelength-tuning control. The time consumed by the beam steering limits the system's suitability for mobile users. Its major benefits are for delivery of dense high-capacity services to nomadic users. TCP measurements show 940Mbit/s transfer speeds per user within the FoV $\approx \pm 10$ deg. Real-time high-definition GbE video streaming to laptop computers via the bidirectional OWC link has been demonstrated.

8.6 References

- [1] A.M.J. Koonen, K.A. Mekonnen, Z. Cao, F.M. Huijskens, N.Q. Pham, E. Tangdiongga, "Beam-Steered Optical Wireless Communication for Industry 4.0," *IEEE J. Selected Topics in Quantum Electronics*, vol. 27, no. 6, Nov./Dec. 2021, art. no. 6000510.
- [2] https://en.wikipedia.org/wiki/Wi-Fi_6 [online]
- [3] A.M.J. Koonen *et al.*, "Ultra-high capacity wireless communication by means of steered narrow optical beams," *Philos. Trans. Roy. Soc. A*, 2020, art. no. 19.
- [4] F. Gomez-Agis, S. P. van der Heide, C. M. Okonkwo, E. Tangdiongga, and A. M. J. Koonen, "112 Gbit/s transmission in a 2D beam steering AWG-based optical wireless communication system," *Proc. ECOC2017*, Göteborg, Sep. 17-21, paper Th.2.B.1.
- [5] H. Kazemi, E. Sarbazi, M.D. Soltani, T.E.H. El-Gorashi, J.M.H. Elmirghani, R.V. Penty, I.H. White, M. Safari, H. Haas, "A Tb/s Indoor MIMO Optical Wireless Backhaul System Using VCSEL Arrays," *IEEE Trans. Commun.*, vol. 70, no. 6, p. 3995-4012, June 2022.
- [6] K.A. Mekonnen, C.W. Oh, Z. Cao, A.M. Khalid, N. Calabretta, E. Tangdiongga, A.M.J. Koonen, "PIC-enabled Dynamic Bidirectional Indoor Network Employing Optical Wireless and Millimeter-wave Radio Techniques," *Proc. ECOC2016*, Düsseldorf, Sep. 18-22, paper W.1.D.3.
- [7] A.M. Khalid, P.G.M. Baltus, A.R. Dommele, K.A. Mekonnen, Z. Cao, C.W. Oh, M.K. Matters, A.M.J. Koonen, "Bi-directional 35-Gbit/s 2D beam steered optical wireless downlink and 5-Gbit/s localized 60-GHz communication uplink for hybrid indoor wireless systems," *Proc. OFC2017*, Los Angeles, 19-23 March, paper Th1E.6.
- [8] K. Wang, A. Nirmalathas, C. Lim, K. Alameh, E. Skafidas, "Full duplex gigabit indoor optical wireless communication system with CAP modulation," *Photon. Technol. Lett.*, vol. 28, no. 7, pp. 790-793, Apr. 2016.
- [9] A. Gomez, K. Shi, C. Quintana, M. Sato, G. Faulkner, B.C. Thomsen, D. C. O'Brien, "Beyond 100-Gb/s indoor wide field-of-view optical wireless communications," *Phot. Technol. Lett.*, vol. 27, no. 4, Feb. 2015, pp. 367-370.
- [10] M. Faulwaßer, F. Deicke, T. Schneider, "10 Gbit/s Bidirectional Optical Wireless Communication Module for Docking Devices," *Globecom Workshop on OWC*, Austin, Dec. 2014.
- [11] H. Liu, H. Darabi, P. Banerjee, J. Liu, "Survey of Wireless Indoor Positioning Techniques and Systems," *IEEE Trans. on Systems, Man, and Cybernetics*, vol. 37, no. 6, pp. 1067-1080, Nov. 2007.
- [12] A. Gomez, K. Shi, C. Quintana, G. Faulkner, B.C. Thomsen, D. O'Brien, "A 50 Gb/s transparent indoor optical wireless communications link with an integrated localization and tracking system," *J. Lightw. Technol.*, vol. 34, no. 10, pp. 2510-2517, May 2016.
- [13] N. Q. Pham, K. Mekonnen, E. Tangdiongga, A. Mefleh, T. Koonen, "User Localization and Upstream Signaling for Beam-Steered Infrared Light Communication System," *Phot. Technol. Lett.*, vol. 33, no. 11, pp. 545-548, 2021.
- [14] K. Wang, A. Nirmalathas, C. Lim, E. Skafidas, "Experimental demonstration of a

- novel indoor optical wireless localization system for high-speed personal area networks,” *Optics Lett.*, vol. 40, no. 7, pp. 1246-1249, Apr. 2015.
- [15] A. Nirmalathas, T. Song, S. Edirisinghe, K. Wang, C. Lim, E. Wong, C. Ranaweera, K. Alameh, “Indoor optical wireless access networks — recent progress,” *J. Opt. Commun. Netw.*, vol. 13, no. 2, pp. A178-A186, Feb. 2021.
- [16] A.M.J. Koonen, K. A. Mekonnen, F.M. Huijskens, E. Tangdiongga, “Bi-directional all-optical wireless communication system with optical beam steering and automatic self-alignment,” *Proc. ECOC2022*, Basel, Sep. 18-22, paper Tu4F.1.
- [17] A.M.J. Koonen, F. Gomez-Agis, F.M. Huijskens, and K.A. Mekonnen, “High-capacity optical wireless communication using two-dimensional IR beam steering,” *J. Lightw. Technol.*, vol. 36, no. 19, pp. 4486–4493, Oct. 2018.
- [18] A.M.J. Koonen, K.A. Mekonnen, F.M. Huijskens, N.-Q. Pham, Z. Cao, E. Tangdiongga, “Fully passive user localization for beam-steered high-capacity optical wireless communication system,” *J. Lightw. Technol.*, vol. 38, no. 10, pp. 2842-2848, May 2020.
- [19] TDMA-PON [online]. Available: https://www.itu.int/en/ITU-T/studygroups/2017-2020/15/Documents/OFC2018-2-Q2_v5.pdf
- [20] Fresnel lens concept [online]. Available: https://en.wikipedia.org/wiki/Fresnel_lens
- [21] Triplet lens concept [online]. Available: https://en.wikipedia.org/wiki/Triplet_lens
- [22] Fresnel lens [online]. Available: https://en.wikipedia.org/wiki/Fresnel_lens<https://www.edmundoptics.com/p/098-x-098-020-focal-length-fresnel-lens/42289/>
- [23] Triplet lens [online]. Available: <https://www.edmundoptics.com/f/hastings-triplet-achromatic-lenses/11968/> [online]
- [24] Linear actuators [online]. Available: <https://www.helixlinear.com/Products/Linear-Actuators/PRA-Linear-Actuators/Profile-Rail-Linear-Actuator-PRA-11S-039~PRA-11S-039>
- [25] Plano-convex lens [online]. Available: <https://www.edmundoptics.com/p/200mm-dia-x-200mm-fl-uncoated-plano-convex-lens/5719/>
- [26] Parallax errors in optical systems [online]. Available: <https://en.m.wikipedia.org/wiki/Parallax>

9 Conclusions and outlook on further research

9.1 Conclusions

Optical wireless communication (OWC) techniques offer powerful solutions to resolve the imminent congestion in radio-based communication networks, in particular in local area wireless networks. By deploying steerable narrow infrared optical beams which address each user device individually, it can provide links with ultra-high capacity where and when needed, while also minimizing the power consumption needed and offering high privacy. It can provide the ultimate capabilities for delivering broadband services wirelessly in human-to-machine and machine-to-machine communications. The small footprint of a beam enables the creation of a pico-cell per user device, and thus create a high degree of spatial multiplexing which boosts the total wireless system's throughput. As the beams deliver communication capacity on demand only to those places where and when needed, the system achieves a high efficiency in bringing the data signals to the users and thus can reduce remarkably the power consumption needed with respect to a radio-based mm-wave communication system. Moreover, as nothing travels faster than light in vacuum (and air), a minimum in latency is achieved which makes it also eminently suited for time-critical machine-to-machine interactions. Radio beams travel equally fast, but due to the lower bandwidths accessible in a radio channel extra processing time is needed for signal conditioning, which adds to the radio link's latency.

Optical wireless communication by 2D-steered narrow infrared beams is not foreseen to fully replace radio-based wireless communication, amongst others because it needs line-of-sight and the beam steering processes do not support high user mobility as well as radio-based communication in the ISM band and wide-beam VLC/LiFi communication can do. But it can off-load high-speed traffic loads from radio-based networks and wide-beam OWC networks, and thus give these the room necessary to handle the booming amounts of low-speed intermittent traffic as e.g., generated by the emerging myriad of small internet-of-things devices. Its main application benefits arise in the wireless delivery of broadband services to/from nomadic or static users with no or limited in-service mobility demands.

In this thesis the focus has been on the definition, design, implementation and experimental validation of a short-reach indoor OWC system deploying narrow, individually 2D-steerable infrared beams for bringing broadband services to multiple closely spaced users, and of the key techniques required: emitting and accurately steering multiple narrow beams, localization of the user devices, and receiving the beams for establishing high-capacity links without requiring tedious alignment. The main results are:

- *Definition of an indoor physically point-to-multipoint OWC system architecture*, and its design rules based on wavelength-tuned individual beam steering using passive diffractive modules. It is readily scalable to serve many users wirelessly with broadband services, is maintenance-lean, and by consolidating the OWC beam generation and steering functions in a common central unit it fits effectively in a Fiber-in-the-Home network architecture. *Reported in Ch. 4.*
- *2D (semi-)discrete beam steering by wavelength tuning* in two implementation options (intended for downstream beam steering):
 - *a passive diffractive module deploying a pair of crossed diffraction gratings*. Its design rules have been established, and semi-discrete 2D steering over an angular area of $6^\circ \times 12^\circ$ has been demonstrated by wavelength tuning over 125nm, as well as delivery of 42.8Gbit/s data capacity per beam using PAM-4 modulation.
 - *a passive diffractive module deploying an arrayed waveguide grating router (AWGR)* with its output fiber ports arranged in a 2D matrix put in front of a lens. The design rules have been set, and discrete 2D steering up to 128 beams has been demonstrated over an angular area of $17^\circ \times 17^\circ$ by wavelength tuning using a C+L band composite AWGR with 128 output ports. A transport capacity of 112Gbit/s per beam using PAM-4 modulation has been achieved with an 80-ports C-band AWGR, implying the feasibility of a total optical wireless system throughput beyond 8.9Tbit/s. The steering time is with these diffractive modules mainly limited by the time needed to control the laser wavelength tuning and is within the ms range. *Reported in Ch. 5.*
- *2D beam semi-continuous steering by an active mechanically 2D translating module* deploying a stage of two linear stepper motor translators which moves the output fiber of a laser diode in front of a lens. This steering method is intended for upstream narrow beam steering from the user's module which is cost-sensitive and (typically) battery-operated. The mechanical steering allows the laser diode to operate at an arbitrary wavelength, which reduces costs. The use of stepper motors which do not need powering as soon as beam

alignment has been achieved saves energy from the user's battery. 2D angular tuning within $10.8^\circ \times 10.8^\circ$ has been realized, which fits within the FoV of the upstream receiver, as required. The steering time is mainly limited by the speed of the 2D stepper motor translators and their control, which may be a few seconds for covering the whole user area (128 cells). *Reported in Ch. 5.*

- *Localization of the user for aligning the downstream and upstream beams* by means of beam scanning and a ring-shaped matrix of miniature retro-reflectors around the aperture of the targeted receiver. Localization processing is required at only one side and no pre-existing return link; it enables to set up a connection from scratch, without position calibration. Alignment of the downstream beams is achieved by discrete scanning through wavelength-tuning the oversized $\varnothing 10\text{cm}$ beams by means of the diffractive beam steerer and processing the monitored reflected power. Experimentally, adequate establishment of a downstream link has been achieved in less than 15 seconds, mainly limited by the LabVIEW control of the scanning process and the user area of 128 cells (each $\varnothing 10\text{cm}$). Alignment of the narrow $\varnothing 15\text{mm}$ upstream beams is achieved by nearly-continuous scanning using the 2D mechanical stepper motor stage in conjunction with a center-of-gravity algorithm which processes the monitored reflected power. Adequate upstream beam alignment was experimentally achieved within 10 seconds, mainly limited by the low speed of the stepper motors. *Reported in Ch. 6.*
- *Broadband receiver with large aperture and wide Field-of-View*: a novel receiver concept has been proposed which deploys a 2D matrix of interconnected photodiodes. While enlarging the light-detecting aperture, the $M \times M$ photodiode matrix (PD matrix) provides a bandwidth equal to that of a single photodiode and an output current which is M times larger. By theoretical analysis, the compromise between beam power-to-photodiode coupling and the FoV has been modelled and assessed for realistic beam profiles and lens designs by extensive (home-built) ray tracing. The SNR performance of the PD matrix-based receiver has been analyzed and found to be better than of an angular diversity receiver with similar amount of photodiodes. A receiver with a 4×4 interconnected matrix of $\varnothing 150\mu\text{m}$ photodiodes has been built in conjunction with a commercially available 750MHz transimpedance amplifier and a large-NA $\varnothing 50\text{mm}$ Fresnel lens with $f=10\text{mm}$. In our OWC laboratory testbed, experimentally a -3dB bandwidth of the receiver of 670MHz has been achieved, and an $\text{FoV} \approx \pm 10$ deg. with the Gaussian beams with waist $\varnothing 10\text{mm}$, which aligns well with the ray tracing analyses. Crosstalk from neighbouring cells may occur when shifting the

receiver away from the signal cell's center across the user plane; analysis has shown that with Gaussian $\varnothing 10\text{cm}$ beams and a $\varnothing 50\text{mm}$ receiver lens aperture a shift up to 32mm is allowed for a power penalty $< 0.5\text{dB}$. Regarding the FoV performance, the 4×4 PD matrix receiver is clearly less affected by the shifting than the single-PD receiver. By scaling the photodiode matrix to larger $M\times M$ dimensions, the FoV-vs.-beam-to PD matrix coupling performance can be improved further, although the improvement steps shrink at large M . *Reported in Ch. 7.*

- *Bi-directional all-optical OWC indoor system:* in order to adhere to the advantages of the physical point-to-multipoint architecture, and to most cost-effectively implement the user's terminal, the upstream paths should not just be a copy of the downstream path. A dedicated design with an arbitrary-wavelength laser and mechanical 2D steering with a 2D stepper motor stage as reported in section 6.4 was made. By integrating
 - two ceiling units (containing the AWGR-based diffractive 2D beam steerer as described in section 5.3 and the upstream receiver equipped with 4×4 photodiode matrix, see chapter 7, and retro-reflecting ring for upstream localization, see section 6.4),
 - the user unit (with the mechanical 2D steerer for the $\varnothing 15\text{mm}$ upstream beam, see section 5.4, and the downstream receiver with 4×4 photodiode matrix, a $\varnothing 50\text{mm}$ Fresnel lens with $f=10\text{mm}$, a retro-reflective ring for downstream localization, see section 6.3, and media converter providing the I/O functions to connect a laptop), and
 - the remote headend rack (containing the tunable wavelength transmitters, optical crossconnect switch for selecting a ceiling unit, and the control by means of a laptop computer), the bi-directional OWC system demonstrator has been realized. Its performance for bi-directional GbE data communication has been verified; TCP measurements show 940Mbit/s transfer speeds within the FoV of ± 10 deg. in the user area at link lengths of about 2.5 meter (ceiling-user plane). Live high-definition video streaming to laptop computers has been demonstrated successfully. *Reported in Ch. 8.*

9.2 Outlook and suggestions for further research

The research efforts reported in this thesis were directed towards the design, analysis, implementation and experimental validation of an OWC system for broadband short-reach indoor communication, including its key functions, to nomadic or stationary users. As the beam-steered OWC research is still in its early

phase, it is a fertile domain for next research steps. Some of them are discussed in the following.

9.2.1 Applying the OWC key functions in other OWC domains

Further research steps may be made in translating these efforts towards other OWC application domains in which medium-reach and long-reach communication is needed. Such domains will often involve outdoor settings in which atmospheric conditions may lead to fluctuations in the losses and the phase of the optical path (scintillation). Additional signal conditioning methods (such as space–time block coding [1]) may be investigated.

The key functions as investigated in this thesis for short-reach OWC may *mutatis-mutandis* be applicable for OWC in other domains, such as

- for medium range: in underwater settings (e.g., for controlling underwater unmanned maintenance/repair robots; typically blue-to-green light beams are used) [2], road traffic (car-to-car, car-to-roadside), at street level (shopping areas), in sport stadiums, backhauling for mobile network antenna stations, between drones, fixed wireless drop links to remote buildings, ...
- for long/ultra-long reach: ground-to-satellite, inter-satellite, ground-to-plane, inter-plane

In general, at longer path lengths the angular accuracy of the beam steering and localization becomes more delicate, which requires making their discretization steps in the steering much smaller (or even allow only continuous steering). Also path losses will grow, and beam power and/or receiver sensitivity need to be improved. On the other hand, the angular steering range and the FoV of the receiver can be reduced.

9.2.2 Photonic integration

To bring the OWC modules to a higher TRL, photonic integrated circuit (PIC) technologies are needed in particular where mass applications are sought, such as for indoor short-range OWC. PIC technologies may be beneficial to reduce the physical volume of these modules and their assembly efforts, and to improve their robustness and reproducibility. E.g., the AWGR-based diffractive 2D beam steerer concept as proposed in section 5.3 may be realized in a passive PIC built in a silicon-on-oxide technology, where the AWGR with a very high port count is co-integrated with a 2D array of surface-emitting slanted waveguides; cf. Fig. 9-1. Thus, when co-assembling this PIC with a lens, a compact and robust passive diffractive 2D beam steerer can be built.

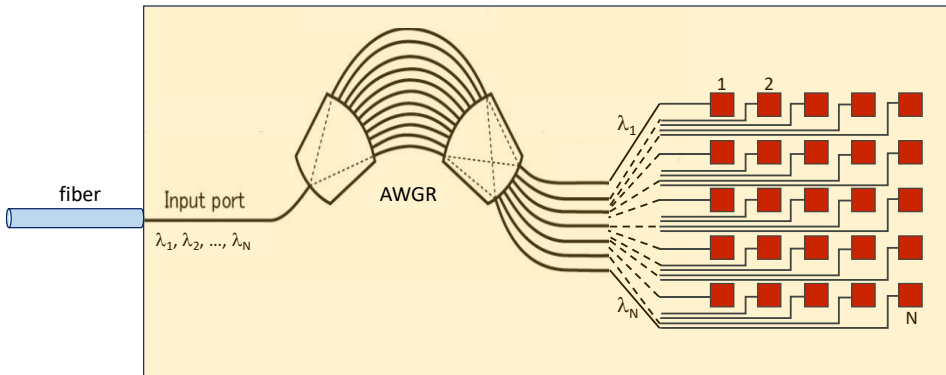


Fig. 9-1 Integrated passive AWGR-based beam steerer (AWGR with N output waveguides, terminated in vertically emitting slanted endfaces)

9.2.3 Next 2D beam steering concepts

The diffractive beam steerer concepts explored in this thesis in fact map a single dimensional variable, the wavelength λ , to 2 orthogonal angular dimensions φ and ψ in order to provide coverage of the 2D user plane (cf. Fig. 4-3). Such mapping inevitably implies discontinuities in the steering (cf. Fig. 5-6 and Fig. 5-17). Hence, the steering cannot be fully continuous, the beams can only make discrete steps and create discrete cells in addressing the user plane. A beam cannot stay centered on the user's receiver when it is moving, so the performance of the downstream link may vary depending on the user's position. When two dimensional variables could be mapped to the orthogonal angular dimensions φ and ψ , continuous steering would be possible, the beam could stay centered on the user's receiver, and the issue of performance variations when moving could be eliminated. Part of the attractiveness of the single variable λ for the 2D tuning is that it can be done with a remote optical source (a tunable laser diode), that this parameter is not prone to random changes when it is brought (by fiber) to the beam steerer, and steering unit (typically at the ceiling) is passive, which is attractive for operation, maintenance and installation. Next to the one-dimensional λ , one can think of a second dimensional optical variable, e.g., the polarization angle θ of a linearly polarized output signal of the λ -tunable laser. In previous work, doubling the number of output beams of an AWGR-based beam steerer without increasing crosstalk levels has been proposed by using two orthogonal polarization states for the even and odd wavelength channels [3]. By introducing a continuously variable linear polarization angle θ , both the wavelength λ and the linear polarization state θ can be mapped to the two

orthogonal angular beam steering dimensions φ and ψ , and 2D continuous steering would be possible. This (λ, θ) tuning can be done independently in each of the optical sources in the remote headend station (in the CCC). Polarization-maintaining fiber will have to be used for bringing the (λ, θ) tuned signals to the 2D beam steerer. A new passive 2D steering module needs to be devised which can steer each beam under the joint control of the beam signal's wavelength λ and its linear polarization state θ . Thus, such a passive module can handle multiple beams independently, and the number of beams to be steered can readily be scaled.

9.2.4 Next localization schemes

Localizing the user by means of beam scanning takes less time if the beam diameter is increased, but then the localization is also less accurate. To reduce scanning time but maintain accuracy it will be beneficial to adapt the beam diameter from relatively large in the initial coarse scanning phase, to small in the finalizing fine scanning phase. Such adaptive control of the beam diameter may be achieved by a lens with a variable focal length, e.g., a tunable liquid lens [4], and may be driven by the localization processor. This concept may not be suited for the downstream beams in the diffractive beam steerers reported in sections 5.2 and 5.3, as they use a lens which is jointly used by all downstream beams. For the upstream links, where only a single beam is launched this concept may be interesting to explore in depth.

9.2.5 Next OWC receiver concepts

Higher data rates and/or longer reach will require a higher OWC receiver sensitivity. Coherent detection techniques in optical fiber transmission have been key for introducing more comprehensive (2-dimensionally modulated, such as QAM) signals with larger information content per symbol, and thus higher data rates within the same bandwidth. Moreover, by means of mixing with a local oscillator, signal amplification is achieved at the receiver's input and thus the receiver sensitivity is enhanced. In line with these coherent technologies for fiber-based transmission, an OWC receiver equipped with coherent detection techniques would be attractive for sensitivity enhancement. The performance of the OWC coherent receiver should not depend on the polarization state of the incoming signal (which may change due to random scintillation). In analogy with coherent receivers in optical fiber networks, the OWC coherent receiver may be designed to include a polarization-diversity scheme. To also reduce the impact of phase noise of the local oscillator laser, the design should also include a phase

diversity scheme. A research challenge will be to devise a coherent OWC receiver which is based on the FoV-enlarging 2D photodiode matrix concept we reported in this thesis and is extended with the coherent polarization- and phase-diversity detection schemes.

9.2.6 New OWC networking aspects

As mentioned in section 8.2 already, in the present bi-directional indoor OWC system demonstrator the upstream receiver in the ceiling unit may need to handle the upstream traffic from multiple users. Therefore, for each upstream link an upstream medium access protocol is needed for which a TDMA protocol like what is used in TDMA-PON may be investigated.

If needed, higher data rates per optical wireless link may be created by putting multiple wavelength channels in a beam. When deploying the AWGR-based beam steerer (see section 5.3), multiple wavelength channels can be multiplexed into the same beam if their wavelengths are separated by (a multiple of) the FSR of the AWGR, causing them to emerge from the same output port of the AWGR. This requires a large wavelength tuning range of the beam generating laser diodes which can cover multiple FSRs of the AWGR. Alternatively, an AWGR with multiple input fiber ports may be employed (cf. [6]). By making use of the wavelength-cyclic routing characteristics of an AWGR, additional input fibers can carry wavelength channels which are cyclically multiplexed into the beam emerging from the same output port of the AWGR. E.g., Fig. 9-2 illustrates this for two input fibers of the AWGR, by which the capacity of a beam can be doubled.

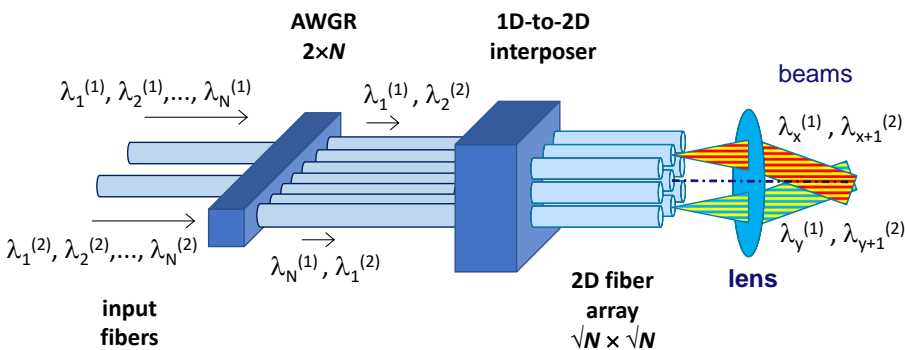


Fig. 9-2 Wavelength multiplexing of signals into the same 2D steered beam by adding input ports to the AWGR

The wavelength channels in the beam subsequently need to be separated (i.e., demultiplexed) by free-space optical filters which will feed them to separate OWC receivers.

In narrow-beam-steered OWC communication systems as studied for indoor application in this thesis, the beams may be regarded as ‘virtual fibers’. To follow up on this analogy, in further studies for the OWC modules the equivalents of fiber network functions may be investigated, such as optical cross-connecting, add-drop multiplexing, label-controlled wavelength routing, optical repeating with optical amplification, and others.

9.3 References

- [1] Space–time block code [Online]. Available: https://en.wikipedia.org/wiki/Space_time_block_code
- [2] Ke Wang, T. Song, Y. Wang, C. Fang, J. He, A. Nirmalathas, C. Lim, E. Wong, S. Kandeepan, “Evolution of Short-Range Optical Wireless Communications,” *J. of Lightw. Technol.*, Vol. 41, No. 4, Feb. 2023, pp. 1019-1040. (<https://doi.org/10.1109/JLT.2022.3215590>)
- [3] X. Zhang, C. Li, Y. Jiao, E. Tangdionga, Y. Liu, Z. Cao, A.M.J. Koonen, "Crosstalk-mitigated AWGR-based two-dimensional IR beam-steered indoor optical wireless communication system with a high spatial resolution," *J. of Lightw. Technol.*, Vol. 37, No. 15, Aug. 2019, pp. 3713-3720. (<https://doi.org/10.1109/JLT.2019.2917835>)
- [4] Edmund Optics liquid lenses [Online]. Available: <https://www.edmundoptics.com/knowledge-center/application-notes/imaging/introduction-to-liquid-lenses/>
- [5] TDMA-PON [online]. Available: https://www.itu.int/en/ITU-T/studygroups/2017-2020/15/Documents/OFC2018-2-Q2_v5.pdf
- [6] Z. Fan, J. Zhao, J.-J. He, "High Performance Demonstration of a 16×16 Silica-based Cyclic Arrayed-Waveguide Grating Router," *Proc. 2021 19th Internat. Conf. on Optical Communications and Networks (ICOON)*, 23-27 Aug. 2021, Qufu, PR China

Appendix A: 3D ray tracing

A.1 Elementary 3D ray tracing algorithms

Algorithms for 3D ray tracing in an optical system by means of vector calculus have been developed and implemented in MATLAB. Optical systems consisting of segmented homogeneous media are considered (e.g., lenses consisting of several homogeneous elements), in which the rays follow piecewise linear paths. This piecewise linear ray tracing reduces calculation times and makes the tracing of high numbers of rays feasible, which enables e.g., a comprehensive analysis of lens aberrations and their impact on the optical imaging characteristics.

A.1.1. 3D ray propagation modelling

An optical ray $\overline{s(t)}$ emerging from a point $\overline{S_0}$ into a direction $\overline{e_s}$ may be modeled by

$$\overline{s(t)} = \overline{S_0} + t \overline{e_s} \quad (\text{A-1})$$

where the unity vector $\overline{e_s}$ in the 3D space is given by its azimuth angle φ and elevation angle θ according to (see Fig. A- 1)

$$\overline{e_s} = (\sin \theta \cos \varphi, \sin \theta \sin \varphi, \cos \theta) \quad \text{where } |\overline{e_s}| = 1 \quad (\text{A-2})$$

and where t is the parameter equal to the physical path length travelled.

A point \overline{x} is located in a plane A which is defined by a point $\overline{P_A}$ located in A and the normal unity vector $\overline{n_A}$ with $|\overline{n_A}| = 1$ if (see Fig. A- 2)

$$\overline{n_A} \circ (\overline{x} - \overline{P_A}) = 0 \quad (\text{A-3})$$

The intersection point $\overline{S_1}$ of the ray \overline{s} with the plane A can then be found by

$$\overline{S_1} = \overline{S_0} + t \overline{e_s} \quad \text{where } t = \frac{\overline{n_A} \circ (\overline{P_A} - \overline{S_0})}{\overline{n_A} \circ \overline{e_s}} \quad (\text{A-4})$$

The distance d of a point \overline{Q} to the ray $\overline{s(t)}$ can be found from (see Fig. A- 3)

$$(\overline{Q} - \overline{s(t)}) \perp \overline{e_{s0}} \quad \text{hence } t = (\overline{Q} - \overline{S_0}) \circ \overline{e_{s0}} \quad (\text{A-5})$$

where $\overline{a} \circ \overline{b}$ denotes the inner-product of vectors \overline{a} and \overline{b} , which yields

$$d^2 = |\bar{Q} - \bar{s}(t)|^2 = |\bar{Q} - \bar{S}_0|^2 - [(\bar{Q} - \bar{S}_0) \circ \bar{e}_{s0}]^2 \tag{A-6}$$

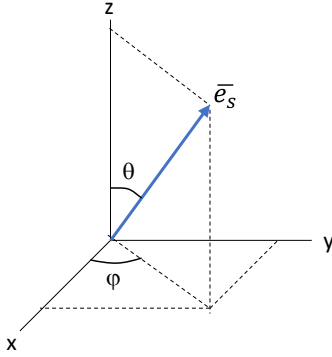


Fig. A-1 Unity vector \bar{e}_s

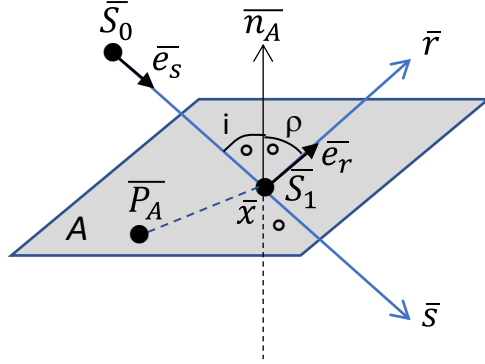


Fig. A-2 Transmission and reflection at plane A

Light rays may be blocked at a limiting aperture; see Fig. A-4. Assume a circular aperture with radius R_{CA} at position \bar{x}_{CA} in a plane A. The intersection point \bar{S}_1 with A is at

$$\bar{S}_1 = \bar{S}_0 + t \bar{e}_s \text{ for } t = \frac{\bar{n}_A \circ (\bar{x}_{CA} - \bar{S}_0)}{\bar{n}_A \circ \bar{e}_{s0}} \tag{A-7}$$

where \bar{n}_A is the normal unity vector ($|\bar{n}_A| = 1$)

The ray passes through the aperture if $|\bar{S}_1 - \bar{x}_{CA}| < R_{CA}$.

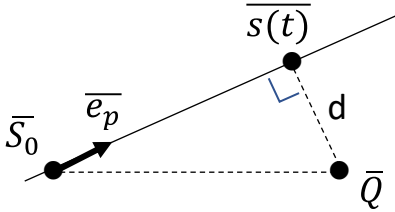


Fig. A-3 Distance from point \bar{Q} to ray $\bar{s}(t)$

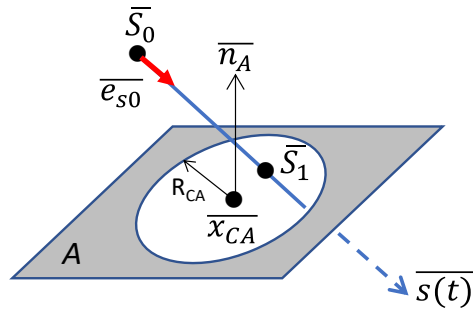


Fig. A-4 Impact of a limiting aperture

A.1.2. Reflection

The ray $\overline{r}(t)$ which is the reflection of $\overline{s}(t)$ in point \overline{S}_1 follows from the law of reflection $i=\rho$. Its unity vector \overline{e}_r is found by mirroring the \overline{n} - component in \overline{s} (see Fig. A- 2)

$$\overline{e}_r = \overline{e}_s - 2 (\overline{e}_s \circ \overline{n}) \overline{n} \quad (\text{where } |\overline{e}_r| = 1) \quad (\text{A-8})$$

and

$$\overline{r}(t) = \overline{S}_1 + t \overline{e}_r \quad (\text{A-9})$$

A.1.3. Ideal thin lens

A ray is refracted by an ideal thin lens according to the model shown in Fig. A- 5, where the refracted ray is defined by the intersection point \overline{S}_1 of the incident ray with the lens

$$\overline{S}_1 = \overline{P}_0 + t_1 \overline{e}_{s0} \quad \text{with} \quad t_1 = \frac{\overline{n}_L \circ (\overline{O} - \overline{P}_0)}{\overline{n}_L \circ \overline{e}_{s0}} \quad (\text{A-10})$$

where \overline{n}_L denotes the orientation of the lens and \overline{O} its center. The direction of the refracted ray \overline{e}_{s1} is found by determining the intersection point \overline{P}_1 of a ray through \overline{O} parallel to the incident ray with the lens' focal plane. The focal plane contains the focal point \overline{F} and is located at a distance equal to the focal length f . The direction \overline{e}_{s1} follows from

$$\begin{aligned} \overline{P}_1 &= \overline{O} + t_2 \overline{e}_{s0} \\ \overline{n}_L \circ (\overline{P}_1 - \overline{F}) &= 0 \\ t_2 &= \frac{\overline{n}_L \circ (\overline{F} - \overline{O})}{\overline{n}_L \circ \overline{e}_{s0}} = \frac{f}{\overline{n}_L \circ \overline{e}_{s0}} \\ \overline{e}_{s1} &= \frac{\overline{P}_1 - \overline{S}_1}{|\overline{P}_1 - \overline{S}_1|} \end{aligned} \quad (\text{A-11})$$

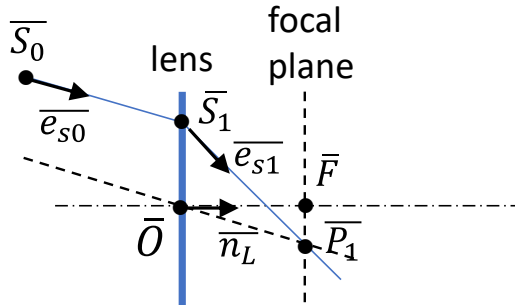


Fig. A- 5 Refraction by ideal thin lens

A.1.4. Refraction at a plane surface boundary

The refraction of a ray by a boundary plane between a medium with refractive index n_1 and a medium with n_2 is governed by Snellius law (see Fig. A- 6)

$$n_1 \sin i = n_2 \sin r \tag{A-12}$$

The direction of the refracted ray \overline{e}_{s1} follows from

$$\overline{e}_{s1} = a \overline{e}_{s0} + b \overline{n}_A \tag{A-13}$$

in which a and b are to be solved:

$$\begin{aligned} \overline{e}_{s0} \circ \overline{n}_A &= |\overline{e}_{s0}| |\overline{n}_A| \cos i = \cos i \\ \overline{e}_{s1} \circ \overline{n}_A &= |\overline{e}_{s1}| |\overline{n}_A| \cos r = \cos r \\ \overline{e}_{s0} \circ \overline{e}_{s1} &= |\overline{e}_{s0}| |\overline{e}_{s1}| \cos(i - r) = \cos i \cos r + \sin i \sin r \\ \rightarrow a &= \frac{n_1}{n_2} \quad \text{and} \quad b = \cos r - \frac{n_1}{n_2} \cos i \end{aligned} \tag{A-14}$$

where $\cos r = \sqrt{1 - \left(\frac{n_1}{n_2}\right)^2 (1 - (\cos i)^2)}$ and $\cos i = \overline{e}_{s0} \circ \overline{n}_A$

Total reflection will occur at surface A when $n_1 > n_2$ if incidence angle i exceeds the critical angle

$$i > \arcsin\left(\frac{n_2}{n_1}\right) \quad \text{so if} \quad \cos i < \sqrt{1 - \left(\frac{n_2}{n_1}\right)^2} \tag{A-15}$$

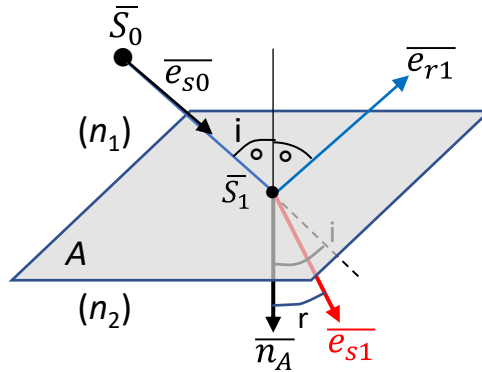


Fig. A- 6 Refraction and reflection of a ray at a surface boundary between media with different refractive indices

A.1.5. Refraction at a spherical surface boundary

By deploying a spherical surface boundary, ray refraction by lens operation occurs. Fig. A- 7 shows the entry of a ray at the convex side of such spherical

boundary between media with different refractive indices n_1 and n_2 . This boundary is part of a sphere with center \bar{x}_M and radius R .

For the intersection point \bar{S}_1 of the incident ray $\bar{s}_0(t) = \bar{S}_0 + t \bar{e}_{s0}$ holds $|\bar{S}_1 - \bar{x}_M| = R$, hence

$$t = -\bar{e}_{s0} \circ (\bar{S}_0 - \bar{x}_M) - \sqrt{(\bar{e}_{s0} \circ (\bar{S}_0 - \bar{x}_M))^2 + R^2 - |\bar{S}_0 - \bar{x}_M|^2} \quad (\text{A-16})$$

The unity normal vector \bar{n}_{S1} in \bar{S}_1 of the spherical surface is $\bar{n}_{S1} = \frac{\bar{S}_1 - \bar{x}_M}{R}$ and the incidence angle of ray \bar{e}_{s0} at \bar{S}_1 is given by $\cos i = -\bar{e}_{s0} \circ \bar{n}_{S1} \geq 0$, from which the direction \bar{e}_{s1} of the refracted ray is

$$\bar{e}_{s1} = a \cdot \bar{e}_{s0} + b \cdot \bar{n}_{S1} \quad \text{with } a = \frac{n_1}{n_2} \quad \text{and } b = -\cos r + \frac{n_1}{n_2} \cos i \quad (\text{A-17})$$

where $\cos r = \sqrt{1 - \left(\frac{n_1}{n_2}\right)^2 (1 - (\cos i)^2)}$

Similarly, Fig. A- 8 shows the entry of a ray at the concave side of a spherical surface boundary. The intersection point $\bar{S}_1 = \bar{S}_0 + t \bar{e}_{s0}$ is on the spherical surface, hence $|\bar{S}_1 - \bar{x}_M| = R$ and now

$$t = -\bar{e}_{s0} \circ (\bar{S}_0 - \bar{x}_M) + \sqrt{(\bar{e}_{s0} \circ (\bar{S}_0 - \bar{x}_M))^2 + R^2 - |\bar{S}_0 - \bar{x}_M|^2} \quad (\text{A-18})$$

With the unity normal vector $\bar{n}_{S1} = \frac{\bar{S}_1 - \bar{x}_M}{R}$ and incidence angle i of ray \bar{e}_{s0} at \bar{S}_1 given by $\cos i = \bar{e}_{s0} \circ \bar{n}_{S1} \geq 0$ follows

$$\bar{e}_{s1} = a \bar{e}_{s1} + b \bar{n}_{S1} \quad \text{with } a = \frac{n_1}{n_2} \quad \text{and } b = \cos r - \frac{n_1}{n_2} \cos i \quad (\text{A-19})$$

where $\cos r = \sqrt{1 - \left(\frac{n_1}{n_2}\right)^2 (1 - (\cos i)^2)}$

Total reflection at the spherical surface will occur if $n_1 > n_2$ and $\frac{n_1}{n_2} \sin i = \sin r > 1$ so if

$$\cos i < \sqrt{1 - \left(\frac{n_2}{n_1}\right)^2} \quad (\text{A-20})$$

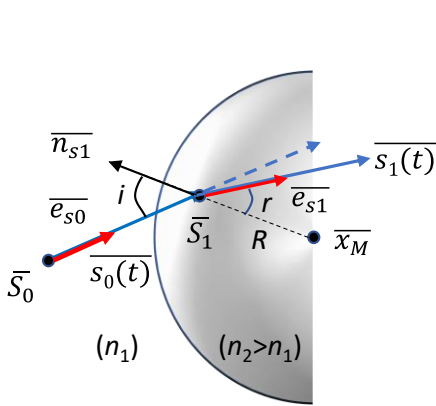


Fig. A- 7 Ray entry at convex side of spherical surface boundary between media with refractive indices n_1 and $n_2 > n_1$

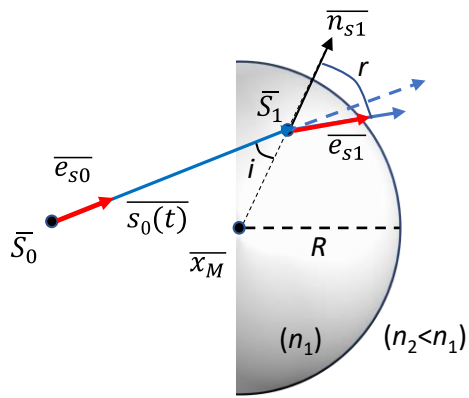


Fig. A- 8 Ray entry at concave side of spherical surface boundary between media with refractive indices n_1 and $n_2 < n_1$

A.2 Homogeneous ray launching

For the ray tracing analysis of imaging in an optical system for different intensity profiles of the incident beam, adequate modelling is needed of an extended optical source. This source should have a specified diameter and emit a specified number of rays which are launched according to a homogeneously distributed spatial density and follow a specified intensity profile.

As shown in Fig. A- 9, a circular extended source may be assumed with an aperture radius R_a , of which the ray emitters are grouped in $N+1$ adjacent concentric rings, each having a width $\Delta r = r_n - r_{n-1}$ where r_n and r_{n-1} are the outer and inner radius of ring n , respectively. The m^{th} ray emitter in ring n ($n=0, 1, \dots, N$) is located at polar coordinates $(r_s(n), \varphi_{mn})$, where $m=1, 2, \dots, M(n)$. For a homogeneous distribution, a ray is emitted per elementary area A_E . The area $A(n)$ of ring n is

$$A(n) = \pi (r_n^2 - r_{n-1}^2) \text{ for } n \geq 1 \text{ where } A(0) = \pi r_0^2 \tag{A-21}$$

In ring n , $M(n)$ rays are launched from radial position $r_s(n) = \frac{1}{2}(r_n + r_{n-1})$. For equidistant launching, the distance between the emitters $d \approx 2\pi n \Delta r / M(n) \equiv \Delta r$ hence $M(n) = 2\pi n$. As $M(n)$ has to be an integer, we take $M(n) = 6n$ for $n \geq 1$, with $M(0) = 1$.

All the elementary areas should jointly fill the whole aperture, so when in total K rays are to be launched

$$A_E = \frac{A(n)}{M(n)} = \frac{\pi (r_n^2 - r_{n-1}^2)}{6n} = A(0) = \pi r_0^2 = \frac{\pi R_a^2}{K} \quad (\text{A-22})$$

yielding $r_0 = \frac{R_a}{\sqrt{K}}$ and thus

$$r_n^2 = r_0^2 (1 + \sum_{l=1}^n M(l)) = r_0^2 [1 + 3n(1+n)] \quad \text{so} \quad (\text{A-23})$$

$$r_n = R_a \sqrt{\frac{1+3n(1+n)}{K}}$$

The total number of rays K which are launched when N emitter rings are deployed is

$$K = \sum_{n=0}^N M(n) = 1 + \sum_{n=1}^N 6n = 1 + 3N(1+N) \quad (\text{A-24})$$

Fig. A- 11 illustrates the fast growth of the number of rays launched K when the number of rings N is increased.

The intensity profile of a Gaussian beam propagating in the $+z$ direction is given by [1]

$$I(r, z) = I_0 \left(\frac{w_0}{w(z)} \right)^2 \exp \left(\frac{-2r^2}{w(z)^2} \right) \quad (\text{A-25})$$

where I_0 is the intensity at the center of the beam at its waist, w_0 is the waist radius at $z=0$, and the beam waist $w(z)$ is

$$w(z) = w_0 \sqrt{1 + \left(\frac{z}{z_R} \right)^2} \quad (\text{A-26})$$

with Rayleigh range $z_R = \pi w_0^2 n / \lambda$ where n is the refractive index of the medium. The power of the beam passing through an aperture with radius R in the transversal plane at position z is then

$$P(r, z) = \int_{\varphi=0}^{2\pi} \int_{r=0}^R I(r, z) r dr d\varphi = P_0 \left\{ 1 - \exp \left(\frac{-2R^2}{w^2(z)} \right) \right\} \quad (\text{A-27})$$

For creating a Gaussian beam with total power P_{beam} , waist radius w , and launching aperture $R_a = R_{lens}$, the power launched by each of the $M(n)$ emitters in ring n for $n \geq 1$ (with $P(n)$ the power launched by ring n) is

$$P_s(n) = \frac{P(n)}{M(n)} = \frac{P_{beam}}{6n} \left\{ \exp \left(-\frac{2r_{n-1}^2}{w^2} \right) - \exp \left(-\frac{2r_n^2}{w^2} \right) \right\} \quad \text{for } n \geq 1 \quad (\text{A-28})$$

$$P_s(0) = P(0) = P_{beam} \left\{ 1 - \exp \left(-\frac{2r_0^2}{w^2} \right) \right\} \quad \text{for } n=0$$

As the Gaussian beam profile theoretically extends infinitely, a finite launching

aperture implies omitting part of the beam's power. The fraction of the beam power which is passing the aperture versus the aperture/beam diameter ratio is shown in Table A- 1.

Table A- 1 Fraction of Gaussian beam power passing through an aperture

R_aper/R_beam	P_aper/P_beam	1-P_aper/P_beam
1	0,864664717	0,1353353
1,53	0,990737673	0,0092623
2	0,999664537	0,0003355
3	0,999999985	1,523E-08

For creating a uniform beam with total power P_{beam} , radius R_{beam} , and lens radius R_{lens} , we have

- if $R_{beam} < R_{lens}$: launching aperture $R_a=R_{beam}$ and
 $P_{aperture} = P_{beam}$ (A-29)
- if $R_{beam} \geq R_{lens}$: $R_a = R_{lens}$ and $P_{aperture} = (R_{lens}/R_{beam})^2 P_{beam}$

The power launched by each of the $M(n)$ emitters in ring n for $n \geq 1$ (with $P(n)$ the power launched by ring n) is

$$P_s(n) = \frac{P(n)}{M(n)} = \frac{1}{3} \left(\frac{\Delta r}{R_a} \right)^2 P_{aperture} \quad \text{for } n \geq 1$$

$$P_s(0) = P(0) = \left(\frac{\Delta r}{2 R_a} \right)^2 P_{aperture}$$
(A-30)

Examples of homogeneously launching $K=1027$ rays for a Gaussian beam with waist diameter $\varnothing 15\text{mm}$ and $\varnothing 100\text{mm}$ are given in Fig. A- 10.a and Fig. A- 10.c, respectively; for a uniform beam with diameter $\varnothing 15\text{mm}$ and $\varnothing 100\text{mm}$ in Fig. A- 10.b and Fig. A- 10.d, respectively. Fig. A- 11 shows the number of rings N needed for the homogeneous launching of K rays, and Table A- 2 the launching data for ring n .

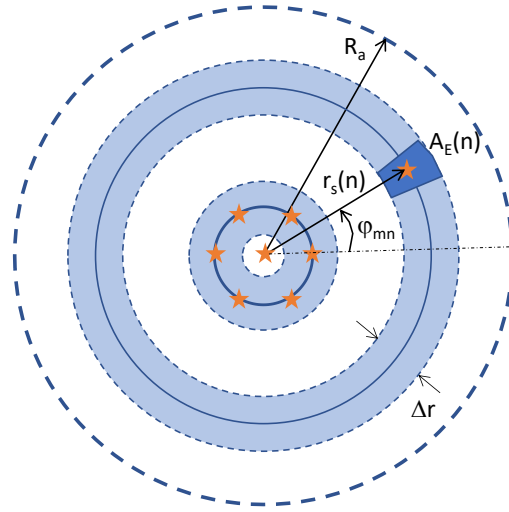
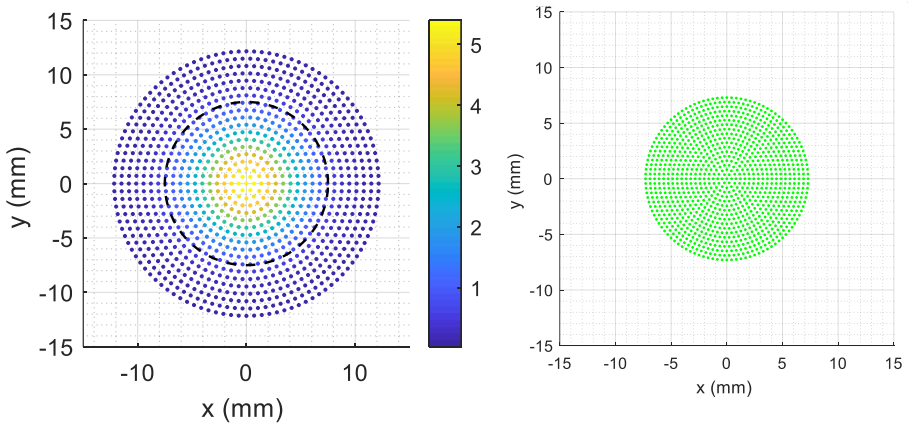
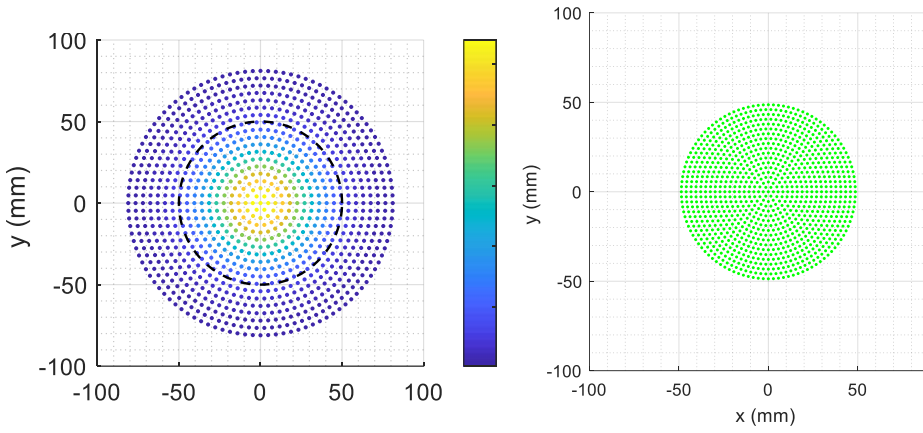


Fig. A- 9 Extended optical source launching homogeneously distributed rays



a) Gaussian beam with $D_{beam}=\varnothing 15\text{mm}$ waist diameter (dashed line)

b) Uniform beam with $D_{beam}=\varnothing 15\text{mm}$



c) Gaussian beam with $D_{beam}=\varnothing 100\text{mm}$ waist diameter (dashed line)

d) Uniform beam with $D_{beam}=\varnothing 100\text{mm}$

Fig. A- 10 Homogeneous ray launching (for $K= 1027$ rays launched)

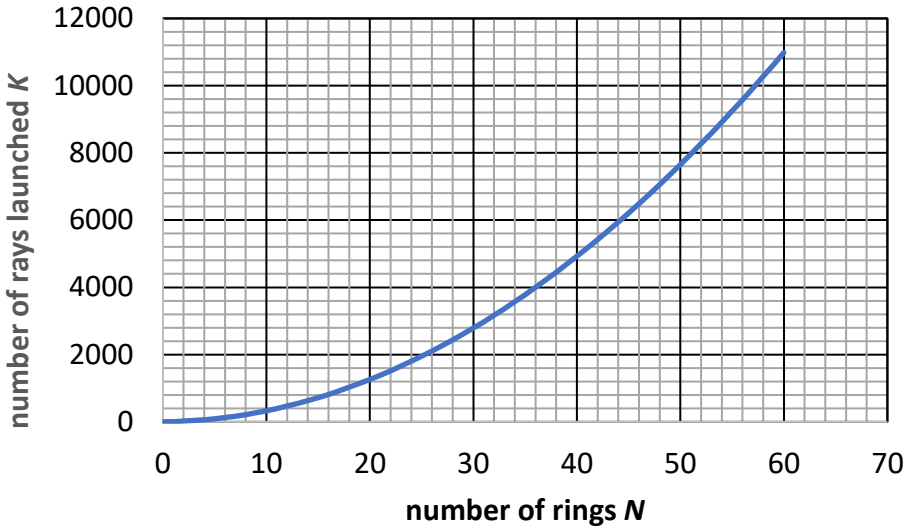


Fig. A- 11 Number of rays launched K vs. number of launching rings N

Table A- 2 Homogeneous ray launching from ring n , when launching with N rings (where $N=10$ rings cover a beam diameter of $\varnothing 25\text{mm}$).
Data: $M(n)$: number of ray emitters in ring n ; K : total number of rays launched; r_n : radius of ring n (in mm); A_n : area of ring n (in mm^2), AE_n : area of an emitter in ring n (in mm^2); w_n : width of ring n (in mm)

ring	elements	K		ring area	ray area	ring width
n	M(n)	cum # rays	r_n	A_n	AE_n	w_n
0	1	1	0,687062	1,483003	1,483003	
1	6	7	1,817796	8,898015	1,483003	1,130733
2	12	19	2,994834	17,79603	1,483003	1,177039
3	18	37	4,179236	26,69405	1,483003	1,184401
4	24	61	5,366127	35,59206	1,483003	1,186891
5	30	91	6,554155	44,49008	1,483003	1,188028
6	36	127	7,742797	53,38809	1,483003	1,188642
7	42	169	8,931808	62,28611	1,483003	1,189011
8	48	217	10,12106	71,18412	1,483003	1,18925
9	54	271	11,31047	80,08214	1,483003	1,189413
10	60	331	12,5	88,98015	1,483003	1,18953
11	66	397	13,68962	97,87817	1,483003	1,189616
12	72	469	14,8793	106,7762	1,483003	1,189682
13	78	547	16,06903	115,6742	1,483003	1,189733
14	84	631	17,2588	124,5722	1,483003	1,189773
15	90	721	18,44861	133,4702	1,483003	1,189806
16	96	817	19,63844	142,3682	1,483003	1,189833
17	102	919	20,8283	151,2663	1,483003	1,189855
18	108	1027	22,01817	160,1643	1,483003	1,189873
22	132	1519	26,7778	195,7563	1,483003	1,189924
26	156	2107	31,53757	231,3484	1,483003	1,189953
32	192	3169	38,67739	284,7365	1,483003	1,189978
37	222	4219	44,62732	329,2266	1,483003	1,18999
41	246	5167	49,3873	364,8186	1,483003	1,189997
50	300	7651	60,09732	444,9008	1,483003	1,190007
58	348	10267	69,6174	516,0849	1,483003	1,190012
71	426	15337	85,08759	631,7591	1,483003	1,190017
82	492	20419	98,17779	729,6373	1,483003	1,190019
91	546	25117	108,888	809,7194	1,483003	1,190021
100	600	30301	119,5982	889,8015	1,483003	1,190022
115	690	40021	137,4485	1023,272	1,483003	1,190023
129	774	50311	154,1088	1147,844	1,483003	1,190024
141	846	60067	168,3891	1254,62	1,483003	1,190024
163	978	80197	194,5696	1450,377	1,483003	1,190025
173	1038	90307	206,4699	1539,357	1,483003	1,190025
183	1098	101017	218,3701	1628,337	1,483003	1,190025

A.3 Aspheric Fresnel lens modelling

A Fresnel lens is composed of many concentric circular grooves with carefully designed facets. Notifying that the light refraction is taking place at the surfaces, such a lens may perform the same light focusing function as a plano-convex lens (see Fig. A- 12). But a Fresnel lens can be much thinner, thus have less volume and weight. By optimizing the shape of each concentric groove, a lens with an aspherical profile can be emulated. Thus, a Fresnel lens may combine a large aperture D with a small focal length f , and achieve a large numerical aperture NA according to

$$NA = n \sin \theta = n \sin \left(\text{atan} \left(\frac{D}{2f} \right) \right) = \frac{n}{\sqrt{1 + (2f/D)^2}} \quad (\text{A-31})$$

A Fresnel lens is typically used for light collecting, such as in solar cells, and thus may also be attractive for application in the optical beam receivers in OWC systems. Fresnel lenses can be manufactured readily by injection-molding with optical-quality plastics. Their imaging properties may be less good than those of a conventional lens due to the discrete profile of the Fresnel lens with its distinct grooves. By applying a higher groove density and lower groove profile, the imaging can be improved.

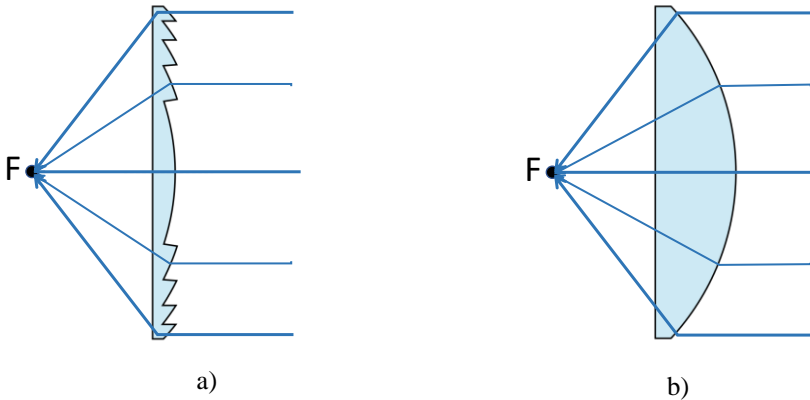


Fig. A- 12 Light collection by a) a Fresnel lens and b) a plano-convex lens

We devised a ray modelling approach for an ideal aspherical Fresnel lens profile which has an infinitesimally small profile height; see Fig. A- 13. The lens is optimized by tailoring the inclination angle $a(r)$ of each concentric groove such that spherical aberration is fully compensated: i.e., independent of the radial position r at which the ray is incident, each ray passes through the focal point F which is positioned at a back focal length (BFL) f_b from the lens' planar facet.

For this, three design equations need to be fulfilled:

- 1) $r = r_1 + r_2 = d \tan \theta_i + f_b \tan \theta_r$
- 2) $n_1 \sin \theta_i = n_0 \sin \theta_r$ (Snellius law) (A-32)
- 3) $n_0 \sin \alpha(r) = n_1 \sin \rho = n_1 \sin(\alpha(r) - \theta_i)$

which implies solving x from

$$d x + \frac{f_b \cdot x}{\sqrt{a^2 + (a^2 - 1) x^2}} = r \text{ where } x = \tan \theta_i \text{ and } a = \frac{n_0}{n_1} \tag{A-33}$$

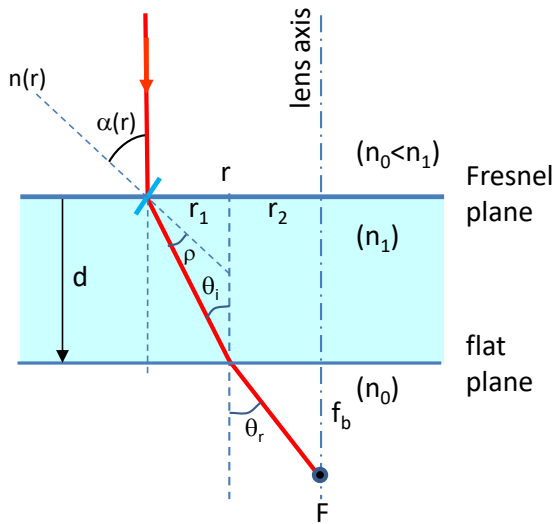


Fig. A- 13 Modelling an ideal aspheric lens, fully compensated for spherical aberration

By Newton-Raphson's zero-seeking algorithm (see [2]), which is known to converge fast (roughly doubling the number of correct digits every iteration step), x can be solved from $g(x)=0$ by the iteration

$$x_{n+1} = x_n - \frac{g(x_n)}{g'(x_n)} \tag{A-34}$$

wherein $g(x) = d x + \frac{f_b \cdot x}{\sqrt{a^2 + (a^2 - 1) x^2}} - r$ and $g'(x) = d + \frac{a^2 f_b}{[a^2 + (a^2 - 1) x^2]^{3/2}}$

As the starting point for the iteration, we may take $x_0 = \tan \theta_i = \frac{r}{d} \left(1 - \frac{f_b}{f_e}\right)$

where the effective focal length (EFL) $f_e = \frac{r}{\tan \theta_r}$ follows from

$$f_e = f_b + \frac{a d}{\sqrt{1 + (1 - a^2) \left(\frac{r}{f_e}\right)^2}} \approx f_b + a d \quad (\text{A-35})$$

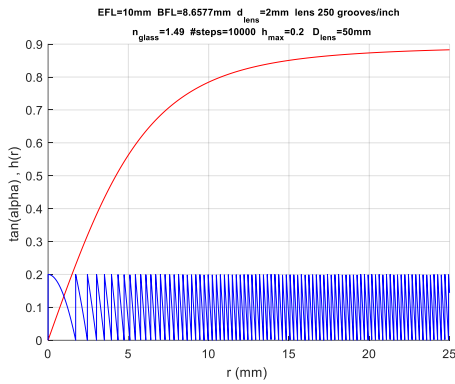
After having solved x , we can determine the optimized groove inclination angle $\alpha(r)$ at radial position r by

$$\tan \alpha(r) = \frac{x}{1 - a \sqrt{1 + x^2}} \quad (\text{A-36})$$

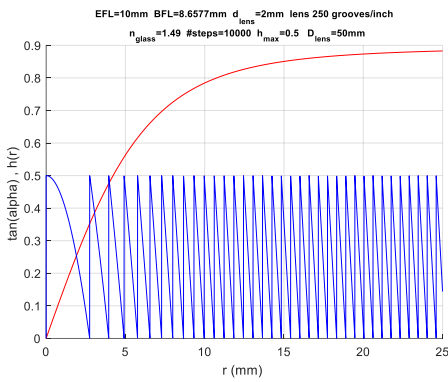
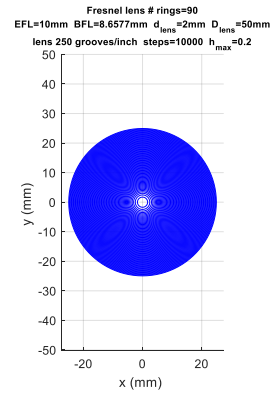
A.3.1. Some Fresnel lens design results

The profiles for a Fresnel lens fully compensated for spherical aberration have been calculated when using 10000 discretization steps in the Newton-Raphson's zero-seeking algorithm algorithm. The results for a Fresnel lens with focal length $f=10\text{mm}$ and aperture $D_{lens}=50\text{mm}$, as used in the ray tracing for the downstream receiver in chapter 7 are shown in Fig. A- 14.a and Fig. A- 14.b, when the maximum profile height of the lens (cf. Fig. A- 12.a) $h_{max}=0.2\text{mm}$ and $=0.5\text{mm}$, respectively. For a Fresnel lens with focal length $f=5\text{mm}$ and aperture $D_{lens}=25\text{mm}$, as used in the ray tracing for the upstream receiver in chapter 7, the results are shown in Fig. A- 15.a and Fig. A- 15.b, when $h_{max}=0.2\text{mm}$ and $=0.5\text{mm}$, respectively.

While the Fresnel lens has been corrected for spherical aberration, other aberrations (such as astigmatism) will occur when the beam incidence angle $\alpha \neq 0$. These aberrations will affect the imaging by the Fresnel lens at larger incidence angles α . By ray tracing, the off-axis imaging quality for the Fresnel lens with $f=10\text{mm}$ and $D_{lens}=50\text{mm}$ has been assessed when a Gaussian beam with waist diameter $\varnothing 100\text{mm}$ (the downstream case in chapter 7) is received. The results are shown in Fig. A- 16 for beam incidence angles $\alpha=0$ and $\alpha=5$ deg. when no defocusing is applied (so $p=0$) and when a defocusing $p=20\%$ is applied. These results clearly show the impact of the off-axis aberrations of the Fresnel lens on the imaging.



a)



b)

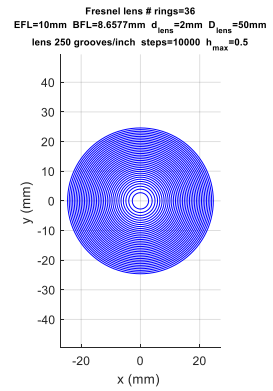


Fig. A- 14 Fresnel lens with $f=10mm$ and aperture $D_{lens}=50mm$, with maximum profile height a) $h_{max}=0.2mm$, and b) $h_{max}=0.5mm$

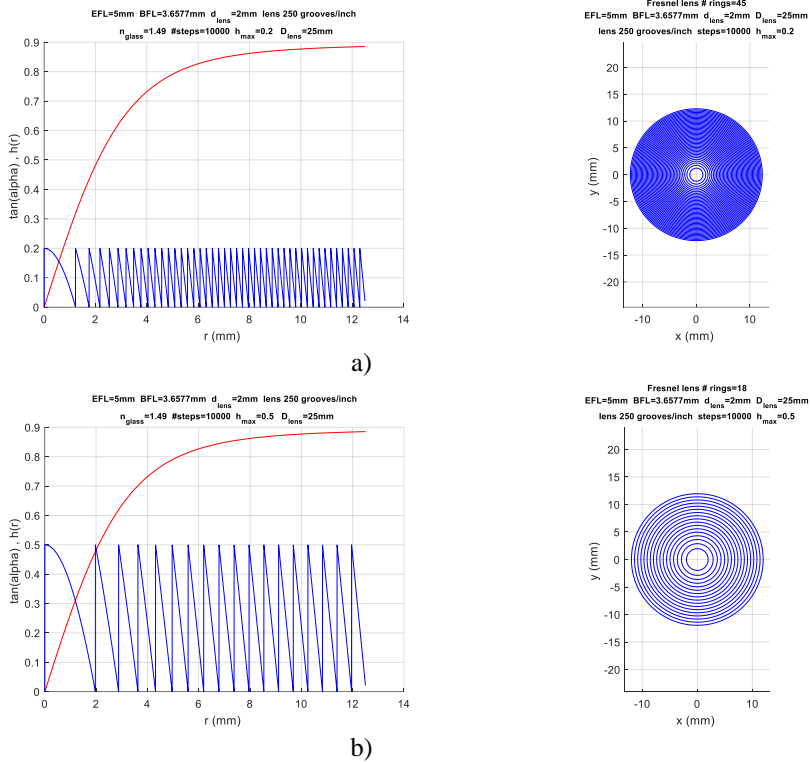


Fig. A- 15 Fresnel lens with $f=5\text{mm}$ and aperture $D_{lens}=25\text{mm}$, with maximum profile height a) $h_{max}=0.2\text{mm}$, and b) $h_{max}=0.5\text{mm}$

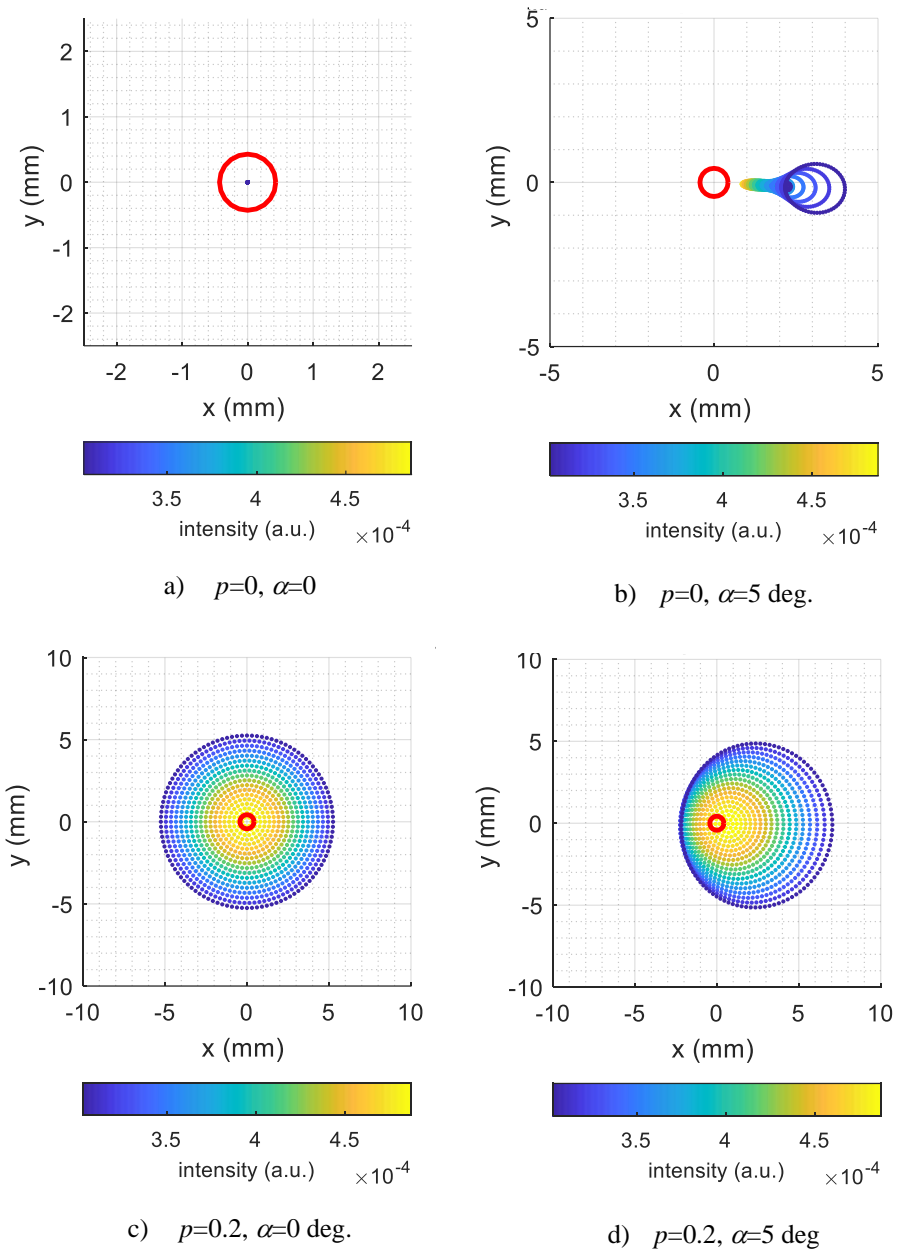


Fig. A- 16 Imaging of Gaussian beam $\varnothing 100\text{mm}$ by Fresnel lens $D_{lens} = \varnothing 50\text{mm}$, $f=10\text{mm}$ for focused ($p=0$) and defocused ($p=0.2$) operation, at beam incidence angles $\alpha=0$ and $\alpha=5$ deg.

A.4 References

- [1] Gaussian beam [Online]. Available: https://en.wikipedia.org/wiki/Gaussian_beam
- [2] Newton–Raphson’s method, a numerical root-finding algorithm [Online]. Available: https://en.wikipedia.org/wiki/Newton%27s_method

List of publications

A non-exhaustive list is given of publications relevant to the material reported in this thesis of which Ton Koonen is 1st author.

Journal publications (1st author)

- [1] A.M.J. Koonen, K.A. Mekonnen, F.M. Huijskens, E. Tangdiongga, “Bi-directional all-optical wireless Gigabit Ethernet communication system using automatic self-aligned beam steering,” *IEEE/OPTICA J. Lightw. Technol.*, Vol. 41, No. 11, June 2023, pp. 3446-3454. (<https://doi.org/10.1109/JLT.2022.3231438>)
- [2] A.M.J. Koonen, K.A. Mekonnen, Z. Cao, F.M. Huijskens, N.-Q. Pham, E. Tangdiongga, “Beam-steered optical wireless communication for industry 4.0”, *IEEE J. of Sel. Topics in Quantum Electron.*, Vol. 27, No. 6, Nov./Dec. 2021, art. 6000510 (10 pp.). (<https://doi.org/10.1109/JSTQE.2021.3092837>).
- [3] A.M.J. Koonen, K.A. Mekonnen, F.M. Huijskens, N.-Q. Pham, Z. Cao, E. Tangdiongga, “Fully passive user localization for beam-steered high-capacity optical wireless communication system,” *IEEE/OSA J. Lightw. Technol.*, vol. 38, no. 10, pp. 2842-2848, May 2020. (<https://doi.org/10.1109/JLT.2020.2980428>)
- [4] A.M.J. Koonen, K. A. Mekonnen, Z. Cao, F. M. Huijskens, N.-Q. Pham, E. Tangdiongga, “Ultra-high capacity wireless communication by means of steered narrow optical beams,” *Philosophical Trans. Royal Soc. A*, Mar. 2020, 19 pp. (<https://doi.org/10.1098/rsta.2019.0192>)
- [5] A.M.J. Koonen, F. Gomez-Agis, F.M. Huijskens, K.A. Mekonnen, Z. Cao, E. Tangdiongga. “High-capacity optical wireless communication using two-dimensional IR beam steering,” *IEEE/OSA J. Lightw. Technol.*, Vol. 36, No. 19, pp. 4486–4493, Oct. 2018. (<https://doi.org/10.1109/JLT.2018.2834374>)
- [6] A.M.J. Koonen, ‘Indoor optical wireless systems: Technology, trends, and applications,’ *IEEE/OSA J. Lightw. Technol.*, vol. 36, no. 8, pp. 1459–1467, Apr. 2018, <https://doi.org/10.1109/JLT.2017.2787614> .
- [7] A.M.J. Koonen, C.W. Oh, K.A. Mekonnen, Z. Cao, E. Tangdiongga, Ultra-high capacity indoor optical wireless communication using 2d-steered

- pencil beams,” *IEEE/OSA J. Lightw. Technol.*, Vol. 34, No. 20, pp. 4802–4809, Oct. 2016. (<https://doi.org/10.1109/JLT.2016.2574855>)
- [8] A.M.J. Koonen, E. Tangdiongga, “Photonic home area networks,” *IEEE/OSA J. Lightw. Technology*, vol. 32, no. 4, Feb. 2014, pp. 591-604. (<https://doi.org/10.1109/JLT.2013.2283145>)
- [9] A.M.J. Koonen, H.P.A. van den Boom, E. Ortego Martinez, A. Pizzinat, Ph. Guignard, B. Lannoo, C.M. Okonkwo, and E. Tangdiongga, “Cost optimization of optical in-building networks”, *OSA Opt. Exp.*, vol. 19, no. 26, pp. B399-B405, Nov. 2011. (<https://doi.org/10.1364/OE.19.00B399>)
- [10] A.M.J. Koonen, M. Garcia Larrode, “Radio-over-MMF techniques – part II: microwave to millimeter-wave systems”, *IEEE/OSA J. Lightw. Technol.*, vol. 26, no. 15, pp. 2396-2408, Aug. 2008. (<https://doi.org/10.1109/JLT.2008.927182>)

Conference publications (1st author)

- [1] Ton Koonen, “High-Capacity Optical Wireless Communication by Directed Narrow Beams,” *Proc. 28th Optoelectronics and Communications Conference (OECC2023)*, Shanghai, July 2-6, 2023, keynote paper OECC2023-0319-30, 6 pp.
- [2] Ton Koonen, Ketema Mekonnen, “Recent Progress in High-capacity Optical Wireless Communication,” *Proc. 2022 Asia Communications and Photonics Conference (ACP 2022)*, Shenzhen, Nov. 5-8, 2022, keynote paper, pp. 1819-1822.
- [3] A.M.J. Koonen, K. A. Mekonnen, F.M. Huijskens, E. Tangdiongga, “Bi-directional all-optical wireless communication system with optical beam steering and automatic self-alignment,” *Proc. ECOC 2022*, Basel, Sep. 18-22, paper Tu4F.1.
- [4] Ton Koonen, Zizheng Cao, “Photonic integrated circuits for optical wireless communication”, *Proc. 2021 Asia Communications and Photonics Conference (ACP 2021)*, Shanghai, Oct. 24-27, 2021, tutorial paper M5D.1, 3 pp.
- [5] A.M.J. Koonen, K.A. Mekonnen, F.M. Huijskens, N.-Q. Pham, Z. Cao, E. Tangdiongga, “Optical Wireless GbE Receiver with Large Field-of-View,” *Proc. ECOC2021*, Bordeaux, Sep. 2021, paper Th1B.6.
- [6] Ton Koonen, “Optical technologies to disclose the spatial diversity dimension in systems and networks,” *Proc. ACP 2020*, Beijing, 26 Oct. 2020, plenary talk, paper M1A1.
- [7] A. M. J. Koonen, K. A. Mekonnen, F. M. Huijskens, Z. Cao, E. Tangdiongga, “Novel Broadband OWC Receiver with Large Aperture and Wide Field of View”, *Proc. ECOC 2020*, Brussels, Dec. 2020, paper

- Tu2G.6.
- [8] Ton Koonen, Ketemaw Mekonnen, Frans Huijskens, Ngoc-Quan Pham, Zizheng Cao, Eduward Tangdiongga, "Recent advances in ultra-broadband optical wireless communication," *Proc. 2019 Asia Communications and Photonics Conference (ACP 2019)*, Chengdu, Nov. 2-5, 2019, Invited paper M3C.4, 3 pp.
 - [9] A.M.J. Koonen, K.A. Mekonnen, F.M. Huijskens, E. Tangdiongga, "Fully passive user localisation for beam-steered high-capacity optical wireless communication system," in *Proc. ECOC 2019*, Dublin, paper Tu.3.C.4, Sep. 22-26, 2019.
 - [10] Ton Koonen, Jiun-Yu Sung, Zizheng Cao, Ketemaw Mekonnen, Frans Huijskens, Eduward Tangdiongga, "Recent Advances in Optical Technologies for creating Ultra-High Capacity Wireless Indoor Networks," *Proc. 2018 Asia Communications and Photonics Conference (ACP 2018)*, Hangzhou, Oct. 26-29, 2018, Invited paper S4E.2, 3 pp.
 - [11] A.M.J. Koonen, A.M. Khalid, C.W. Oh, F. Gomez-Agis, and E. Tangdiongga, "High-capacity optical wireless communication using 2-dimensional IR beam steering," *Proc. OECC 2017*, Singapore, Jul. 31 – Aug. 4, 2017, paper 1-4K-3.
 - [12] A.M.J. Koonen, F. Gomez-Agis, Z. Cao, K.A. Mekonnen, F.M. Huijskens, E. Tangdiongga, "Indoor ultra-high capacity optical wireless communication using steerable infrared beams," in *Proc. MWP 2017*, Beijing, Oct. 2017, keynote paper.
 - [13] A.M.J. Koonen et al., "High-capacity optical wireless communication using AWG router for 2-dimensional IR beam steering," in *Proc. OECC 2017*, Singapore, July 31 – Aug.4, 2017, paper 1-4K-3.
 - [14] A.M.J. Koonen, C.W. Oh, A.M. Khalid, K.A. Mekonnen, M. Torres Vega, Z. Cao, and Eduward Tangdiongga, "2D beam-steered high-capacity optical wireless communication," *Proc. IEEE Summ. Top. 2016*, Newport Beach, paper TuC2.2.
 - [15] A.M.J. Koonen, C.W. Oh, K. Mekonnen, E. Tangdiongga, "Ultra-high capacity indoor optical wireless communication using steered pencil beams," in *Proc. MWP 2015*, Paphos, Oct. 25-29, 2015, paper WeC-5.
 - [16] A.M.J. Koonen, C.W. Oh, E. Tangdiongga, "Reconfigurable free-space optical indoor network using multiple pencil beam steering," *Proc. OECC/ACOFT 2014*, Melbourne, July 2014, paper Tu3F-1.
 - [17] Ton Koonen, "Home area networks," *Proc. OFC/NFOEC 2013*, Los Angeles, Feb. 22-27, tutorial OTh1G.1, 86 slides.
 - [18] Ton Koonen, Yan Shi, Shihuan Zou, Chigo Okonkwo, Henrie van den Boom, Eduward Tangdiongga, "Recent progress in photonic in-building

- networks,” *Proc. OECC 2012*, Busan, July 2-6, 2012, invited paper 6A3-1, 2 pp.
- [19] A.M.J. Koonen, Y. Shi, N.C. Tran, C.M. Okonkwo, H.P.A. van den Boom, E. Tangdiongga, “A perspective from Europe on in-home networking,” *Proc. OFC 2012*, Los Angeles, Mar. 4-8, 2012, invited paper NTh1D.1, 3 pp.
- [20] A.M.J. Koonen, N.C. Tran, and E. Tangdiongga, “The merits of reconfigurability in WDM-TDM optical in-building networks,” in *Proc. OFC/NFOEC 2011*, Los Angeles, Mar. 2011, Paper JWA63.
- [21] A.M.J. Koonen, H.P.A. van den Boom, I. Tafur Monroy, G.-D. Khoe, “High capacity multi-service in-house networks using mode group diversity multiplexing”, in *Proc. OFC/NFOEC 2004*, Anaheim, Feb. 2004, Paper FE-H.
- [22] A.M.J. Koonen, H. van den Boom, G.-D. Khoe, “Broadband access and in-house networks – extending the capabilities of multimode fibre networks”, in *Proc. ECOC 2003*, Rimini, Sep. 2003, paper Mo3.1.5.

Patents

- [1] A.M.J. Koonen, “Bi-directional all-optical wireless communication system with autonomous optical beam steering,” Dutch patent application No. 2032214, ref. P096073NL, filed June 17, 2022
- [2] A.M.J. Koonen, “Receiver for optical wireless communication with large aperture and wide angle of view,” Patent PCT/EP2020/080594, published May 6, 2021, priority date Oct. 31, 2019, EP4052390A1 published Sep. 7, 2022.
- [3] A.M.J. Koonen, “Two-dimensional optical beam steering module,” Patent PCT/EP2017/080716, published June 7, 2018, priority date Nov. 29, 2016.
- [4] Antonius Marcellus Jozef Koonen, Peter G.M. Baltus, Antonio Liotta, “Two-dimensional optical beam steering module,” US patent 9246589 B2, WO patent 2013107853, priority date Jan. 20, 2012, filing date Jan. 18, 2013.
- [5] A.M.J. Koonen, “Werkwijze en stelsel voor het via een multi-modus optische vezel overdragen van microgolfsignalen” (Method and system for transport of microwave signals via a multimode optical fibre), Dutch patent NL1019047, issued April 2, 2003.
- [6] A.M.J. Koonen, “Re-configurable fibre wireless network”, US Patent No. 6,674,966, filed Oct. 12, 1999, issued Jan. 6, 2004.

Miscellaneous

- [1] Ton Koonen, “Light work(s),” Valedictory lecture, Eindhoven University of Technology, Sep. 24, 2021. ISBN 978-90-386-5365-5, NUR 959. Available: <https://research.tue.nl/en/publications/light-works>
- [2] A.M.J. Koonen, “Optical wireless systems: technology, trends and applications,” webinar IEEE Phot. Soc., Feb. 21, 2018 [online]. Available: <https://ieeephotonics.org/webinars/optical-wireless-communication/>

Curriculum vitae



Ton (Antonius Marcellus Jozef) Koonen was born in Oss, 20 Oct. 1954. He received an MSc cum laude in Electrical Engineering from Eindhoven University of Technology (TU/e) in 1979. He subsequently worked in applied research at Philips' Telecommunicatie Industrie (1979-1984), AT&T Network Systems (1984-1987), and Lucent Technologies–Bell Laboratories (1994-2000), initially as Member of Technical Staff, and since 1987 as Technical Manager. Ton was a part-time professor in the Telecommunication Systems group at the University of Twente (1991-2000). He was appointed as a full-time professor of “Breedbandige netwerken” (Broadband Networks) in the Department of Electrical Engineering at TU/e on Jan. 1, 2001, and officially retired on Feb. 19, 2021.

Ton chaired the Electro-Optical Communication Systems group (2004-2021) in the Department of Electrical Engineering (EE). He was vice-dean of the EE department (2012-2020), and Scientific Director of the Institute for Photonic Integration (formerly COBRA; 2016-2019).

Ton is a Bell Labs Fellow (1998, first one in Europe), IEEE Fellow (2007), Fellow of the Optical Society of America (2013) and High-level Visiting Scientist at Beijing University of Posts and Telecommunications (111 Program, 2018-2023). He is a Principal Investigator in the Dutch Gravitation programs ‘Center for Integrated Nanophotonics’ and ‘Networks’ (both 2013-2023). He is co-initiator and co-leader of the Dutch NWO Perspective program ‘FREE - Optical Wireless Superhighways’ (Sep. 2021-Aug. 2026). Ton received the ICTRegie Award in 2009. In 2012, he received the prestigious Advanced Investigator Grant of the European Research Council on optical wireless communication, followed by a Proof-of-Concept Grant in 2018. With this research, Ton was one of the six finalists in the national Huibregtsen prize competition in 2018. At his valedictory lecture on Sep. 24, 2021, he received the Dutch Royal distinction ‘Ridder in de Orde van de Nederlandse Leeuw’ (‘Knight in the Order of the Dutch Lion’).

Ton initiated and managed a wide range of national and international projects in optical systems research and secured more than €30M in funding. He (co-)authored more than 750 conference and journal papers, with 12726 citations, h-index 51 (according to Google Scholar, Nov. 11, 2023), and filed/holds 12 patents.

Acknowledgments

While arriving at the end of writing this thesis, it feels for me like completing a challenging, demanding, but also very interesting and enjoyable journey. It may look a bit curious to complete a PhD thesis after having delivered a valedictory lecture... I gave this lecture on Sep. 24, 2021, following my 'official' retirement on Feb. 19, 2021. The lecture had the title "Light work(s)", reflecting not only the great potential which light has proven to have for communication (and many other application domains), but also that working in optical communication feels 'light', as it was truly enjoyable in all these years since 1979 when I started my career in it. This has been a mixed career, which began in 1979 in applied research in industry (Philips' Telecommunication Industry, AT&T and Philips Telecommunications, AT&T Bell Laboratories, Lucent Technologies Bell Laboratories), next included a first step into the academic world by a part-time professor position in University of Twente (1991-2000), and then completely stepped into the academic world with my full-time professor appointment in Eindhoven University of Technology since January 2001. So, looking back, it has been a nearly 50/50% industrial/academic career, which for me felt like enjoying the best of both worlds. And the 'red thread' was my preference for 'applied research', research which can be applied in real life. Nevertheless, after having graduated more than 40 PhD students as promotor, it felt like a link was somewhat missing in the career chain, namely doing a PhD myself, for which I did not get (or take...) the opportunity... So, being retired now, and stimulated by the encouragement of our former EE dean prof. Bart Smolders and the nice PhD graduation example of my brother-in-law and contemporary peer dr. Herman Kaiser, I took up the bold challenge to start writing...

To compile into a single booklet my research activities and series of publications during the optical wireless communication journey since 2012 took more effort than I originally expected. These efforts were aggravated by the so-called 'progressing insights' gained while making the journey... These had to be accommodated in the booklet too, as well as entailed some restructuring as a thesis is not necessarily a chronological story. The journey started in 2012, when I learned that the European Research Council had awarded my proposed project 'BROWSE - Beam-steered Reconfigurable Optical-Wireless System for Energy-efficient communication' with an Advanced Investigator Grant, the ERC's most prestigious personal grant. After BROWSE was finished in 2017, funding by a smaller Proof of Concept grant 'BROWSE+' from ERC followed in 2018, which enabled to add further steps to my pioneering concepts, plus since 2018 also funding from the Dutch Research Council (NWO, Nederlandse Organisatie voor

Wetenschappelijk Onderzoek) as part of the Gravitation program ‘Center for Integrated Nanophotonics’, and since 2021 support from NWO in the Perspective program ‘FREE – Optical wireless superhighways’ which is led by prof. Eberhard Gill of Delft University of Technology and myself. I was so lucky to recruit a very talented team of young researchers as my travel companions, plus the support of strong colleagues.

The work reported in this thesis has truly been a joint effort, for which I owe sincere thanks to my many PhD students, colleagues and friends without whom the journey would not have been possible...

Let me start by thanking the members of my PhD committee for the precious time they devoted, and the very valuable suggestions they made. Firstly, my thanks go to prof. Sonia Heemstra de Groot with whom I worked since my first academic steps in University of Twente, for being my first promotor and scrutinizing my thesis, and to dr.ir. Eduward Tangdiongga, my colleague and travel companion from the start of BROWSE, for being my second promotor. I thank the international members of my PhD committee, prof. Dominic O’Brien, prof. Volker Jungnickel, prof. Jose Capmany, for their expert advice and being such great colleagues to cooperate with in optical communication research. I thank prof. Bart Smolders who persuaded me to do a PhD even after retirement, prof. Marion Matters-Kammerer for also joining in in the BROWSE journey, and last but not least prof. Ignas Niemegeers who actually was the one who seduced me to step into the academic world by recruiting me as part-time professor in University of Twente.

Next to the committee members, I thank prof. Giok-Djan Khoe for convincing me to come to Eindhoven University of Technology, and to succeed him as chairman of the Electro-Optical Communication systems (ECO) group which has been a real pleasure to chair for more than 16 years. In addition, I am grateful to the other ECO staff for their collegiality and friendship, dr. Huug de Waardt, ir. Henrie van den Boom, dr. Oded Raz, dr. Nicola Calabretta, dr. Patty Stabile, dr. Chigo Okonkwo, dr. George Exarchakos, prof. Idelfonso Tafur Monroy, to prof. Harm Dorren and ing. Johan van Zantvoort who sadly are no longer with us, and last but certainly not least to ing. Frans Huijskens for his great technical support. And, of course, to Jose Hakkens for her continuous invaluable support in every detail of my ECO roles, recently also with help from Ginny Toes.

The research described in this thesis could not have been done without the great work by my PhD students. First of all, I owe a lot of thanks to dr. Ketemaw Addis Mekonnen, who was a member of the BROWSE team and meticulously did most of the experimental work described in this thesis, after his PhD graduation also

as post-doctoral researcher. Next, to the other graduated BROWSE PhD students dr. Joanne (Chin Wan) Oh, dr. Maria Torres Vega (supported by prof. Antonio Liotta), and dr. Bindi Wang (supported by prof. Peter Baltus, prof. Marion Matters-Kammerer, and dr. Dusan Milosevic). Great work in optical wireless has been done as well by my PhD graduates dr. Zizheng Cao, dr. Xuebing Zhang, dr. Carina Ribeiro Barbio Corrêa, dr. Haotian Zheng, dr. Ngoc Quan Pham, dr. Liuyan Chen, dr. Yu Lei, and is being done by Yu Wang, Yuchen Song, Mikolaj Wolny, and Eduardo Muller. Moreover, thanks are due to post-doctoral researchers dr. Fausto Gomez Agis and dr. Amir Khalid for their record-breaking OWC experiments. In radio-over-fiber research, I was most happy to have guided my PhD graduates dr. Anthony Ng'oma, dr. Maria Garcia Larrodé, dr. Jim (Shihuan) Zou, dr. Hejie Yang, dr. Netsanet Merawi Tessema, dr. Solomon Tesfay Abraha, dr. Yan Shi, and dr. Federico Forni. In fiber access and fiber indoor networks research, my thanks go to dr. Nguyen-Cac Tran, dr. Nikos Sotiropoulos, dr. Bas Huiszoon, dr. Patryk Urban, dr. Archi Delphinanto, dr. Jeffrey Lee, and dr. Robbert van der Linde. In mode group division multiplexing (and spatial division multiplexing), I am indebted to dr. Haoshuo Chen and dr. Christos Tsekrekos.

Without any doubt, I would not have reached this stage if not with the support of the 'homefront'. I owe very much to my father and mother, who supported me unconditionally. Unfortunately, they cannot witness this last academic episode, but they were there when I started the first one in University of Twente. I am deeply grateful to our three sons Martijn, Robin and Laurens, for overcoming the sometimes too busy times of their dad, and many thanks also to our 'daughters-in-law' Eva and Misha. Above all I am profoundly grateful to Annemie, my great love since more than 46 years, who surprises me every day with her unexpected remarks and endless understanding, even when I was from time to time hardly approachable... Annemie: I love you, and more relaxed times are coming now!

Ton Koonen
Nuenen, Dec. 2023